STUDIES OF HOLLOW CATHODE HE-CD LASERS

C.A. Pirrie

A Thesis Submitted for the Degree of PhD
at the
University of St Andrews

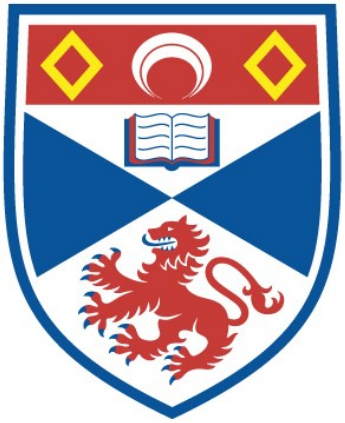

1985

STUDIES OF HOLLOW CATHODE He-Cd LASERS

A thesis presented by C. A. Pirrie, B.Sc., to the University of St. Andrews in application for the Degree of Doctor of Philosophy.

January, 1984

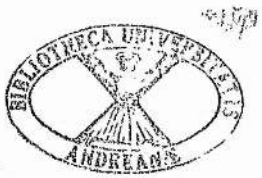

DECLARATION

I hereby certify that this thesis has been composed by me, and is a record of work done by me, and has not previously been presented for a higher degree.

This research was carried out in the Physical Sciences Laboratory of St.Salvator's College, at the University of St.Andrews, under the supervision of Dr.A.Maitland.

C.A.Pirrie.

CERTIFICATE

I certify that C.A.Pirrie has spent nine terms at research work in the Physical Sciences Laboratory of St.Salvator's College, in the University of St.Andrews, under my direction, that he has fulfilled the conditions of Ordinance No.16 (St.Andrews) and that he is qualified to submit the following thesis in application for the Degree of Doctor of Philosophy.

Dr.A.Maitland

Research Supervisor.

ACKNOWLEDGEMENT

I wish to thank Dr. A. Maitland, of the Department of Physical Sciences, University of St. Andrews, and Mr. H. Menown, of the English Electric Valve Co., Ltd., for their help encouragement and advice throughout this work. I gratefully acknowledge the help of Mr. R. McCraw and his workshop staff for their technical assistance, and Mr. F. Akerboom for the glasswork. Finally, I wish to thank the Directors of the English Electric Valve Co., Ltd., who provided the sponsorship for this work.

ABSTRACT

Novel segmented-electrode discharge tubes which operate as sealed-off He-Cd hollow cathode lasers and which do not require a flowing gas system to distribute cadmium vapour are reported. The electrode geometry is arranged to produce a net axial electric field so that cadmium distribution is enhanced by cataphoresis, a process which is not normally associated with He-Cd hollow cathode lasers. The conditions under which the segmented-electrode tubes exhibit the properties of hollow cathode discharges are determined from their current and voltage characteristics. One system studied consists of alternate anode and cathode segments with glass insulating sections arranged axially, and behaves as a series of hollow cathode discharges under appropriate conditions. Each anode/hollow cathode pair is separated from its neighbouring segments by insulating glass sections of length D, which provide a recombination site and prevent adjacent discharges from overlapping each other. A calculation shows that adjacent discharges will remain isolated provided that $D > 2.85$cm, in helium at 10 Torr and 700 K. Another segmented-electrode system studied consists of a series of metal segments equal in length. This system does not have discrete anode segments and exhibits the positive Volt-Ampere (VI) characteristics normally expected of hollow cathode discharges only at low values of discharge current. A transition point in the characteristics exists, and, for discharge currents above this, the VI slope is negative. This behaviour is explained in terms of the plasma length, which is defined as the axial extent of the negative glow within a cylindrical segment, and

which increases with increasing discharge current. At low values of discharge current (several mA), the plasma length is less than the length of the metal segments, and the discharge tube operates as a series of hollow cathodes. Under these conditions, each segment has a negative glow discharge partially penetrating the bore from one end, while the other end performs as an anode for the next segment, and so on. The last segment is at power supply earth potential and has no anodic function. The transition points in the VI characteristics occur when the discharge current is increased to a value such that the plasma length equals the length of the metal segments. For discharge currents above this value, only the last segment at power supply earth potential continues to operate as a hollow cathode. The results of these studies provide guidelines for the design of segmented-electrode He-Cd hollow cathode laser discharge tubes in terms of the axial order and optimum spacing of anode and cathode segments.

It is shown that large axial temperature variations can exist in thin-walled (0.9mm) hollow cathode structures, implying that the current density distribution at the cathode surface is not uniform. A differential equation is derived to describe heat flow within a cylindrical conductor heated at one end and cooled by natural convection and radiation along its length. Approximate solutions are obtained for both thick-walled and thin-walled conductors. The results of the thick-walled approximation yield thermal design criteria for hollow cathodes, where moderate cathode temperatures (350^{o}C) and minimal axial temperature variations are required. The thin-walled approximation yields results which provide design criteria for the protection from high temperature failure of components such as cylindrical glass/metal seals and 'O' rings. Studies of a further two sealed-off discharge tubes,

designed in accordance with the results of the thermal analysis, are reported. Maximum axial variations of $10^{o}C$ were recorded on the cathodes of these tubes. Spectroscopic studies of the discharges show that hydrogen exists as a major impurity and manifests itself in the appearance of violet-degraded molecular bands due to Cd H. A calculation shows that the majority of Cd atoms present in the discharge may be in the Cd ($5s\ 5p\ ^{3}P_{2,1,0}$) state. The following energetically favourable reaction is thus the most likely formation process for Cd H,

$$H_2 + Cd\ (5s\ 5p\ ^{3}P_{2,1,0}) \longrightarrow Cd\ H + H$$

Several other reactions which involve hydrogen and which may affect laser performance are proposed. A broad-band absorption experiment revealed the presence of a transient species (unidentified) which was detected only while a discharge was established. An absorption coefficient of 8% per metre was measured in the vicinity of the red and green CdII laser transitions.

In addition to the studies of He-Cd lasers having novel electrode geometries, design calculations for multilayer dielectric laser mirrors are also given, using a novel technique based on flow-graphs. The flow-graph calculations are developed and the results are compared with those obtained by using established ray summation and matrix methods. The flow-graph method is applied to the design of dielectric multilayer mirrors required for 'white-light' He-Cd lasers. Multilayer structures for two output couplers and a 'total' reflector are presented, where the alternate dielectric layers are MgF_2 and ZnS (refractive indices 1.38 and 2.3 respectively).

CONTENTS

CONTENTS

Chapter Two: Segmented Discharge Tube Structures

CONTENTS

CONTENTS

Chapter Four: Design, Construction and Spectroscopy of Tubes Nos. 5 and 6

CONTENTS

CHAPTER ONE

REVIEW OF He-Cd LASERS

1.1 General Introduction.

The first observations of cw laser emission from the positive column of a helium discharge seeded with cadmium vapour were reported in 1968 (Silfvast, 1968). Since then, the efforts of many workers have provided an insight into the processes responsible for observed experimental behaviour, such as upper laser level pumping mechanisms and output power saturation. In particular, improvements in tube design and studies of the factors affecting the "sealed-off" lifetime have led to more reliable operation of this type of laser. As a result of this research and development, positive column helium-cadmium lasers with lifetimes in excess of 1000 hours soon became commercially available (for example RCA Model Ld 2194, Spectra Physics Model 185). The same however is not true for hollow cathode He-Cd lasers, which utilize the negative glow of the gas discharge. The first hollow cathode He-Cd laser was reported in 1970 (Shuebel,1970), and because of its

multispectral output, in particular the visible laser transitions in blue, green and red, it has been studied in depth over the last decade as a potential candidate for reliable "white-light" laser operation.

This introductory chapter traces the chronological development of both positive column and hollow cathode He-Cd lasers, compares the various excitation mechanisms and highlights the problems associated with each type. However, before this is undertaken, the inherent differences between the positive column and the negative glow are such that a more general approach in terms of gas discharge phenomena is desirable. The next section is devoted to this end.

1.2 The D.C. Glow Discharge at Low Pressures.

A cylindical gas discharge vessel, length 20 cm and diameter 1 cm, with a planar electrode at either end, is illustrated in fig 1.1. The vessel contains gas at low pressure (eg helium at 10 Torr). When a discharge of several tens of milliamperes is established, four distinct regions with different characteristics are observed. The region nearest the cathode, the cathode dark space, is short (<0.5 mm) and at higher pressures is almost unobservable. Moving towards the anode, the second region encountered is the intensely luminous negative glow, which is brighter towards its cathode end, and drops off in intensity towards the Faraday dark space, a region of low luminosity. Beyond

the Faraday dark space, the positive column, a (generally) uniform region of high luminosity fills the rest of the vessel almost to the anode.

The distribution of potential down the length of such a discharge is also illustrated in fig 1.1. There is a sharp rise in potential, the "cathode-fall", across the cathode dark space, which levels off abruptly as the negative glow is encountered. The magnitude of the cathode fall depends on gas composition, electrode material and discharge current. In the negative glow there is little or no change in potential. The potential starts to rise again across the Faraday dark space, and rises linearly (typically 10-100 V/cm, depending on tube radius) through the positive column, almost to the anode, where there is another small rise in potential. Of these regions, the positive column and the negative glow are used as excitation media for low pressure gas discharge lasers.

1.2.1 The Positive Column.

If the discharge tube illustrated in fig 1.1 was increased in length with gas pressure, current and tube diameter remaining the same, the positive column would occupy the extra volume, the other regions being unchanged. Thus, a long optical path length in the positive column can be achieved easily, if the power supply can provide the extra voltage required to maintain the discharge. A long optical path length is necessary where the laser

gain per unit length is small (5 % per metre in He-Cd, using Cd of natural isotopic abundance, Silfvast, 1968). Also, the positive column is homogeneous (although, under certain conditions, discharge striations which lead to noise in laser output are present - these will be discussed briefly in section 1.4).

The positive column has a uniform axial electric field, which, from Poisson's equation, implies that the net charge density is zero, thus the numbers of positive and negative charge carriers are equal. In positive column He-Cd lasers, the reduced electric field value (E/p) generally lies in the range 4-16 Volts/cm-Torr, while the electron density is 1-5 x 10^{12} cm^{-3} (Dunn,1972; Mizeraczyk,1975; Mori et al,1977).

The form of the electron distribution function in the positive column is frequently assumed to be Maxwellian, and correspondingly an electron temperature can be defined from $eV = kT_e$. Although, in general, the electron distribution function in a positive column is not strictly Maxwellian, the deviation in most probable energy incurred by making this assumption is only a few eV (Mainwaring and Swift,1972). The most serious error occurs in the high energy tail of the distribution where significantly fewer electrons have sufficient energy to excite higher lying levels in atoms and ions than the assumed Maxwellian distribution would indicate (Mori et al,1977).

1.2.2 The Negative Glow and Cathode Region.

The basic processes in the region of the cathode are qualitatively well understood. Electrons leaving the cathode are accelerated across the dark space by the cathode fall voltage, and collisionally excite and ionise atoms to give electron multiplication, M. The positive ions, excited neutrals and photons formed by this process impinge upon the cathode surface, releasing secondary electrons. If, for each of the (M - 1) electrons produced in the gas, γ secondary electrons are released at the cathode by these various processes, then in a self-sustained discharge we have

$$\gamma (M-1) = 1 \qquad (1)$$

where γ and M depend on gas composition, discharge current and cathode material. The negative glow is a result of ionisation and excitation by electrons which are accelerated by the cathode fall voltage. In thermionic or "hot" cathode discharges, there is almost no cathode fall voltage and correspondingly no negative glow. In this case, secondary emission from the cathode is unnecessary for maintainance of the discharge because electrons are supplied thermionically.

Returning to the discharge tube illustrated in fig 1.1, the anode may be moved towards the cathode until there is no positive column or Faraday dark space, and the truncated discharge comprises only cathode dark space and negative glow. However, the negative glow in this form is unsuitable for laser

excitation because the optical path length is short, and the glow lacks homogeneity, being brighter towards its cathode end. Both of these problems are overcome in a hollow cathode geometry but, before considering the principles underlying its operation, an examination of the terminal volt-ampere characteristics is appropriate.

The truncated discharge tube is illustrated in fig 1.2, together with "typical" VI characteristics. At the lower range of currents (a few mA), the cathode surface is only partly covered in negative glow. The area of cathode covered by negative glow is proportional to the discharge current and thus the current density at the cathode surface remains constant (Hehl's law). This is the "normal glow" regime and is characterised by constant current density and discharge voltage. Once the current is increased sufficiently to cover the entire cathode surface with negative glow, a further increase in discharge current results in increased current density and discharge voltage. This is termed the "abnormal glow" regime.

The electron distribution function in the negative glow is strongly non-Maxwellian in form and has three distinct groups of electrons present. A typical distribution function is shown in fig 1.3, which is taken from Gill and Webb, 1977, who used a differentially pumped retarding field analyser to obtain their results. The three groups of electrons are as follows.

(1) A "beam" component, comprising electrons accelerated through the entire cathode fall voltage having energy eV_c.

(2) A high energy tail, which follows a 20 eV gap corresponding to the first excitation potentials of helium. The electrons in this

part of the distribution have undergone one or more inelastic collisions.

(3) At low energy (< 25 eV) there is a "plasma" component for which the most probable energy lies in the range 5-10 eV.

Although the results of Gill and Webb apply to a planar cathode, they emphasize the most significant difference between the positive column and the negative glow. In the negative glow, a significant proportion of electrons have sufficiently high energy to excite the ionic levels of the carrier gas, in this case helium.

1.2.3 The Hollow Cathode Effect.

A long optical path length can be obtained in the negative glow if the discharge tube has a long parallel-plane electrode configuration, as illustrated in fig 1.4(a). However, a stronger glow may be obtained from a double cathode geometry as illustrated in fig 1.4(b), where the intercathode spacing is such that the negative glows from each cathode coalesce. Taking this process a stage further, a cylindrical cathode, fig 1.4(c), or a "slotted" cathode, fig 1.4(d), will provide an even stronger coalescence because the cathode now represents an infinity of cathode pairs diametrically opposite each other.

The important features of a hollow cathode discharge are current densities which are larger than those for the planar cathode case, for the same cathode fall, and a negative glow which

gives high intensity spectral lines characteristic of the gas and/or cathode material.

The hollow cathode effect for planar electrodes becomes apparent for ap values below 3 torr-cm, where a is the intercathode separation and p is the (helium) pressure.

The electron density in a hollow cathode discharge in pure helium has been observed to increase linearly with discharge current and lies in the range 10^{13} - 10^{14} cm^{-3} for current densities appropriate to laser oscillation (Dunn and Belal, 1978).

The mechanisms responsible for the increase in cathode current density are qualitatively well understood. Photons and positive ions formed in the discharge cannot escape from the discharge region as easily as they may in a planar cathode discharge. Thus secondary emission at the cathode surface due to ion bombardment and the photoelectric effect is enhanced. Correspondingly, the opposite effect is apparent (reduced current density for a given cathode fall voltage) where convex cathodes (such as rods or spheres) are used.

Several different cathode structures, all of which utilize the hollow cathode effect to a greater or lesser degree, have been designed and operated as He-Cd lasers by various workers since 1970, and these are described in section 1.5 of this chapter.

1.3 Development of the Positive Column He-Cd Laser.

The first cw dc discharge He-Cd laser oscillating on the 441.6 nm line of Cd II ($5s^2\ ^2D_{5/2} - 5p\ ^2P_{3/2}$ transition) was reported in 1968 (Silfvast, 1968), although essentially cw operation at the same wavelength from an ac excited discharge had been reported earlier (Fowles and Hopkins, 1967). Silfvast obtained output powers in the range 5-50 mW for discharge currents of 10-125 mA, from a 1m length discharge tube. Isotopically enriched Cd^{114} placed either directly in the discharge tube or at 15 cm intervals in small side-cups provided a sufficiently uniform distribution of cadmium vapour. Silfvast expected a factor of four increase in gain by using the single Cd^{114} isotope instead of Cd of natural isotopic abundance because of the latter's larger isotopic linewidth. Subsequent measurements of gain by Silfvast showed this to be justified (20% per metre for Cd^{114}, 5% per metre for natural cadmium). The discharge tube was mounted in a tubular furnace which maintained the discharge at a chosen temperature in the range 150 - 250 ^{o}C. The observed dependence of output power on discharge current and helium pressure, and the lack of laser emission when neon was substituted for helium, led Silfvast to propose that Penning ionisation was the predominant mechanism responsible for populating the upper laser level:

$$He(metastable) + Cd(ground) \rightarrow He + Cd(5s^2\ ^2D_{5/2}) + e^-(\Delta E). \qquad (2)$$

Thus a collision between a helium metastable atom and a ground state cadmium atom simultaneously ionises the cadmium atom and

excites it to higher ionic levels. The excess energy ΔE, being the energy difference between He(metastable) and Cd II ($5s^2\ ^2D_{5/2}$), is carried off as kinetic energy by the ejected electron. A partial energy level diagram for helium and cadmium showing the relevant energy states is illustrated in fig 1.5. Silfvast further proposed that a similar reaction to that above may give rise to laser oscillation on the 325.0 nm line of cadmium ($5s^2\ ^2D_{3/2} - 5p\ ^2P_{1/2}$). This was soon reported, along with other metal ion transitions in zinc and tin (Silfvast 1969). The behaviour of the 325.0 nm line with respect to discharge current, helium pressure and cadmium vapour density was observed to be similar to that of the 441.6 nm line, although the laser output is generally up to an order of magnitude lower in power.

A limitation inherent in the original design by Silfvast was the influence of discharge heating on the tube temperature. Discharge current and metal vapour pressure could not be optimised independently of one another. As a consequence, maximum laser output of 50 mW, which occurred at the top of the current range investigated, was obtained only for a short period of time.

This problem was overcome by the introduction of a cataphoretic technique for the distribution of metal vapour in the discharge region, (Goldsborough, 1969; Sosnowski, 1969). Cataphoresis is the process whereby, in a positive column discharge in a two component gas mixture, the lowest ionisation potential component (Cd in this case) is preferentially driven towards the cathode end of the discharge. Experimentally, the magnitude of the cataphoretic effect has been noted to be proportional to ion

current (Goldsborough, 1969) while theoretically several models have been developed to explain the effect, among them being those of Druyvestyn (1934) and Freudenthal (1967).

The discharge tube designed by Goldsborough is illustrated in fig 1.6, and differs little in basic design from the commercially available He-Cd tubes today. The cadmium metal source is located in a bulb or sidearm near to the anode. In operation, cadmium vapour is continuously fed into the discharge and is transported by cataphoresis down the bore where it condenses on cool surfaces near the cathode. The cadmium source requires only a small heater element which obviates the need for the cumbersome furnaces hitherto used. Furthermore, provided discharge heating can maintain the bore temperature above that of the cadmium source, cadmium vapour pressure in the discharge depends only on source temperature. Discharge current and metal vapour pressure may thus be optimised independently of one another. As a consequence, Goldsborough obtained 200 mW of laser power at 441.6 nm using cadmium of natural isotopic abundance and a tube with an active length of 143 cm. Optimum output power occurred at a helium pressure of 3.4 Torr and a discharge current of 110 mA. Under these conditions, the rate of usage of cadmium was 1.5 gram/1000 hours.

A relatively simple tube of short length (26 cm), with a segmented bore, and having several cadmium sources distributed along the length of the discharge, was reported in 1971 (Silfvast and Szeto, 1971). In this design, the cadmium was heated by discharge current alone and output powers of 10 mW at 441.6 nm and 2.5 mW at 325.0 nm were obtained for a discharge current of

65 mA.

A more complicated design incorporating a recirculation geometry was introduced by Hernqvist (1972). Cadmium was continuously recirculated from its sources near the anodes at each end of the tube, along the bore to the centrally situated cathode, and then back through a return path of large diameter to the sources. This design also used cataphoresis to ensure that the flow of cadmium was directed away from the anodes at each end of the tube, towards the centrally situated cathode. By this means, the Brewster angled windows were protected from cadmium condensation by forming a cataphoretic "bottle" with the discharge electrodes.

The loss of helium by various clean-up processes was found to be a major factor affecting the sealed-off lifetime of He-Cd positive column lasers (Sosnowski and Klein, 1971). Through a series of simple experiments, it was shown that the major cause of helium loss was helium ion entrapment in soft cadmium deposits condensed on regions near the discharge. This could account for a loss of up to 38 millitorr/litre-hour which is a large loss rate in tubes whose initial pressure generally lies in the range 3-4 Torr. This loss process was eliminated by allowing cadmium to condense only on cool regions sufficiently far away from the discharge to ensure that the helium ion density was negligibly small. Diffusion of helium through the glass walls was found to contribute much less to the overall losses. However, where lifetimes of several thousands of hours are required, diffusion losses need to be taken into account. Modern commercial He-Cd lasers include a gas ballast volume connected to the discharge via a thin silica membrane. When

heated, the rate of helium diffusion through the membrane from the ballast volume to the discharge increases, thus making up for any helium loss that may have occurred, (for example, Kimmon Electric Co He-Cd laser, model CDR 15SG; Liconix He-Cd laser, model 4210).

Random fluctuations in output power levels have also been observed as a troublesome characteristic of He-Cd positive column lasers. Typical noise levels of around 20% peak-to-peak in the frequency range 0-500 kHz have been reported (Brown and Ginsberg, 1974). The origin of noise in the output has been attributed to several factors, including local variations in the density of excited cadmium ions (Gelikonov and Zaitsev, 1977) and striation waves in the positive column (Johnstone and Kolb, 1976) However, by careful selection of helium pressure, discharge current and cadmium vapour density, noise levels below 1% can be achieved although sometimes at a slight sacrifice in output power (Silfvast and Szeto, 1971; Weiger and Nemec, 1978).

1.4 Excitation Mechanisms in the Positive Column.

Since Silfvast first proposed that Penning reactions were responsible for producing the population inversion in the cadmium ion, much of the research involving He-Cd positive column lasers has been directed towards gaining a more detailed understanding of the processes responsible for the observed experimental behaviour. In particular, the saturation of laser output power as a function of pressure, current and metal vapour

density has been the subject of investigation by many workers. Giallorenzi and Ahmed (1971) suggested that the primary cause of saturation effects lies in the inelastic electron collisions which depopulate the the He metastable levels. Starting with the assumption that Penning ionisation was the predominant excitation mechanism, they found that the behaviour of laser output and sidelight line intensities could be adequately described in terms of relatively simple rate equations. Direct measurements of the helium triplet and singlet metastable densities as functions of helium filling pressure, cadmium vapour density and discharge current were obtained by Browne and Dunn (1973), using a line absorption technique. Their results showed that in a pure helium discharge, metastable densities displayed pronounced maxima at a helium pressure of 2 Torr and reached saturation at currents above 20 mA. The addition of a small amount of cadmium vapour to the discharge was found to increase the current at which metastable densities saturated (to 120 mA) and to halve the value of the maximum metastable densities achieved. They concluded that the observed optimum performance of He-Cd lasers is directly related to the behaviour of the metastable densities, thereby emphasizing the importance of Penning ionisation as a pumping mechanism. Furthermore, they found that the dominant loss mechanism for metastables was ionisation by electrons, reinforcing the results of Giallorenzi and Ahmed (1971).

Meanwhile, the work of others indicated that there may be at least two processes involved in the inversion mechanism. Csillag et al, (1970) showed that the presence of striations in the discharge enhanced laser oscillation at 441.6 nm. Willgloss and

Thomas (1973, 1974) showed that a "break point", which could be easily overlooked, occurred in the curve of laser output versus discharge current, and further demonstrated that an increase in current above the break point was accompanied by the onset of discharge striations. They attribute these striations to the "SESER" effect (Source of Electrons in a Selected Energy Range). Briefly, this occurs when a group of low energy electrons encounters a spatial potential drop of 10-20 eV, thereby increasing their energy. The electrons then lose this energy by inelastic collisions with the gas, which manifests itself as a striation. From their experimental observations of line intensities in sidelight and endlight, they conclude that direct electron excitation to the upper laser level occurs together with Penning ionisation.

The work of Mori et al, 1977, 1978 and Goto et al, 1976 has provided much information on the population densities of various atomic and ionic levels in positive column He-Cd discharges. In particular, direct measurements of the upper and lower population densities involved with the 441.6 nm transition have been made using a modified line absorption and gain technique (Mori et al, 1978). Their results show that the population density of the laser lower level is significantly large to warrant its inclusion in the interpretation of saturation mechanisms. Furthermore, they find that the observed laser output power performance cannot be explained solely in terms of Penning excitation. Besides the Penning process, they conclude that stepwise electronic excitation from the Cd II ground state is a major pumping mechanism for the Cd II 441.6 nm upper laser level.

Futher experimental evidence has recently substantiated these findings (Goto et al, 1981, Hane et al, 1981).

1.5 Development of Hollow Cathode He-Cd Lasers.

Stimulated emission from a hollow cathode He-Cd discharge (cw) was first observed in 1970 by Schuebel, (1970), who reported six new laser wavelengths, all attributable to transitions in Cd II. These were in the green (533.7 and 537.8 nm), hitherto only observed in pulsed discharges, the red (635.5 and 636.0 nm), and the near infra-red (723.7 and 728.4 nm) regions of the spectrum. The transverse discharge was maintained in a structure consisting of an outer Kovar anode tube, 9.4 mm ID, and an inner Kovar cathode rod in which a 2 mm slot had been machined. The active length was 45 cm and the cadmium source consisted of wire laid along the internal anode surface opposite the cathode slot. The anode could then be heated or cooled externally. Discharge voltage was typically 300 V and threshold current for oscillation lay in range 130 - 180 mA, increasing in the sequence of wavelengths 728.4, 723.6, 636.0, 537.8, 636.5, 533.7 and 441.6 nm. Schuebel attributed the new transitions to charge transfer reactions between helium ions and ground state cadmium atoms:

$$He^{+} + Cd(\text{ground}) \rightarrow He(\text{ground}) + (Cd^{+})^{*} \qquad (3)$$

where * denotes excited levels of Cd^+.

A partial energy level diagram (fig 1.7) shows the relevant helium and cadmium (ionic) energy states together with the laser transitions observed by Schuebel, and other transitions which have since displayed laser oscillation.

An alternative design of hollow cathode which has arguably proved to be the most successful in terms of output power and stability is the so-called "flute-type" geometry (Piper and Webb, 1973). In this case, the cathode is a heavy-wall stainless steel tube which has a series of anode sidearms spaced 7.6 cm apart (fig 1.8(a)). The cathode bore was 6.35 mm and its active length 85 cm. Cadmium was supplied from a sidearm located at the tube centre. Helium was passed slowly (100 Atmos cc/Min) through the tube from the central oven to each end to distribute cadmium vapour and preserve cleanliness in the discharge. With each anode being individually ballasted by resistors to ensure equal current division, typical discharge voltages of 300 V at currents up to 5 A were reported. Laser oscillation on 10 transitions of Cd II was observed, with typical helium pressures of 8 Torr and cadmium oven sidearm temperatures of 320 ^{o}C. No attempt was made to optimise the laser output in terms of varying the transmittance of the ouput coupler and no power measurements were made for the He-Cd lines. Several other metal vapour systems were investigated with the same device (He-Zn, He-Se, He-I_2) which, together with He-Cd, yielded a total of 39 lines ranging from 325.0 nm to 880.4 nm.

Fukuda and Miya (1974) used a self-heated sectioned hollow cathode structure of metal and ceramic construction (fig 1.8(b)) to obtain simultaneous oscillation between selected

groups of transitions. Nine individual Kovar cathode segments, each 5 cm long with a 4.2 mm bore, provided an active length of 45 cm. The cathode sections were operated from a common external anode (24 mm ID) with cadmium laid along the internal surface. Because the metal vapour density depended on discharge current and voltage, this was essentially a lower current device than the flute-type. Thus, typical discharge currents of 100 mA per cathode were used, the total tube current being 1 A for the 45 cm active length. Under these conditions, current saturation was observed for both green and red Cd II transitions; no oscillation characteristics for the blue 441.6 nm transition were reported.

A modified flute-type geometry hollow cathode comprising a perforated copper pipe (fig 1.8(c)) enclosed in a pyrex tube provided data for the first reports of simultaneous oscillation on visible transitions in cadmium (Fujii et al, 1975). Cadmium was evaporated from the internal anode surface solely by discharge heating, so current and cadmium vapour pressure could not be optimised independently of one another. Correspondingly, the maximum current investigated was 600 mA. The cathode pipe was 80 cm long with a 4 mm bore and supplied by ten equally spaced anodes. Auxiliary anodes at each end of the tube prevented diffusion of cadmium vapour to the Brewster angled windows by cataphoresis. Simultaneous oscillation of the visible Cd II transitions was obtained using broad band mirrors at pressures in the range 7 - 16 Torr for cathode temperatures between 230 ^{o}C and 270 ^{o}C.

Laser oscillation at lower source temperatures was achieved by the use of Cd-halides, which generally have a lower

melting point and higher vapour pressure at a given temperature than the pure metal (Piper and Brandt, 1974). The hollow cathode structure used was of the flute-type (Piper and Webb,1973), again using a flowing helium system to distribute metal halide vapour and maintain cleanliness. Output powers obtained were always lower with the halides (CdI_2, $CdBr_2$ and $CdCl_2$) than with the pure metal, and threshold currents were higher. Some Cd II lines observed with the metal failed to oscillate when a metal halide was used (eg. 636.0 nm with any of halides, or 635.5 nm with CdI_2 and $CdCl_2$).

Another hollow cathode structure consisting of eight 10 cm stainless steel slotted segments placed in a ceramic insulator was developed in 1977 (fig 1.8(d), Csillag et al, 1977). The anode was in the form of tungsten wire placed under the cathode slot and was surrounded by ceramic insulator. The cadmium was placed close to the anode in another slot in the ceramic insulator, thus this tube was "self-heated" by the discharge current. Gain measurements of 6%, 5.8% and 4% per metre were observed for the green (537.8 nm), blue (441.6 nm) and red (636.0 nm) lines respectively, under optimum discharge conditions for each line. Peak currents (up to 7 A) were obtained with low average power by using half wave rectified 50 Hz ac, saturation of laser output generally occurring at 2 - 5 A for the visible transitions.

A long term problem associated with hollow cathodes is the effect of sputtering of the cathode surface (White, 1959) which may lead eventually to anode-cathode short circuits and gas clean-up. By careful control of the cathode temperature, it was proposed that cadmium "monolayer" coverage could be achieved for cathode surface protection (Hernqvist, 1978). Using this

technique, together with the cataphoretic "bottle" technique for Brewster angled window protection, Hernqvist achieved "sealed-off" lifetimes of 1000 hours for a hollow cathode 441.6 nm He-Cd laser.

Fujii et al (1979) formulated guidelines for the design of both pyrex-envelope flute-type and concentric cylinder type hollow cathodes, fig 1.8(e), basing their analyses on cathode fall theory. Earlier work by Fujii, (1974, 1975) had established the conditions under which the negative glow would be confined within the hollow cathode, rather than striking to the external cathode surfaces, for both the pyrex envelope flute-type and concentric cylinder type. Successful white-light operation was achieved for the flute type geometry, but initially some difficulty was experienced in obtaining blue oscillation at 441.6 nm in the concentric cylinder type, (Fujii et al, 1979). This was attributed to insufficient Cd metal vapour and high temperatures at the internal cathode, which could not dissipate heat efficiently. In a later publication however, successful white-light oscillation was reported from a concentric cylinder type hollow cathode (Fujii et al, 1980). In this case, the internal cathode was perforated with holes of two different diameters. The larger diameter holes (4 mm), of which there were 80, served to confine the discharge within the hollow cathode, while the smaller diameter holes (1.6 mm), of which there were 76, allowed additional diffusion of cadmium vapour from the internal surface of the anode into to the cahode bore. Altogether, these holes accounted for a 16 % loss of effective cathode area and correspondingly a reduction in hollow cathode effect, a fact to which the authors draw attention. The concentric cylinder hollow cathode had an active length of 80 cm,

and a 4 mm bore. White-light operation was obtained for anode temperatures of 200 - 230 ^{o}C; pressure and current dependence were not reported.

A more complicated design than the above was reported by Otaka et al, 1981. A mesh grid electrode was incorporated in this design to improve discharge stability, and the anode took the form of a rod which ran the length of the tube (fig 1.8(f)). White-light oscillation was observed for external cathode temperatures in the range 230-280 ^{o}C and pressures from 10 Torr, below which the discharge was unstable, to 14 Torr, above which no red oscillation was obtained.

An improved flute type geometry essentially similar to that of Piper and Webb, but giving powers in excess of 100 mW/line for blue and green under optimum conditions was reported by Grace and McKintosh, 1979. In this case the active length was 60 cm with a 4 mm bore. There were several refinements in this design over that of Piper and Webb, but a factor of 10 improvement in output power is difficult to explain. The interanode spacing was smaller (4 cm compared to 7.6 cm) and the oven design included a premixing chamber where incoming helium at the tube centre was mixed with metal vapour before being pumped away at varying rates along the tube bore to each end of the tube. Apart from these differences the two designs are very much the same.

A sealed-off tube of short active length comprising two 5 cm cathode sections and yielding output powers of 10 mW (blue), 3.5 mW (green) and 1.5 mW (red) was reported more recently (Wang, 1980). In this design, the tube is of metal-ceramic construction. A cadmium oven situated at the tube centre supplies

metal vapour, with the geometry that is shown in fig 1.8(g). Optimum pressures were 7 - 8 Torr for red and blue, while the green oscillation increased monotonically with pressure up to 20 Torr within the range investigated. Discharge current was in the range 120 mA (threshold) to 240 mA per cathode section. Apart from the visible Cd II transitions, another seven transitions ranging from the ultra violet (325.0 nm) to the near infra red (723.7, 728.4, 806.7, 853.1, 865.2 and 887.8 nm) were observed.

Another recent publication (Kin-hung and Grey-Morgan, 1983a) reports a flute type geometry enclosed in a glass envelope. This tube yielded successful white-light operation over a broad range of reservoir temperatures (260 - 380 ^{o}C) and helium pressures (5 - 25 mBar). In this case deployment of cadmium vapour is facilitated by flowing helium through the oven located at the tube centre to each end of the tube, where it is pumped away. Total output powers of 40 mW (simultaneous oscillation) were obtained for a discharge current of 2 A, above which tube failure occurred.

It is well known that hollow cathode lasers of the various designs described above are unstable to a greater or lesser extent. Instabilities are generally attributed to non-uniform distributions of Cd vapour, thermal effects and uneven current sharing by different regions of the laser cathodes. These are problems which must be overcome for reliable laser operation.

1.6 Hollow Cathode Excitation Mechanisms.

Much of the information available about the excitation mechanisms relevant to He-Cd hollow cathode lasers has come from diagnostic investigations of discharge afterglows. There is general agreement that the dominant excitation mechanism responsible for populating the higher ionic levels of Cd II, from which the green, red and infra red transitions originate, is a thermal energy charge-transfer reaction of the form

$$He^{+} + Cd\ (ground) \rightarrow He\ (ground) + Cd^{+*} \qquad (4)$$

as proposed by Schuebel, although there is evidence that molecular He_2^+ ions and He_2 metastables also play a role (Rajbar et al,1977; Kamin and Chanin, 1976), particularly in the case of the green transitions (Kin-Hung and Grey Morgan, 1983).

Collins et al, (1971) used a static gas pulsed afterglow technique in conjuction with line absorption measurements in the form of decay rates for the population densities of relevant excited species. The observed decay rates of the 441.6 nm and 325.0 nm Cd II lines were found to follow closely the decay rate for the helium ($2s^3S$) triplet metastable density, indicating that Penning reactions were responsible for the population of these levels. The measured decay rates for the 635.5, 636.0, 533.7 and 537.8, 723.7 and 728.4 nm lines were, however, different, leading the authors to the conclusion that reaction (4) provided the majority of excitation for these levels, either directly (for the 635.5, 636.0, 723.7 and 728.4 nm lines) or by cascade pumping from

higher levels (for the 533.7 and 537.8 nm lines).

Quantitative estimates of the relative reaction rates for the production of the Cd II levels excited by charge transfer collisions were obtained by measuring the line intensities in a flowing afterglow and using calculated transition probabilities in the analysis of experimental results (Turner-Smith et al, 1973). The largest reaction rates were found to be for Cd II levels lying in the energy range 0.1 - 0.4 eV below the He^+ ionic ground state. The authors conclude that the 723.7, 728.4 and 636.0, 635.5 nm laser transitions are populated directly in charge transfer reactions, while the 866.7, 853.0 and 537.8, 533.7 nm laser transitions are populated by radiative cascade from higher-lying direct charge-transfer excited levels.

Meanwhile, evidence was presented that the population densities of the higher lying Cd II levels were not solely determined by charge transfer processes and subsequent radiative de-excitation (Latush et al, 1973). Line emission studies from a pulsed after-glow suggested that collisional de-excitation by electrons also played an important role. Further investigation of these "superelastic" collisions, in which a Cd II ion is de-excited by a slow electron, showed that collisional de-excitation was comparative with radiative decay for those ionic levels with lifetimes in excess of 100 ns (Green and Webb, 1975). Thus the Cd II ($9p\ ^2P$) level, with a calculated lifetime of 480 ns, is severely "quenched" by electronic de-excitation, which accounts for up to 95% of the de-excitation from this level. However, the upper levels of Cd II laser transitions generally have lifetimes of 5 - 30 ns and correspondingly little or no de-excitation from these

levels occurs.

More recently, the helium triplet ($2s^3S$) metastable densities have been measured in a hollow cathode flute-type He-Cd laser (McIntosh and Grace, 1979) with a view to clarifying the excitation mechanism of the 441.6 nm line. Results showed that Penning ionisation is only partly responsible for producing the upper level population; direct electron impact excitation was the major pumping mechanism. The authors concluded that the observed saturation of the 441.6 nm line with discharge current is due to the faster rate of electron impact excitation for the lower laser level over the upper laser level.

1.7 Thesis Overview.

In Chapter Two, several longitudinal segmented discharge tube structures are described, in which the deployment of cadmium vapour is achieved by combined diffusion and cataphoresis. The conditions under which these structures behave as hollow cathodes are described and conlusions are drawn regarding their applicability for $He-Cd^+$ lasers.

A more conventional thin-walled hollow cathode structure is described in Chapter Three. The severe axial temperature variations and other problems associated with this tube provide the motivation for a careful thermal analysis of hollow cathodes, the results of which are applied to the design of the two tubes described in Chapter Four. Also in Chapter Four, the results

of a spectroscopic investigation of the discharges obtained in these two tubes are presented. Conclusions are drawn regarding the influence of impurities, and corrective measures to overcome these difficulties are suggested.

An important component part of a "white light" He-Cd laser is the optical cavity. Chapter Five describes a novel application of flow-graphs to the analysis of optical thin films for laser mirrors. Designs based on the flow-graph method are described for three broadband mirrors (a "total" reflector and two output couplers).

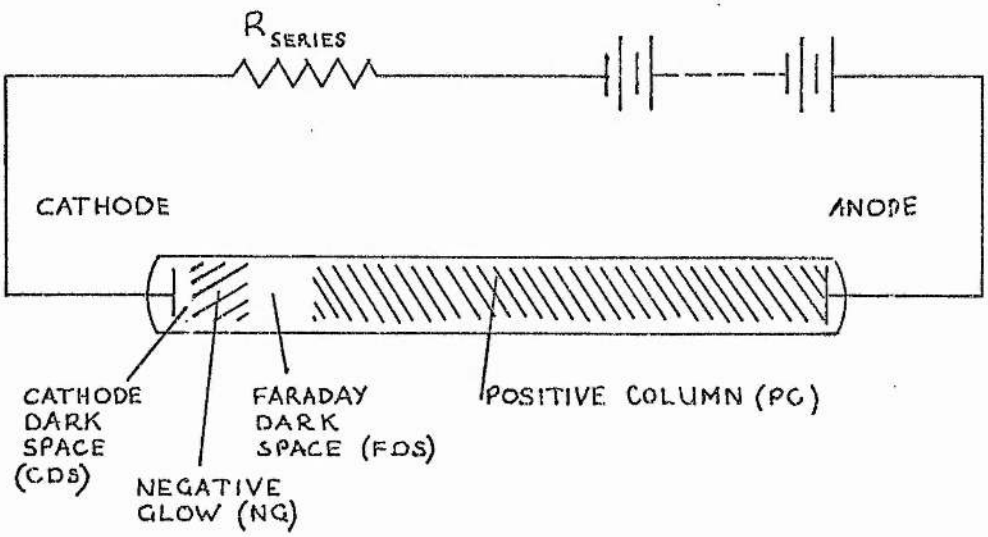

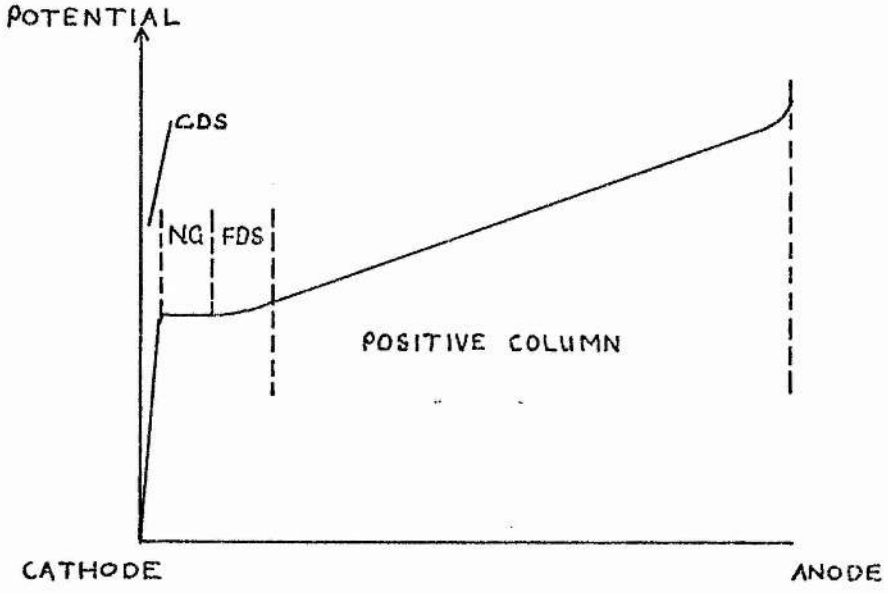

FIG 1.1 THE FOUR REGIONS AND POTENTIAL DISTRIBUTION IN A CYLINDRICAL GAS DISCHARGE VESSEL.

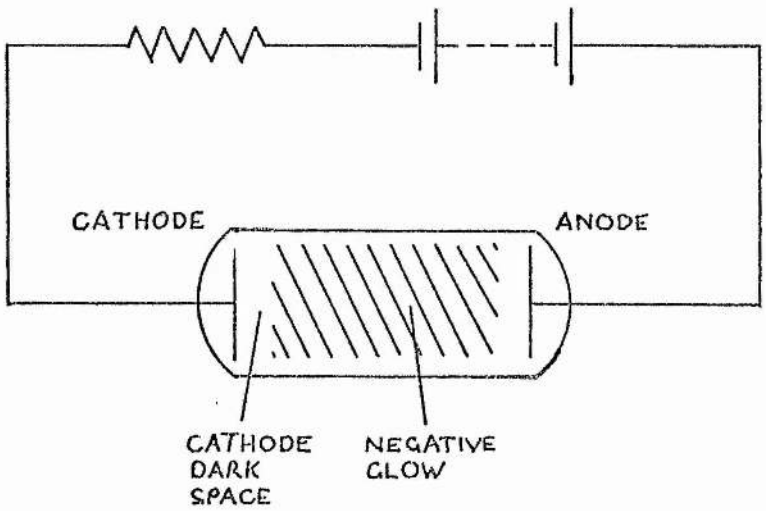

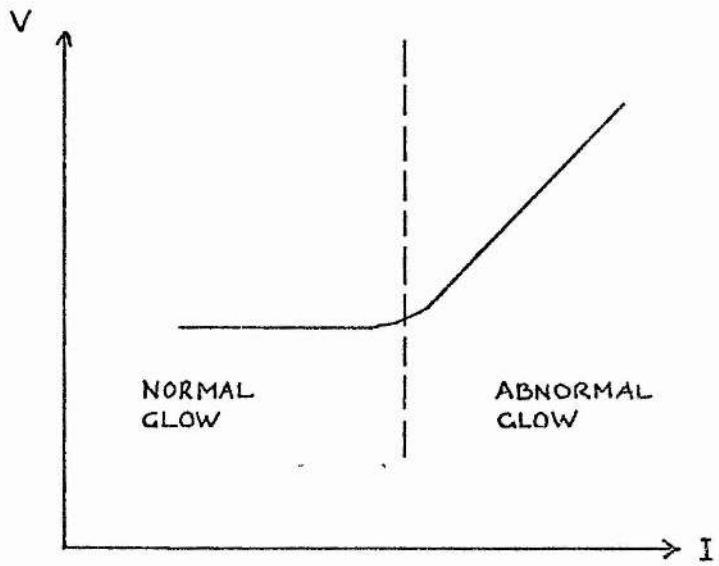

FIG 1.2 TRUNCATED NEGATIVE GLOW DISCHARGE TUBE AND TYPICAL VI CHARACTERISTICS.

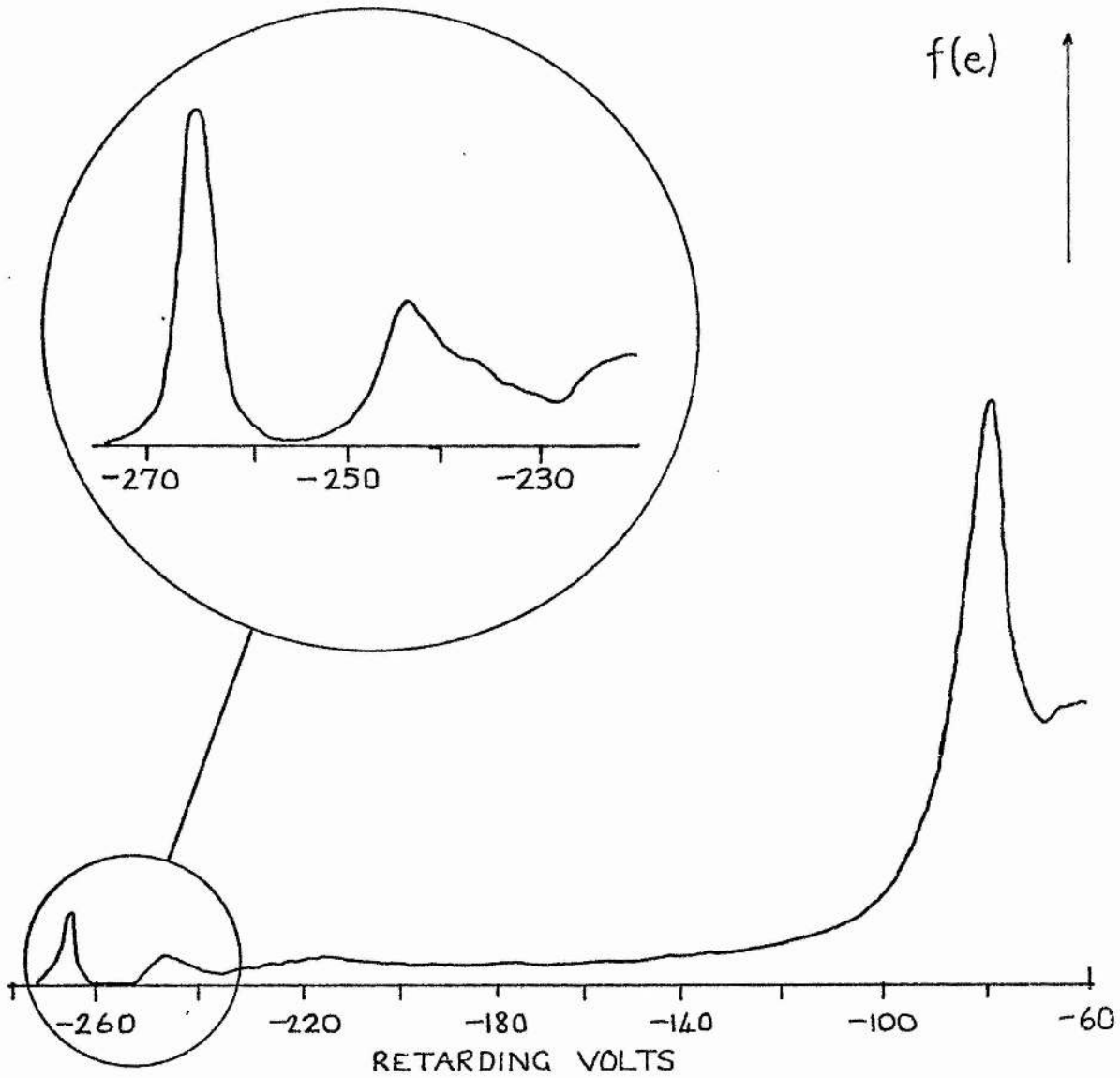

FIG 1.3. ELECTRON ENERGY DISTRIBUTION IN THE NEGATIVE GLOW (GILL AND WEBB, 1977)

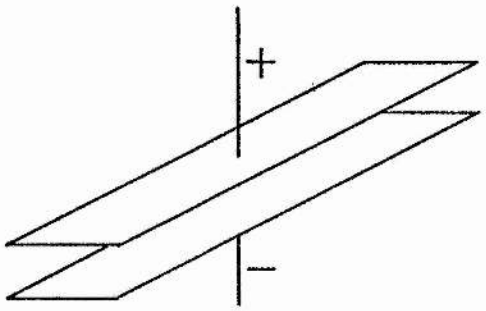

FIG 1·4(a) PARALLEL PLANE ELECTRODE CONFIGURATION.

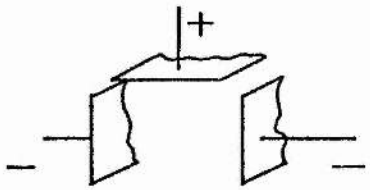

FIG 1·4(b) DOUBLE CATHODE GEOMETRY.

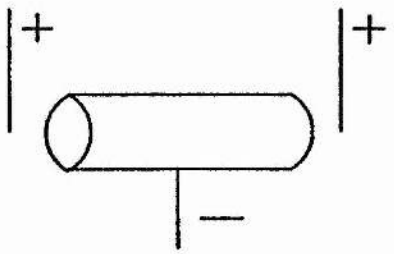

FIG 1·4(c) CYLINDRICAL HOLLOW CATHODE.

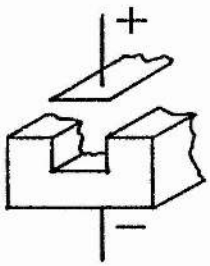

FIG 1·4 (d) SLOTTED HOLLOW CATHODE.

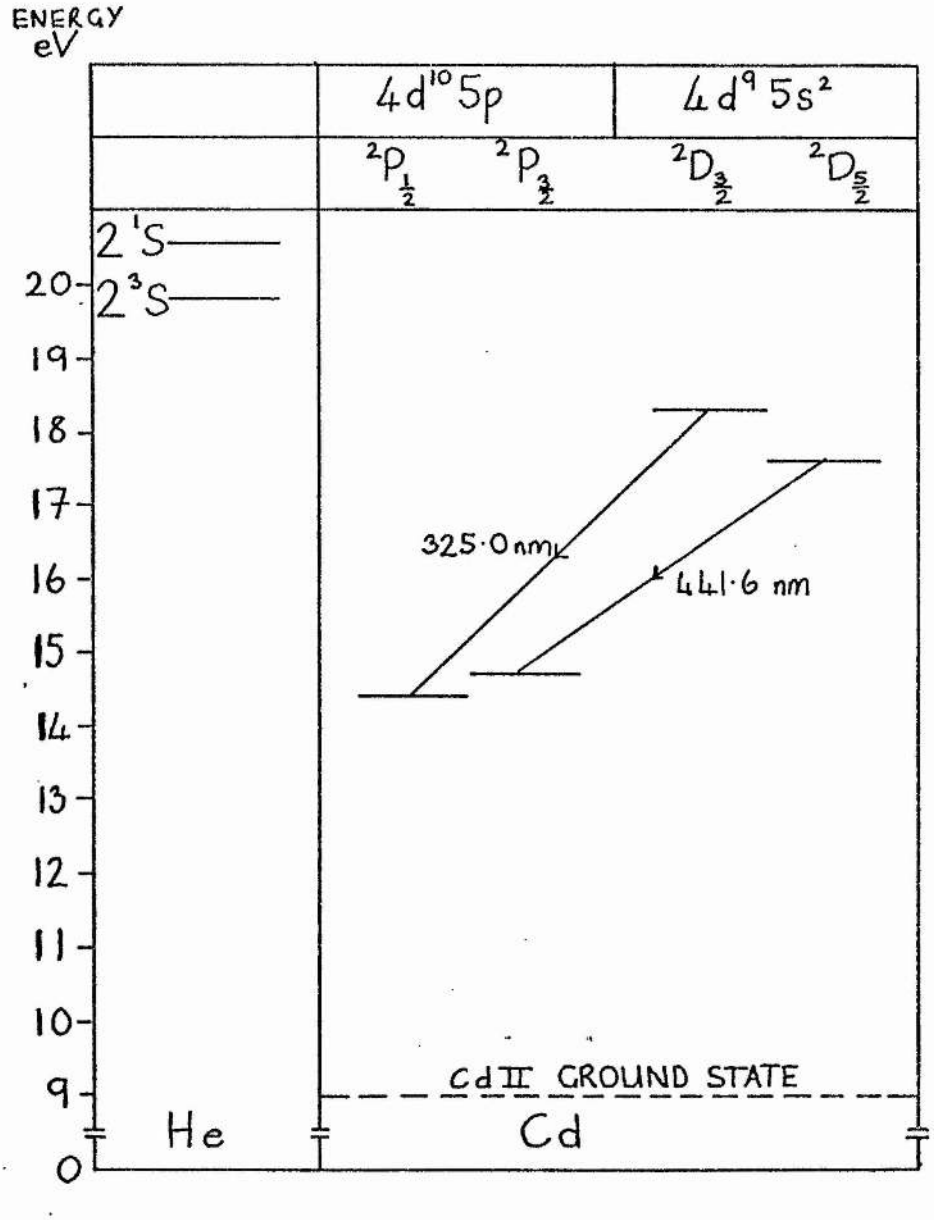

FIG 1.5. PARTIAL ENERGY LEVEL DIAGRAM FOR He AND Cd II

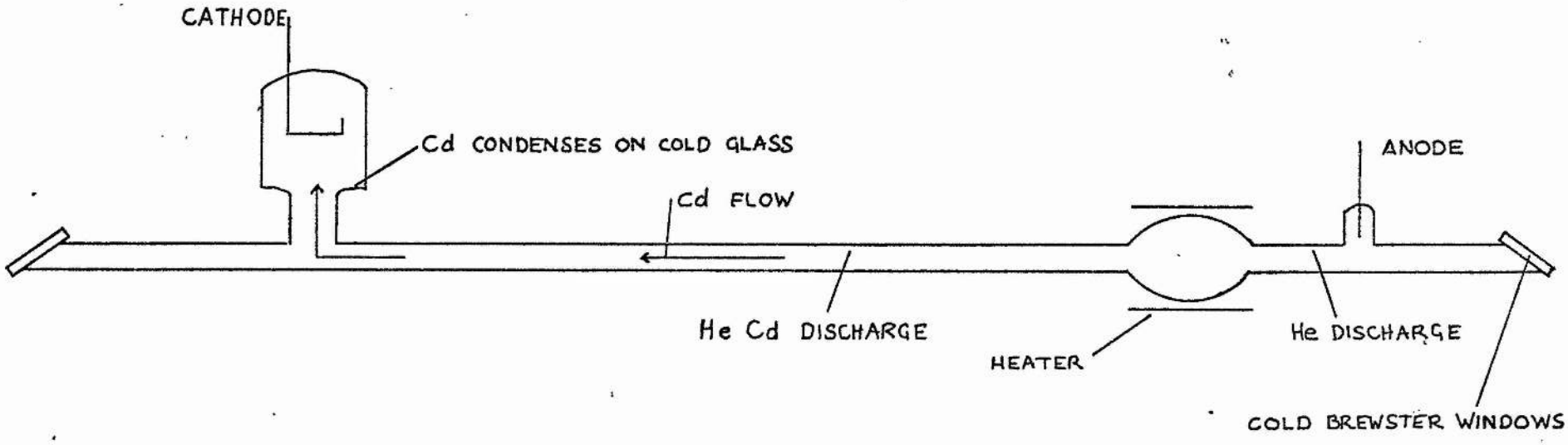

FIG 1.6 CATAPHORETIC He Cd LASER DISCHARGE TUBE.

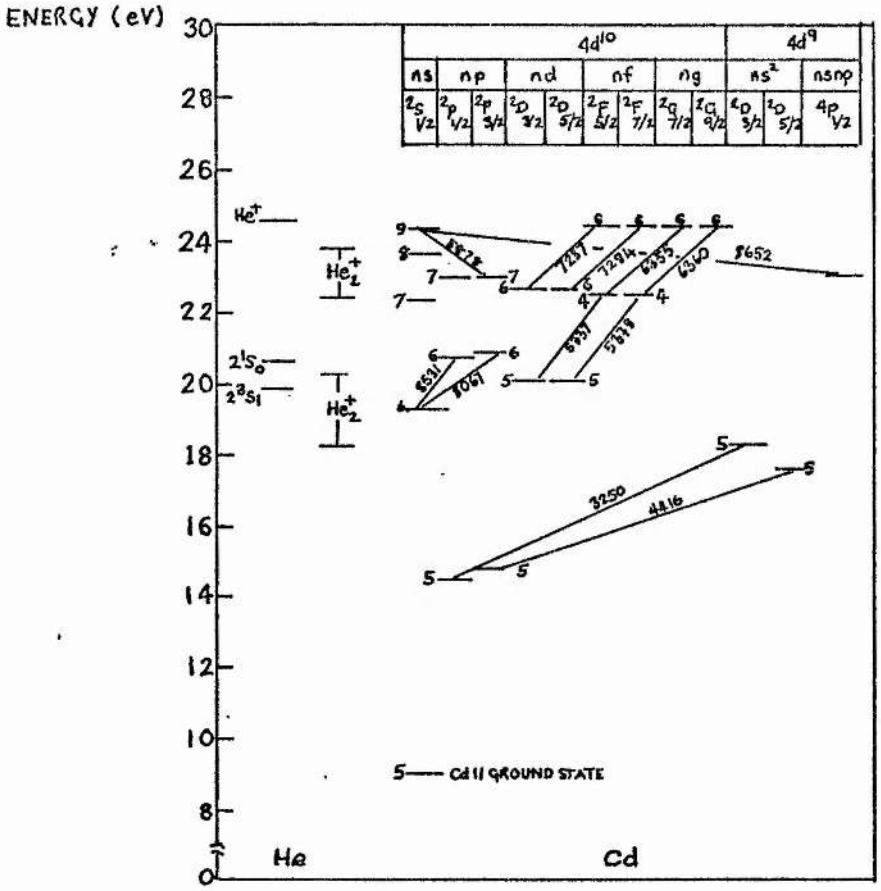

FIG 1.7 PARTIAL ENERGY LEVEL DIAGRAM OF Cd^+ AND He

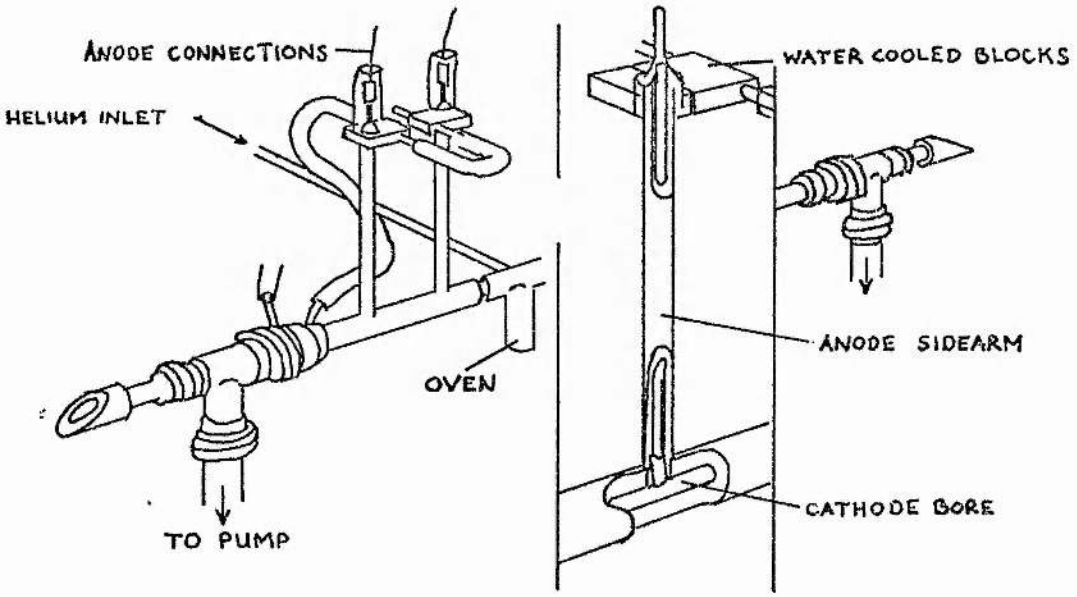

FIG 1.8(a) FLUTE TYPE OF HOLLOW CATHODE (PIPER AND WEBB, 1973)

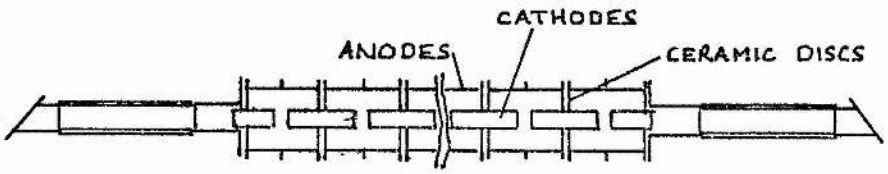

FIG 1.8(b) SELF HEATED METAL CERAMIC TUBE (FUKUDA AND MIYA, 1974)

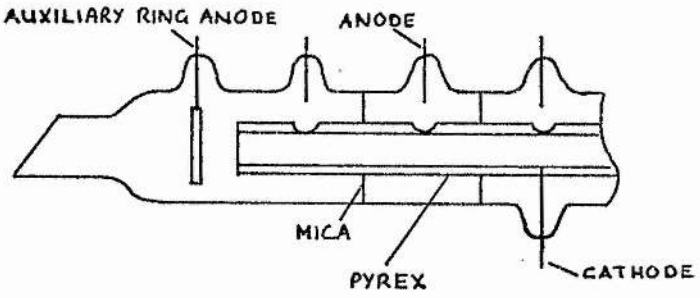

FIG 1.8(c) MODIFIED FLUTE TYPE HOLLOW CATHODE (FUJII ET AL, 1975)

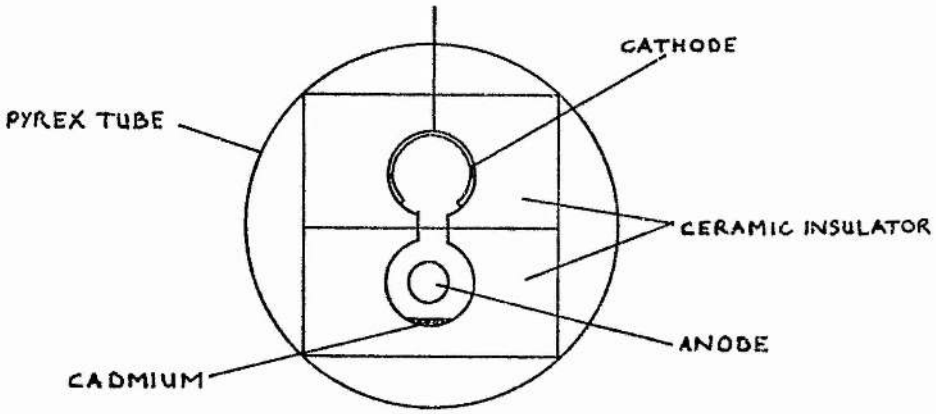

FIG 1.8(d) CROSS SECTION OF HOLLOW CATHODE (CSILLAG ET AL, 1977)

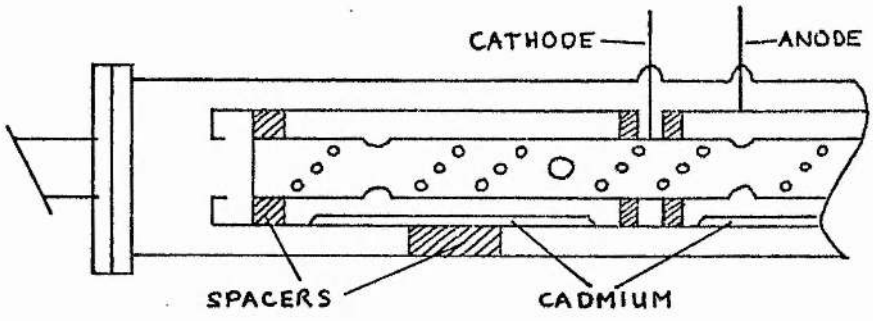

FIG 1.8(e) HYBRID HOLE CONCENTRIC CYLINDER HOLLOW CATHODE
(FUJII ET AL, 1980)

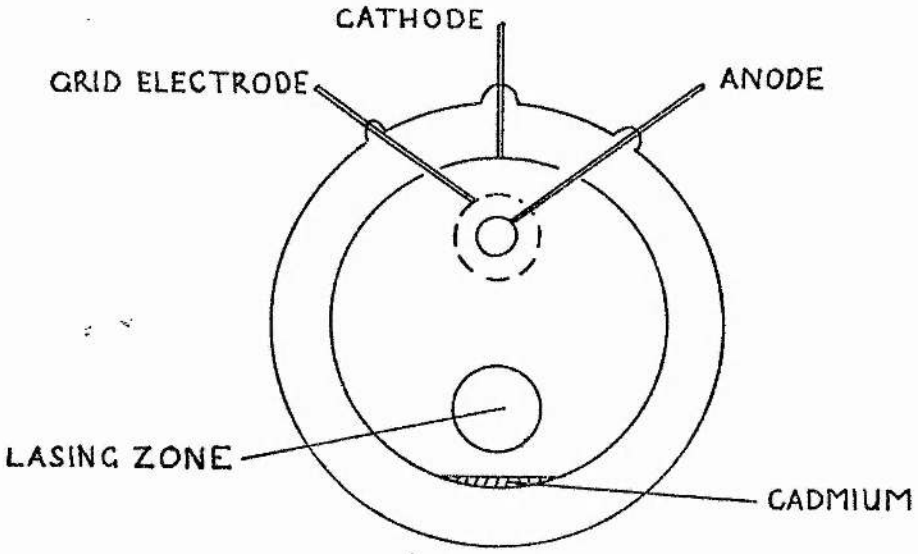

FIG. 1.8(f) CROSS SECTION OF MESH GRID HOLLOW CATHODE (OTAKA ET AL, 1981.)

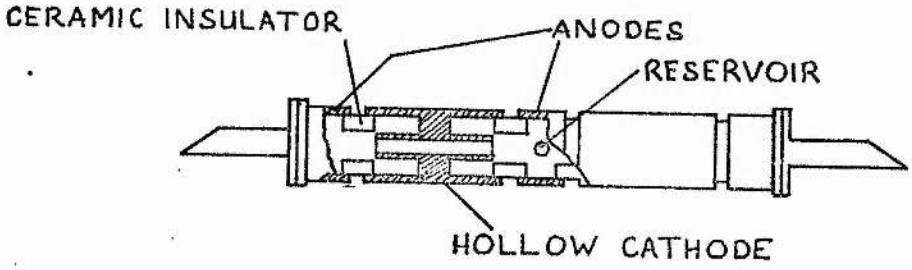

FIG. 1.8(g) SHORT ACTIVE LENGTH HOLLOW CATHODE (WANG, 1980)

CHAPTER ONE BIBLIOGRAPHY

BROWN, D.C. and GINSBURG, N.

Appl. Phys. Lett.,24,287-289,1974.

BROWN, P.G. and DUNN, M.H.

J. Phys. B : Atom. Molec. Phys.,6,1103-1117,1973.

COLLINS, G.J., JENSEN, R.C. and BENNET, W.R.

Appl. Phys. Lett.,19,125-128,1971.

CSILLAG, L., JANOSSY, M., KANTOR, K., ROZSA, K. and SALAMON, T.

J. Phys. D : Appl. Phys.,3,64-68,1970.

CSILLAG, L., NAM, C.Z., JANOSSY, M. and ROZSA, K.

Opt. Commun.,21,39-41,1977.

DUNN, M.H.

J. Phys. B : Atom. Molec. Phys.,5,665-671,1972.

DRUYVESTYN, M.J.

Physica,2,255-266,1935.

FOWLES, G.R. and HOPKINS, B.D.

I.E.E.E. J. Quant. Electron.,QE-3,419,1967.

FREUDENTHAL, J.

Physica,36,354-364,1967.

FUJII, K.

Japan. J. Appl. Phys.,13,571-572,1974.

FUJII, K., TAKAHASHI, T. and ASAMI, Y.

IEEE J. Quant. Electron.,QE-11,111-114,1975.

FUJII, K.

Japan. J. Appl. Phys.,14,1339-1344,1975.

FUJII, K., MIYAZAWA, S., TAKAHASHI, T., ASAMI, Y.

IEEE J. Quant. Electron.,QE-15,35-44,1979.

FUJII, K., OSHIMA, T., OTAKA, M., NAGASHIMA, S., MIYAZAWA, S. and OIKAWA, T.

IEEE J. Quant. Electron.,QE-16,590-592,1980.

FUKUDA, S. and MIYA,M.

Japan. J. Appl. Phys.,13,667-674,1974.

GELIKONOV, V.M. and ZAITSEV, Yu.I.

Sov. J. Quant. Electron.,7,1353-1357,1977.

GIALLORENZI, T.G. and AHMED, S.A.

IEEE J. Quant. Electron.,QE-7,11-17,1971.

GILL, P. and WEBB, C.E.

J. Phys. D : Appl. Phys.,10,299-311,1977.

GOLDSBOROUGH, J.P.

Appl. Phys. Lett.,15,159-161,1969.

GOTO, T., MORI, M. and HATTORI, S.

Appl. Phys. Lett.,29,358-360,1976.

GOTO, T. and ARAI, T.

J. Phys. D : Appl. Phys.,14,581-586,1981.

GOTO, T., HANE, K. and HATTORI, S.

J. Phys. D : Appl. Phys.,14,587-592,1981.

GRACE, J.R. and MCINTOSH, A.I.

J. Phys. D : Appl. Phys.,12,2043-2051,1979.

GREEN, J.M. and WEBB, C.E.

J. Phys. B : Atom. Molec. Phys.,8,1484-1500,1981.

HERNQVIST, K.G.

IEEE J. Quant. Electron., QE-8, 740-743, 1972.

HERNQVIST, K.G.

IEEE J. Quant. Electron., QE-14, 129-132, 1978.

JOHNSTON, T.F. and KOLB, W.P.

IEEE J. Quant. Electron., QE-12, 482-493, 1976.

KAMIN, M. and CHANIN, L.M.

Appl. Phys. Lett., 29, 756-758, 1976.

KIN-HUNG, W. and GREY MORGAN, C.

J. Phys. D : Appl. Phys., 16, L1-L4, 1983a

KIN-HUNG, W. and GREY MORGAN, C,

XVI International Conference on Phenomena
in Ionised Gases,
216-217, Aug. 1983, Dusseldorf, W. Germany.

LATUSH, E.L., MIKHALEVSKII, V.S. and SEM, M.F.

Opt. Spectrosc., 34, 120-123, 1973.

MCINTOSH, A.I. and GRACE, J.R.

Aust. J. Phys., 32, 561-573, 1979.

MAINWARING, M.H. and SWIFT, J.D.

J. Phys. D : Appl. Phys.,5,1433-1437,1972.

MIZERACZYK, J.K.

IEEE J. Quant. Electron.,QE-11,218-220,1975.

MORI, M., GOTO, T. and HATTORI, S.

J. Phys. Soc. Japan,43,662-668,1977.

MORI, M., TAKASU, K, GOTO, T. and HATTORI, S.

J. Appl. Phys.,48,2226-2230,1977.

MORI, M., MURAYAMA, H., GOTO, T. and HATTORI, S.

IEEE J. Quant. Electron.,QE-14,427-433,1978.

NEIGER, H. and NEMEC, V.

Z. Naturforsch,34a,260-261,1979.

OTAKA, M., OSHIMA, T., TAKEUCHI, H., OIKAWA, T. and FUJII, K.

IEEE J. Quant. Electron.,QE-17,414-417,1981.

PIPER, J.A. and WEBB, C.E.

J. Phys. D : Appl. Phys.,6,400-407,1973.

PIPER, J.A. and BRANDT, H.

J. Appl. Phys.,48,4486-4494,1977.

SCHUEBEL, W.K.

Appl. Phys. Lett.,16,470-472,1970.

SILFVAST, W.T.

Appl. Phys. Lett.,13,169-171,1968.

SILFVAST, W.T.

Appl. Phys. Lett.,15,23-25,1969.

SILFVAST, W.T. and SZETO, L.H.

Appl. Phys. Lett.,19,445-447,1971.

SOSNOWSKI, T.P.

J. Appl. Phys.,40,5138-5144,1969.

SOSNOWSKI, T.P. and KLEIN, M.B.

IEEE J. Quant. Electron.,QE-7,425-426,1971.

RAJBAR, F., HARRIS, H.H. and LEVENTHAL, J.J.

Appl. Phys. Lett.,31,385-387,1977.

TURNER-SMITH, A.R., GREEN, J.M. and WEBB, C.E.

J. Phys. B : Atom. Molec. Phys.,6,114-130,1973.

WANG, S.C.

Proceedings of the Society of Photo-Optical Istrumentation Engineers,232,42-46,1980, (Inernational Optical Computing Conference, 1980).

WHITE, A.D.

J. Appl. Phys.,30,711-719,1959.

WILLGLOSS, R.A. and THOMAS, G.C.

J. Phys. D : Appl. Phys.,6,L121-L123,1973.

WILLGLOSS, R.A. and THOMAS, G.C.

J. Phys. D : Appl. Phys.,7,3369-2276,1974.

CHAPTER TWO

SEGMENTED DISCHARGE TUBE STRUCTURES

2.1 General Introduction

One of the problems associated with hollow cathode He-Cd lasers is maintaining a sufficiently uniform distribution of cadmium vapour along the active length of the cathode bore. Radial and axial variations which may occur represent a departure from the conditions under which optimum laser performance occurs. The design of the various existing hollow cathode structures described in Chapter One incorporate either a flowing gas system (for example, the flute-types of Piper and Webb, 1973; Kin-Hung and Grey-Morgan, 1983) or several sources of cadmium distributed along the length of the discharge (for example, the designs of Fujii et al, 1974 and 1979).

In the flowing gas systems, radial variations in the metal vapour partial pressure occur and the rate of usage of cadmium is high. Furthermore, these systems are unsuitable as

candidates for sealed-off lasers with long life.

For those lasers with a distributed source of cadmium, the metal vapour density cannot be optimised independently of discharge current since these designs are generally of the self-heated variety.

The exception to these two categories is the design of Wang, 1981, in which deployment of cadmium vapour is achieved by diffusion and cataphoresis from a centrally situated oven. However, the tube is of short modular design (10 cm), and longer active lengths require extra oven sources of cadmium.

These problems of hollow cathode lasers contrast markedly with the relative simplicity of positive column lasers using cataphoretic distribution of cadmium vapour.

In this chapter, three discharge tube designs are described in which the deployment of cadmium vapour is achieved through combined diffusion and cataphoresis by an arrangment of discharge electrodes which gives a net axial electric field. The main design objective was to obtain a substantial net axial field to achieve cataphoretic distribution of cadmium vapour, and technical difficulties were subservient to this. The conditions under which the designs display the characteristics of hollow cathodes are determined.

2.2 Tube No.1

The first tube was of Kovar/glass construction with a segmented bore consisting of alternate anode and cathode sections (fig 2.1). Each of the four anode sections was 12 mm in length with a 6 mm bore, and each of the cathode sections was 50 mm in length with a 4 mm bore. An oven situated between the first anode and cathode sections contained cadmium of natural isotopic abundance in the form of 2 mm diameter wire (Johnson-Matthey Chemicals Ltd., "Specpure" product range).

The construction of this tube presented several problems. Each of the anode and cathode sections was of 16 mm OD Kovar rod, as illustrated in fig 2.2(a) and (b). A 3 mm lip was machined in each end of each section to provide a suitable sealing site for the intermediate glass sections. The lip requires a sufficiently thin wall to allow the glass to seal on both the internal and external metal surfaces to give a completed glass/metal seal as illustrated in fig 2.2(c). The sections were held together in a mechanical "jig", and the seal was made with an ECH (Eddy Current Heater) machine using standard vacuum and gas-filled tube technology. The mechanical jig had a controlled "drop" of approximately 1.5 mm, which determined how far the metal lip penetrated the glass sleeve. However, alignment of the tube proved difficult and the completed tube had a badly sighted bore, with approximately 50% obscuration. Furthermore, the weight of the cathode sections made the tube structure inherently weak, and proved to be a limiting factor in the length of the tube. By constructing one glass/metal seal in the ECH machine and carefully

annealing it before the next seal was attempted, the completed tube was limited to four cathode sections giving a potential active length of 20 cm. A tube with six cathode sections giving an active length of 30 cm, which was originally planned, was not feasible with the available equipment.

As illustrated in fig 2.1, the completed tube incorporated a glass side-arm and a gas inlet/outlet at each end, and was equipped with Brewster angled windows.

2.3 Principle of Operation

The principles underlying the operation of the segmented bore anode/cathode structure described above are based upon the qualitative observations of cathode behaviour discussed in Chapter One. For a single planar cathode with an adjacent anode, the area of cathode surface covered by negative glow is approximately proportional to the discharge current at low currents, and the current density at the cathode is constant. When the discharge current has reached a value such that the cathode surface is completely covered by negative glow, further increases in current result in increased current density at the cathode (abnormal glow regime). In the planar cathode discharge, the electric field in the negative glow is essentially zero.

For a cylindrical hollow cathode, the situation is slightly different. Probe measurements have revealed that the on-axis electric field in the negative glow in a cylindrical

cathode is non-zero. The potential is observed to decrease as the distance from the anode is increased and falls rapidly to zero as the end of the glow is encountered (fig 2.3). This result implies that the current density at the cathode is likely to be a function of length within the cylindrical cathode. However, the existence of an axial electric field within a hollow cathode is clearly established, and thus transport of cadmium will occur by cataphoresis as well as by diffusion.

With the discharge tube connected to a power supply as indicated in fig 2.4, the first anode draws current from the first cathode section. The second anode, which is connected to the first cathode externally and thus is at the same potential, draws current from the second cathode section, and so on, down the length of the tube. Under these circumstances, the flow of current should then be as indicated by the arrows in fig 2.4, where the resistors R_1 are of a high value and are included to help discharge initiation. Tube No.1 should thus operate as a series of four discrete anode/hollow cathode pairs. Each anode/hollow cathode pair is separated from its neighbour by a distance D = 2 cm (in fig 2.4). External electrical connections between adjacent anode/cathode pairs then carry the tube current. The following two questions then arise: Firstly, how critical is the choice of D in ensuring that each anode/hollow cathode discharge is isolated from its neighbour? Distance D represents "dead space" between laser mirrors in which there is little or no optical gain and thus should be made as small as possible. Secondly, what differences, if any, will occur if the electrical connections between adjacent anode/hollow cathode pairs are made internally as a continuous

conducting cylinder, rather than externally as a wire? The first of these questions is examined with in detail on a theoretical basis in Section 2.12, and the second question is dealt with experimentally, in the design and operation of tubes Nos. 2 and 3.

2.4 Gas Handling System

The gas handling system used throughout the course of this study is illustrated schematically in fig 2.5. The diffusion pump, rotary pump and liquid nitrogen cold trap are mounted together on a metal base plate (GEC General Vacuum Products, Bench Pumping Unit PL44) for which the pumping speed is 15 l/sec and ultimate vacuum is 5×10^{-6} torr. Thermocouple and ionisation gauges are included between the cold trap and the discharge tube. Tube pressure in the range 0-40 torr is monitored by an Edwards "Speedivac" capsule-dial gauge. Interconnecting pipes are either of 1/2 " OD copper or 1/4 " OD stainless steel. Valves other than those on the bench pump unit are "Nupro" needle valves, and an Edwards leak valve is incorporated between the helium cylinder and the discharge tube. Vacuum seals are either "O" rings or metal ferrule fittings. A flexible bellows connected between the pump unit and the discharge tube minimizes pump vibration at the tube.

Initially, grade A helium (BOC) was used, but this was later substituted for Research Grade helium (also BOC).

2.5 Power Supply

The power supply is a 15 kV 1 amp dc smoothed laboratory-built unit, supplied by 3-phase input to minimise ripple. No current or voltage stabilization is included in the supply.

2.6 Operating Characteristics of Tube No.1.

Attempts to obtain reproducible operation of the discharge were frustrated by air leaks, which occurred mainly in the glass sections, and thus little quantitative data could be obtained from tube No.1. The glass sections fractured and were subsequently repaired three times altogether, always within several hours after switching the discharge off. The fourth fracture was more serious because it occurred at a glass/metal seal, and could not be repaired. This behaviour is thought to be due to different cooling rates for the glass sections which cool quicky, and the metal sections, which are much more massive and correspondingly cool more slowly.

Operation of a discharge in the tube revealed that the discharge impedance increased monotonically as a function of time, after an initial short term decrease. An increasing discharge impedance is a characteristic associated with "leaky" operation, although the mechanisms by which this occurs are not completely clear. There are two possible processes which may

produce this effect. Firstly, electronegative gases, such as oxygen, can effectively remove electrons form the discharge and correspondingly a higher cathode fall voltage is required to increase the production of secondary electrons necessary for discharge maintainance (Francis, 1956). Alternatively, impurities present may contaminate the cathode and decrease the yield of secondary electrons for a given cathode fall.

Despite these difficulties, some useful information was obtained from tube No.1, in the form of current characteristics and qualitative observations of the distribution of cadmium vapour down the discharge length.

With the tube connected in the circuit illustrated in fig 2.6, the currents I_1 and I_2, the tube voltage V, and the cathode temperature T were monitored as a function of time. Typical results are given in fig 2.7, which illustrates the increasing discharge impedance mentioned above, and fig 2.8, which gives the warm-up time for the tube. The resistors R_1 (100 k) were removed since it was found that the discharge would initiate readily without them.

Cadmium supplied from the sidearm could be introduced into the region between the first anode and cathode by thermal evaporation. The heater was in the form of nichrome tape wound longitudinally on a silica former which was then carefully positioned in a drilled hole in a firebrick. The firebrick could then be positioned at the cadmium source such that the sidearm projected into the the hole in the firebrick. The nichrome element was heated by a "Variac" auto-transformer directly, no attempt being made at this stage to control the temperature

electronically. A thermocouple placed between the silica former and the sidearm monitored the cadmium source temperature. Upon switching the sidearm heater on, the current was slowly increased until cadmium lines were observed in the region between the first anode and cathode pair. The lines monitored (qualitatively at this stage with a hand held spectroscope) were the Cd II green lines, at 533.7 nm and 537.8 nm. Within several minutes, the same lines were equally observable at the "tail" end of the last cathode section, provided that the tube temperature monitored at the cathode sections was above that of the sidearm. This indicated that cadmium was being transported down the length of the tube. Further evidence that the cadmium transport was aided by the axial electric field was provided by the relatively large amount of cadmium deposited on the inner surface of the glass behind the tail end of the last cathode section. By comparison, only a small amount of cadmium was deposited in the tube on the first anode side of the "cadmium" sidearm. The observed slightly yellow-brown appearance of the deposited cadmium is also indicative of leaky operation, this colour being characteristic of cadmium oxide.

The ratio I_1/I_2 determines how much of the total discharge current is flowing through the cathode sections. The most significant feature characterising the operation of this tube is that over the range of helium pressures (10-25 Torr), discharge currents (0-110 mA) and cadmium oven temperatures (250-350 ^{o}C) investigated, the measured ratio I_1/I_2 never deviated from unity, within the accuracy of the ammeters used (5%). Furthermore, periodic checks on the voltage distribution down the length of the tube showed that the total discharge voltage was divided equally

between the cathode sections, to within ±5%. Thus it may be concluded that with the present electrode configuration, the longer segments behave as hollow cathodes when operated in series, and that deployment of cadmium vapour is aided by the resulting net axial electric field.

A photograph of tube No.1 after failure (plate 2.1) shows that the glass/metal seals were operated at temperatures sufficiently high to cause the glass to "soften". This occurs at a temperature of ~525 °C for Kodial (Kovar sealing glass).

Attempts made to obtain laser oscillation on the visible lines of Cd II were unsuccessful. The optical cavity comprised two 2m-radius 100% reflectivity broad band mirrors (purchased from CVI Laser Corperstion, U.S.A.) spaced 1 m apart. Tube alignment was made difficult by the partially obscured bore, mentioned above.

2.7 Tube No.2 Description

In view of the difficulties experienced with the fabrication of tube No.1, it was apparent that some design simplifications were required to enable a tube of more reliable and rugged construction to be built. As a step towards this goal, a simpler segmented bore tube was constructed (fig 2.9).

In this case, the tube was of all stainless steel and silica construction with no inter-segment seals, and thus the

problems experienced with the glass/metal seals in the previous tube were eliminated.

A further simplification was introduced by dispensing with the anodes, and making all the sections of equal length (5 cm). It was thus expected that the tail end of each cathode section would serve as an anode for the next cathode section, and so on down the length of the discharge tube. As will be demonstrated later, this assumption is only valid for relatively low current values.

The tube comprised five stainless steel sections, each 9.5 mm OD, separated by silica spacers 1 cm in length, and mounted in a close fitting outer silica tube (10.0 - 10.5 mm ID). This prevented the discharge striking to the outer surfaces of the steel segments (Mizeraczyk and Neiger, 1983) and made bore alignment much easier than in the previous tube. Again, the tube was equipped with Brewster angled windows. Two current feedthroughs in the form of 2 mm diameter tungsten rods were included in the design. One of these rods served as the first anode, and the other, with a threaded nickel tip, was screwed into a tapped hole in the last cathode segment.

2.8 Tube No.2 Operation

Because of the simplicity of construction, the electrical measurements that could be made on this tube were restricted to simple VI characteristics. Figure 2.10 shows a typical VI characteristic, for helium pressures of 10 Torr and 15 Torr, respectively. It is obvious from this figure that above a threshold current of approximately 20 mA, the tube displays a negative VI characteristic, in contrast with the behaviour expected from a negative glow discharge discussed in Chapter One. Thus it may be concluded that above this value of current, the discharge is inherently different in character to the discharges obtained over wide ranges of current, helium pressure and cadmium vapour density in tube No.1. Using the same arrangement as described for tube No.1, cadmium could be introduced into the discharge by slowly increasing the current passing through the nichrome heating element.

Threshold laser oscillation on the green lines of Cd II at 533.7 nm and 537.8 nm was obtained for this tube over a wide range of helium pressures (10 - 40 Torr) and for oven temperatures in the range 320 - 400 ^{o}C. No laser oscillation on the other lines of Cd II was obtained. The current at which green oscillation occurred lay in the range above 100 mA (120 mA was the maximum current applied to the tube).

Above 100 mA, the last cathode segment began to glow red hot, indicating an internal tube temperature of at least 525 ^{o}C. Interestingly, the thermal glow was observed at one end of the last cathode segment only. Two important facts may be deduced

from this uneven heating. Firstly, the power input to that segment was not constant over its length, and secondly, the last cathode segment was dissipating more input power than the other segments. Sputtering was also observed to be greater at the last segment. The spacer between the penultimate and ultimate cathode sections had a disproportionately large amount of sputtered steel than was observed at the other inter-cathode spacers. This can be seen in plate 2.1.

These observations suggested that the last cathode segment was perhaps the only true cathode, the other sections playing a secondary role, if indeed any at all, in obtaining laser oscillation. To investigate this further, the discharge was operated at its current limit of 120 mA, and the cathode heater turned on and allowed to reach 400 ^{o}C. When the Cd II lines were equally observeable between the silica spacers down the length of the discharge, and the optical cavity aligned to produce laser oscillation at 533.7 nm and 537.8 nm, the oven was switched off. By removing the firebrick in which the oven heater element was situated, the sidearm containing the cadmium was allowed to cool quickly. Thus the supply of cadmium to the discharge was also quickly terminated. Over a period of several minutes, the Cd II lines became weaker, firstly at the anode end of the discharge, then towards the middle of the discharge, indicating that the cadmium vapour density was indeed diminishing rapidly. Meanwhile, the green Cd II lines continued to oscillate, and only when the observed Cd II sidelight at the cathode end of the tube grew noticeably weaker did laser oscillation cease.

2.9 Tube No.3 Description

Tube No.3 was constructed in order to help clarify observations obtained from tube No.2, in particular the negative VI characteristics. Tube No.3 is thus similar in electrode configuration to tube No.2, with the important difference that electrical access to each of the cathode sections is allowed for. As can be seen from fig 2.11, this was achieved by constructing tube No.3 using glass/metal seals, where the cathode wall was kept thin (0.5 mm), to alleviate the problems associated with differential cooling experienced with the more massive cathode sections used in the construction of tube No.1. The tube comprises four 6 cm "cathode" Kovar sections, and a 5 cm length Kovar anode section, interspersed by 1 cm lengths of Kodial glass. An oven sidearm was situated between the first (short) anode section and the first "cathode" section. The tube was equipped with Brewster angled windows, and because it was constructed in a double-chuck glass-blowers lathe instead of a static mechanical jig, the tube-bore was well-aligned. Heat sinks in the form of 1/32 " thick brass plates were carefully attached to each of the cathode sections to improve their heat dissipation. Graphite solution (Aqua-Dag) was applied to the area of contact between the brass plates and the Kovar "cathodes" to ensure good thermal contact. With this arrangement, it was found that the tube could be operated over a similar range of currents to that of tube No.2.

2.10 Tube No.3 Operation.

Figs 2.12 and 2.13 give the VI characteristics for tube No.3 at helium pressures of 5 and 10 Torr respectively. These diagrams include the potential at each of the metal sections as a function of discharge current. It can be seen that all cathode sections display a positive VI characteristic until a pressure dependent threshold current is reached. Above this threshold current, the first four cathode sections showed a sudden drop in potential, thereafter exihibiting an almost flat or slightly negative characteristic. Only the last cathode was unaffected at this threshold current and continued to display the positive VI characteristic associated with a cathode glow discharge in which there is no positive column.

Introducing cadmium into the discharge, using the same oven assembly as that described above, again produced laser oscillation on the green lines of Cd II, no oscillation being observed for the other visible lines. A short series of experiments was then conducted to confirm that only the last cathode section played a role in obtaining laser oscillation.

With the circuit connected as illustrated in fig 2.14, where the penultimate cathode section was connected to the power supply earth, running the discharge again produced laser oscillation on the green lines of Cd II. After approximately one hour of operation with this circuit configuration, a cadmium deposit accumulated between the ultimate and penultimate cathode sections. Following this, but with the circuit illustrated in fig 2.15, in which the power supply output was connected to the

penultimate section, discharge heating of the cadmium deposit provided cadmium vapour of sufficient density to obtain laser oscillation on the green Cd II lines again. Similar results were obtained for each of the circuits illustrated in figs 2.16(a)-2.16(d) by operating them for one hour each in the order illustrated. Cadmium deposited at the tail end of the cathode section during operation of the circuit used in fig 2.16(a) by heating the sidearm source then becomes the source of cadmium for the circuit in fig 2.16(b), and so on.

2.11 Discussion of Tubes Nos. 2 and 3.

From the experimental observations of tubes Nos. 2 and 3, it may be concluded that only one of the "cathode" sections in each of the tubes operated as a hollow cathode when the discharge current was increased above a certain transition value. Since the transition value is well below the observed threshold value of discharge current for laser oscillation, it may also be concluded that laser oscillation in both tubes was due to one cathode section only. Thus tubes Nos. 2 and 3 were essentially short active length tubes (5 cm).

The existence of a transition point for these discharges may be understood in terms of the behaviour of the negative glow at the cathode surface as the current is varied. At currents below the transition value, the cathode surface is only partially covered in negative glow. For a cylindrical cathode, it

is convenient to define the "plasma length" as the axial extent of the negative glow associated with one anode, at a given discharge current and helium pressure. Below the transition current, tubes Nos. 2 and 3 behave as a series of hollow cathodes, the tail end of each cathode serving as an anode for the next cathode and so on. When the discharge current is increased such that the plasma length is equal to the cathode length, the transition point is reached and only the last metal section behaves as a hollow cathode for currents above this value. The other segments experience a drop in potential at the transition point. From figs 2.12 and 2.13, a plasma length of 5 cm is obtained for helium pressures of 5 and 10 Torr at 38 $\pm$3 and 24 $\pm$3 mA respectively.

2.12 Discussion of Tube No.1.

In contrast to the observations from tubes Nos.2 and 3, tube No.1 behaved as a series of hollow cathodes over a wide range of helium pressures, discharge currents, and cadmium oven temperatures. The significant difference between tube No.1 and the other two tubes is believed to be the existence of separate anode sections which were connected externally to the preceeding cathode sections.

Figure 2.17 shows three anode/cathode pairs separated from each other by distance D. In the limit of large D, the discharges are isolated and thus when operated in series will perform as hollow cathodes. The question then arises as to how

much D may be reduced and this remain the case.

In the following analysis, a solution to this problem is derived by estimating the distance D, from the "tail" end of the cathode, at which the plasma may be judged to have decayed sufficiently for it not to interfere with an adjoining anode/cathode pair. Then the effects of any perturbations in the discharge which may occur at the tail end of one cathode as a result of the proximity of an adjacent anode/cathode pair are assessed qualitatively.

2.12.1 Preliminary Remarks on the Calculation of D.

Before any calculations are made, it is appropriate at this stage to re-consider the basic discharge tube illustrated in fig 1.1. Ions and photons formed in the discharge cause secondary emission of electrons at the cathode surface. The electrons thus emitted are accelerated by the cathode fall voltage V_c and experience inelastic collisions, resulting in electron multiplication and excitation of atoms, which manifests itself as the negative glow. The negative glow is brighter towards its cathode end, and drops off in intensity as the distance from the cathode increases. Thus as the negative glow is traversed, more and more electrons which originally had energy eV_c will have suffered inelastic collisions and lost energy. In the Faraday dark space, the electrons may be considered to be "thermalised", and thus largely incapable of producing further excitation. The

electric field which originates in the Faraday dark space, and continues throughout the length of the positive column, then accelerates the thermalised electrons, which acquire a drift velocity as they are repeatedly decelerated by inelastic collisions and accelerated by the field. These inelastic collisions then produce sufficient numbers of electrons by ionisation to make good recombination losses at the tube walls.

Although the above picture is a simple one, it serves to illustrate that should the electric field originating in the Faraday dark space be "removed", the discharge would be extinguished. Thus if D in fig 2.17 were made equal to the combined lengths of the cathode dark space, negative glow and Faraday dark space then the diacharges may be considered to be isolated. From experimental observations by other workers, the combined lengths of the cathode dark space, the negative glow and the Faraday dark space is of the order of a few cm for discharges in helium at pressures of a few torr and discharge currents of several tens of mA (Francis, 1956).

2.12.2 Calculation of D.

An estimate of D is made for one anode/cathode pair first, and then the effects of any perturbations which may occur due to the proximity of an adjacent anode/cathode pair are assessed qualitatively. The calculation of D presented below consists of three steps (see fig 2.18).

Firstly, it is shown that the electron multiplication in the cathode dark space is sufficiently small to be neglected for the approximate model developed here, and thus the cathode dark space/negative glow boundary may be treated as a planar source of electrons which have initial energy eV_c, where V_c = 300 volts is the cathode fall voltage. Secondly, the range of these 300 eV electrons in helium at 10 Torr and 700 K is calculated. The range of an electron may be defined as the distance which it will travel on average before its energy is reduced sufficiently to render it incapable of causing further ionisation. The range of electrons so calculated has been observed to agree well with experimental observations of the axial extent of the negative glow (Brewer and Westhaver, 1937) in a variety of gases, including helium. Thirdly, the axial distance over which the "thermalised" electrons may travel before being lost by diffusion or recombination is calculated.

2.12.3 Step 1: Electron Multiplication

Electrons released at the cathode by secondary emission processes are accelerated by the electric field. These electrons may cause ionisation in the dark space as follows:

$$e^-(V) + He \rightarrow He^+ + e^-(0) + e(V-\overline{V_i}) \qquad (2.1)$$

where V is the initial electron energy and $\overline{V_i}$ is the average

energy lost by the ionising electron in such a collision. It is assumed that the ejected electron has a low energy and is thus incapable of producing further ionisation. The collision cross section for ionisation of helium by electron impact is a function of energy. However, in the range 60 - 300 eV, its value is $q_i = 2.8 \times 10^{-17} cm^2$ to within 25%, (Brown, 1961), and this average value will be used. Considering a slab of thickness dx in the cathode dark space, the number of electrons created by N_e electrons entering the slab is:

$$dN_e = N_e n q_i \, dx \qquad (2.2)$$

where n is the helium atom density. Thus, integrating (2.2), the electron multiplication is

$$N_e(x) = N_e(0) \exp(n q_i x)$$

where $N_e(0)$ is the electron density at the cathode and $N_e(x)$ is the electron density at a distance x from the cathode. For the discharges obtained with tube No.1, the length of the cathode dark space was too small to measure with the naked eye, and thus an upper limit estimate of 0.05 cm is used. Hence, an upper limit estimate of 1.2 is obtained for the electron multiplication in the cathode dark space.

2.12.4 Step 2: Range of 300 eV Electrons.

The boundary plane between the cathode dark space and the negative glow, situated at $x = 0$ in fig 2.19, may be treated as a source of electrons with energy 300 eV. Considering a slab of thickness dx situated x cm from the boundary, the energy loss suffered by an electron in travelling from x to $x + dx$ is:

$$dV = - \bar{V}_i \, n \, q_i dx \qquad (2.3)$$

where nq_i is the number of ionising collisions per cm path length and $\bar{V}_i$ is the average energy lost by an electron in an ionising collision. Thus, we have

$$\int_{V_c}^{V_p} dV = - \bar{V}_i \, n \, q_i \int_0^R dx \qquad (2.4)$$

where V_c is the initial electron energy at $x = 0$, V_p is the energy below which the electrons are incapable of causing further ionisation at $x = R$, where R is defined by eq (2.4) as the range of the electron. Hence,

$$R = \frac{V_c - V_p}{\bar{V}_i \, n \, q_i} \qquad (2.5)$$

For the case under consideration, V_c = 300 eV, V_p =24.6 eV, (ionisation potential of He) and q_i = 2.8 x 10^{-17} cm^2 is the average ionisation cross section of helium. Thus, if the average

energy lost by an electron in an ionising collision is $\overline{V_i}$ = 31 eV, (eg Lehman, 1927), we get R = 2.3 cm.

2.12.5 Step 3: Decay of Ionisation.

The axial decay distance of a plasma within a cylindrical container will now be now determined. A plane situated at x = 0 is the source of ionisation (fig 2.20) and in the context of the evaluation of D corresponds to the boundary defining the end of the negative glow. Considering a slab of thickness dx at distance x from the planar source, the following steps may be taken to derive an equation describing the axial decay of ionisation.

From fig 2.20, the number of electrons or ions which enter slab dx from the source per second is given by

$$\frac{N_x \overline{V}}{4} \pi r_o^2 + D_a \frac{dN_x}{dx} \pi r_o^2 \qquad (2.6)$$

where $\overline{V}$ is the average speed of the electrons or ions, r_o is the radial dimension of the cylinder and D_a is the ambipolar diffusion coefficient for electrons and ions in helium at 10 Torr. The first term in eq (2.6) is the impingement flux and the second term represents the diffusion term. The radial average of the ion or electron number density is N_x . The number of electrons or ions which leave the slab to the right per second is given by

$$\frac{N_x \overline{V}}{4} \pi r_o^2 + D_a \frac{d}{dx} \left(N_x + \frac{dN_x}{dx} dx \right) \pi r_o^2 \qquad (2.7)$$

Again, the first term of (2.7) is the impingement flux and the second term is the diffusion term. The number of electrons or ions lost by volume recombination per second is given by

$$\alpha N_x^2 \pi r_o^2 \, dx \qquad (2.8)$$

where α is the recombination coefficient. The number of electrons or ions lost by diffusion to the tube walls per second, where they are neutralised, is

$$\frac{N_x}{\tau} \qquad (2.9)$$

where τ (the average lifetime of an ion or electron against diffusion to the tube walls) may be calculated from the equation

$$D_a \tau = \Lambda^2 \qquad (2.10)$$

in which Λ is the characteristic diffusion length of the container. For an infinite cylinder,

$$\Lambda^2 = \left(\frac{r_o}{2.405} \right)^2 \qquad (2.11)$$

(McDaniel, 1964). In the steady state, we have

$$(2.6) - (2.7) - (2.8) - (2.9) = 0 \qquad (2.12)$$

Equation (2.12) yields the following equation for the axial decay of ionisation

$$\frac{d^2N_x}{dx^2} + \frac{\alpha}{D_a} N_x^2 + \frac{N_x}{D_a\tau} = 0 \qquad (2.13)$$

Equation (2.13) may be reduced to a first order equation by writing

$$\rho = \frac{dN_x}{dx} ; \quad \frac{d}{dx} = \frac{d}{dN_x}\frac{dN_x}{dx} = \rho\frac{d}{dN_x}$$

Thus

$$\frac{d^2N_x}{dx^2} = \rho\frac{d\rho}{dN_x}$$

and eq (2.13) becomes

$$\rho\frac{d\rho}{dN_x} + \frac{\alpha}{D_a}N^2 + \frac{N_x}{D_a\tau} = 0 \qquad (2.14)$$

Seperating the variables and integrating yields

$$\left(\frac{dN_x}{dx}\right)^2 = \left(\frac{dN_x}{dx}_{x=0}\right)^2 + \frac{2\alpha}{3D_a}N_o^3 + \frac{N_o^2}{D_a\tau} - \frac{2\alpha}{3D_a}N_x^3 - \frac{N_x^2}{D_a\tau} \qquad (2.15)$$

which simplifies to

$$\frac{dN_x}{dx} = -\sqrt{\frac{2\alpha}{3D_a}(N_o^3 - N_x^3) + \frac{1}{D_a\tau}(N_o^2 - N_x^2)} \qquad (2.16)$$

Finally, we get

$$x = \int_{N_o}^{0} \frac{dN_x}{\sqrt{\frac{2\alpha}{3D_a}(N_o^3 - N_x^3) + \frac{1}{D_a\tau}(N_o^2 - N_x^2)}} \qquad (2.17)$$

The integral in (2.17) is not easily solved analytically and thus a numerical solution was obtained. The relevant data are:

$$D_a = 300 \text{ cm}^2\text{sec}^{-1}, \text{ (Brown, 1961)},$$
$$\gamma = 3.1 \times 10^{-4}\text{sec}, \text{ (from eqs (2.10) and (2.11))},$$
$$\alpha = 3.5 \times 10^{-11}\text{cm}^3\text{sec}^{-1}, \text{ (Brown, 1961)}$$

The electron density N_o lies in the range 10^{13} - 10^{14}cm^{-3} (Belal and Dunn, 1978). Using $N_o = 10^{13}\text{cm}^{-3}$, χ was calculated as 0.50 cm. If volume recombination is neglected by setting $\alpha = 0$ in eq (2.17), then $\chi = 0.52$ cm and thus volume recombination may be neglected for $N_o = 10^{13}\text{cm}^{-3}$ or less without incurring serious error. The shape of $N_x(x)$ may be obtained by evaluating eq (2.17) over different limits of integration. These shapes are plotted in fig 2.21 for different values of N_o. It can be seen that eq (2.17) yields the surprising result that χ decreases as N_o is increased. However, the rate of recombination is proportional to N_x^2, and with the assumed boundary condition that $\left(\frac{dN_x}{dx}\right)_{x=0} = 0$, the results are self-consistent. Evidence for this lies in the result that χ does not depend on N_o if $\alpha = 0$ (recombination neglected), all values of N_o yielding the result that $\chi = 0.52$ cm. For a finite cylinder of length L, the requirement that the particle flux to the boundaries at $x = \pm L/2$ is zero yields the result that the particle density follows a $\cos\left(\frac{\pi x}{L}\right)$ law.

2.12.6 Evaluation of D.

From steps 1,2 and 3 above, D is calculated as 2.85 cm. Thus it may be concluded that the anode cathode pairs of fig 2.17 will behave as a series of hollow cathodes provided that $D > 2.85$ cm. However, tube No.1 behaved as a series of hollow cathodes with $D = 2.0$ cm, and thus a discrepancy exists. However, the calculated value of D is an "upper limit" estimate based on a simplified model. For example, diffusion losses to the tube walls were neglected in step 2 above, where the implicit assumption was that the electrons originating at the cathode dark space/negative glow boundary maintained their "beam-like" properties until they were unable to produce further ionisation. This is equivalent to ignoring elastic collisions, a process which has a large cross section especially at lower electron energies (for example, $q_{elastic} \simeq 5 \times 10^{-16} cm^2$ for < 4 eV electrons, Brown, 1961).

A further consideration is the effect which the proximity of an adjacent anode/cathode pair may have on D. Since the second anode is at the same potential as the first cathode in fig 2.4, electrons will be unable to reach the second anode, and thus will be trapped within the electrostatic bottle formed by the first cathode and the second anode. Thus it may also be deduced that the size of the bore in the second anode (6 mm in tube No.1) will have an effect on D, the smaller the bore the smaller D may be made without the discharges affecting each other.

2.13 Concluding Remarks

Discharge tube structures similar to tube No.1 exhibit the VI characteristics of hollow cathodes over wide ranges of current, helium pressure and cadmium vapour density. The glass sections which separate each anode/cathode pair are a crucial feature of the design, since they provide a recombination site at the tube walls. It has been shown that these glass sections have a minimum length below which the discharge from one anode/cathode pair interferes with the discharge between an adjacent anode/cathode pair.

Discharge tubes consisting of anode/hollow cathode pairs provide a stable glow discharge suitable for He-Cd hollow cathode lasers. When operated in series, the resulting axial electric field provides an efficient means of distributing Cd vapour from a single oven source by the process of cataphoresis. Multiple sources of cadmium and/or a flowing gas system, which are necessary features of conventional hollow cathode lasers, may thus be dispensed with, and greater stability achieved in the output. Segmented discharge tubes incorporating anode/cathode pairs may be suitable as "sealed-off" devices.

Tubes Nos. 2 and 3 were constructed without discrete anodes and behaved as a series of hollow cathodes only at low values of discharge current. The VI characteristics showed that a transition current value existed above which only the VI curve of the last cathode segment (at power supply earth potential) continued to display the positive slope associated with a negative glow discharge in which there is no positive column. The other

segments exhibited a potential drop as the current was increased above the transition value. This behaviour is explained in terms of the plasma length, defined in Section 2.11. The transition current value is reached when the current-dependent plasma length becomes equal to the segment length.

PLATE 2.1 TOP: TUBE No.1 WITH FRACTURED GLASS / METAL SEAL (AT TUBE CENTRE).

BOTTOM: TUBE No.2. NOTE SPUTTERING BETWEEN METAL SEGMENTS.

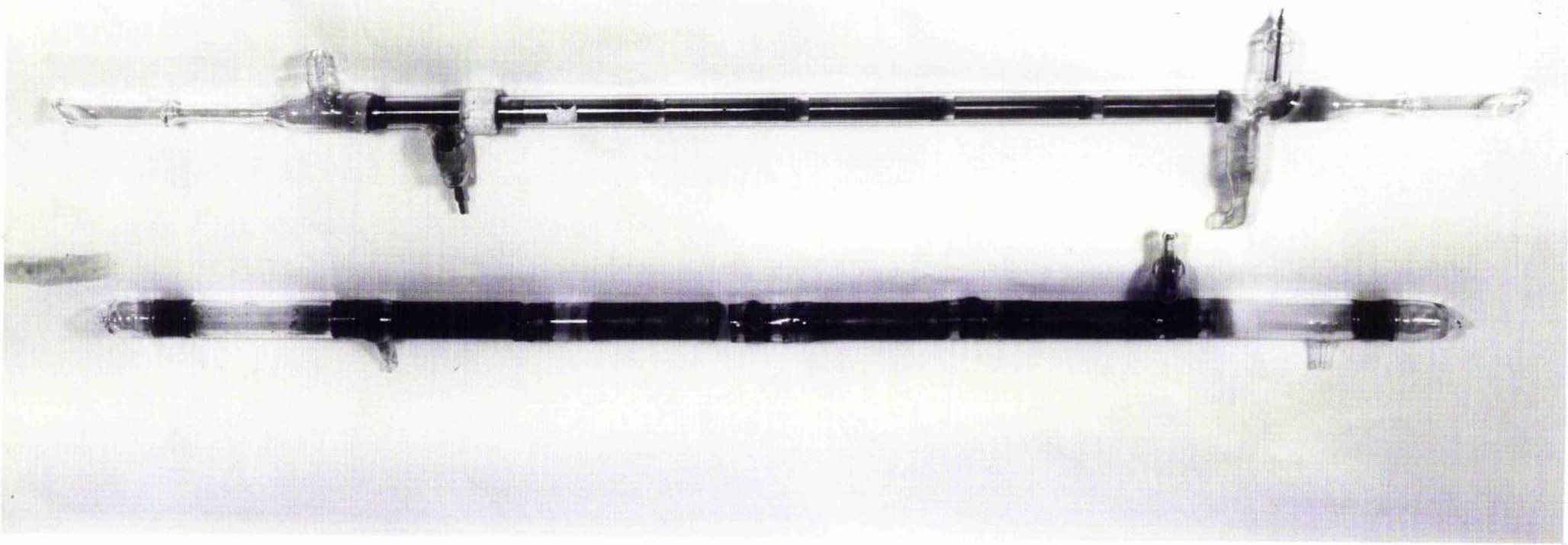

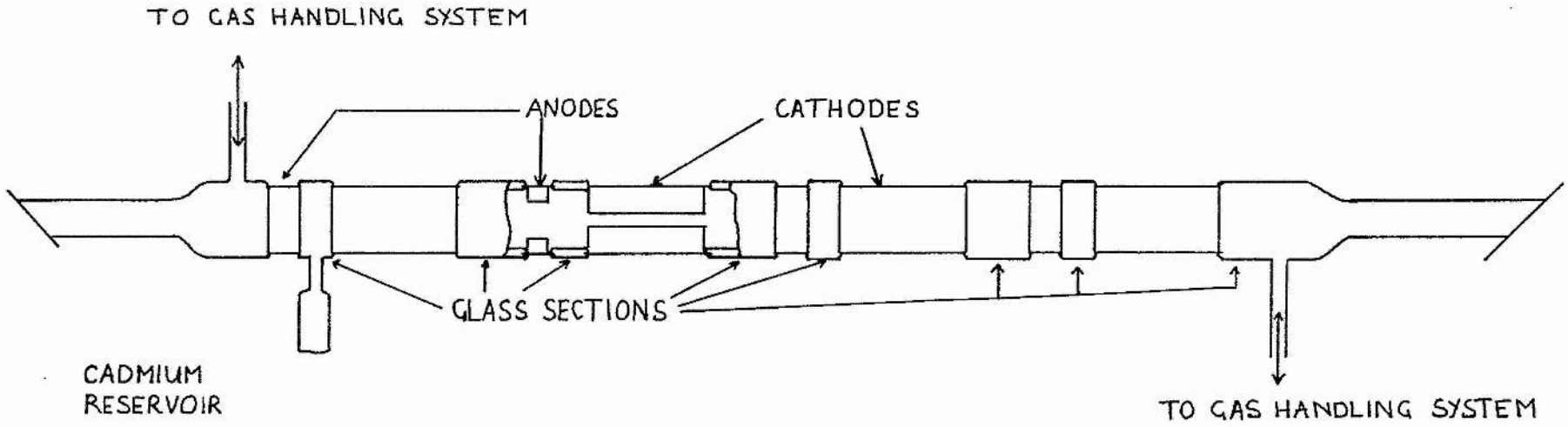

FIG. 2.1 TUBE No.1 COMPRISING FOUR ANODE CATHODE PAIRS

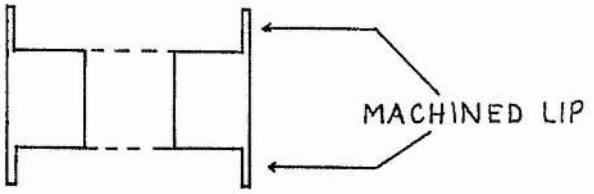

FIG 2.2 (a) ANODE SECTION

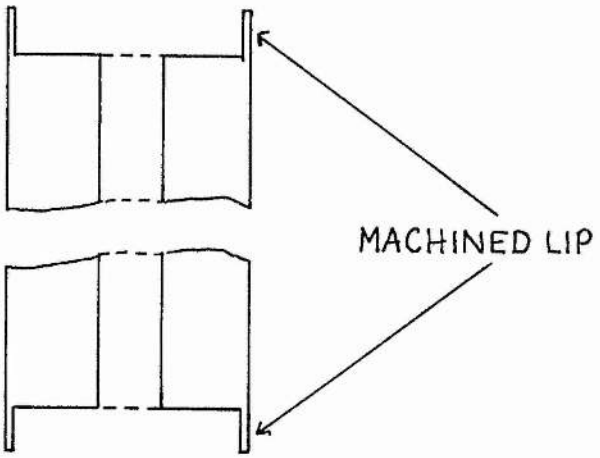

FIG 2.2(b) CATHODE SECTION

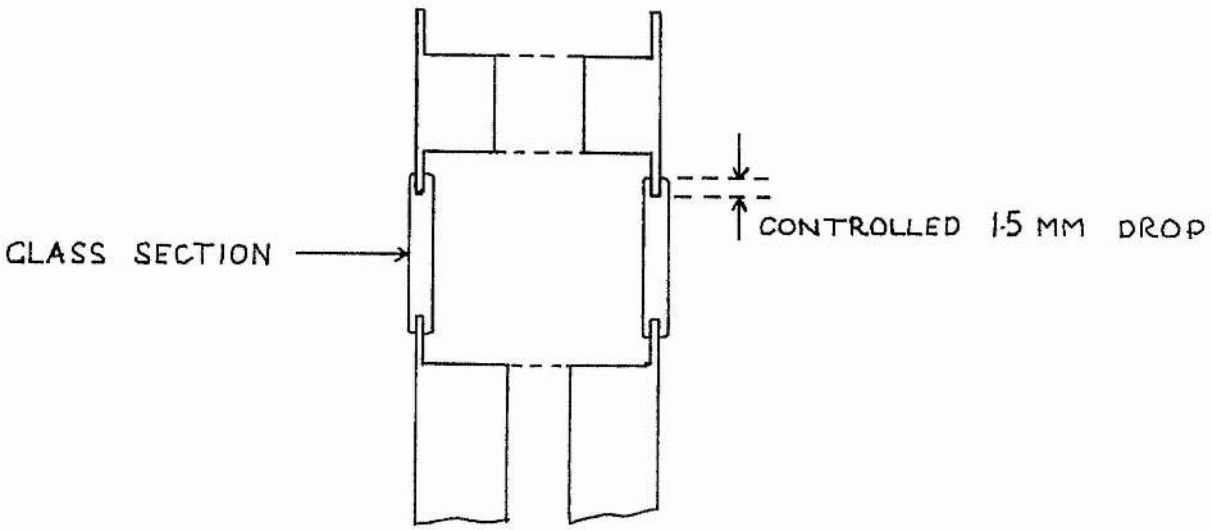

FIG. 2.2(c) GLASS TO METAL SEALS COMPLETED

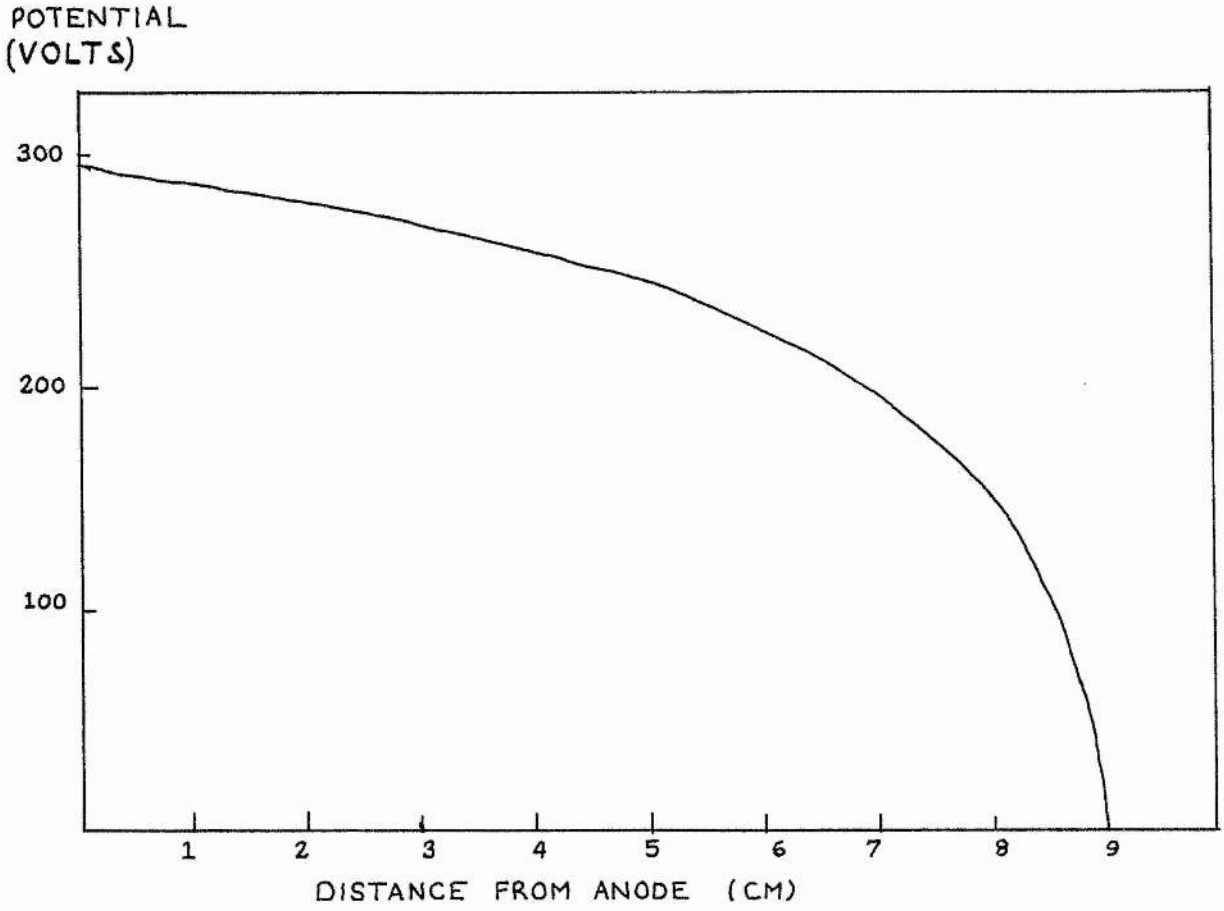

FIG 2.3 POTENTIAL VS DISTANCE FROM ANODE IN A CYLINDRICAL HOLLOW CATHODE UNDER CONDITIONS APPROPRIATE TO LASING (GRACE, 1978)

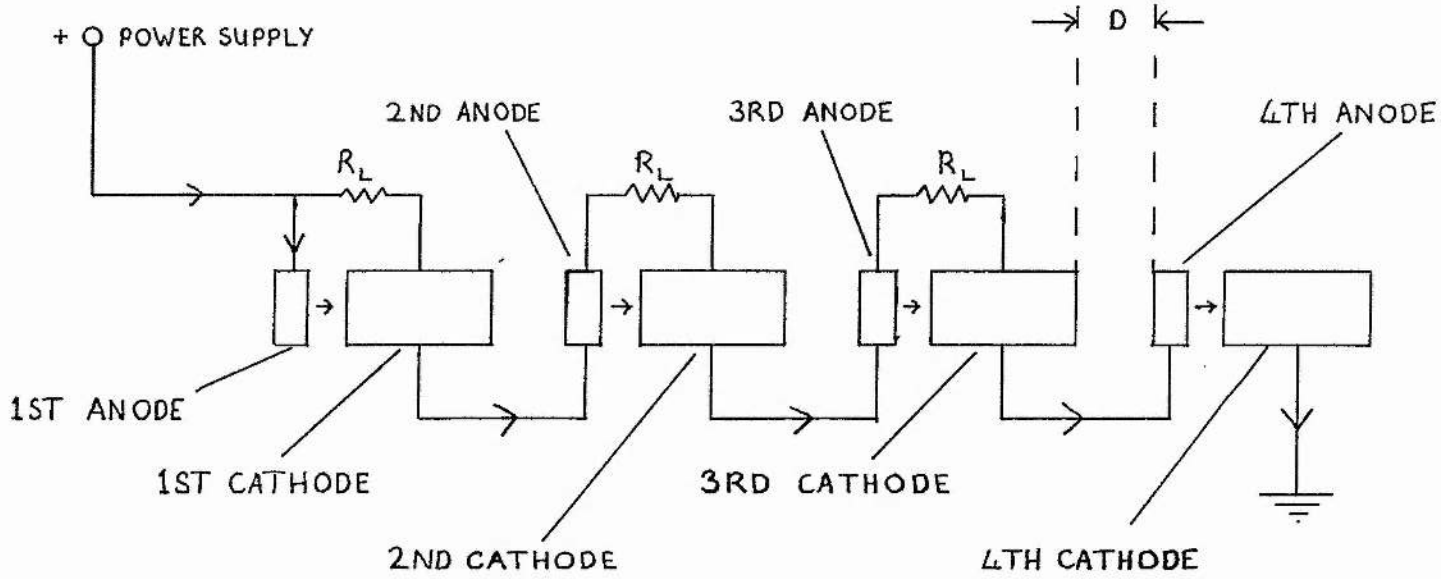

FIG 2.4 DISCHARGE CIRCUIT FOR TUBE No 1

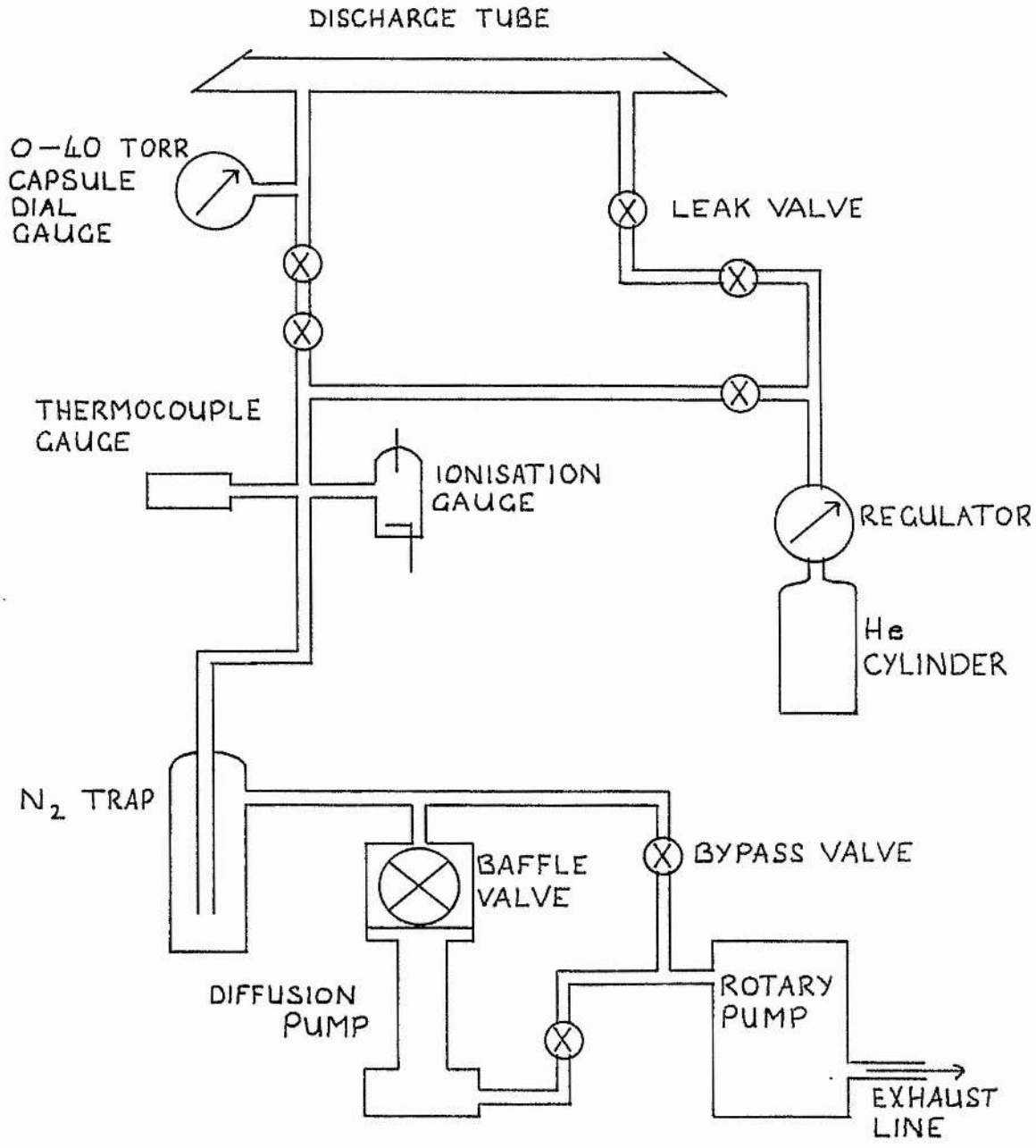

FIG 2.5 SCHEMATIC OF GAS HANDLING SYSTEM

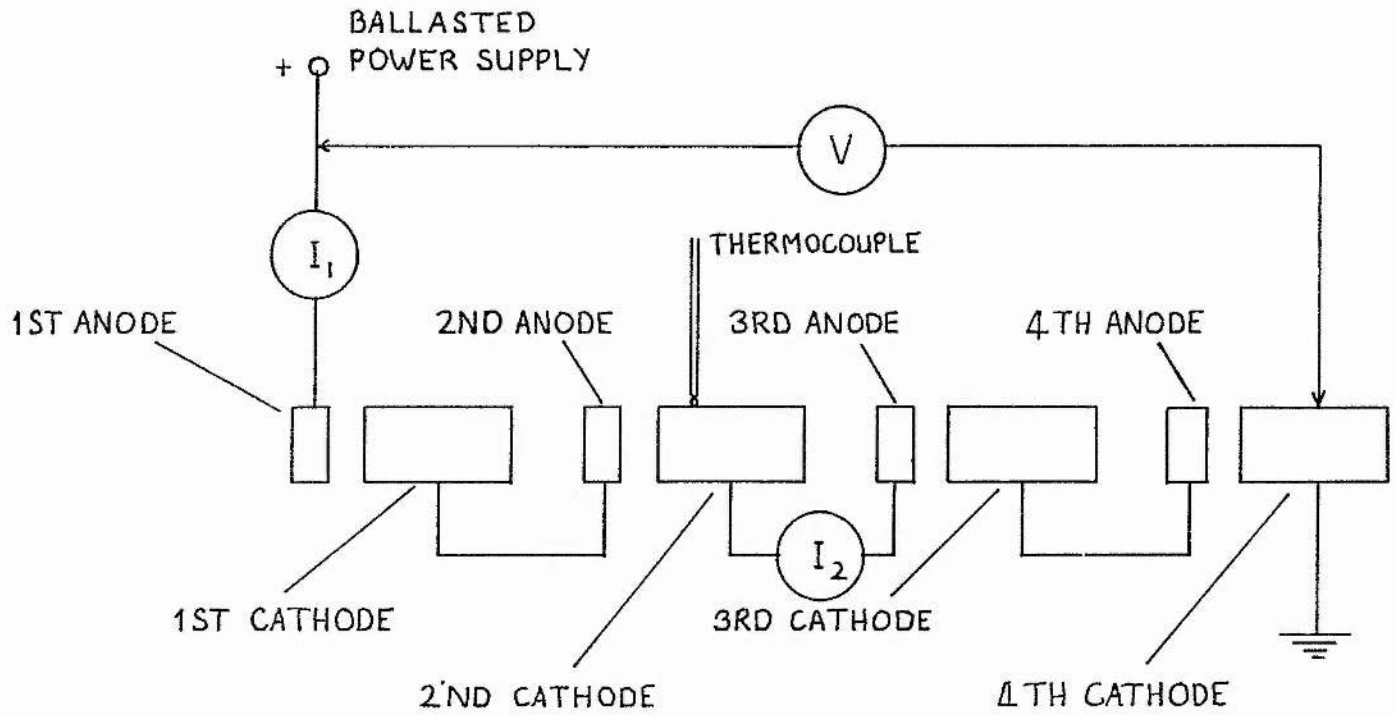

FIG 2.6 DISCHARGE CIRCUIT FOR TUBE No.1

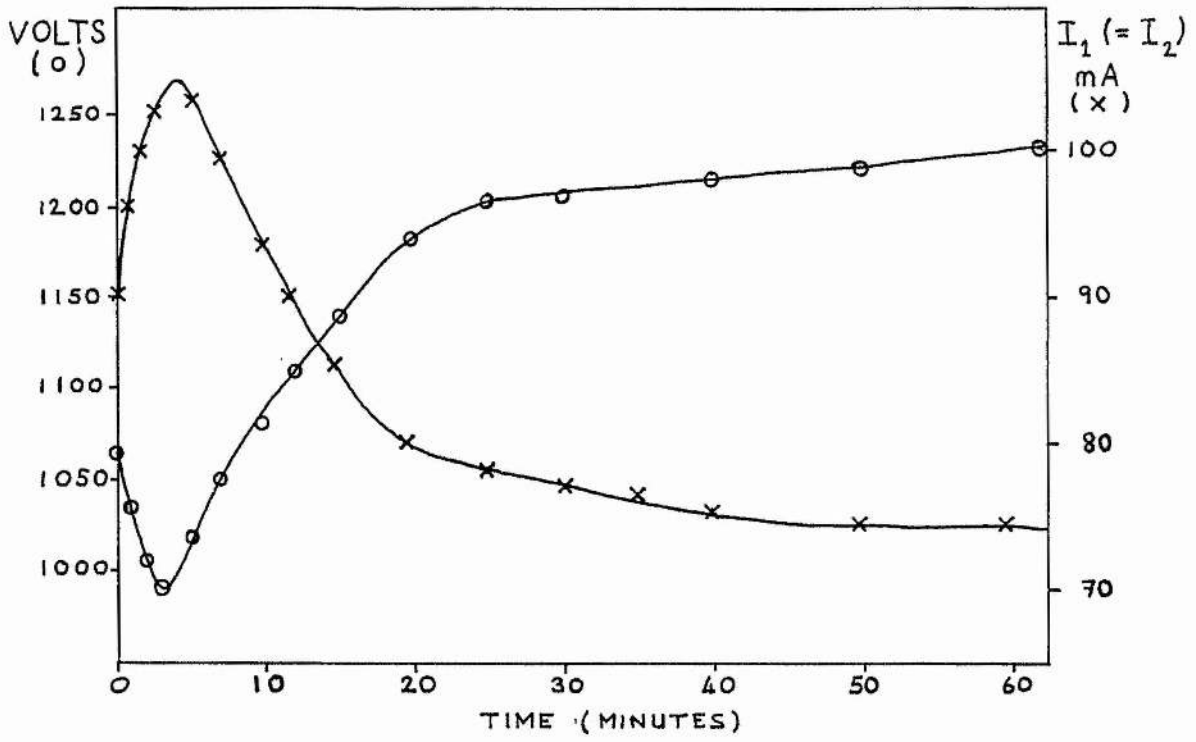

FIG. 2.7 TUBE No 1 VOLTAGE AND CURRENT AS A FUNCTION OF TIME. PRESSURE = 12 TORR HELIUM.

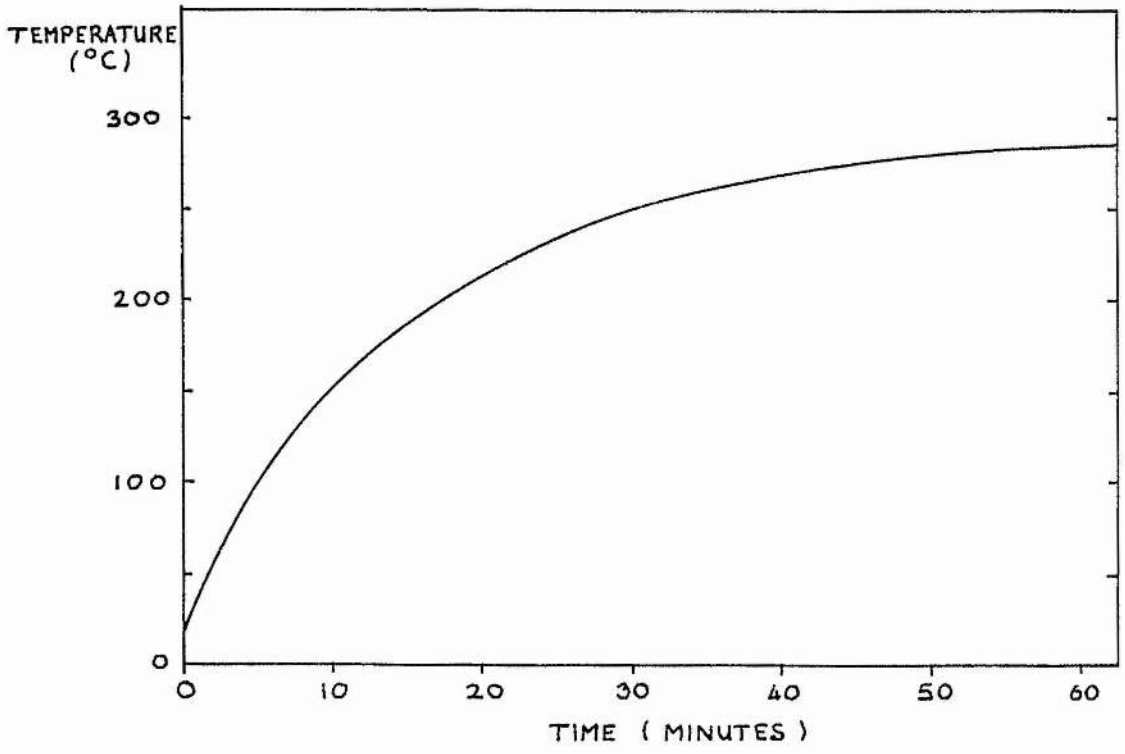

FIG. 2.8 WARM UP TIME FOR TUBE No 1.

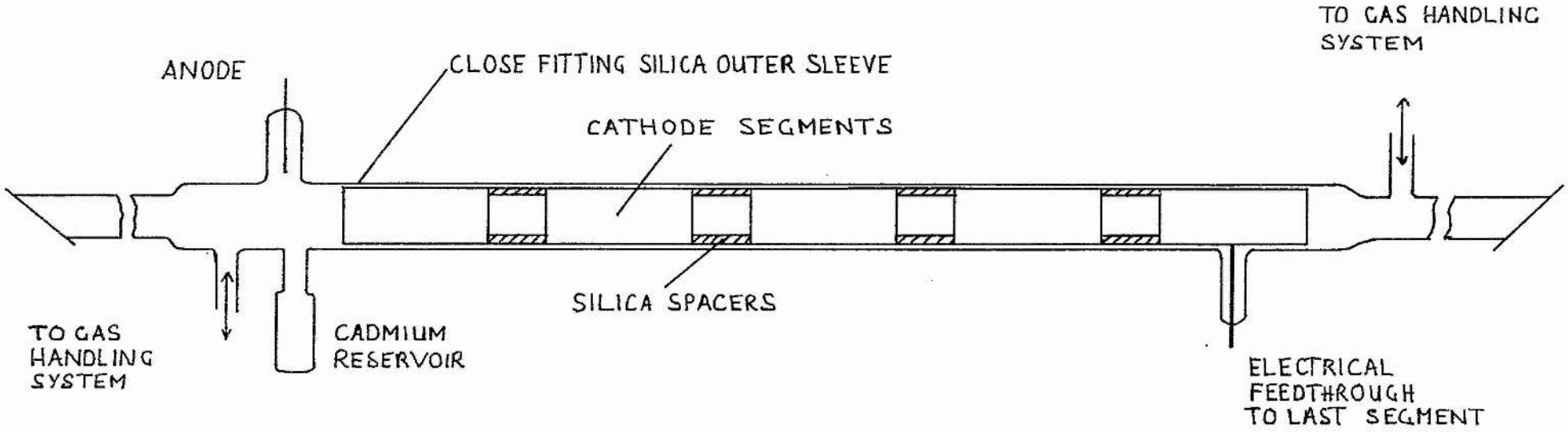

FIG 2.9 TUBE No 2.

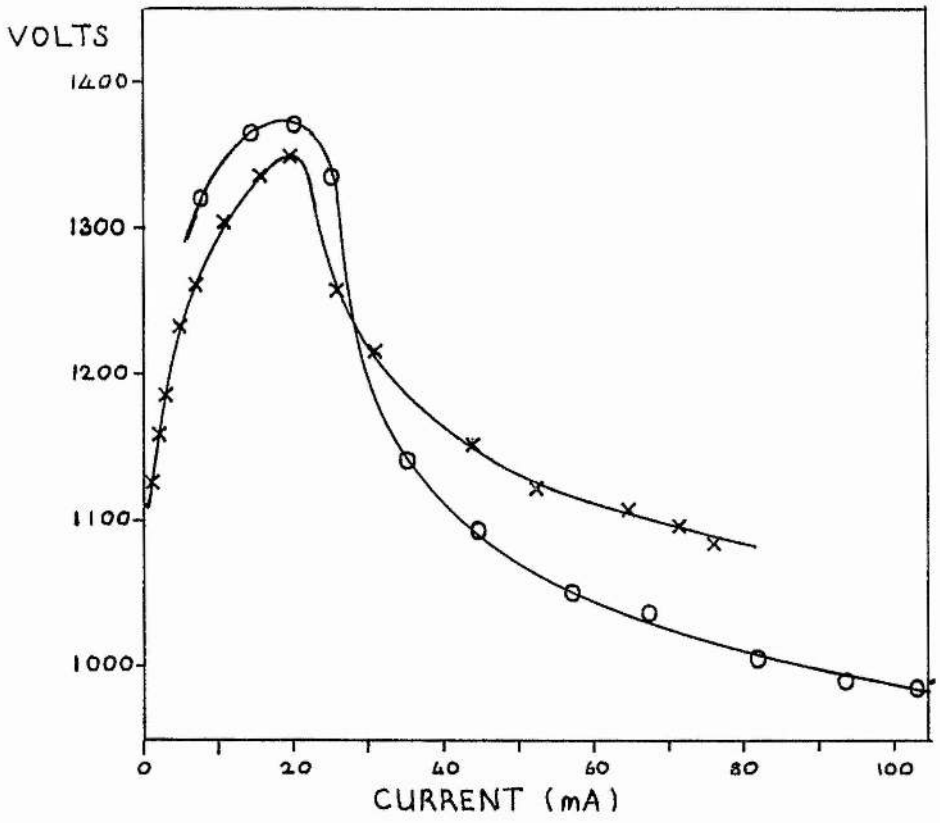

FIG. 2.10 VI CHARACTERISTICS FOR TUBE No. 2 AT 10 TORR (O) AND 15 TORR (X) HELIUM FILLING PRESSURE.

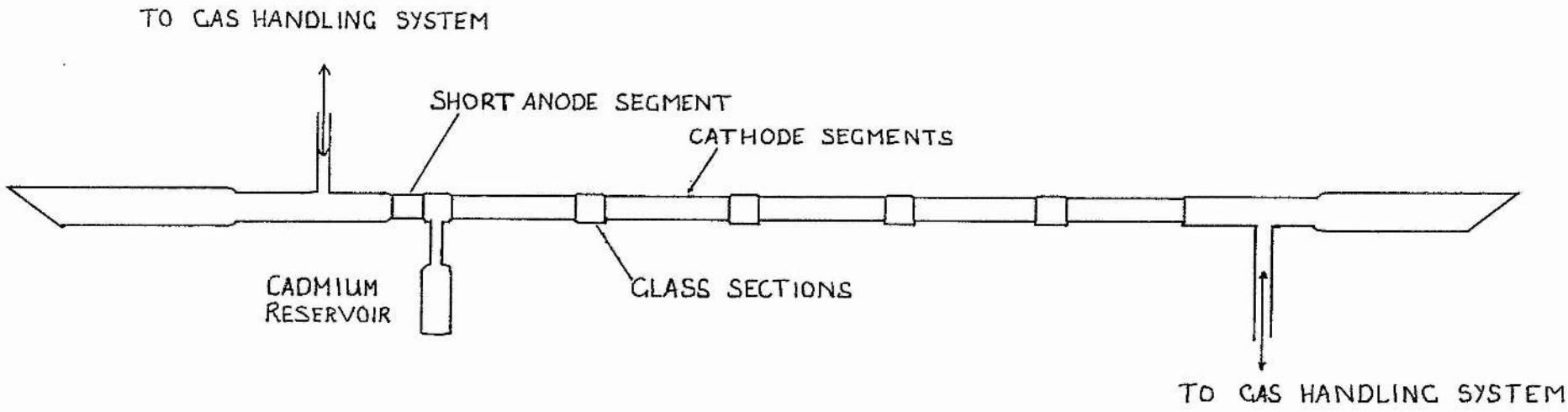

FIG 2.11 TUBE No 3.

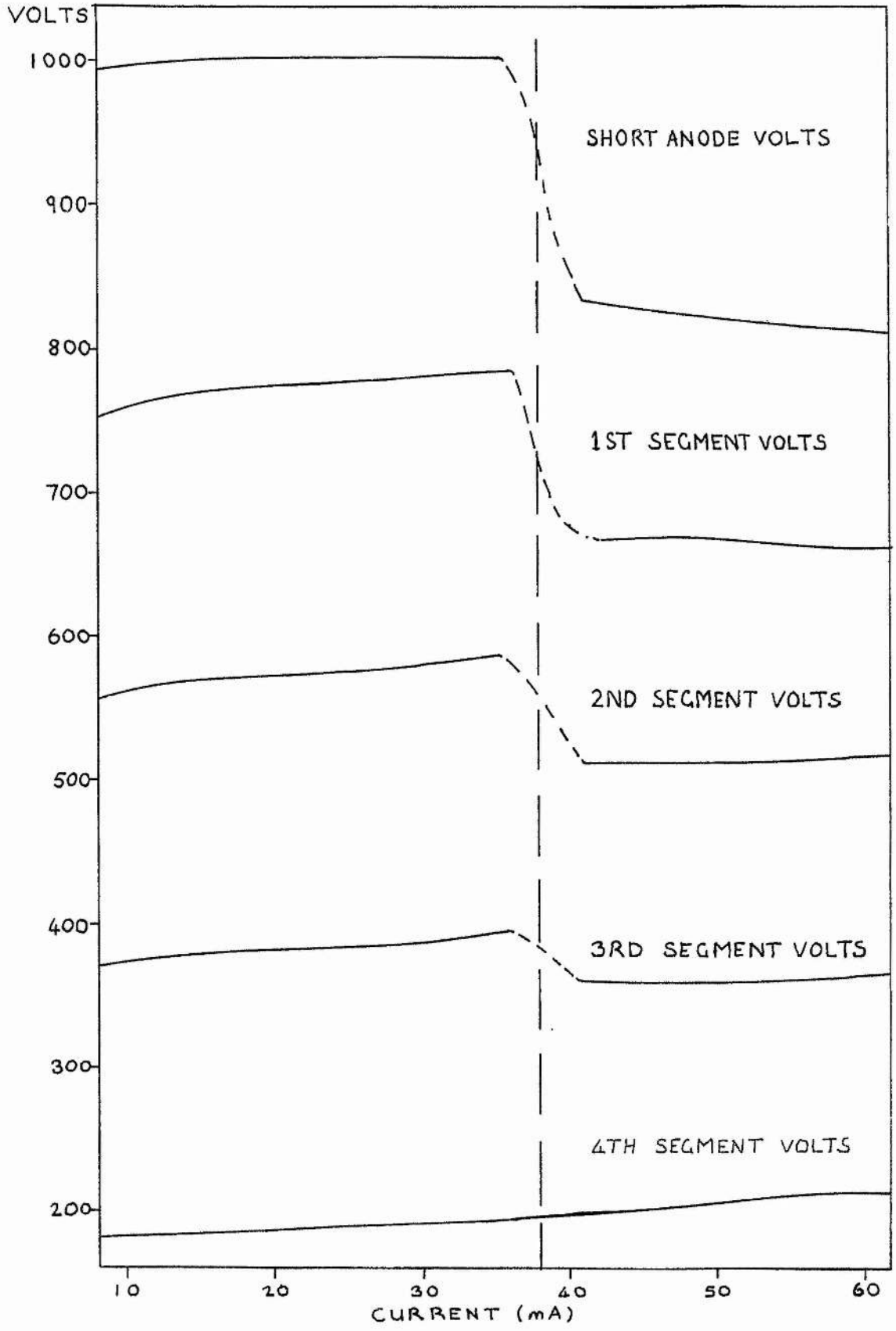

FIG. 2.12 VI CHARACTERISTIC FOR TUBE No.3
HELIUM PRESSURE 5 TORR.

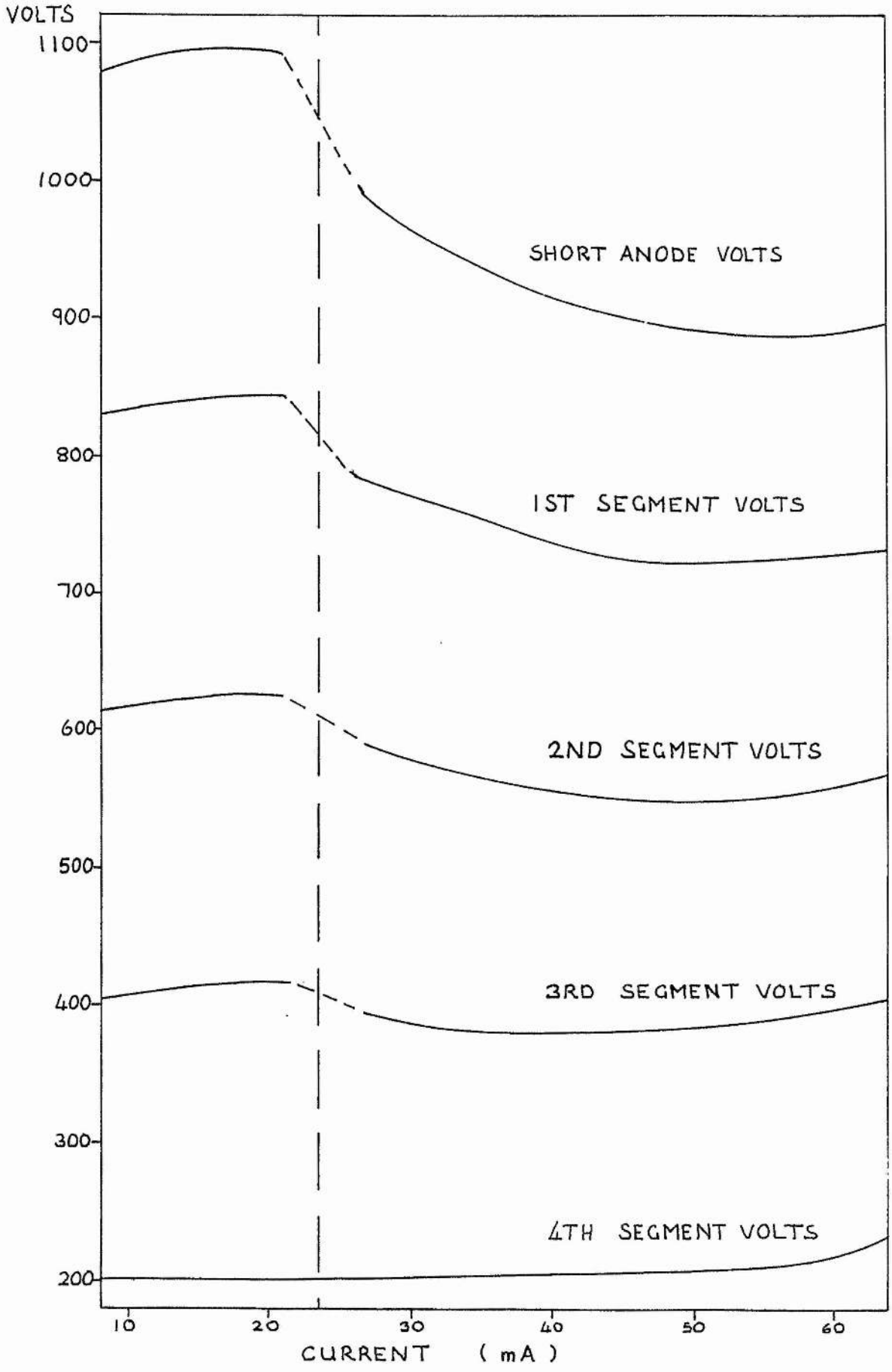

FIG. 2.13 VI CHARACTERISTIC FOR TUBE No. 3
HELIUM PRESSURE 10 TORR.

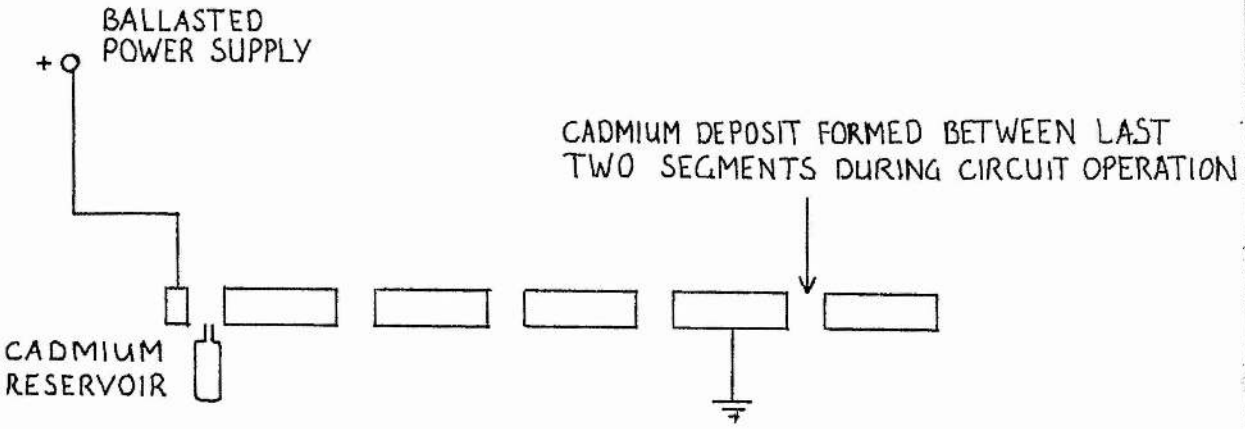

FIG. 2.14 LASER CIRCUIT WITH PENULTIMATE SEGMENT EARTHED.

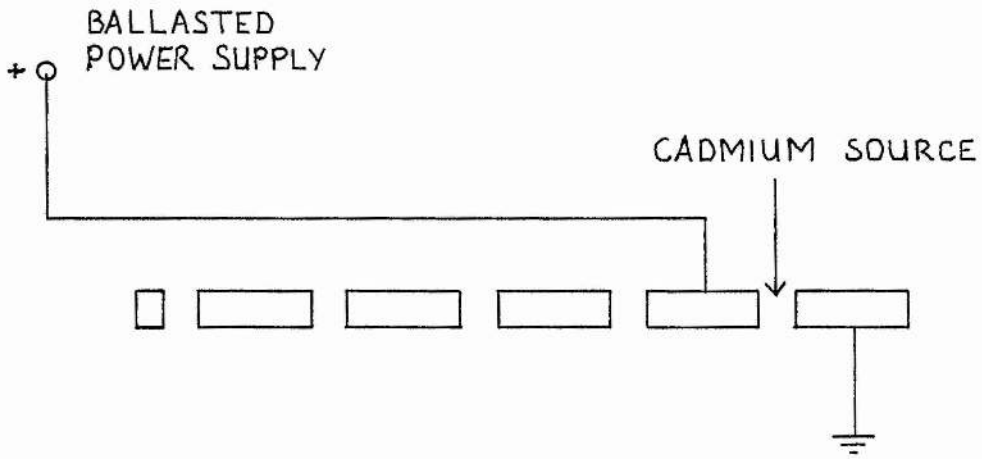

FIG. 2.15 LASER CIRCUIT USING ONLY LAST TWO SEGMENTS.

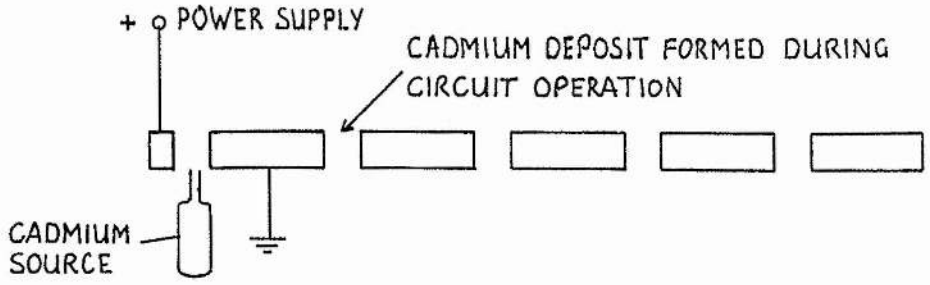

FIG. 2.16 (a)

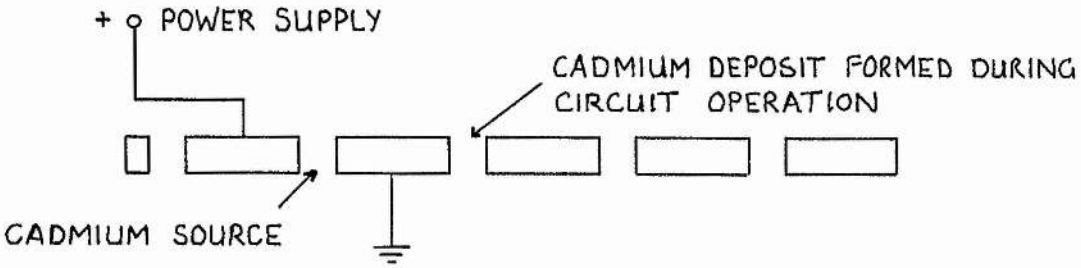

FIG. 2.16 (b)

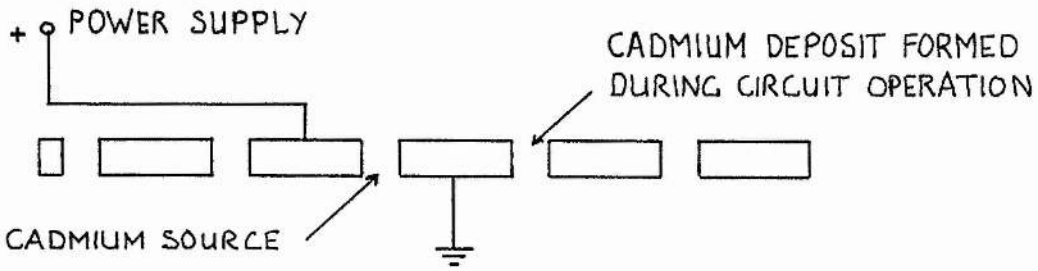

FIG. 2.16 (c)

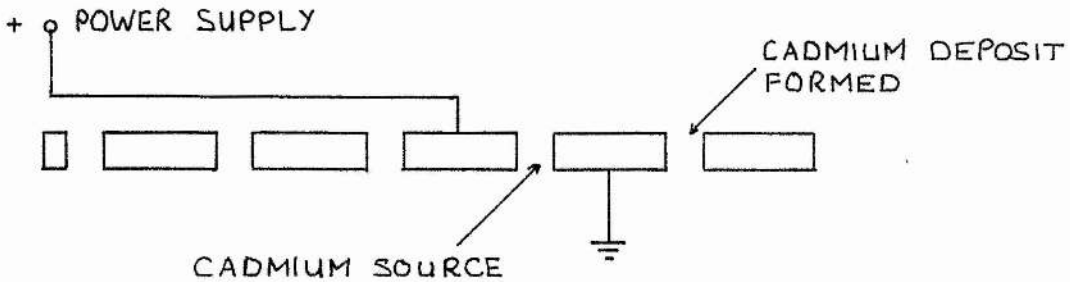

FIG. 2.16 (d)

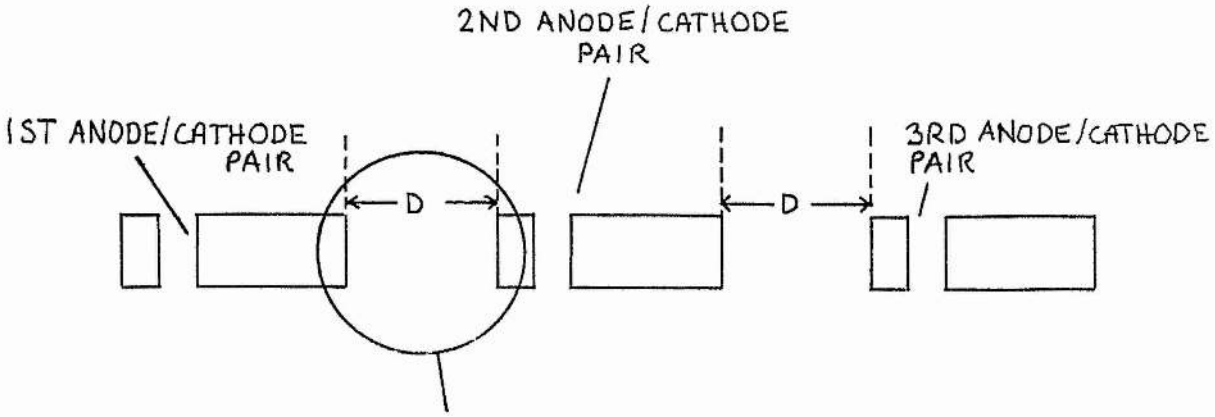

FIG. 2.17 THREE ANODE/CATHODE PAIRS SEPARATED BY DISTANCE D.

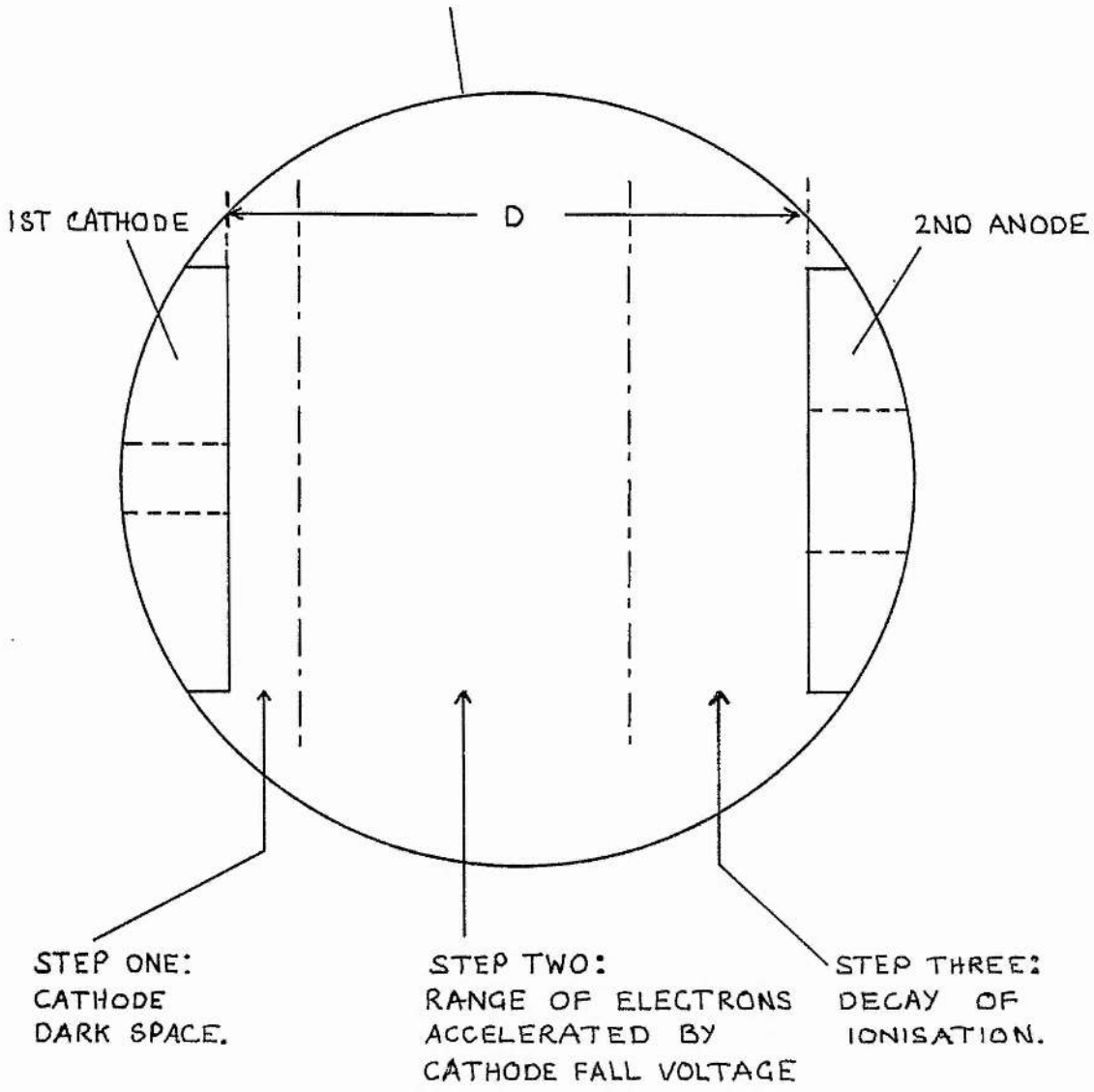

FIG. 2.18 THE THREE STEPS INVOLVED IN THE CALCULATION OF D.

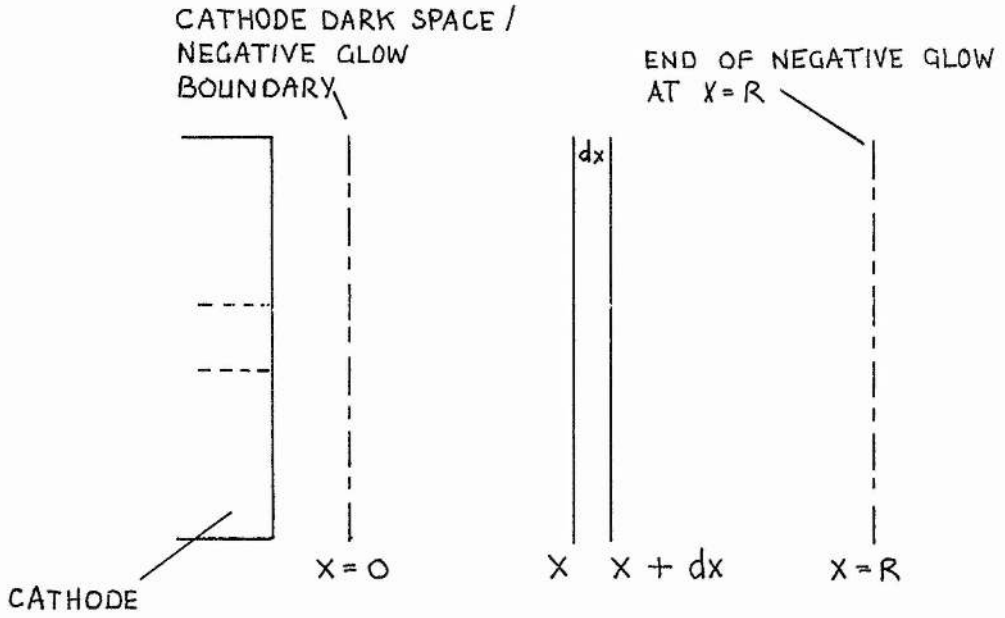

FIG 2.19 STEP TWO : RANGE OF 300 eV ELECTRONS

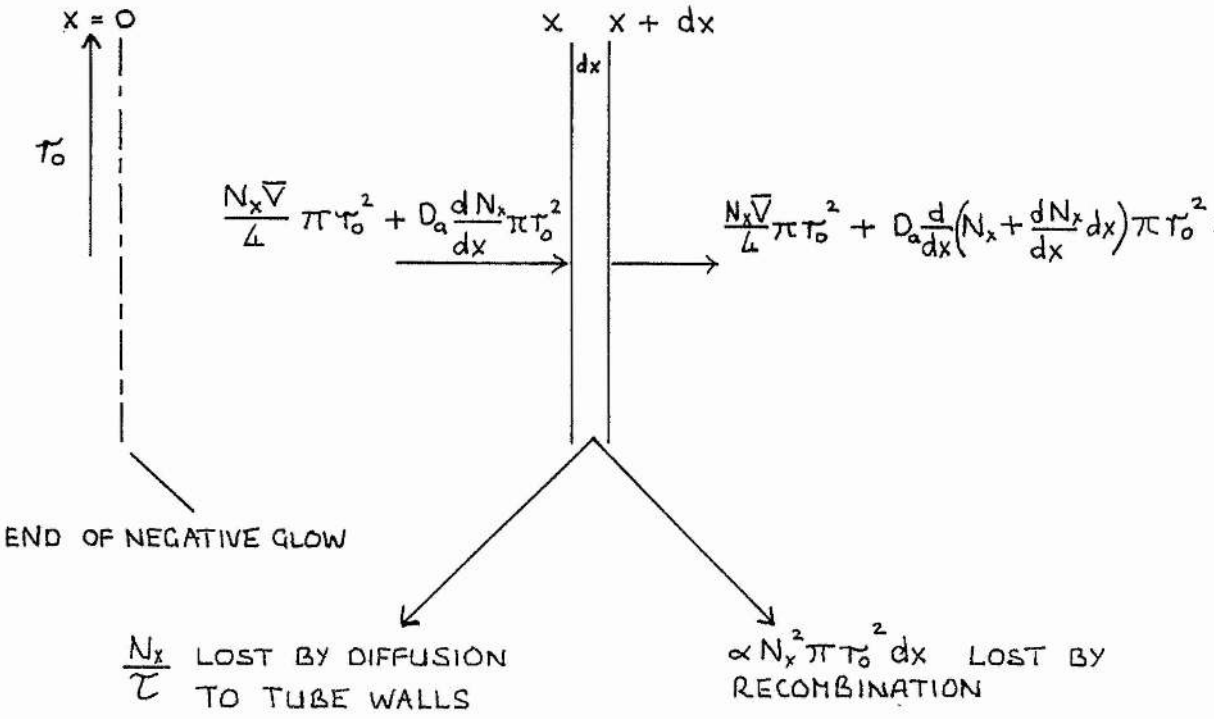

FIG. 2.20 STEP THREE : DECAY OF IONISATION

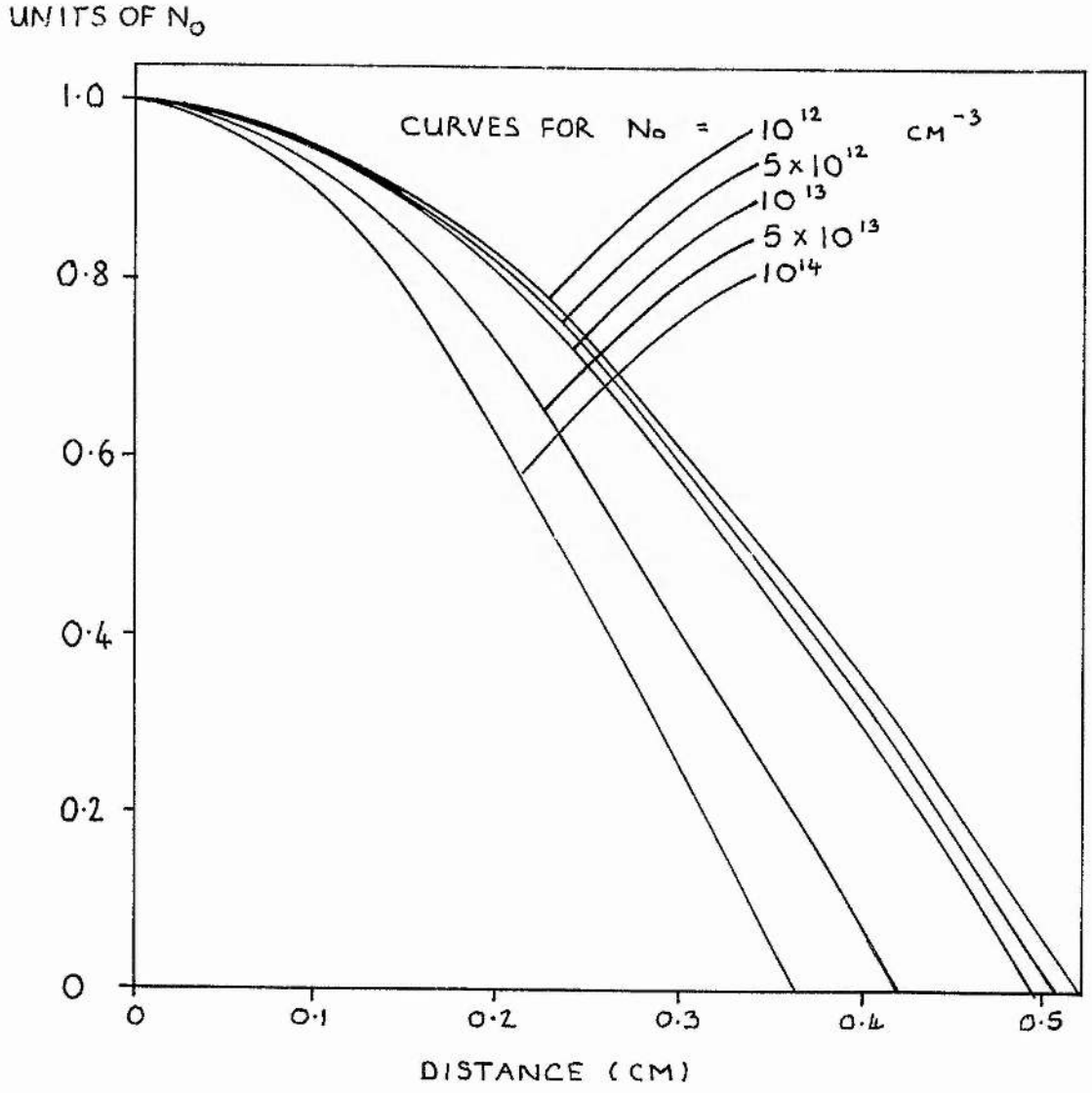

FIG 2.21 SHAPE OF Nx VS DISTANCE FOR DIFFERENT VALUES OF N_o.

CHAPTER TWO BIBLIOGRAPHY.

BELAL, I.K. and DUNN, M.H.

J. Phys. D : Appl. Phys., 11, 313-323, 1978.

BREWER, A.K. and WESTHAVER, J.W.

J. Appl. Phys., 8, 779-782, 1937.

BROWN, S.C.

"Basic Data of Plasma Physics", Wiley (New York) and Chapman and Hall (London), 1961.

FRANCIS, G.

Handbuch der Physik, 22, 54-208, 1956.

FUJII, K., TAKAHASHI, T. and ASAMI, Y.

IEEE J. Quant. Electron., QE-11, 111-114, 1975.

FUJII, K., OSHIMA, T., OTAKA, M., NAGASHIMA, S., MIYAZAWA, S. and OIKAWA, T.

IEEE J. Quant. Electron., QE-16, 590-592, 1980.

GRACE, J.R.

"Hollow Cathode Metal Vapour Lasers", M.Sc. Thesis, University of New England, New South Wales, Australia, 1978.

KIN-HUNG, W. and GREY MORGAN, C.

J. Phys. D : Appl. Phys., 16, L1-L4, 1983.

LEHMAN, J.F.

Proc. Roy. Soc., 115, 624-639, 1927.

MCDANIEL, E.W.

"Collision Phenomena in Ionised Gases", Wiley (New York), 1964.

MIZERACZYK, J. and NEIGER, M.

XVI International Conference on Phenomena in Ionised Gases, 210-211, 1983, Dusseldorf, West Germany.

PIPER, J.A. and WEBB, C.E.

J. Phys. D : Appl. Phys., 6, 400-407, 1973.

WANG, S.C.

Proceedings of the Society of Photo-Optical Instrumentation Engineers, 232, 42-46, 1980, (International Optical Computing Conference, 1980).

CHAPTER THREE

THERMAL DESIGN CRITERIA FOR HOLLOW CATHODE He-Cd LASERS.

3.1 Introduction.

All of the hollow cathode devices used as excitation media for He-Cd lasers depend on thermal evaporation of the metal to maintain the metal atom density within the range over which optimum laser output occurs. Since the number density/vapour pressure of cadmium is strongly temperature dependent, thermal stability is an important feature of all hollow cathode He-Cd lasers. The approximate empirical law relating cadmium vapour pressure and temperature is given by

$$\log_{10} P(\text{Torr}) = 9{\cdot}02 - \frac{5940}{T(K)}$$

(Nesmeyanov, 1963).

For those hollow cathode lasers of the self heated

variety (eg Fujii et al,1975), the whole tube structure needs to be at a uniform temperature otherwise local variations in the cadmium vapour partial pressure may occur. On the other hand, those hollow cathode lasers which have an oven source of cadmium (Piper and Webb, 1973) generally depend on discharge heating to maintain the entire cathode structure at a temperature above that of the oven source.

For both of these categories of laser, axial temperature gradients produce local variations in gas density and cadmium vapour density and thus an axially uniform temperature within the cathode is a desirable design feature.

For slotted hollow cathodes (eg, Schuebel 1970), an axially uniform temperature is facilitated by the use of a distributed anode, and thus the input power per unit length is constant. However, for flute-type geometries with discreet anodes, and concentric cylinder geometries with perforated cathodes, the input power per unit length is not constant and thus axial temperature gradients will occur. The choice of inter-anode spacing for flute-type geometries and the spacing of the perforations in concentric cylinder geometries is thus not solely dependent on the necessary condition of overlapping axial negative glows. The axial temperature gradients which result must also be taken into account.

In this chapter, a twin thin-walled cathode structure with discrete anodes is described. The thermal operating characteristics of this tube, together with those of tubes Nos 1, 2 and 3, show the necessity for a detailed analysis upon which thermal design criteria for hollow cathode lasers may be based.

3.2 Tube No.4 Description.

Tube No.4 is of silica and stainless steel construction, with two 8 cm cathode sections and three tungsten pin anodes arranged as illustrated in fig 3.1. The cathode sections were of thin walled (0.9 mm) stainless steel pipe, each with a 4.5 mm bore. Threaded nickel tipped tungsten rods screwed into the cathode wall served as electrical "feedthroughs" for the cathodes. A centrally situated sidearm contained cadmium of natural isotopic abundance, and the tube was equipped with Brewster angled windows. Auxiliary ovens situated at each end of the discharge region close to the end anodes were included in the design. The outer silica envelope fitted closely over the external cathode surfaces to prevent the discharge from striking to them and generating unwanted heat. The oven heater element consisted of a 50 cm length of 36 swg Eureka wire, wound on a former, and placed over the sidearm, the temperature of which was monitored with a thermocouple. An adjacent thermistor provided the necessary feedback for the "electronic thermostat" described in Appendix One, capable of maintaining a steady sidearm temperature to within ± 2 ^{o}C in the range 250 - 350 ^{o}C.

3.3 Tube No.4 Operation.

The tube was initially operated with the circuit illustrated in fig 3.2(a), each of the three anodes being individually ballasted such that the central anode carried twice as much current as either of the auxiliary anodes.

With the currents set such that $I_1 = I_2 = 120 \pm 5$ mA, the introduction of cadmium into the discharge produced lasing on the green lines of Cd II with the same optical cavity as was described in Chapter Two. However, lasing ceased when the current distribution became uneven, with $I_1 = 175$ mA and $I_2 = 45$ mA. A closer investigation of this with the circuit illustrated in fig 3.2(b) showed that the uneven current distribution occurred in a random fashion. Attempts to overcome this by introducing a variable ballast resistor R_{extra} into the circuit, as illustrated in fig 3.2(b), were unsuccessful.

During the course of these experiments, it was also noted that the cathode was being heated non uniformly. Brightness temperature measurements with an optical pyrometer showed that cathode surfaces nearest to the anodes could attain temperatures of $\sim 850 \pm 100$ °C, while the central area of each cathode never exceeded ~ 525 °C (at which temperature black body radiation emitted by a surface starts to become visible to the naked eye). With a thin-walled cathode structure supplied by discrete anodes it may thus be concluded that non-uniform discharge heating gives rise to large axial temperature variations.

Laser oscillation on the green lines of Cd II was obtained over a broad range of pressures (10 - 40 Torr) for

discharge currents of approximately 110 mA per cathode. However, because of the random occurrence of uneven current division between the two cathodes, laser output varied in a similarly random manner, (correlated with the variations of current division).

3.4 Tube No.4 Discussion.

The two major problems associated with tube No.4 were uneven current division between the two discrete cathodes at the central anode, and the existence of large axial temperature variations within each of the cathodes. It is believed that the first of these problems could be overcome by reducing the intercathode spacing such that the negative glows from each of the cathodes coalesced, or by constructing the tube with one cathode only. However, the axial temperature gradients are a problem which will always exist, to a greater or lesser degree, when discrete anodes are used. The problem may be greatly alleviated by increasing the thickness of the cathode wall, and one of the objectives of the remainder of this chapter is to derive criteria for cathode design from the solution of an equation describing heat transfer within a cylindrical conductor.

Large temperature variations ($\sim$350 K) cause local variations in helium density and cadmium vapour density. The number density is proportional to the inverse of the temperature, and thus if the coolest part of the cathode is at 500 ^{o}C where the number density is n(500), then at the hottest part of the

cathode (850 °C), the number density is given by n(850) = 0.69 n(500). Parametric observations by other workers have shown that laser output power is strongly dependent on helium gas pressure and cadmium vapour pressure.

High temperatures may also affect laser performance by increasing the Doppler broadened linewidth of the laser transitions. This has been judged to have been the cause of lack of laser oscillation in other He-Cd hollow cathode systems (eg, Otaka et al, 1981). However, the analysis presented below, which is carried out for the 441.6 nm laser transition in both natural cadmium and single isotope Cd^{114}, shows that the effects of high temperatures may be less detrimental than the effects of large temperature differences.

3.5 Doppler Broadening of the 441.6 nm Line.

The laser gain $g(\nu)$ in an amplifying medium is proportional to the linewidth factor, $\alpha(\nu)$, where ν is the frequency. Thus the ratio of linewidth factors $\alpha(T_1)/\alpha(T_2)$ at temperatures T_1 and T_2 is a measure of the effect of temperature on the laser gain. The normalised Doppler broadened line shape for an atomic line is given by

$$g(\nu) = \frac{c}{\nu_0}\left(\frac{M}{2\pi kT}\right)^{1/2} \exp\left(-\frac{M}{2kT}\,\frac{c^2(\nu-\nu_0)^2}{\nu_0^2}\right),$$

where ν_0 is the frequency at line centre, M is the atomic mass,

T the temperature and C the speed of light. For a mixture of isotopes, $\alpha(\nu)$ is given by the sum $\sum_i a_i \alpha_i(\nu)$ where a_i is the fraction of isotope i in the sample. For cadmium of natural isotopic abundance, there are eight stable isotopes with mass numbers in the range 106 - 116. The relative proportions of these are given in Table 3.1, together with the observed isotopic splitting (Kuhn and Ramsden, 1956). Thus, for natural isotopic cadmium, we have, for the 441.6nm Cd II line,

$$\alpha(\nu) = a_{106}\alpha_{106} + a_{108}\alpha_{108} + a_{110}\alpha_{110} + a_{111}\alpha_{111} + a_{112}\alpha_{112} + a_{113}\alpha_{113} + a_{114}\alpha_{114} + a_{116}\alpha_{116}$$

where the subscripts refer to the mass numbers.

The lineshape illustrated in fig 3.3 is obtained by summation for the isotopes present. The lineshape for single isotope Cd^{114} is also illustrated in fig 3.3, where the results presented are normalised for the natural isotope lineshape maximum at mass number 112. It can be seen from fig 3.3 that a factor of approximately 2.8 enhancement in peak gain may be realised if Cd^{114} is used instead of natural isotope cadmium at 350 ^{o}C.

The effects of temperature on the lineshape maxima are illustrated for natural and single isotope Cd^{114} in figs 3.4(a) and 3.4(b), respectively. An increase in temperature from 350 ^{o}C to 750 ^{o}C reduces the maximum gain by 13% and 21% for natural and single isotope cadmium, respectively.

It may be concluded that the effect of high temperatures themselves are less important than the existence of large temperature differences on the hollow cathodes of He-Cd lasers.

3.6 Heat Transfer Analysis for Hollow Cathodes.

The heat transfer analysis presented below yields design criteria for overcoming two major problems encountered with the operation of tubes Nos. 1,2,3 and 4, and is applicable to the design of hollow cathodes for lasers generally.

The first of these problems is the protection of glass/metal seals from excessive temperatures. Figure 3.5(a) shows a glass/metal seal attached to a section of hollow cathode, via a metal cylinder AB. We assume that the discharge is confined within the cathode bore, which, under conditions of thermal equilibrium, is at temperature t_H . Under these conditions, discharge generated heat flows from the cathode section towards the glass/metal seal by conduction along the metal cylinder. The external surface of the metal cylinder loses heat by natural convection and radiation. The question then arises as to what value the equilibrium temperature t_c at the glass/metal seal will be. Temperature t_c will be a complicated function of the radial and axial dimensions and surface emissivity of the metal cylinder.

The second thermal problem is the axial variation in temperature which occurs on a cylindrical hollow cathode as a result of non-uniform power per unit length input by the discharge. Axial temperature variations represent a departure from optimum operating conditions, and thus should be minimised.

As a starting point in tackling these problems, a one-dimensional equation describing the temperature distribution in

a cylindrical conductor is derived. Since radial temperature variations are initially neglected, this equation represents a "thin-walled" approximation. Results obtained from its solution can be used directly to determine the required dimensions of the metal cylinder AB in fig 3.5(a) for thermal protection of the glass/metal seal. Radial temperature gradients are then included in the solution ("thick-walled" approximation), and results yield design criteria for hollow cathodes.

3.6.1 Derivation of the Thermal Flow Equation.

A cylindrical conductor of length l, with thermal conductivity k, and inner and outer radii r_1 and r_2 is illustrated in fig 3.5(b). This "worst-case" derivation assumes that all the input power is at $x = 0$, which is equivalent to assuming that one end of the cylindrical conductor (at $x = 0$) is in contact with a hot reservoir at temperature t_H. Under conditions of thermal equilibrium, the other end of the conductor attains the temperature t_c, where the heat transfer processes taken into account are conduction in the cylinder, and convection and radiation losses from the external surfaces.

Convection losses are assumed to follow the empirical law

$$\mathring{Q}_c = h_c A (t - t_o) , \qquad (3\cdot1)$$

where A is the surface area, t_o is the ambient temperature,

and h_c is a temperature dependent film coefficient for laminar flow. The film coefficient h_c is given by

$$h_c = 1{\cdot}32\left(\frac{t - t_o}{2r_2}\right)^{1/4}, \qquad (3.2)$$

for a horizontal cylinder of outer radius r_2 (Rogers and Mayhew, 1967).

Radiation losses follow Stefan's Law

$$\dot{Q}_R = e\sigma A (t - t_o)^4, \qquad (3.3)$$

where e is the surface emissivity and Stefans constant is $\sigma = 5.67 \times 10^{-8}$ Watts/(m^2 K^4).

Consideration of an elemental length dx at x leads to a second order non linear differential equation in the following manner.

The conducted heat entering element dx from the hot end of the cylinder is

$$\dot{Q}_1 = -k\pi (r_2^2 - r_1^2) \frac{dt}{dx}, \qquad (3.4)$$

where the minus sign indicates that t decreases with increasing x. The radiation losses from element dx are given by

$$\dot{Q}_2 = 2\pi r_2 e\sigma (t^4 - t_o^4)\, dx. \qquad (3.5)$$

The convection losses from element dx are

$$\dot{Q}_3 = 1{\cdot}32\pi (2r_2)^{3/4} (t - t_o)^{5/4}\, dx, \qquad (3.6)$$

and the conducted heat leaving the element dx in the direction of increasing x is given by

$$\dot{Q}_4 = -k\pi(r_2^2 - r_1^2)\frac{d}{dx}\left(t + \frac{dt}{dx}dx\right). \quad (3.7)$$

Under conditions of thermal equilibrium, we have

$$\dot{Q}_1 - \dot{Q}_2 - \dot{Q}_3 - \dot{Q}_4 = 0 \quad (3.8)$$

from which the differential equation describing the temperature distribution is obtained:

$$k\pi(r_2^2 - r_1^2)\frac{d^2t}{dx^2} = 1{\cdot}32\pi(2r_2)^{3/4}(t - t_0)^{5/4} + 2\pi r_2 e\sigma(t^4 - t_0^4). \quad (3.9)$$

3.6.2 Solution of Equation (3.9).

Equation (3.9) may be written as

$$\frac{d^2t}{dx^2} = a(t^4 - t_0^4) + b(t - t_0)^{5/4}, \quad (3.10)$$

where we have

$$a = \frac{2r_2 e\sigma}{k(r_2^2 - r_1^2)},$$

$$b = \frac{1{\cdot}32\,(2r_2)^{3/4}}{k(r_2^2 - r_1^2)} \quad . \tag{3.11}$$

Changing the variable to $p = \frac{dt}{dx}$ and using

$$\frac{d}{dx} = \frac{d}{dt}\left(\frac{dt}{dx}\right) = p\,\frac{d}{dt} \Rightarrow \frac{d^2t}{dx^2} = p\,\frac{dp}{dt}\,, \tag{3.12}$$

we get

$$p\,\frac{dp}{dt} = a(t^4 - t_o^4) + b(t - t_o)^{5/4}, \tag{3.13}$$

which gives

$$\int_{\left(\frac{dt}{dx}\right)_{x=0}}^{\left(\frac{dt}{dx}\right)} p\,dp = \int_{t_H}^{t} a(t^4 - t_o^4) + b(t - t_o)^{5/4}\,dt. \tag{3.14}$$

Integration of (3.14) yields

$$\frac{dt}{dx} = -\sqrt{\left[\left(\frac{dt}{dx}\right)_{x=0}^2 + \frac{2a}{5}(t^5 - t_H^5 - 5t_o^4(t - t_H)) + \frac{8b}{9}((t - t_o)^{9/4} - (t_H - t_o)^{9/4})\right]}. \tag{3.15}$$

Before proceeding further, an expression for $\left(\frac{dt}{dx}\right)_{x=0}$ is required. This can be obtained by integrating (3.14) between limits changed as follows:

$$\int_{\left(\frac{dt}{dx}\right)_{x=0}}^{\left(\frac{dt}{dx}\right)_{x=l}} p\,dp = \int_{t_H}^{t_c} a(t^4 - t^4) + b(t - t)^{5/4}\,dt \,, \tag{3.16}$$

The upper limit of integration in eq (3.14) has been changed from $\left(\frac{dt}{dx}\right)$ at a general point x where the temperature is t, to $\left(\frac{dt}{dx}\right)_{x=l}$ at the point $x = l$, where the temperature is t_c. Integration yields

$$\left(\frac{dt}{dx}\right)_{x=0} = -\sqrt{\left[\frac{2a}{5}(t_H^5 - t_c^5 - 5t_o(t_H - t_c)) + \frac{8b}{9}\left((t_H - t_o)^{9/4} - (t_c - t_o)^{9/4}\right)\right]}, \tag{3.17}$$

where $\left(\frac{dt}{dx}\right)_{x=l}$ is taken to be zero. This is discussed more fully in Appendix Two. Equation (3.15), although separable, cannot be solved analytically, and therefore a numerical solution yielding x as a function of t was obtained using the NAG library sub-routines package available on the local St. Andrews Digital VAX/VMS computer.

3.7 Thin Walled Approximation Results.

The results which the solution of equation (3.15) yield are directly applicable to the protection of cylindrical glass/metal seals from disastrous temperature effects, a problem encountered with tubes Nos. 1 and 3, and discussed in Chapter Two. Solutions of eq (3.15) were obtained for a wide variety of different combinations of the parameters t_c, t_H, t_o, r_2, e, and wall thickness ($r_2 - r_1$).

It is convenient to define a length of cylinder such that the temperature at $X = L$ is t_c. We call this length the "sleeve length" (AB of fig 3.5(a)). The parameters contributing to a given sleeve length can vary over certain restricted ranges and for each parameter, borrowing from computer jargon, we define a default value of a given parameter as a value which lies within its allowed range. Default values for each of the parameters t_o, t_c, t_H, r_2, $(r_2 - r_1)$, and e are given in Table 3.2. The results presented below show sleeve length as a function of a chosen parameter, with the other parameters set to their chosen default values. The surface emissivity is in general unknown and will depend on the state of oxidation of the metal surface, etc. However, it is possible to treat a metal surface so that the emissivity approaches 1.0 (for example, with lampblack or grate polish) and thus a default value of 0.8 is assumed. The default value for wall thickness was chosen as 0.5 mm because commercially available cylindrical glass/metal seals are generally supplied with a metal sleeve which has this value of wall thickness.

In all the calculations, the thermal conductivity of

the metal is taken to be 20.0 Watts/^{o}C m and thus the results are approximately applicable to both Kovar (k = 16.7 Watts/^{o}C m, and stainless steel (k = 16 - 25 Watts/^{o}C m)

Temperature distributions for convection losses, radiation losses, and combined convection and radiation losses, using the default values of Table 3.2, are illustrated in fig 3.6. It appears that, for the given conditions, convection losses and radiation losses are equal to within several percent. The integrated heat loss from the sleeve may be evaluated from

$$\dot{Q}_{loss} = \int_{0}^{l} \left[a(t^4 - t_{\infty}^4) + b(t - t_{\infty})^{9/4} \right] dx \, . \tag{3.18}$$

Substituting $dx = \left(\frac{dx}{dt}\right) dt$, using (3.15) and changing the limits accordingly yields

$$\dot{Q}_{loss} = \int_{t_H}^{t_c} \frac{a(t^4 - t_o^4) + b(t - t_o)^{9/4} \, dt}{\sqrt{\left[\left(\frac{dt}{dx}\right)^2_{x=0} + \frac{2a}{5}\left[t^5 - t_{\infty}^5 - 5t_o^4(t - t_H)\right] + \frac{8b}{9}\left[(t - t_o)^{9/4} - (t_H - t_o)^{9/4}\right]\right]}} \, , \tag{3.19}$$

which is evaluated numerically.

Integrating (3.18) first with $a = 0$, then with $b = 0$, yields 9.9 Watts for convection alone and 11.4 Watts for radiation alone.

Figures 3.7 - 3.12 show the variation of sleeve length as a function of r_2 , e , $(r_2 - r_1)$, t_c , t_o and t_H , respectively. These figures show that the sleeve length is only weakly dependent on t_o , r_2 and t_H , and more strongly dependent on emissivity, t_c , and wall thickness.

3.8 Thick Walled Approximation Results.

The radial temperature drop in a cylindrical conductor is given by

$$\Delta T_r = \frac{\dot{Q}_r}{2\pi k} \ln\left(\frac{r_2}{r_1}\right) , \qquad (3.20)$$

where $\dot{Q}_r$ is the heat loss from the surface of the cylinder per unit length. Incorporating eq (3.20) with eqs (3.15) and (3.16) yields the thick-walled approximation for the temperature distribution in a cylindrical conductor where radial temperature gradients are allowed for. The procedure for obtaining a solution is basically the same as for the thin-walled approximation, except that the extra parameters t_{bh} and t_{bc}, representing the bore temperatures at $x = 0$ and $x = l$, respectively, are required. The program which computes the solution was altered accordingly to accept values of t_{bh} as input data and then to calculate t_H using eq (3.20). Then eqs (3.15) and (3.16) are solved, and t_c is calculated. Another application of eq (3.20) to t_c then calculates t_{bc}.

The value of $\dot{Q}_r$ in eq (3.20) used in the computer program was an average value of input power per unit length based on an input voltage of 350 V and discharge current of 3.2 amps per metre in a tube with a 4 mm bore.

The results are based on an inter-anode spacing of 8 cm (as effectively used in tube No.4); this again represents a "worst-case" calculation. For flute-type geometries, interanode spacings of between 4 cm (Grace and McKintosh, 1978) and 7.6 cm

(Piper and Webb, 1973) have been used. Since the discharge current and voltage in a system with a flute-type geometry are assumed to be symmetrical about each anode, the solution to the thick walled approximation need only be sought over a 4 cm length of cathode. The value of $\mathring{Q}_r$ for 350 V at 3.2 amps per metre is thus 1.123 KW/metre and therefore a 4 cm length dissipates 45 Watts.

The solution of eqs (3.15) and (3.17) yields a sleeve length, which gives useful information for the protection of glass/metal seals from excessive temperatures. However, in these cathode calculations, a "sleeve length", or "cathode length" of 4 cm is effectively input data, rather than output data. Hence, iterative methods were required to calculate t_{bh} and t_{bc}, with the constraint that the cathode length was 4 cm. A further complication arose since the 4 cm cathode length is also constrained to dissipate 45 Watts. Examining the heat loss terms due to convection and radiation reveals that heat loss depends on emissivity e, temperature t, and outer radius r_2. Thus only two of these three parameters can be given as input data; the other must be calculated iteratively. Hence, with the two constraints of a 4 cm cathode length and a power dissipation of 45 Watts, the program then requires two nested iterative loops, and the number of input parameters is reduced from five (t_o, t_c, t_H, r_2, e) to only three (e, t_o and r_2). Solutions were obtained for values of emissivity e in the range 0 - 1.0 using a default value for outer radius of 15.9 mm (3/4"), and also for values of emissivity 0.2, 0.4, 0.6 and 0.8 where the outer radius was altered from 3 mm to 21 mm for each value of e. The default value used for r_1 was 2 mm (ie, a 4 mm bore). The program then supplies values for

t_{bh}, t_{bc}, t_H and t_c as output data. Figure 3.13 shows t_{bh} against emissivity for the default value of r_2 = 15.9 mm, and fig 3.14 shows t_{bh} plotted against r_2, for different values of emissivity.

As discussed in Section 3.1 above, axial temperature variations which exist in hollow cathode discharges produce axial variations in helium and cadmium densities, and represent a departure from optimum conditions for laser preformance. Under conditions of simultaneous oscillation, the three colours emitted by He-Cd lasers have been observed by some workers to show markedly different output power dependencies on helium pressure and cadmium vapour density (eg, Fujii et al, 1975; Csillag et al, 1977; Wang, 1980). It is thus especially important to minimise axial temperature variations for white light hollow cathode lasers. The thick-walled approximation yields results which show the relationship between such axial temperature variations and the cathode outer radius. Figure 3.15(a) shows the bore temperature drop (t_{bh}-t_{bc}) plotted against hollow cathode outer radius, for different values of outer emissivity. As can be seen from the figure, the curves for different emissivities are superimposed, except for smaller values of outer radius, where a degree of spread occurs. This is shown more clearly in fig 3.15(b). The magnitude of axial temperature variations depends on cathode outer radius, but is independent of emissivity for most practical purposes.

At this stage in the analysis, the computer program was modified to accept values of t_{bh} as input data and the constraints of power dissipation (45 Watts) and cathode length (4 cm) were removed. Figure 3.16 shows the variation of

t_{bh} with dissipated power for an emissivity of 0.8 and an outer radius of 15.9 mm. The functional relationship is approximately linear. Another parameter S may thus be defined as the temperature difference in ^{o}C experienced by the cathode when the heat dissipated by the cathode is increased or decreased by one Watt. Thus S is a measure of the sensitivity of the cathode temperature to changes in the input power. A low sensitivity is a desirable feature of hollow cathodes, especially those of the self-heated variety. The voltage across a He-Cd hollow cathode discharge is dependent on the partial pressure of cadmium vapour in the discharge, and increases monotonically as the cadmium partial pressure is increased, from approximately 220 V (pure He at 15 Torr) to 400 V with a high partial pressure of cadmium (eg, Grace and McIntosh, 1978). If the cathode temperature in a self-heated tube is strongly dependent on the dissipated cathode heat (high S), then at constant current, a small increase in voltage will increase the cathode temperature and thus the partial pressure of cadmium. The voltage will correspondingly increase because of the increase in cadmium partial pressure, producing a "runaway" effect.

Figure 3.17 shows the cathode sensitivity in $^{o}C/Watt$ against emissivity for the default value r_2 = 15.9 mm, for a 4 cm length of cathode dissipating 45 Watts. Figure 3.18 shows S as a function of r_2 for different values of emissivity with the same constraints.

3.9 Concluding Remarks.

In this chapter, an attempt has been made to establish thermal design criteria for hollow cathode He-Cd lasers. The criteria derived have been presented in graphical form using the one dimensional second order non linear differential equation derived in section 3.6.1

Although the model is based on a "worst-case" approximation, where all the power dissipated by the laser cathode is input near the anode (ie at X = 0 in fig 3.5(a)), the results may be used directly to explain the severe temperature differences recorded with tube No.4, and mentioned in section 3.4. Figure 3.15 shows that under the worst circumstances (of an anode-cathode arc, for example) the temperature drop along a 4 cm length of cathode with a 0.9 mm bore dissipating 45 Watts will be 1150 K in the steady state.

Since the solution of eq (3.15) relies heavily on computing techniques, a sample program used to obtain results for the thin-walled approximation is given in Appendix Three.

ATOMIC MASS NUMBER	RELATIVE NATURAL ABUNDANCE	ISOTOPE SPLITTING OF 441·6 nm LINE (Hz X 10^8)
106	1·22 %	
		16·8
108	0·88	
		15·7
110	12·4	
		1·6
111	12·8	
		14·1
112	24·0	
		2·2
113	12·3	
		12·4
114	28·8	
		10·4
116	7·6	

TABLE 3·1 RELATIVE NATURAL ABUNDANCE OF THE ISOTOPES OF Cd AND ISOTOPIC SPLITTING OF 441·6 nm LINE OF Cd II (KUHN AND RAMSDEN, 1956).

PARAMETER	DEFAULT VALUE
t_c	200 °C
t_H	450 °C
t_0	20 °C
r_2	9·525 MM
$(r_2 - r_1)$	0·5 MM
e	0·8

TABLE 3·2 DEFAULT VALUES USED IN THERMAL CALCULATIONS (THIN - WALLED APPROXIMATION).

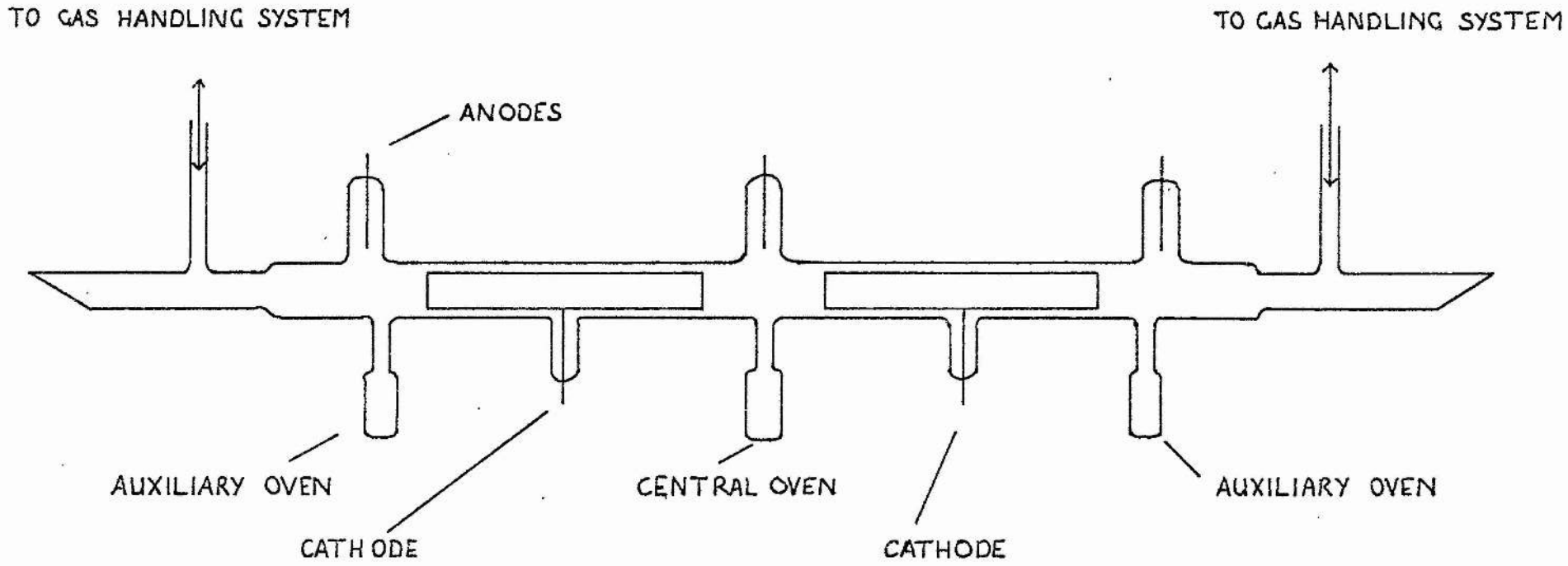

FIG 3.1 TUBE No. 4

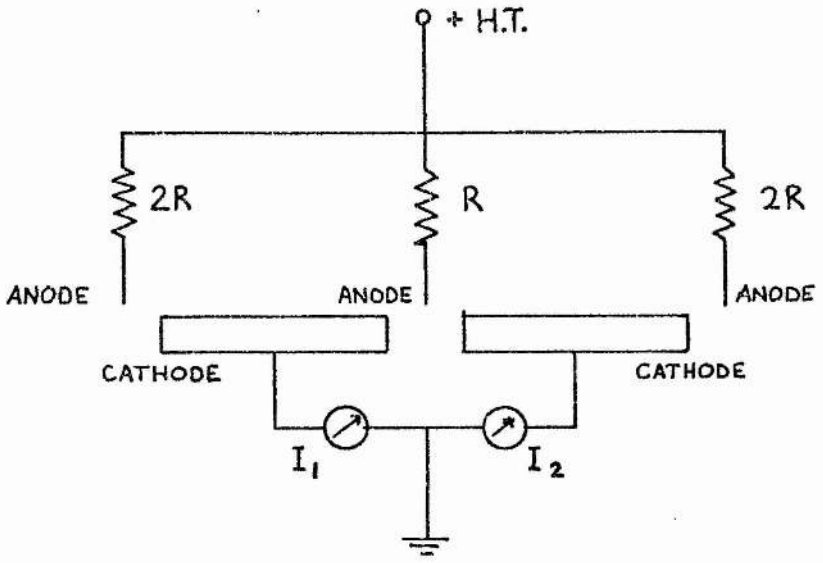

FIG 3.2 (a) LASER CIRCUIT FOR TUBE No. 4 WITH $R = 6.7 k\Omega$

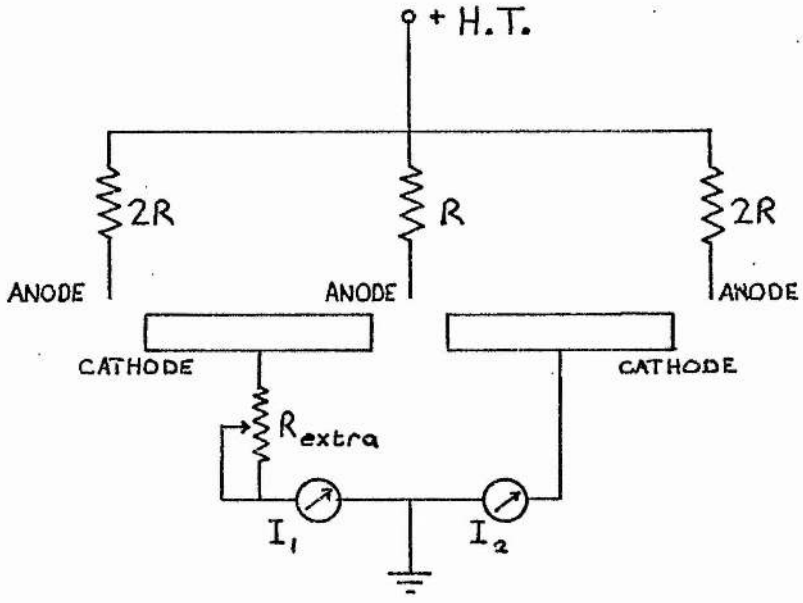

FIG 3.2(b) ATTEMPT TO OBTAIN EVEN CURRENT DISTRIBUTION BY INTRODUCING $R_{extra} = 0 - 1\ k\Omega$.

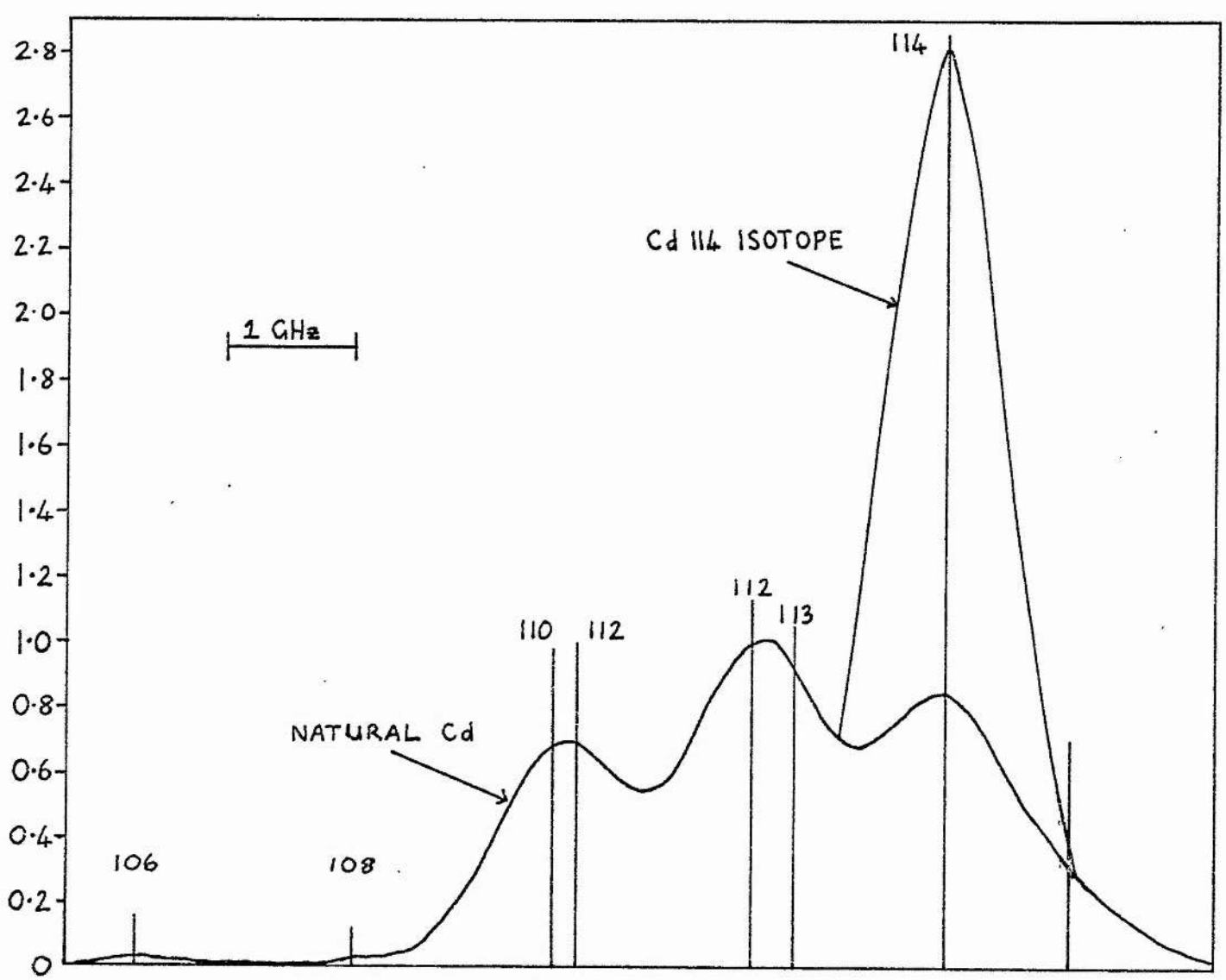

FIG 3.3 LINESHAPES FOR NATURAL Cd AND Cd 114 ISOTOPE. RELATIVE MASS NUMBER LOCATIONS ARE AS INDICATED.

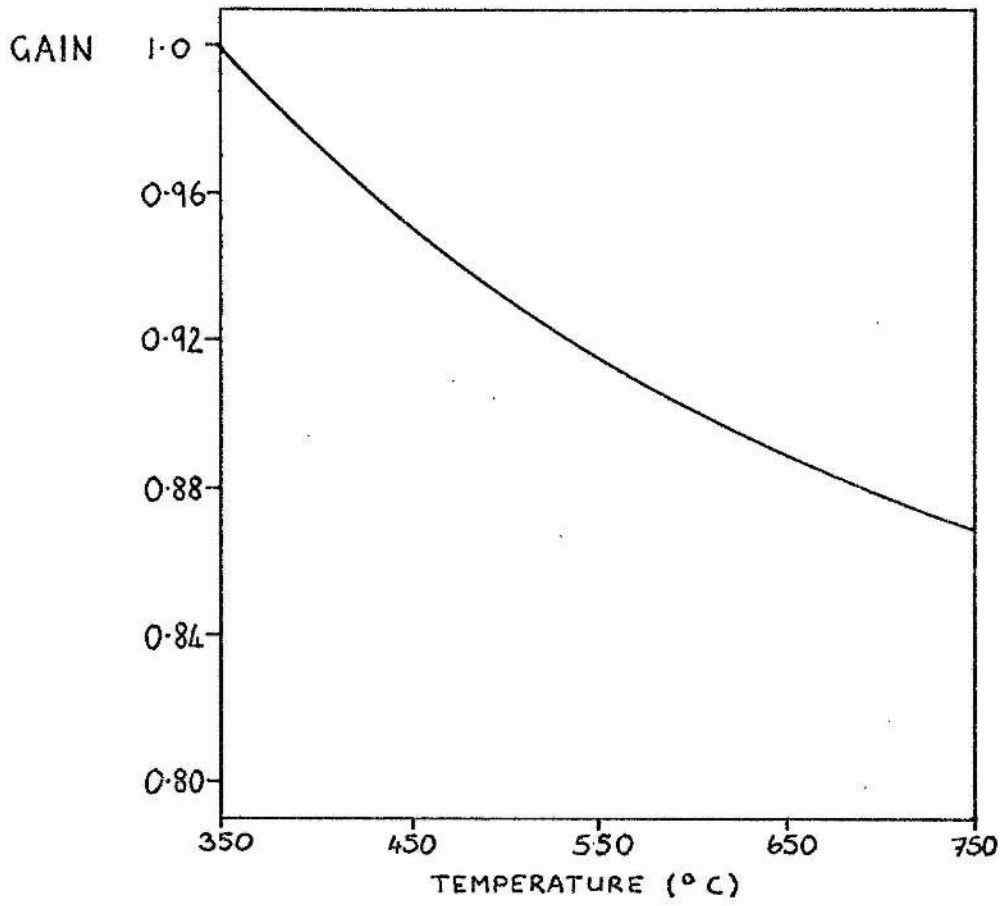

FIG. 3.4 (a) GAIN VS. TEMPERATURE FOR NATURAL Cd. NORMALISED FOR A TEMPERATURE OF 350°C.

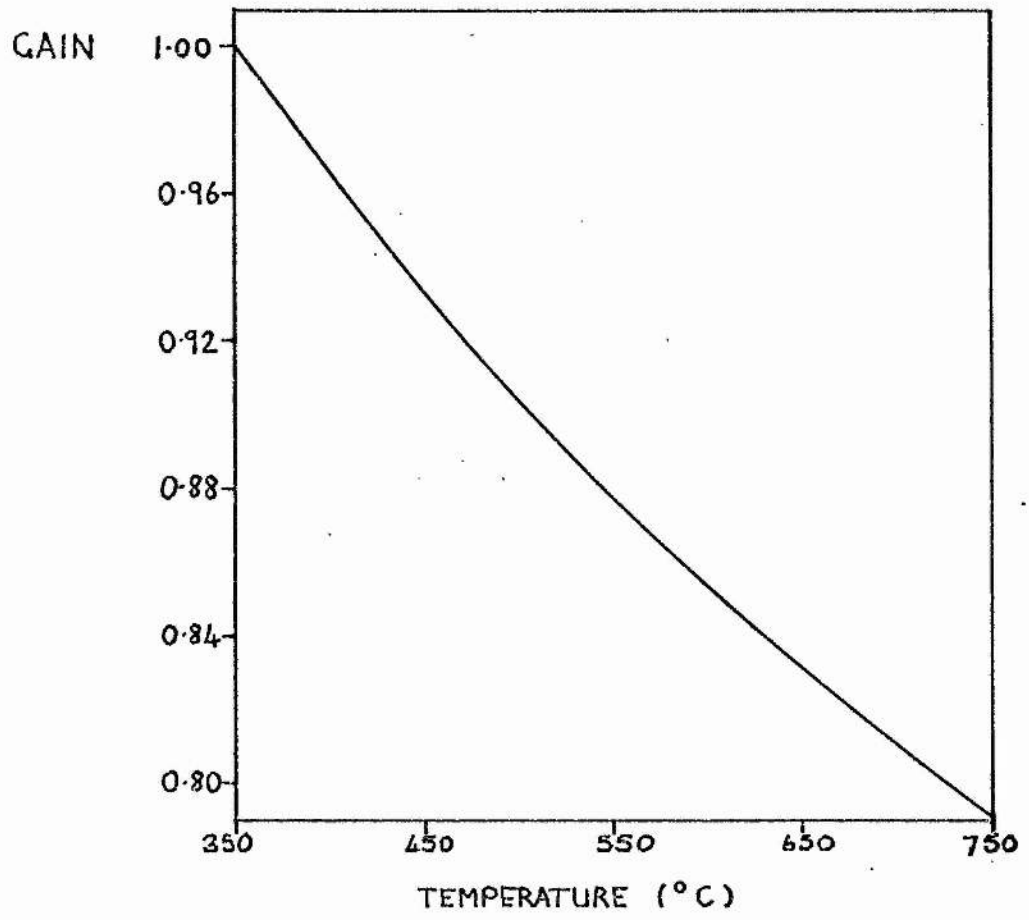

FIG. 3.4 (b) GAIN VS. TEMPERATURE FOR Cd 114.
NORMALISED FOR A TEMPERATURE OF 350 °C.

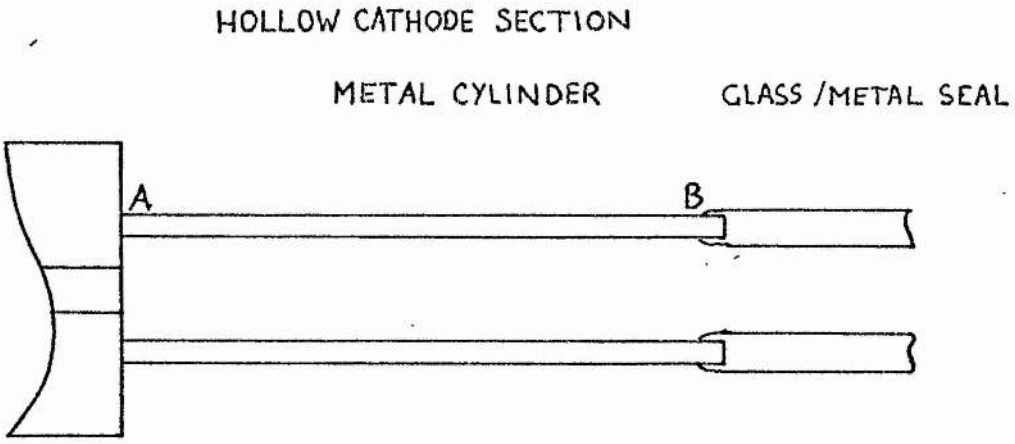

FIG 3.5(a) GLASS/METAL SEAL ATTACHED TO SECTION OF HOLLOW CATHODE VIA METAL CYLINDER AB.

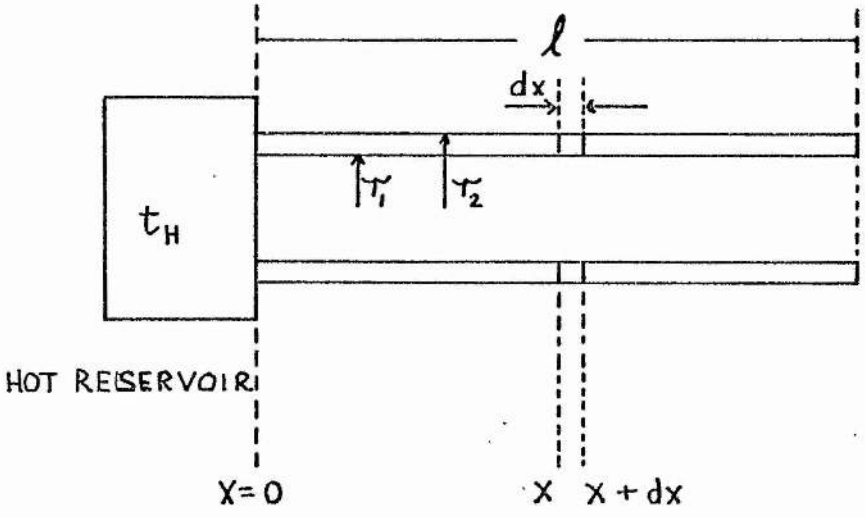

FIG. 3.5(b) METAL CYLINDER IN THERMAL CONTACT WITH HOT RESERVOIR AT TEMPERATURE t_H.

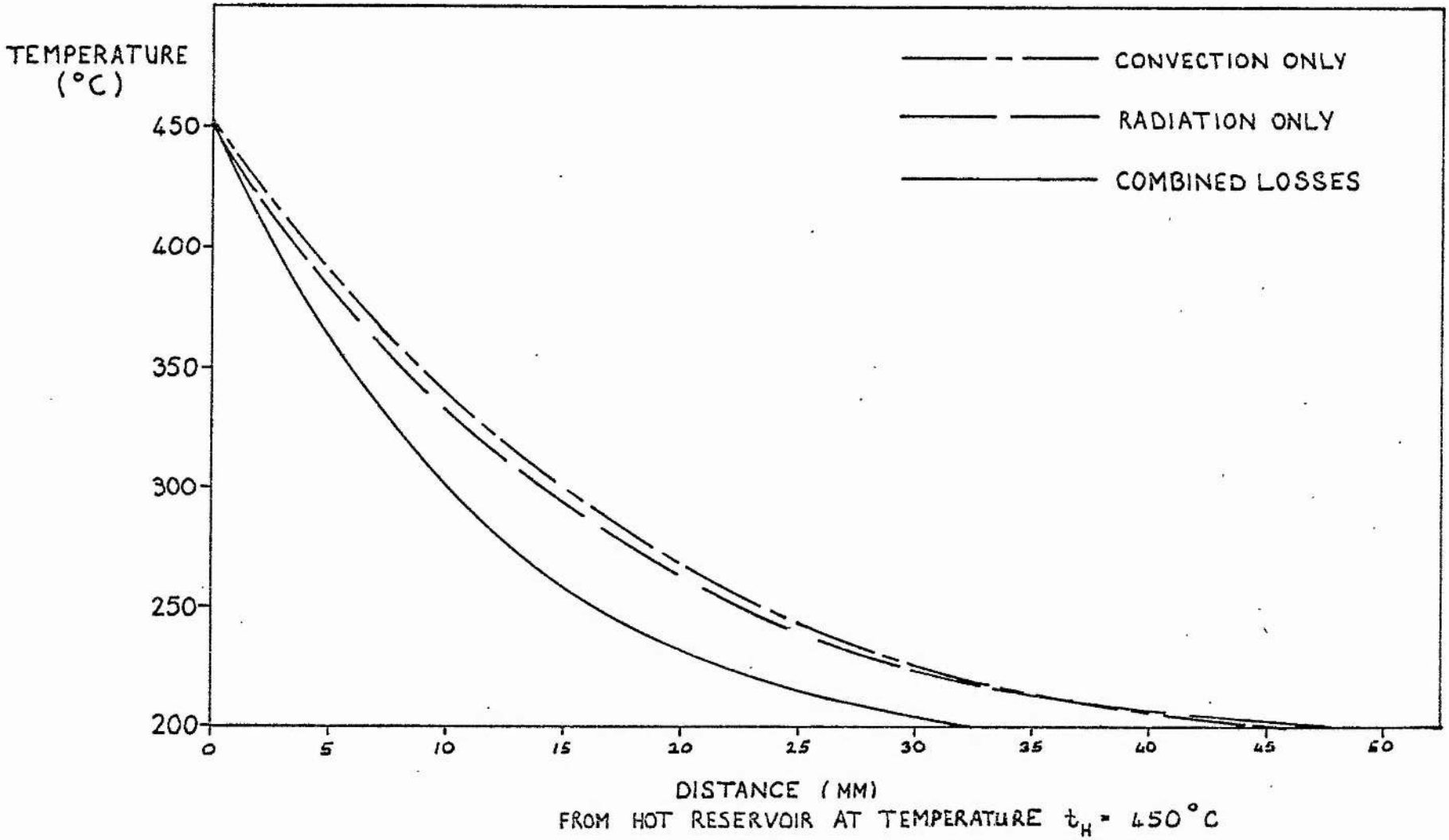

FIG 3.6 TEMPERATURE DISTRIBUTIONS FOR CONVECTION, RADIATION AND COMBINED LOSSES.

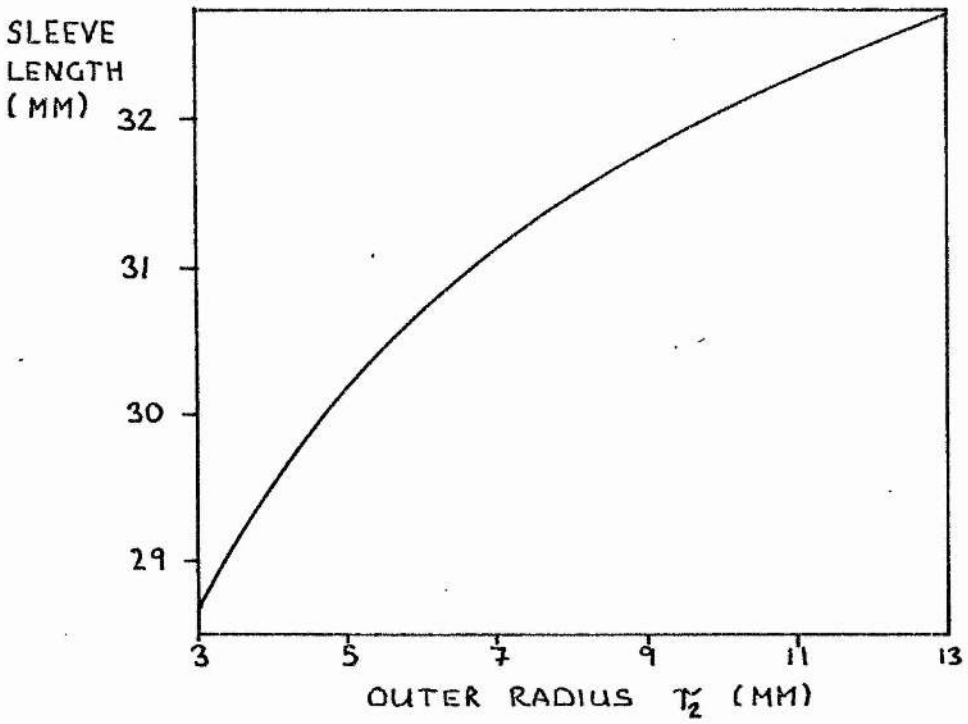

FIG 3.7 SLEEVE LENGTH VS OUTER RADIUS r_2

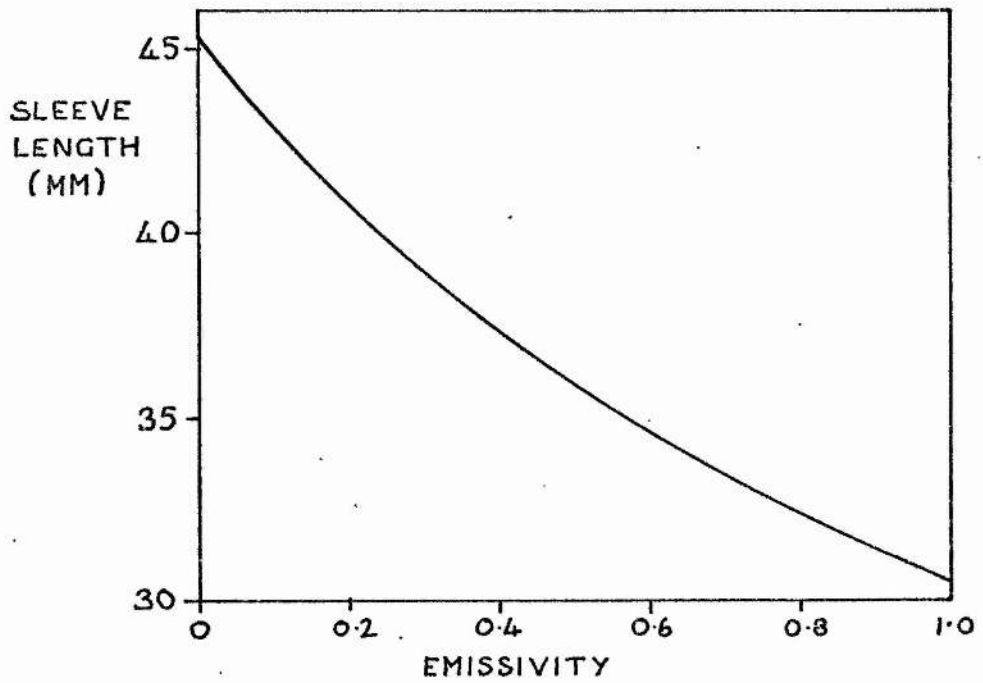

FIG 3.8 SLEEVE LENGTH VS EMISSIVITY.

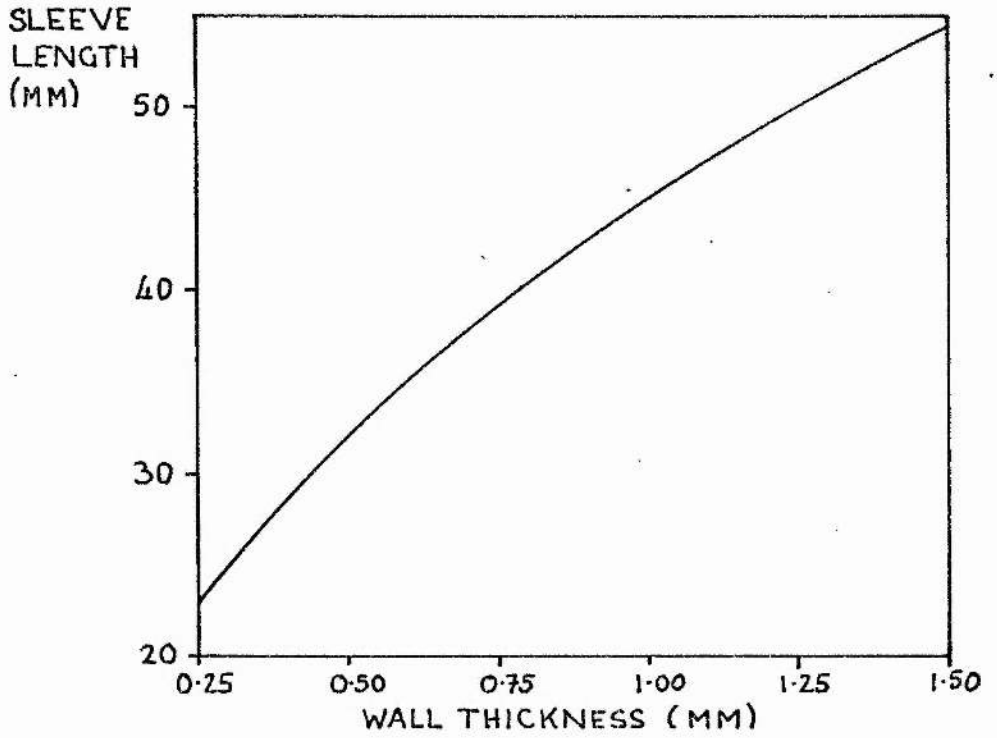

FIG 3·9 SLEEVE LENGTH VS WALL THICKNESS.

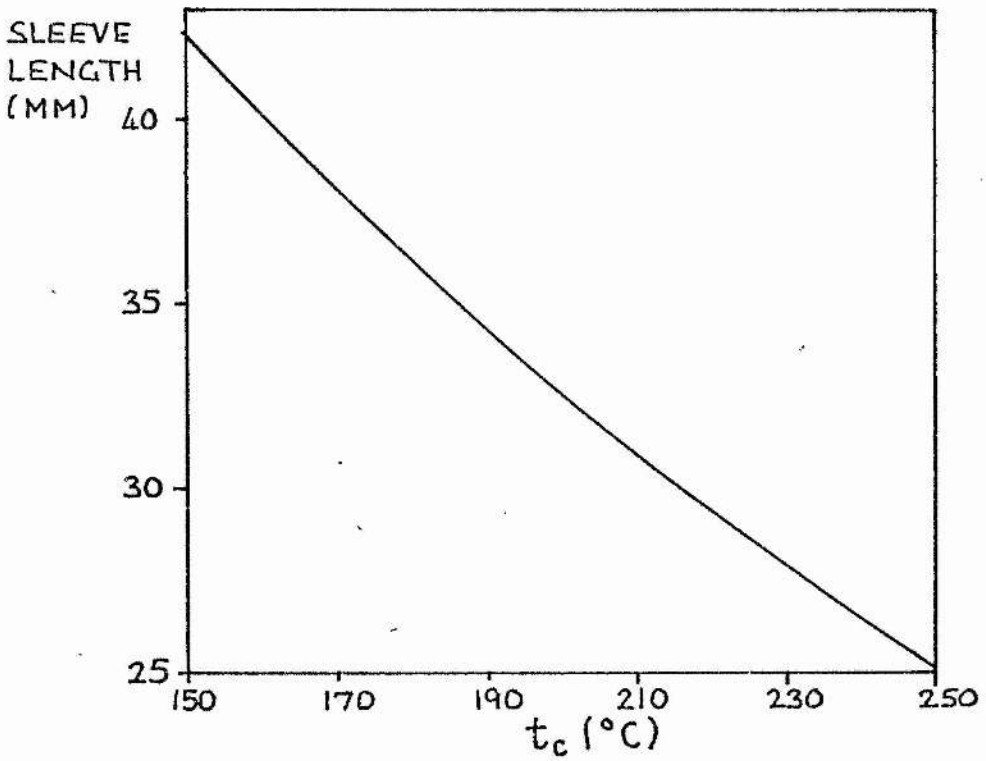

FIG 3.10 SLEEVE LENGTH VS t_c.

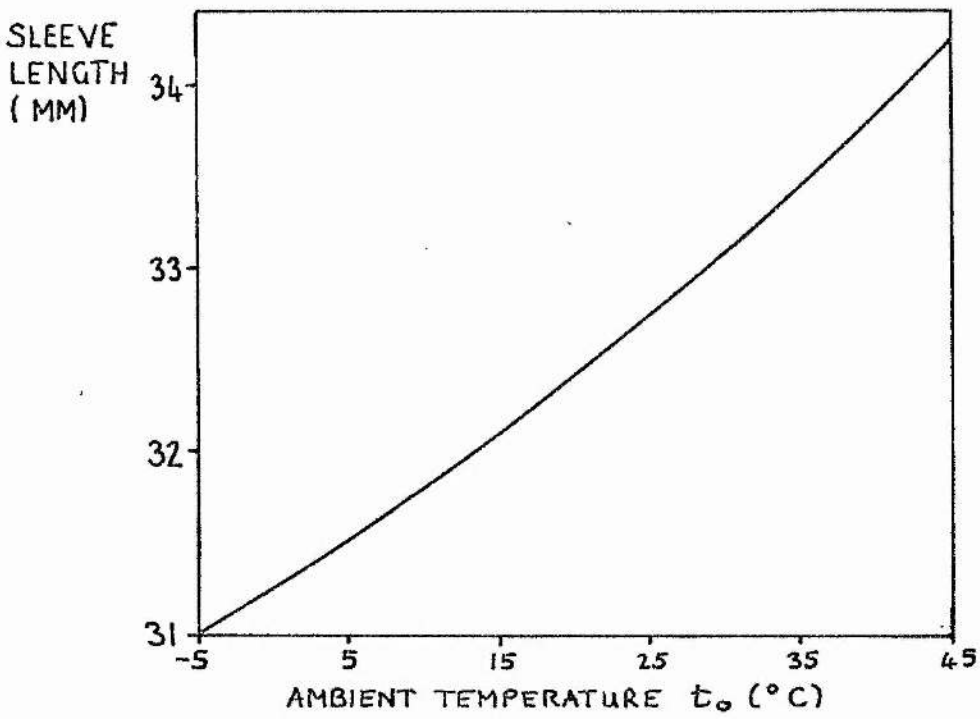

FIG 3.11 SLEEVE LENGTH VS AMBIENT TEMPERATURE t_o.

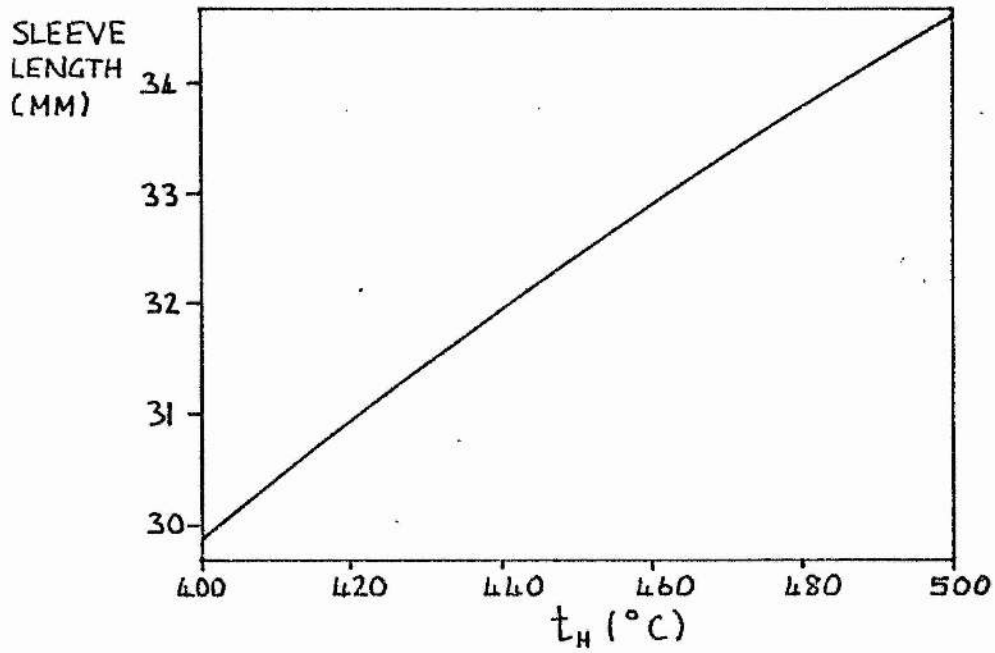

FIG 3.12 SLEEVE LENGTH VS HOT RESERVOIR TEMPERATURE t_H.

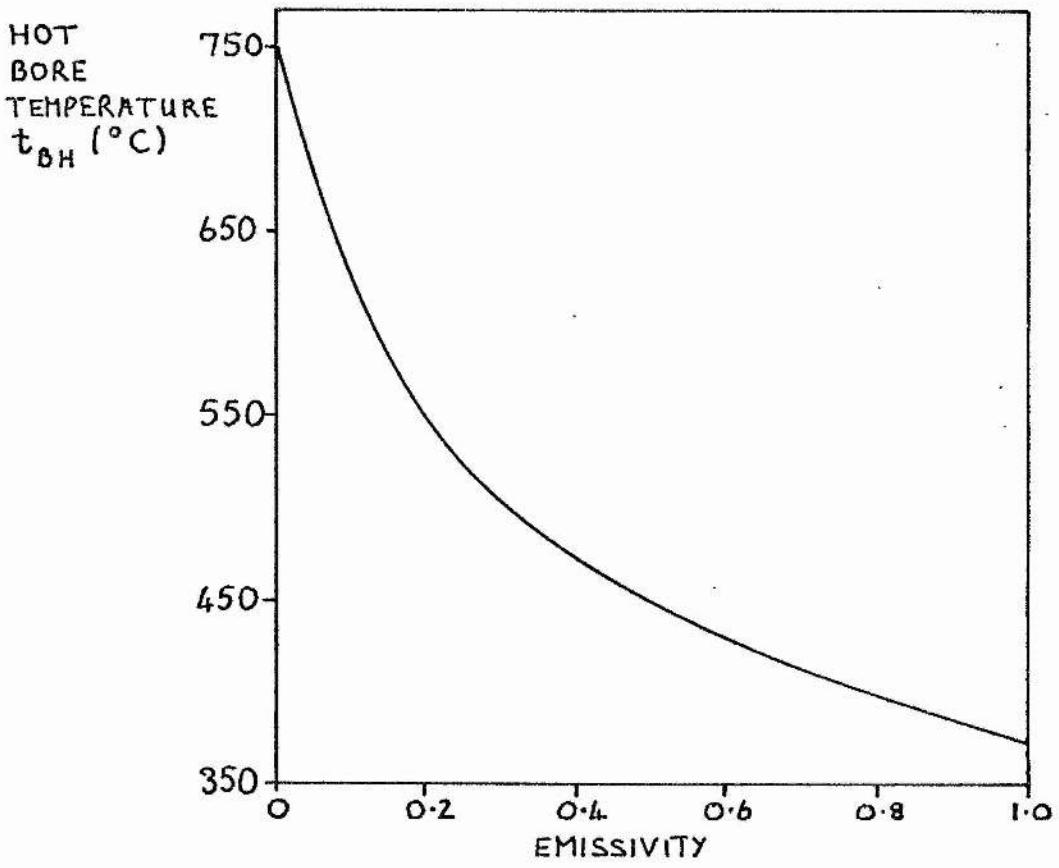

FIG 3.13 t_{BH} VS EMISSIVITY WITH CONSTRAINTS.
OUTER RADIUS = 15·9 MM (DEFAULT VALUE).

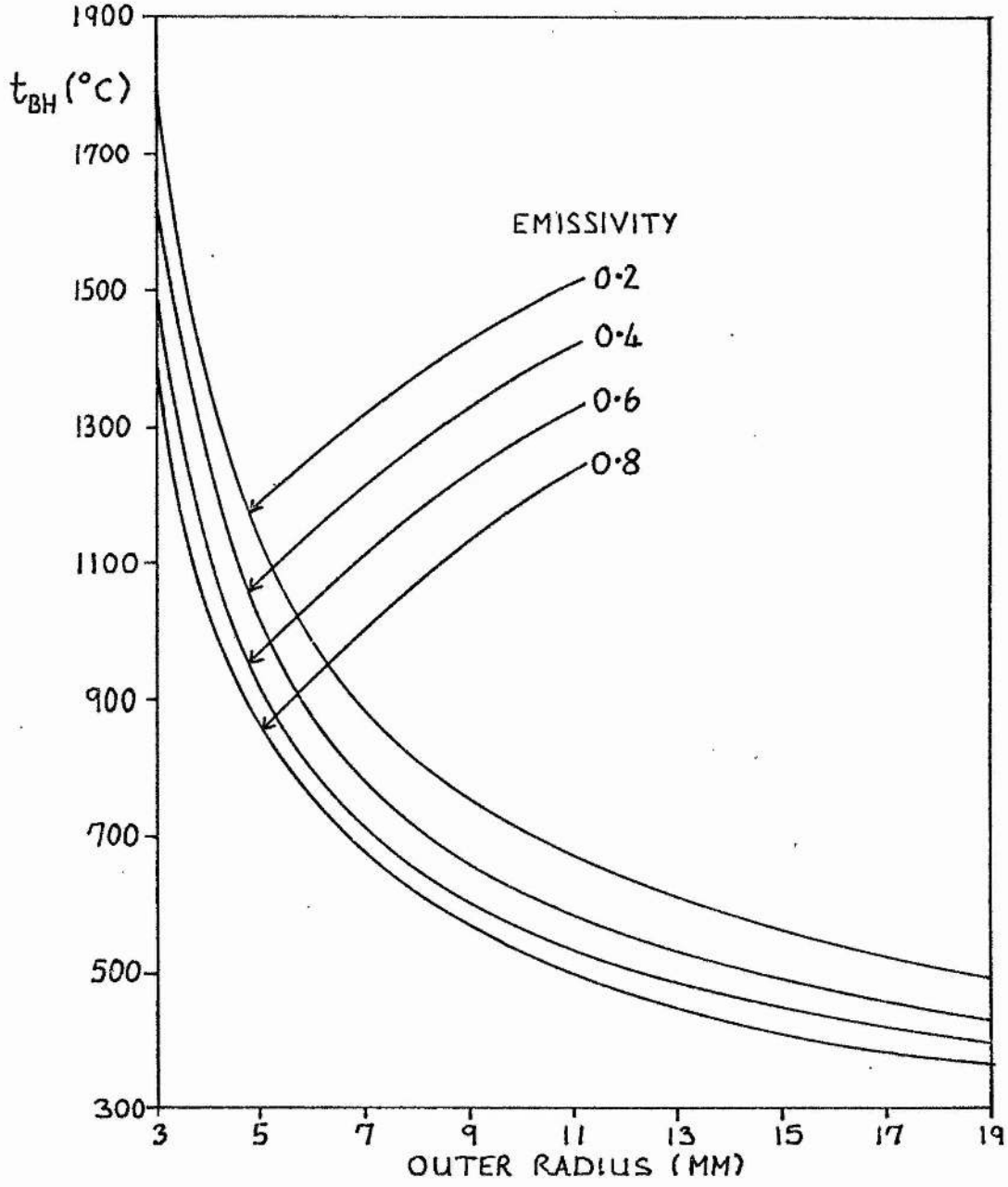

FIG 3.14 HOT BORE TEMPERATURE t_{BH} VS OUTER RADIUS FOR DIFFERENT EMISSIVITIES.

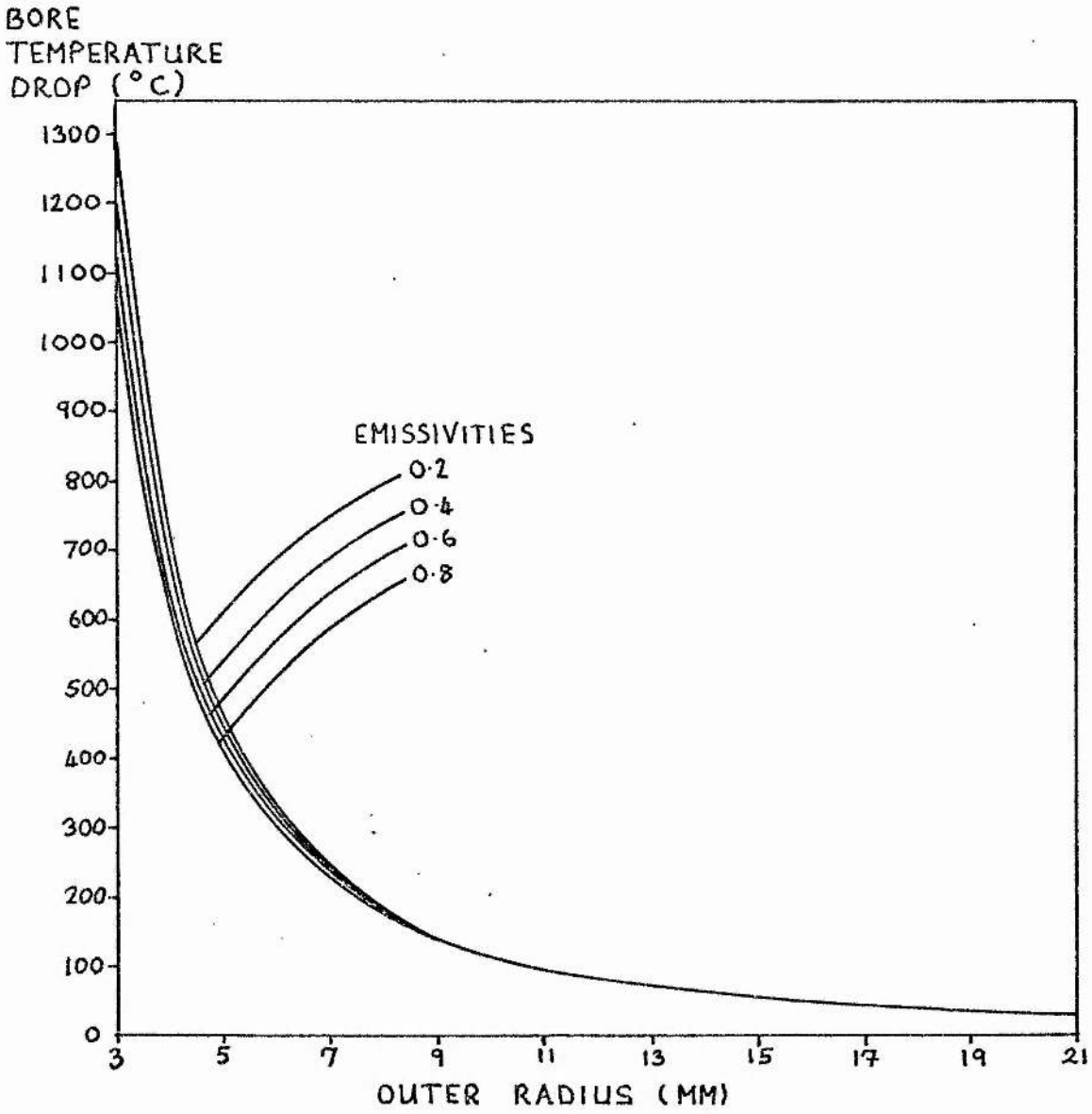

FIG 3.15(a) BORE TEMPERATURE DROP VS OUTER RADIUS FOR DIFFERENT EMISSIVITIES. (4 CM CATHODE LENGTH CONSTRAINED TO DISSIPATE 45 WATTS.)

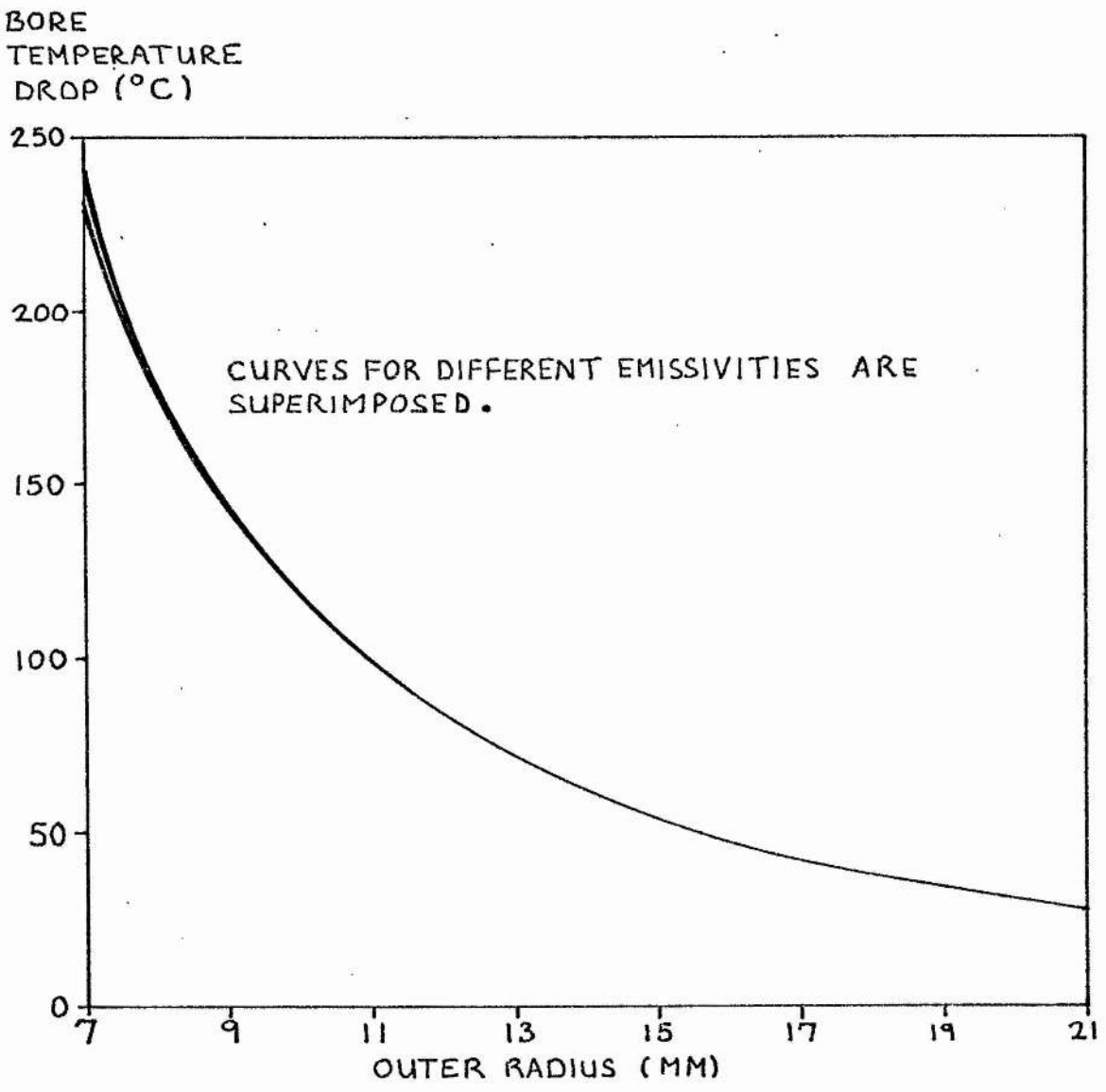

FIG 3.15(b) BORE TEMPERATURE DROP VS OUTER RADIUS FOR DIFFERENT EMISSIVITIES. SAME CONSTRAINTS AS FIG 3.15(a).

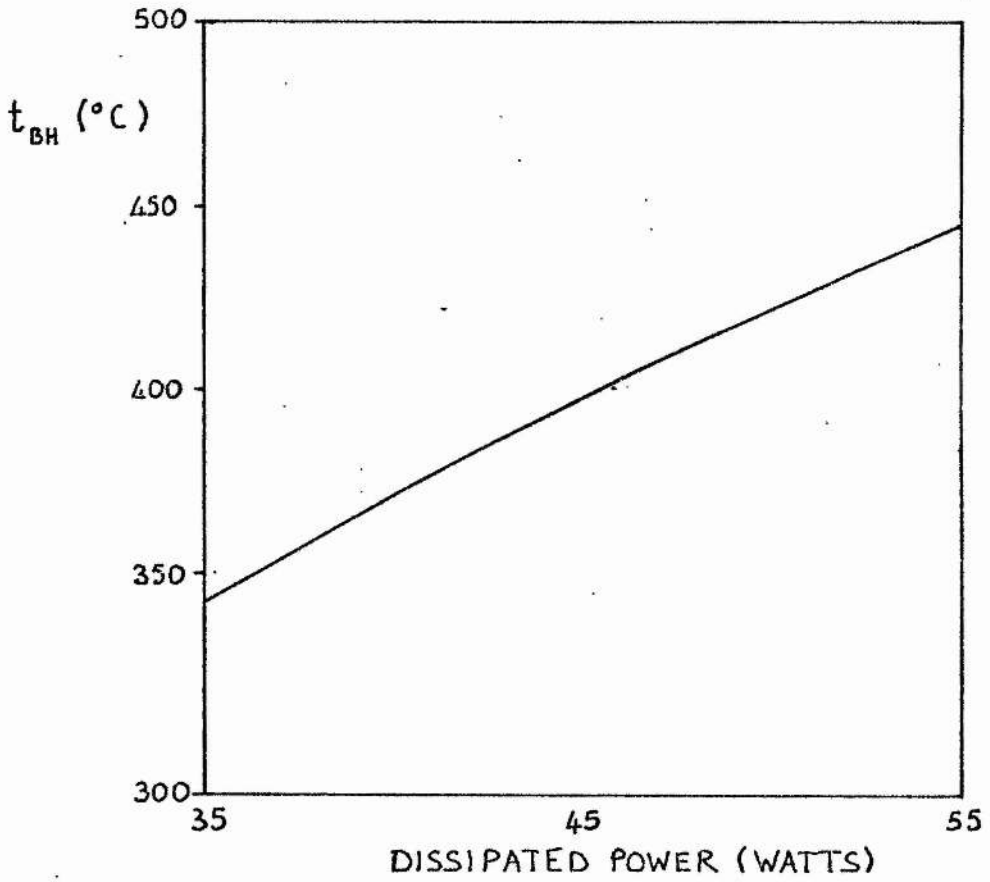

FIG 3.16 HOT BORE TEMPERATURE (t_{BH}) VS DISSIPATED POWER.

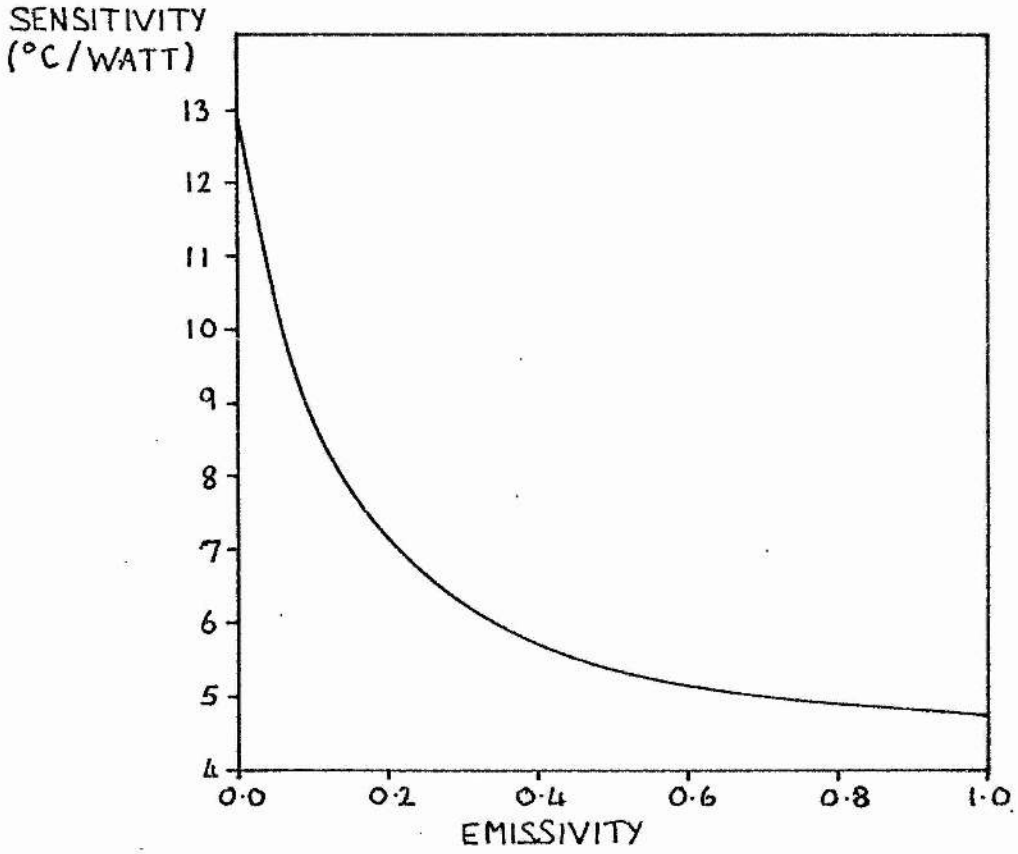

FIG 3.17 SENSITIVITY VS EMISSIVITY (WITH DEFAULT VALUE 15·9 MM FOR τ_2) .

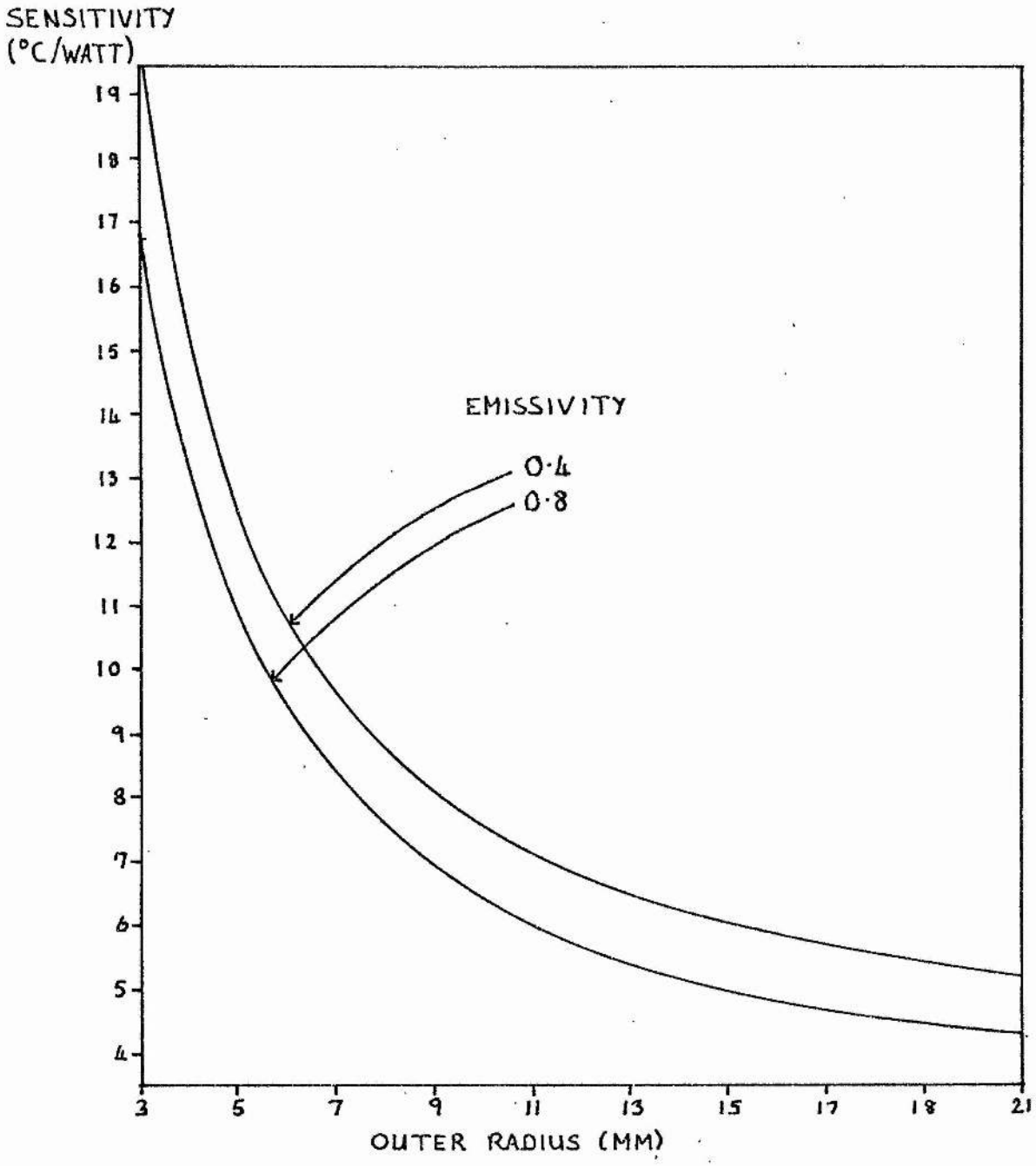

FIG 3.18 CATHODE SENSITIVITY VS OUTER RADIUS FOR DIFFERENT VALUES OF EMISSIVITY

CHAPTER THREE BIBLIOGRAPHY.

CSILLAG, L. NAH, C.Z. JANOSSY, M. and ROZSA, K.
Opt. Commun.,21,39-41,1977.

FUJII, K. TAKAHASHI, T. and ASAHI, Y.
IEEE J. Quant. Electron.,QE-11,111-114,1975.

GRACE, J.R. and MCINTOSH, A.I.
J. Phys. D : Appl. Phys.,12,2043-2051,1979.

KUHN, H.G. and RAMSDEN, S.A.
Proc. Roy. Soc.,237,485-495,1957.

NESMEYANOV, N.
"Vapour Pressure of the Chemical Elements",
Elsevier, London, 1963.

OTAKA, M., OSHIMA, T., TAKEUCHI, M., OIKAWA, T. and FUJII, K.
IEEE J. Quant. Electron.,QE-17,414-417,1981.

PIPER, J.A. and WEBB, C.E.
J. Phys. D : Appl. Phys., 6,1973.

ROGERS, G.F.C. and MAYHEW, Y.R.

"Engineering Thermodynamics Work and Heat Transfer", Longman (London and New York), 1967.

SCHUEBEL, W.K.

Appl. Phys. Lett., 16, 470-472, 1970.

WANG, S.C.

Proceedings of the Society of Photo-Optical Instumentation Engineers, 232, 45-46, 1980, (International Optical Computing Conference, 1980).

CHAPTER FOUR

DESIGN, CONSTRUCTION AND SPECTROSCOPY OF TUBES NOS. 5 AND 6.

4.1 Introduction.

In this chapter, the designs and construction techniques for a further two hollow cathode structures (tubes Nos.5 and 6) are described. Both structures have cylindrical cathodes and discrete anodes, where the cathode wall thicknesses and anode sleeve lengths are dictated by the thermal design criteria established in Chapter Three. Tube No.5 has a short active length (15 cm) and a single centrally situated source of cadmium, while tube No.6 is of longer active length (50 cm) and has multiple sources of cadmium. Laser emission on the green lines of Cd II was obtained from both tubes, but the other visible transitions in the blue and red did not oscillate.

Spectroscopic studies of the discharges obtained in both tubes provide some evidence that impurities which appear soon

after discharge initiation are responsible for the lack of three-colour laser output.

The presence of impurities, and the random manner in which measured line and band intensities varied, made it impossible to obtain reproducible parametric observations about variations of Cd II line intensities with discharge current, helium pressure and temperature of the Cd source.

4.2 Design and Construction of Tube No.5.

Tube No.5 had a short active length (15 cm), a stainless steel cathode with a 4 mm bore, and discrete anodes. The cathode wall was approximately 31 mm OD, and thus, from fig 3.15(a), the largest axial temperature variations which may occur under steady state conditions is 44 ^{o}C. This figure applies to a 4 cm length of cathode constrained to dissipate 45 Watts, and represents the "worst case" situation of an anode/cathode arc, where all of the power input to the cathode occurs close to the anode. In practice, we expect this figure to be much smaller when the discharge is covering the internal cathode bore. The overall construction of the tube is illustrated in fig 4.1(a), with details of the central and auxilliary anode structures illustrated in figs 4.1(b) and 4.1(c), respectively. The inner surfaces of the Kovar/stainless steel anode sleeves are masked from the anode rods to prevent the discharge from covering the internal surfaces of the anode sleeves, thus avoiding the generation of unwanted heat near

the glass/metal seals. There is recent evidence to suggest that such measures are necessary (Mizeraczyk, 1983). Masking is achieved by constructing the anode assemblies with a re-entrant housing in glass (pyrex). As illustrated in figs 4.1(b) and 4.1(c), this results in trapped volumes which then require an extra pumping outlet. The pumping outlets were connected to a glass gas manifold, as shown in plate 4.1.

The anode sleeves were designed using the results of the "thin-walled" approximation (Chapter Three). They thus function as "thermal resis tors", preventing the conduction of discharge heat generated at the cathode from overheating the glass/metal seals. Each sleeve is approximately 5 cm long, with a wall thickness of 0.5 - 0.7 mm. Thus, if the laser cathode operates at 450 ^{o}C (worst case), a temperature below 150^{o}C is expected at the glass/metal seals, in accordance with fig 3.10 in Chapter Three.

The glass/metal seals are provided with a 2.5 cm length of Kovar sleeve, to which a mating ring and a 2.5 cm length of stainless steel were argon-arc-welded. After welding, the glass required annealing. The cathode body was constructed in three sections. Attempts to construct a one-section cathode using a long reach drill and boring from either end were unsuccessful. However this problem could be overcome by the use of gun-barrel drills, which have a much longer reach than standard drills and a cutting head designed to prevent the bored hole straying from its original centre. The three cathode sections were also argon-arc-welded together, where a small gap ($\sim$1mm) was left between the section faces internally to minimise trapped volumes. A series of blind

holes was drilled into the cathode wall for thermocouple junctions.

During construction of the tube, all metal component parts were degreased in an acetone ultrasonic bath prior to welding. Each weld was leak tested with a helium sensitive mass spectrometer before a successive weld was attempted. Although three of the welds on the tube were between dissimilar metals (stainless steel and Kovar), the resulting joints were leak tight.

The centrally situated cadmium source could be operated in two ways. Initially, an oven appendage consisting of a 5 cm length of stainless steel tubing, 0.9 mm wall thickness, was filled with cadmium and attached to the laser body (fig 4.2(a)). A leak-tight seal was provided by a gyrolock metal ferrule seal bolted onto a threaded mate which had been welded to the laser body. A perforated disc separated the upper oven chamber from the tube bore to prevent the discharge arcing from the central anode into the oven. When operated in this "oven mode", the tube temperature was maintained above 350 ^{o}C, while the oven containing the cadmium was maintained at a lower temperature in the range 250 - 350 ^{o}C, using the electronic temperature controller described in Appendix One.

Alternatively, the oven appendage could be removed altogether and cadmium inserted directly into the upper oven chamber below the perforated disc, (fig 4.2(b)). A gyrolock nut fitted with an end-cap ferrule then provided a leak tight seal when tightened onto the threaded mate welded to the laser body. In this "cathode mode", the cadmium vapour pressure in the tube is dictated by the cathode temperature.

Preliminary operation in helium showed that the discharge did not provide sufficient heat to maintain the tube temperature above the desired 350 ^{o}C, when used in the "oven mode". Thus an electrically insulated wire element heater, necessary for operation in the "cathode mode" anyway, was wrapped around the cathode body. A thin layer of thermal insulation was then wrapped over the heater element ("Fibrasil", product no.T-T4, Chemical Insulating Co. Ltd.).

4.3 Operation of Tube No.5.

Tube processing prior to operation consisted of baking the cathode, using the cathode heater, at a temperature of 220 ^{o}C while under vacuum. Background pressure during bakeout generally settled at a value in the range 1 - 5 x 10^{-5} Torr. After bakeout, the tube was filled with 15 Torr He and a discharge of 200 mA per anode established. The tube temperature was allowed to reach 350 ^{o}C, then the discharge was switched off again and the tube pumped out. Care had to be taken at this stage to ensure that the gas flow during pump-down was slow enough to avoid cadmium condensation on the Brewster windows. This process was repeated three times.

After this initial processing the cathode heater was usually kept on continuously, to maintain the cathode temperature at a minimum of 220 ^{o}C throughout the lifetime of the tube. Attempts were then made to obtain three-colour laser output.

Despite the wide ranges of helium pressures (5 - 40 Torr), cadmium source temperatures (250 - 350 ^{o}C) and discharge currents (50 - 200 mA per anode) investigated, these attempts were unsuccessful.

The optical cavity used was the same as that described earlier. The reflection characteristics of the broad band mirrors are illustrated in fig 4.3, where it can be seen that the reflectivity falls rapidly in the region 400 - 450 nm. However, to ensure that the reflectivity at 441.6 nm (Cd II blue) was adequate, the mirrors were used on an existing positive column device (70 cm active length) and produced laser oscillation easily. Since the mirrors also give adequate coverage of the red transitions of Cd II at 635.5 and 636.0 nm, maintaining 100% nominal reflectivity up to 650 nm, it may be concluded that the optical cavity was adequate for three colour operation.

Axial temperature gradients within the cathode body were minimal, the maximum temperature difference recorded being $\Delta T \sim 8$ ^{o}C at the highest current values investigated (200 mA per anode). Running the discharge at a higher current than this produced discharge instabilities which manifested themselves as discharge flaring when viewed along the cathode bore.

Since the general discharge conditions of helium pressure, discharge currents and cadmium source temperatures were favourable for three colour output, and since the laser optics were also adequate, a spectroscopic investigation of the discharge was undertaken to identify any impurities which may be responsible for quenching laser oscillation on the blue and red transitions. Laser oscillation on the green Cd II transitions was obtained, but the output was generally too unstable to make parametric observations

output was generally too unstable to make parametric observations of its behaviour in respect of discharge conditions such as He pressure, discharge current and cadmium source temperature.

4.4 Optical Measuring System.

The optical measuring system used to investigate the discharge is illustrated schematically in fig 4.4. Light from the discharge is apertured and focused onto the monochromator slit. The monochromator is by Carl Zeiss, model SPM2, with a recorder drive, and fitted with a prism to eliminate second order effects. The wavelength range of the prism is 360 nm to the infra red. A photomultiplier tube (PMT in fig 4.4, model 9558QB EMI) driven by a Fluke power supply 415B monitors the dispersed light.

Signal processing, which eliminates the effect of stray light, is achieved by chopping the input signal from the discharge at a frequency of approximately 1.4 kHz and detecting the modulated signal using a Princeton Applied Research Lock-In amplifier (model JB5). A reference signal modulated at the same frequency is provided by a photodiode positioned as illustrated in fig 4.4. An oscilloscope (Tektronix 545B) monitored the phase relationship between the reference and signal inputs.

The system is adequate for monitoring spectra in the range 360 - 650 nm, and has a resolution better than 0.1 nm in the blue region of the spectrum.

4.5 Emission Spectroscopy of Tube No.5.

The scanning speed at which the spectrum (360 - 650 nm) can be covered is limited by the response of the chart recorder. With minimal recorder damping and no RC signal filtering, it was found that the minimum time to record the spectrum was 90 minutes. At scanning speeds above this, fine structure detail could be easily "overlooked" by the recorder. Attempts were made to measure the spontaneous emission line intensities as a function of current, pressure and cadmium source temperature. However it was found that results suffered from a lack of reproducibility, particularly where the waiting time between measurements was more than a few minutes, as for example when the cathode temperature was being altered. Because of the nature of the discharges obtained with tube No.5, the results obtained are largely of a qualitative nature.

Scans of the spectrum were recorded after the discharge tube had reached thermal equilibrium. Spectral lines were identified either using the Hartmann dispersion formula (R.Sawyer, 1963) or by cubic interpolation between known lines. Initial wavelength calibration was achieved with a mercury lamp. However, once the major helium and cadmium spectral lines had been identified, the mercury lamp was no longer necesary. The Hartmann dispersion formula is an approximation for wavelength calculation where the dispersing element in a prism :

$$\lambda = \lambda_o + \frac{C}{d_o - d} \quad .$$

The determination of the constants λ_o, d_o and c necessitates the use of three known lines, λ_1, λ_2 and λ_3 whose distances on the chart paper from an arbitrary point are d_1, d_2 and d_3 respectively.

Spectra were obtained for a wide variety of discharge conditions. At low cathode temperatures, below 120 °C, only atomic lines attributable to He were detected. At cathode temperatures above 220 °C, weak H_α (656.3 nm) and H_β (486.3 nm) lines were detected, together with weak lines attributable to Cd I and Cd II. For higher cathode temperatures, where the cadmium vapour density is sufficiently high for laser oscillation, molecular bands and stronger Cd I and Cd II lines were observed, superimposed on weak background radiation extending from 380 - 500 nm. The source of this background radiation has not been positively identified, but is probably due to molecular spectra such as hydrogen and the broad band continuum of the Cd_2 molecule. (Pearse and Gaydon, 1950). The molecular bands which appeared were much more intense than the background radiation, and were degraded towards the violet. The bands generally increased in intensity with increasing cathode temperature and/or increasing discharge current. Operating the discharge at different pressures had little or no effect on the behaviour of the bands. Comparison with known molecular spectra identified the bands as transitions in the cadmium hydride (Cd H) molecule. Bandheads were observed at six wavelengths as follows:

$$4509 \text{ and } 4491 \; (^2\Pi_{1/2} - {}^2\Sigma),$$
$$4791 \text{ and } 4777 \; (^2\Pi_{1/2} - {}^2\Sigma),$$
$$4313 \text{ and } 4298 \; (^2\Pi_{3/2} - {}^2\Sigma).$$

(nanometers)

Figure 4.5(a) shows a typical example of the molecular spectra as they appeared on the chart recorder output. Figure 4.5(b) shows the energy levels and bandhead origins of the Cd H molecule.

4.6 Discussion of Results From Tube No.5.

Tube No.5 showed good thermal stability throughout the duration of its operation. The maximum axial temperature difference recorded, between the coolest and hottest parts of the cathode, was 8 ^{o}C. This occurred at the highest discharge current at which the tube was operated (600 mA total tube current). The thin-walled metal cylinders, which connected the glass/metal seals to the cathode body, fulfilled their role as thermal resistors, and the problems encountered in tubes Nos. 1 and 3 with thermal failure of the glass/metal seals did not occur.

The flexibility of design permitted two different modes of operation for tube No.5. Firstly, an oven appendage, attached to the cathode and situated diametrically opposite the central anode, could be heated independently of the cathode. When operated in this way (oven mode), the cathode temperature was maintained above that of the oven appendage by discharge heating and an auxiliary cathode heater. The cadmium vapour density thus depended on the temperature of the oven appendage, and the

discharge current could be altered independently of cadmium vapour pressure. Alternatively, the oven appendage could be removed and then cadmium inserted directly into the upper oven chamber, close to the cathode bore. In this cathode mode of operation, the discharge provides most of the heat necessary to raise the cathode temperature to the desired value, in the range 250 - 350 ^{o}C. The extra heat required is supplied by the cathode heater, which maintains the temperature at the desired value by means of the electronic temperature controller described in Appendix One. The discharge current could again be altered without affecting the cadmium vapour density thermally.

Emission spectroscopy of the discharges obtained in tube No.5 identified hydrogen as a major impurity. Although the H_{α} and H_{β} lines detected were themselves weak, several strong violet-degraded molecular bands attributable to transitions in the Cd H molecule were observed.

The tube was continuously baked at above 100 ^{o}C and thus it is unlikely that the hydrogen present was due to residual water vapour. This is further borne out by the lack of emission bands due to O_2^+, in particular the strongest violet degraded band at 602.6 nm, and other strong bands in the spectrum covered attributable to the First and Second Negative systems of the O_2^+ molecule. The absence of these O_2^+ bands also indicates that the vacuum system and discharge tube were relatively free from air leaks.

The likeliest source of the hydrogen detected in the discharge is the stainless steel cathode. Hydrogen becomes entrapped within metals during their formation processes, and the

subsequent rate of diffusion of the entrapped hydrogen increases rapidly with temperature (Kohl, 1967). This is supported by the observed occurence of the H_α and H_β lines only at elevated temperatures.

Hydrogen may also permeate through the Kovar, used in the glass/metal seals, at a rate which is strongly temperature dependent. However, the concentration of H_2 in dry air is less than 1 ppm, and it is unlikely that this could be a source. The Kovar components used in the electron tube industry are generally nickel plated to reduce hydrogen evolution and oxidation. These precautions were not taken in the construction of tube No.5.

Other gases which are commonly entrapped in stainless steels are H_2 and CO. Neither of these impurities was positively identified in the discharge spectra of tube No.5, although some weak band-like structures were observed in the region 420 - 430 nm. The comet-tail system of CO^+ and the molecular spectrum of N_2^+ both have their strongest emission bands in this region.

Since the system was sealed-off rather than continuously purged by flowing gas, impurities were not being removed from the discharge as they appeared. Instead, the concentration of hydrogen and other lower level impurities would continue to increase for as long as the discharge was running.

The presence of hydrogen may affect the discharge in a number of ways. Molecular cadmium hydride may be formed as the result of a collision between an excited cadmium atom and a hydrogen molecule,

$$Cd(5p\,^3P_{2,1,0}) + H_2 \rightarrow Cd\,H(\text{ground}) + H, \quad (4.1)$$

In this collision, the total energy available is the sum of the excitation energy of the cadmium atom (3.78 eV) and the dissociation energy of the Cd H molecule (0.67 eV), which amounts to 4.45 eV. This lies very close to the dissociation energy of the H_2 molecule (4.46 eV), and therefore makes it an energetically favourable process (Bender, 1930).

Once Cd H is formed, charge exchange pumping by He^+ ions in collisions with Cd H molecules cannot populate the upper levels of the Cd^+ ion ($6g\ ^2G_{7/2,9/2}$) from which the red transitions originate:

$$He^+ + CdH \rightarrow Cd(6g\ ^2G_{7/2,9/2}) + He + H, \quad (4.2)$$

The total energy available for excitation of Cd II in this case is the helium ionisation energy minus the dissociation energy of the Cd H molecule (0.67 eV), which amounts to 24.11 eV. Since, however, the Cd II ($6g\ ^2G_{7/2,9/2}$) levels lie approximately 0.2 eV below the helium ionisation energy (Turner-Smith et al, 1972), the extra 0.67 eV required to dissociate the Cd H molecule renders this reaction energetically unfavourable.

To obtain an order of magnitude estimate of the number density of Cd H molecules present in the discharge, we require the equilibrium constant for reaction (4.1) above. This is given by

$$k = \frac{[CdH][H]}{[Cd(5p\ ^3P_{2,1,0})][H_2]} \quad (4.3)$$

and thus we have

$$[Cd\,H] = k\,\frac{[Cd\ 5p\ ^3P_{2,1,0}][H_2]}{[H]} \quad . \qquad (4.4)$$

Of the terms on the RHS of eq (4.4), we can obtain an order of magnitude estimate for $[Cd\ ^3P_{2,1,0}]$. The relative number densities of Cd ($5p\ ^3P_{2,1,0}$) may be calculated using the Saha equation,

$$\frac{n_{Cd(^3P_o)}}{n_{Cd(^1S)}} = \frac{g(^3P_o)}{g(^1S)}\ \exp\left(-\frac{E(^3P_o)}{kT_e}\right), \qquad (4.5)$$

where $g(^3P_o)$ and $g(^1S)$ are the degeneracies of the ^3P_o and the ground states, $E(^3P_o)$ is the excitation energy of the ^3P_o state (3.8 eV), and T_e is the electron temperature. Although the electron distribution function is strongly non-Maxwellian, it is known that the majority of electrons in a hollow cathode discharge constitute a "plasma" component, for which the most probable electron energy is $\sim$5 eV. This is approximately equivalent to $T_e \sim 5 \times 10^4$ K. Applying the Saha equation to the other two triplet states ($^3P_1$ and $^3P_2$) yields

$$\frac{n_{Cd(^3P_1)}}{n_{Cd(^1S)}} = \frac{g(^3P_1)}{g(^1S)}\ \exp\left(-\frac{E(^3P_1)}{kT_e}\right), \qquad (4.6)$$

and

$$\frac{n_{Cd(^3P_2)}}{n_{Cd(^1S)}} = \frac{g(^3P_2)}{g(^1S)}\ \exp\left(-\frac{E(^3P_2)}{kT_e}\right). \qquad (4.7)$$

We then obtain

$$n_{Cd(^3P_0)} = 0{\cdot}5\, n_{Cd(^1S)} ,$$

$$n_{Cd(^3P_1)} = 1{\cdot}4\, n_{Cd(^1S)} ,$$

$$n_{Cd(^3P_2)} = 2{\cdot}3\, n_{Cd(^1S)} , \qquad (4.8)$$

from which we finally get

$$n_{Cd(^3P_{2,1,0})} = 4{\cdot}2\, n_{Cd(^1S)} . \qquad (4.9)$$

Although we can proceed no further because we have no information about k in eq (4.4), this result suggests that conditions are favourable for the production of Cd H. The $(^3P_{2,1,0})$ level of Cd is a necessary precursor for the formation of Cd H via reaction (4.1) above, and it appears that the majority of Cd atoms present in the discharge may be in this excited state.

Aside from the formation and effects of Cd H, the presence of atomic hydrogen may give rise to the following Penning reaction which which depletes the $6g\ ^2G_{7/2,9/2}$ state of Cd II;

$$Cd\,II(6g\,^2G_{7/2,9/2}) + H \rightarrow Cd\,II(ground) + H^+ + e(\Delta E). \qquad (4.10)$$

In this case, the energy available is 15.39 eV, this being the

difference between Cd II ($^2G_{7/2,9/2}$ at 24.4 eV) and the ionic Cd II ground state (9.0 eV). The ejected electron carries off the excess energy ΔE = 1.8 eV, (this being the difference between the available energy and the ionisation energy of H, 13.6 eV). A similar reaction with Cd II ions in the upper levels of the green transitions is much less likely to occur because this level lies only 13.4 eV above the Cd II ground state, and thus there is insufficient energy available for ionisation of H atoms. Since, however, the upper levels of the green laser transitions are thought to be cascade pumped from the red transitions, at least in part, reaction (4.10) above will reduce the population inversion between the energy states corresponding to both red and green laser wavelengths.

Hydrogen present in the discharge may also affect the helium metastable and ion densities, both of which play important roles in the pumping mechanisms of hollow cathode He-Cd lasers. The helium metastable density may be depleted via the following Penning reaction

$$He(2s\,^3S) + H_2 \rightarrow H + H^+ + He(ground) + e(\Delta E), \qquad (4.11)$$

The ejected electron removes the excess energy, given by

$$\Delta E = E(He\ 2s\,^3S) - E(dissociation) - E(ionisation)$$
$$= 19.8 - 4.46 - 13.59 = 1.75\ eV.$$

Helium ions are produced in the discharge by direct electron impact

$$e + He \rightarrow He^{+} + 2e \,. \qquad (4.12)$$

The maximum cross section for this reaction is $0.3 \times 10^{-16} cm^2$ (Brown, 1961), and occurs for incident electron energies in the range 80-100 eV. The following reactions, however, are likely to occur when hydrogen is present

$$e + H \rightarrow H^{+} + 2e \,, \qquad (4.13)$$

$$e + H_2 \rightarrow H_2^{+} + 2e \,, \qquad (4.14)$$

Reactions (4.13) and (4.14) have maximum cross sections similar to of $0.3 \times 10^{-16} cm^2$ and $1.0 \times 10^{-16} cm^2$, respectively, and which also occur for electron energies in the range 80-100 eV. The threshold value for ionisation of atomic and molecular hydrogen are 13.6 eV and 16.0 eV, respectively, and are lower than that for helium (24.6 eV). It is thus likely that a larger fraction of electrons in the discharge are available for reactions (4.13) and (4.14), than is the case for reaction (4.12). The net result is that the He^{+} ion density will be lowered in the presence of hydrogen, and there will correspondingly be fewer charge exchange reactions, which pump the upper levels of the red and green transitions. Reactions (4.13) and (4.14) are also in competition with the following reaction

$$e + Cd \rightarrow Cd^{+} + 2e \,. \qquad (4.15)$$

Stepwise electron excitation is thought to play an important role in producing the population density of Cd II ($4d^9 5s^2\ ^2G_{5/2}$), which is the upper level of the blue transition.

Finally, it is well known that population of molecular vibrational states by electron impact produces a decrease in the mean electron energy (lowering of T_e).

4.7 Tube No.6 Overall Design.

Tube No.6 had a stainless steel cylindrical cathode, 50 cm in length with a 4 mm bore, and OD 38 mm. Ten anodes spaced 5 cm apart were interspersed by nine equally spaced cadmium wells and situated diametrically opposite the anodes (see fig 4.6). The anode assemblies are illustrated in fig 4.7. A silica sleeve was inserted in the anode sleeve, as indicated in fig 4.7, to prevent the discharge from the anode striking to the internal surfaces of the anode sleeves and generating unwanted heat near the glass/metal seals. The Brewster window assemblies were mounted at each end of the tube using "O" ring seals (fig 4.8). The "O" rings require protection from temperatures in excess of 100 ^{o}C, and thus a 7 cm length of thin walled (0.5 mm) sleeve connects the Brewster assemblies with the tube cathodes. With the laser cathode at its maximum operating temperature of 350 ^{o}C, the sleeves should provide adequate protection for the "O" ring seals.

An insulated heater element (26 swg Eureka, 4 m

length) was wound on the cathode. A thermistor mounted on the cathode provided the necessary temperature monitoring for the electronic temperature controller described in Appendix One. It was found that the triac in the temperature controller would not fire properly into a high inductance load and so the heater was double wound in a bifilar manner.

Tube No.6 was designed to be partially heated by discharge power, with the cathode heater providing the extra power required to bring the cathode up to the operating temperature range 280 ^{o}C - 350 ^{o}C.

The anode sleeves served to protect the glass/metal (Kovar) seals from excessive temperatures, dimensions being chosen in accordance with the thermal design criteria established in Chapter Three.

A series of blind holes bored into the external cathode wall provided sites for thermocouple junctions for cathode temperature measurement.

4.8 Tube No.6 Construction.

The cathode body was constructed from five 38 mm OD stainless steel sections which were then argon-arc-welded together. The anode sections were also argon-arc-welded together, each weld being leak tested individually before the next weld was attempted. Again, although there are a total of ten welds between Kovar and stainless steel in the whole tube, the technique yielded

a system which proved to be leaktight. Seven out of the ten Kovar/stainless steel welds were leak tight after welding once, and the remaining three required an extra "run" to achieve this. The cadmium wells were drilled diametrically opposite the anodes and spaced equally between them. The drilled holes were sealed by argon-arc-welding stainless steel plugs into them.

The completed anode assemblies were then welded onto the cathode body, with the silica sleeves in situ. This was necessary because the glass tended to narrow internally at the glass/metal seal, by up to 1.5 mm in some cases. If thinner silica sleeves had been inserted after assembly, they would not have fitted as closely to the internal anode sleeves, and would thus be less effective at preventing the discharge striking there. The completed tube was given a final leak test, and then the cadmium wells were filled with cadmium. This was achieved by placing cadmium granules at one end of the tube and pushing them along the bore until the first well was filled. This was repeated until all the wells were filled. A 5 cm length of silica sleeve was then inserted into the Brewster sleeves at either end of the tube to prevent the discharge extending axially from the 4 mm bore region.

4.9 Operating Conditions.

Tube No.6 was operated in the circuit illustrated, fig 4.9, with each of the ten anodes individually ballasted with a 6 KΩ resistor chain. The total tube current was limited to 1100 mA by the power supply, and this current was the value at which the tube was generally operated for the optical measurements described below. Tube processing consisted of bakeout at 220 °C under vacuum overnight. The tube was maintained at this temperature with the cathode heater, and thus the anode sleeves themselves were not baked at this temperature. The tube was then filled with 15 Torr helium and a discharge established at 1100 mA. When combined discharge heating and cathode heating brought the cathode temperature up to 350 °C, the discharge was switched off and the tube repumped with the cathode heater maintaining the cathode temperature at 220 °C. Again, care was necessary during this operation, to keep the gas flow during pump-down slow enough to prevent cadmium deposits forming on the Brewster windows. The process of running a discharge in 15 Torr at 1100 mA was repeated several times before any optical measurements were taken.

Attempts to obtain three colour operation from tube No.6 were also unsuccessful. As with tube No.5, a wide range of helium pressures (5 - 40 Torr), tube temperatures (250 - 350 °C) and discharge currents (500 - 1100 mA) were investigated. The optical cavity was the same as used for tube No.5. Only intermittent oscillation of the green lines at 533.7 and 537.8 nm was obtained, generally at currents above 800 mA, tube temperatures above 320 °C and at helium pressures in the range 5 - 40 Torr.

However, random fluctuations rendered parametric observations of power output vs current, temperature and pressure somewhat pointless.

4.10 Spectroscopic Investigation of Tube No.6.

The same optical system as described in Section 4.4 was used to obtain emission spectra from tube No.6. Discharge conditions during the scan were 1100 mA total tube current, 15 Torr helium pressure and 350 ^{o}C tube temperature. The results of the scan were qualitatively identical with those obtained with tube No.5. Strong emission bands, attributed to Cd II transitions, were again observed, as were weak H_{α} and H_{β} lines.

During cavity alignment, with a beam-stirred He-Ne laser, it was observed that the reflected spot from the back mirror appeared to vary in intensity on the pin hole card (see fig 4.10). This suggested that there was perhaps some optical absorption ocurring at 632.8 nm. This neon line was not observed in emission which suggested that the suspected absorption may be of a continuous nature (ie. broad band molecular absorption). To investigate this further, the optical system was altered as illustrated in fig 4.11. A broad band source (tungsten filament bulb) was placed on the system optical axis at the far end of the tube. The monochromator was then set to accept a wavelength (634.0 nm) close to the red laser transitions at 635.5 nm and 636.0 nm, but at which there was no discharge emission. The bulb alone was

then switched on, and the bulb output monitored at 634.0 nm. This was stable to within ± 2% over a period of one hour. The discharge was then initiated and thus any absorption occurring at the monitored wavelength should produce a drop in signal intensity from the bulb. Such signal attenuation was indeed observed. The general time behaviour after discharge initiation is illustrated in fig 4.12. Prior to discharge initiation, the tube had been pumped and baked at 220 ^{o}C then refilled with 15 Torr helium. An initial drop in measured intensity was observed, the discharge attenuating up to 56 % of the bulb's light within 20 minutes. However, this recovered somewhat after a further 10 minutes, and settled at a level representing an attenuation of 8 % per metre. Figure 4.12 shows the result of switching the discharge on and off several times, after the initial settling down period. When switched off, the measured intensity of the bulb reverted to its initial value, before discharge initiation. Re-establishing the discharge caused the measured bulb intensity to drop almost instantaneously to the level which it attained after settling down.

The general time behaviour of absorption was found to be reproducible provided that the tube was pumped then refilled with fresh He (to 15 Torr). A similar absorption scan was taken at a wavelength close to the green transitions and approximately equal absorption was measured. No absorption measurements could be made close to the blue transition because of background radiation in the vicinity of the line.

4.11 Discussion of Results from Tube No.6.

As with tube No.5, tube No.6 displayed excellent thermal stability during the course of its operation. The thermal resistors provided adequate protection for the glass/metal seals at the anodes, and for the "O" ring seals situated in the Brewster angled window mounts. Axial temperature gradients were minimal (5 ^{o}C) at the maximum discharge current of 1100 mA.

Laser gains of approximately 5% per metre have been measured in He-Cd hollow cathode lasers for all of the transitions in the visible Cd II transitions, under optimum discharge conditions for each line (Csillag et al, 1977). The absorption observed in the plasma of tube No.6 can thus account for the lack of three colour output. The absorption was due to a species which was formed only when the discharge was running, and which decayed when the discharge was switched off (see fig 4.12). The species, however, remains unidentified.

4.12 Conclusions

The results of the thermal analysis developed in Chapter Three were applied to the designs of tubes Nos.5 and 6. The problems encountered in tubes Nos.1 and 3 with the failure of the glass/metal seals due to overheating were successfully overcome. Furthermore, the severe axial temperature variations measured on the cathodes of tube No.4 were successfully eliminated

by designing tubes Nos.5 and 6 with thicker walled cathodes. The largest axial temperature variations recorded occurred at the highest discharge currents operated in tube No.5 (200 mA per anode), and were less than 10 ^{o}C. This permitted the use of multiple sources of cadmium distributed along a 50 cm active length in tube No.6, a desirable design feature for sealed-off long active length tubes where cadmium distribution is not enhanced by gas flow.

Emission spectroscopy of the discharges obtained in tube No.5 identified Cd H as a major impurity. It has been shown (Section 4.6) that the presence of hydrogen in a He-Cd discharge may give rise to several reactions, all of which have a detrimental affect on the pumping mechanisms which produce the population inversions on the visible laser transitions of Cd II.

Absorption spectroscopy of the discharges obtained in tube No.6 showed that a transient species, formed while the discharge was running, could account for the lack of three colour output, from that tube. The species responsible remains unidentified.

The poor oscillation characteristics obtained from tubes Nos. 5 and 6 are largely attributable to impurities present in the discharge. There are two likely sources of impurities in sealed-off devices such as tubes Nos. 5 and 6. Firstly, the material used in the construction of the tube cathodes was of commercial grade, and apart from degreasing the machined component parts, no special surface preparation processes were adopted. Techniques such as baking in a forming gas atmosphere, acid polishing and nickel plating have been developed, and are used

extensively, in the electron tube industry. Such techniques are generally found to be necessary for all types of sealed-off devices. Moreover, component parts are generally manufactured from high purity materials. Secondly, tube processing prior to operation posed several problems and, in retrospect, may have been inadequate. The presence of cadmium in the tube and the lack of proper bakeout facilities limited the maximum bakeout temperature to 220 ^{o}C, which was lower than the temperatures at which the tube was operated. It is thus likely that the rate of outgassing of the cathode increased when a discharge was established, and that impurities adsorbed on the cathode surfaces persisted after bakeout. In contrast, the temperatures used during processing in the electron tube industry are generally as high as the component parts can withstand, which usually represents a temperature which is higher than the maximum recommended temperatures at which devices may be operated.

The upper limit imposed on bakeout temperature by the existence of cadmium in the tubes could possibly be overcome by baking in two stages. The first bakeout would be at as high a temperature as component parts could withstand without the presence of cadmium. The tube could then be allowed to cool and let up to air before inserting the cadmium source. The second bakeout, at a lower temperature (200-250^{o}C) could then be initiated to eradicate water vapour from the cadmium sample and from any other surfaces which may have become recontaminated as a result of letting the tube up to air after the first bakeout.

In conclusion, it is thought that with the expertise in processing techniques available in the electron tube industry,

together with careful thermal design, successful sealed-off operation of white light He-Cd lasers could be obtained. Since, however, three-colour He-Cd lasers are not yet commercially available, it would appear that development work is still required, especially in the tube materials and processing areas.

PLATE 4.1. TUBE NO. 5.

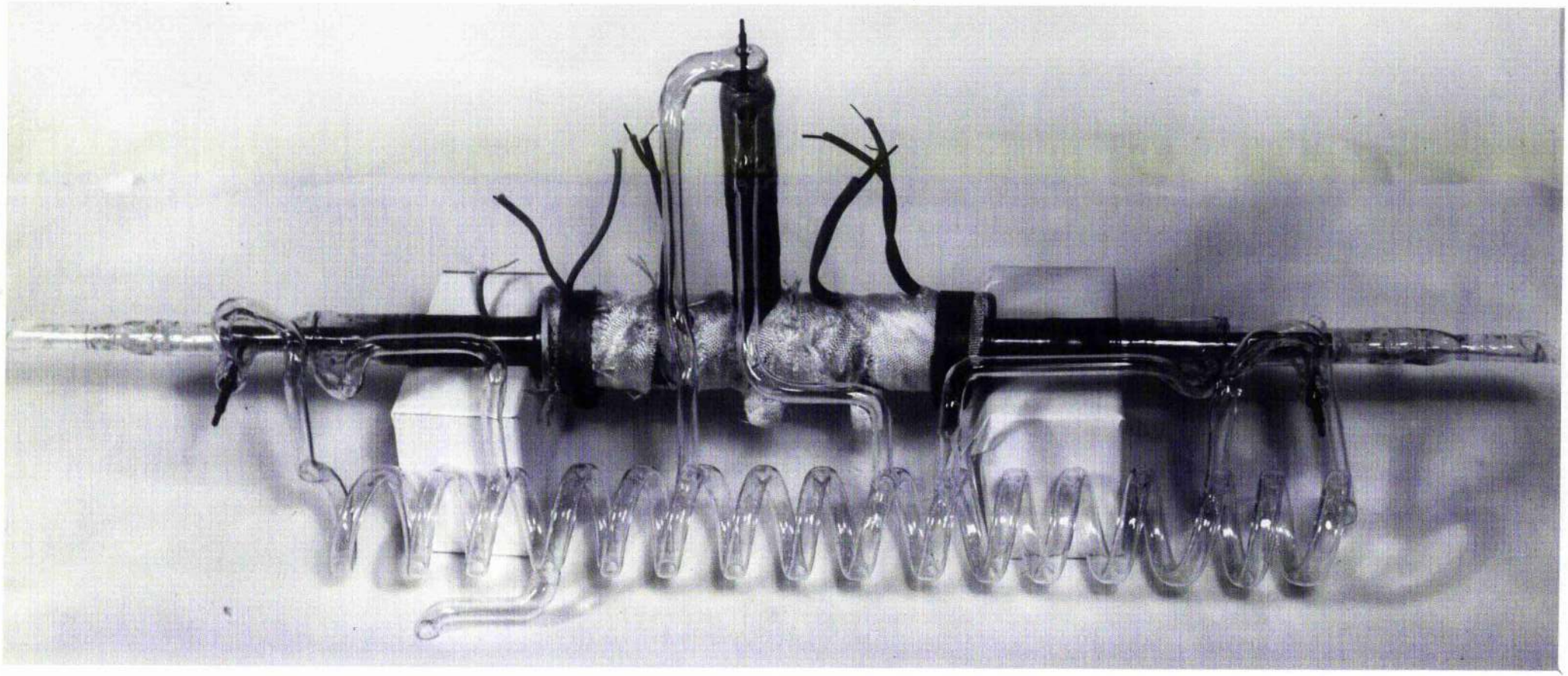

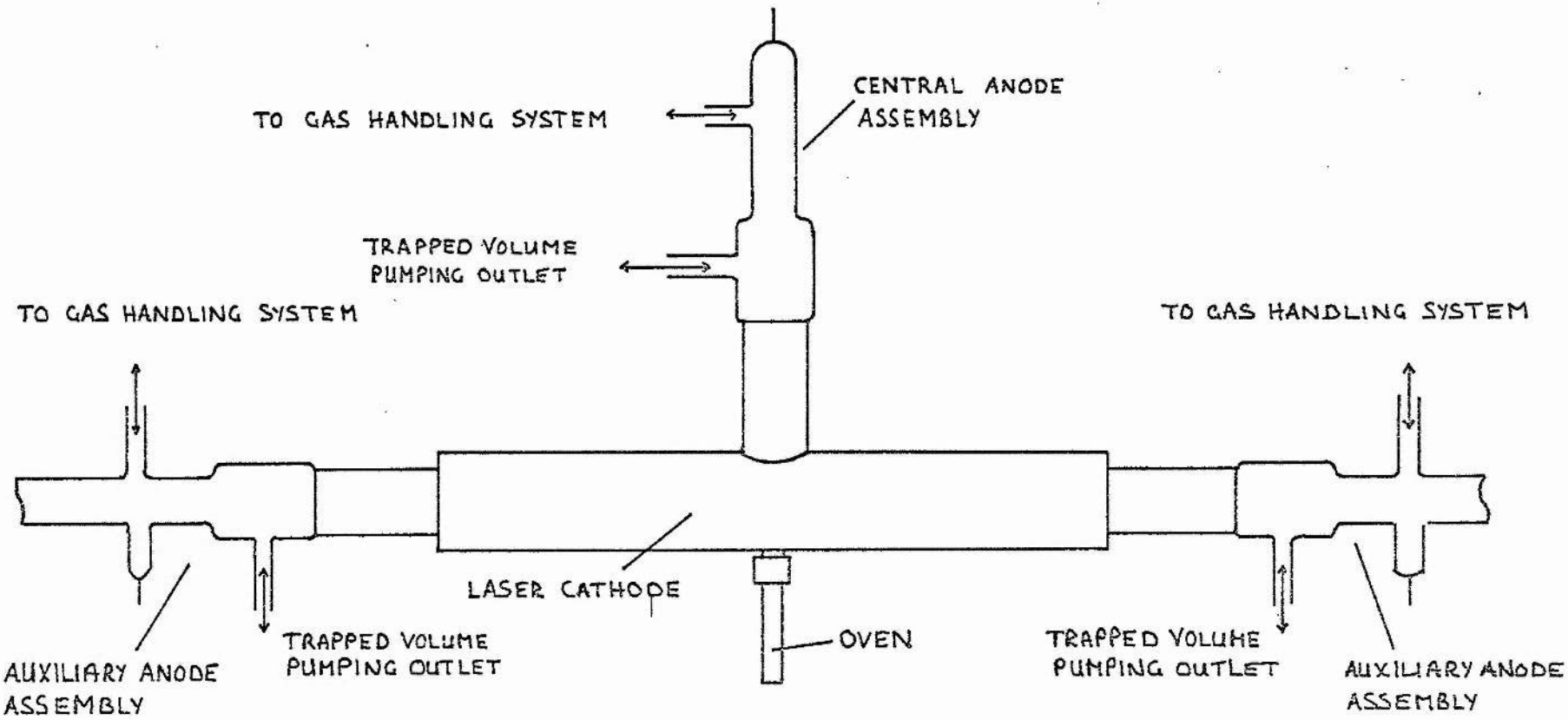

FIG 4.1 (a) OVERALL VIEW OF TUBE No.5. EQUIPPED WITH BREWSTER ANGLED WINDOWS (NOT DRAWN).

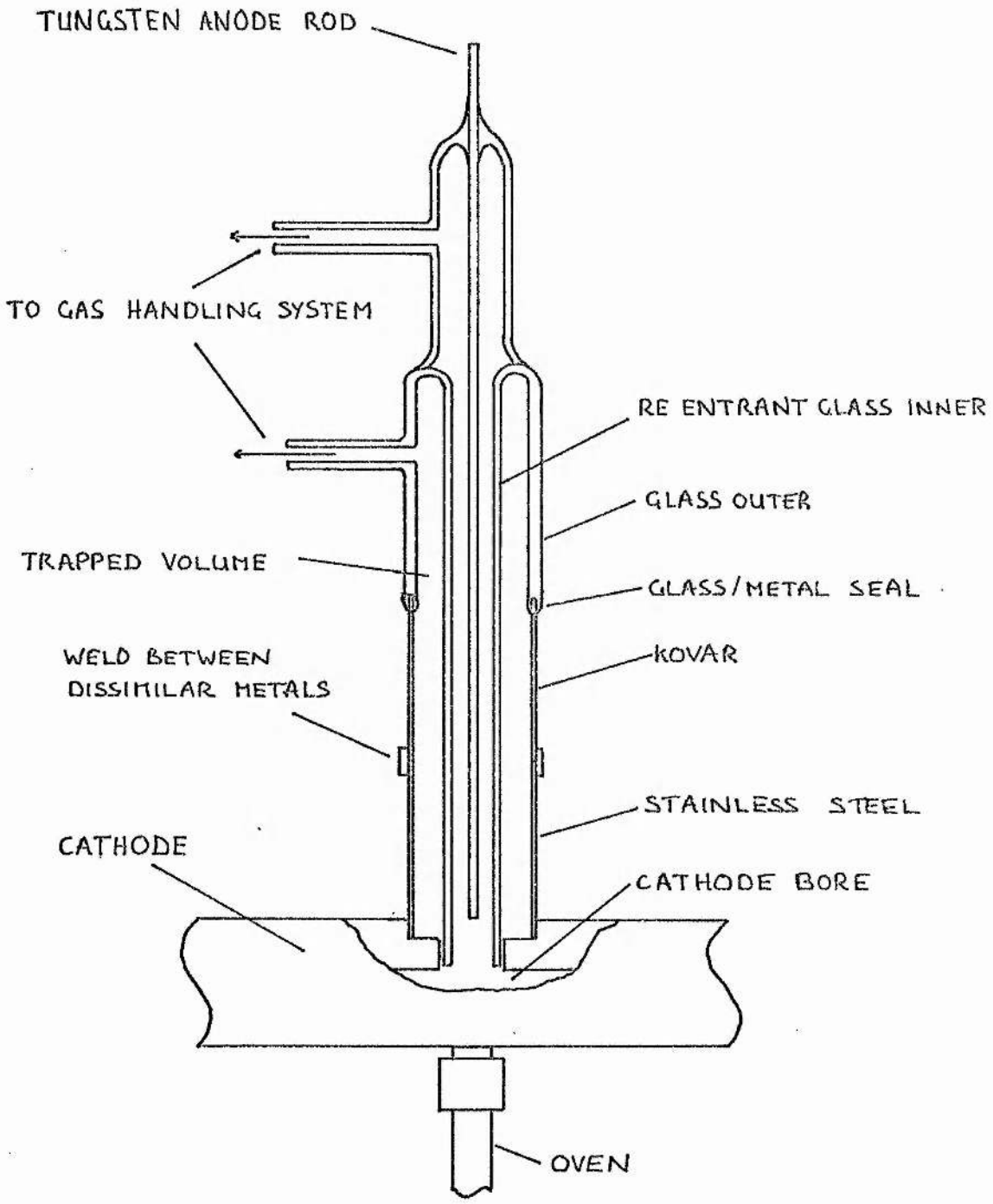

FIG. 4.1(b) CENTRAL ANODE ASSEMBLY (TUBE No. 5)

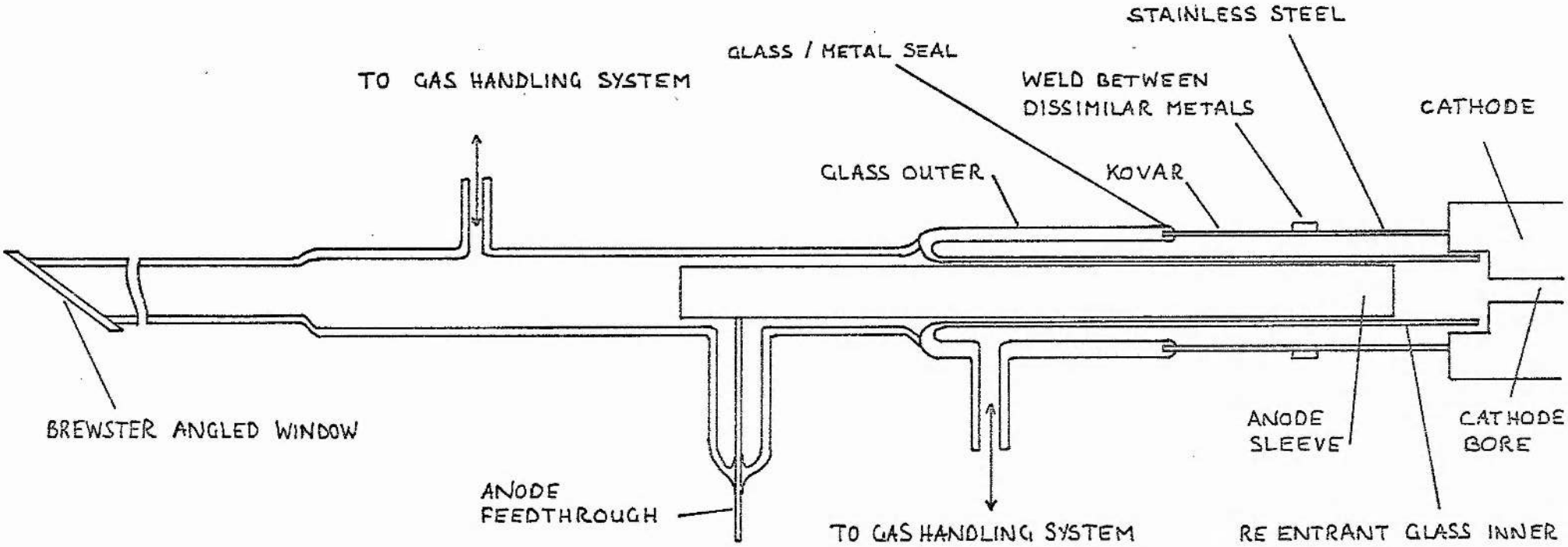

FIG 4.1 (c) AUXILIARY ANODE ASSEMBLY FOR TUBE No. 5.

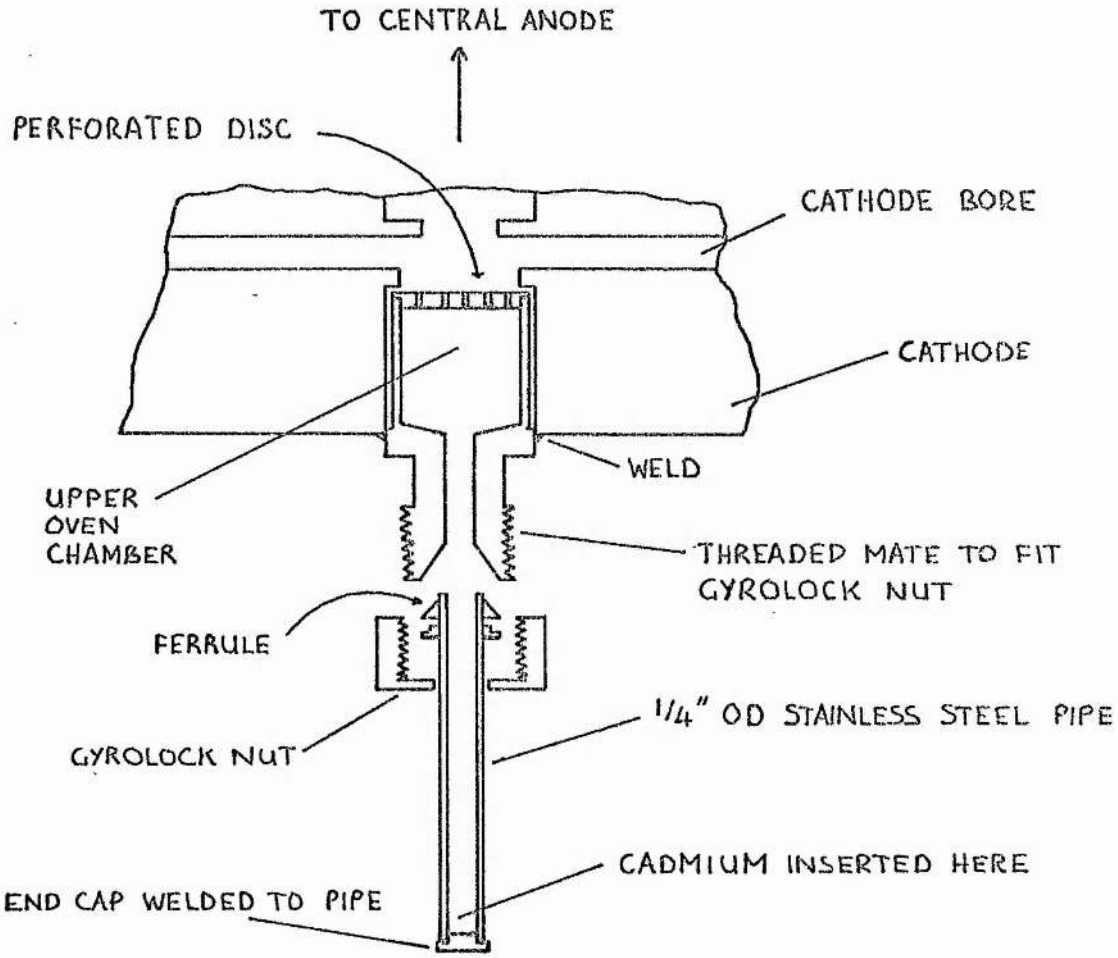

FIG 4.2 (a) OVEN APPENDAGE FOR OPERATION OF TUBE No. 5 IN "OVEN" MODE.

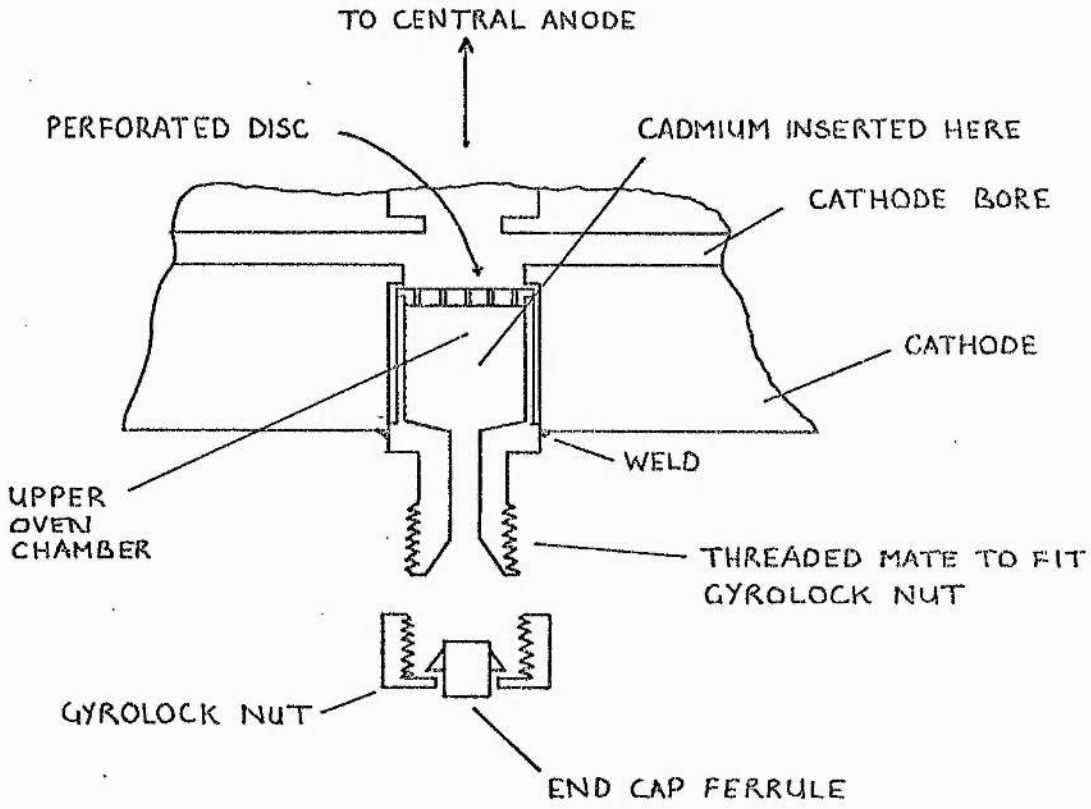

FIG 4.2 (b) CADMIUM RESERVOIR ARRANGEMENT FOR OPERATION OF TUBE No. 5 IN "CATHODE" MODE.

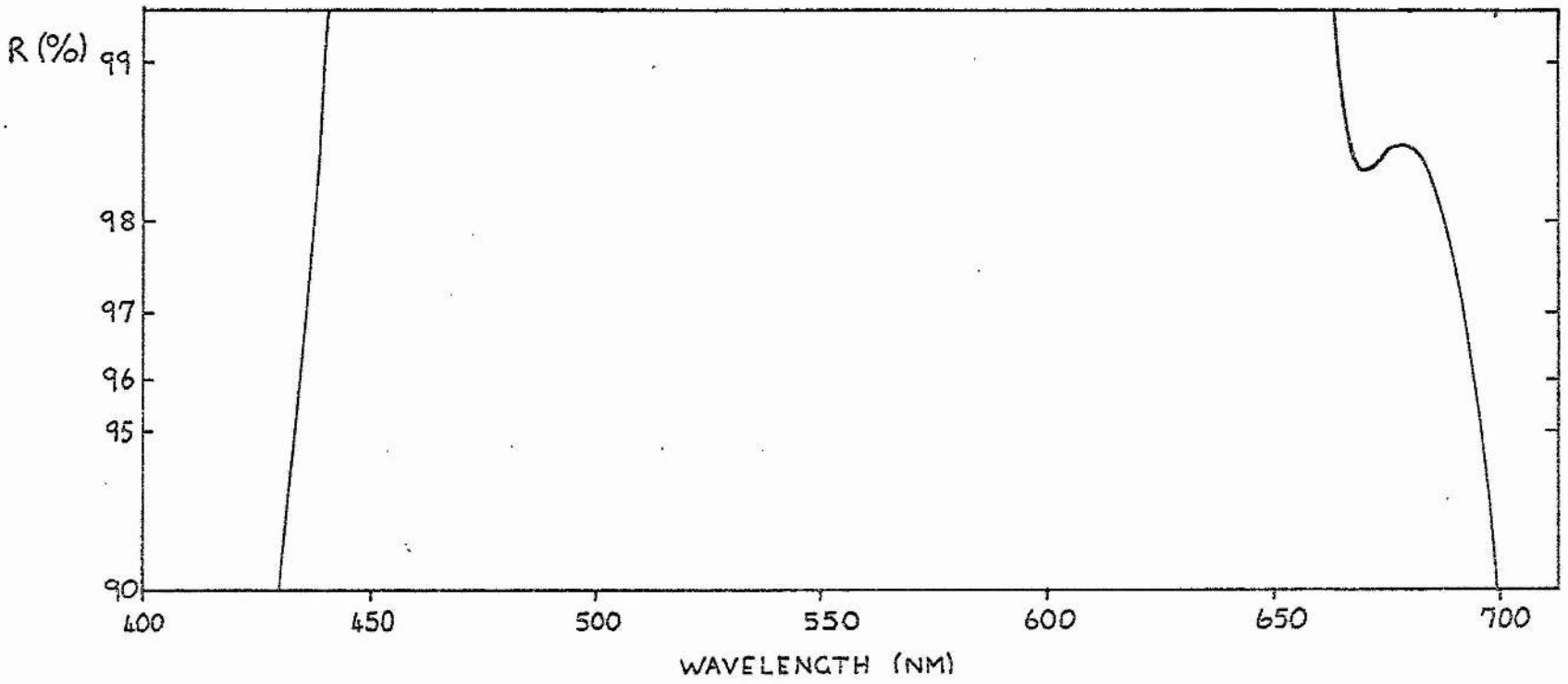

FIG 4.3 REFLECTIVITY R (%) VS WAVELENGTH (NM) FOR BROADBAND LASER MIRRORS USED THROUGHOUT COURSE OF THIS WORK. R > 99·2 % FOR REGION 440 - 650 NM (BOTH MIRRORS)

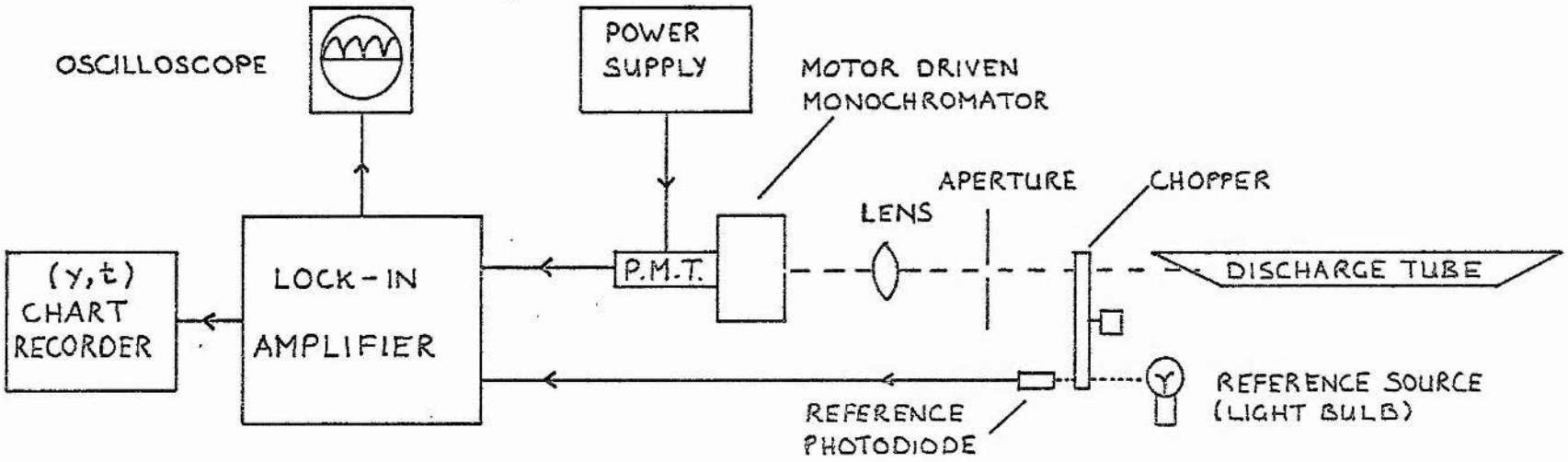

FIG 4.4 SCHEMATIC DIAGRAM OF OPTICAL MEASURING SYSTEM USED FOR INVESTIGATION OF DISCHARGES OBTAINED IN TUBE No. 5.

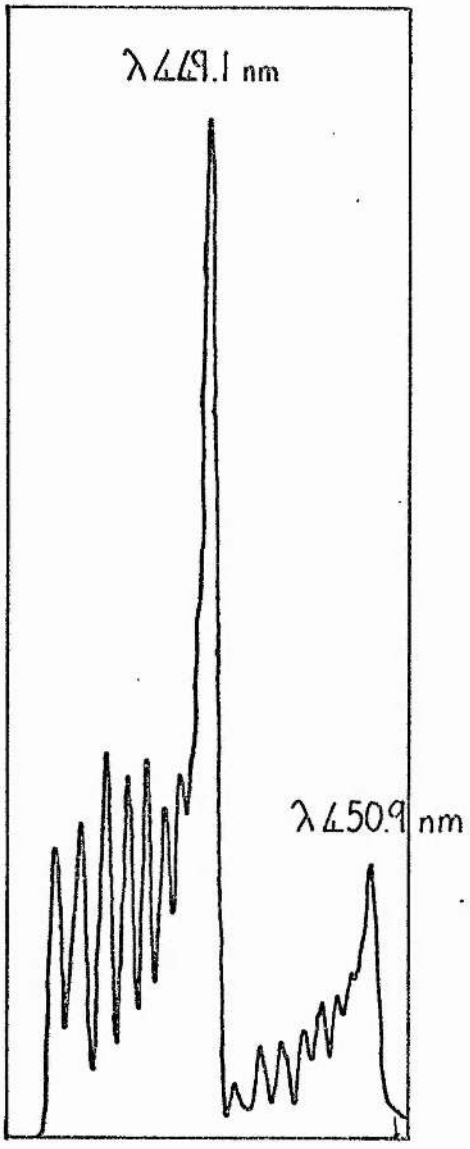

FIG 4.5(a) VIOLET DEGRADED MOLECULAR BAND STRUCTURE, DUE TO Cd H.

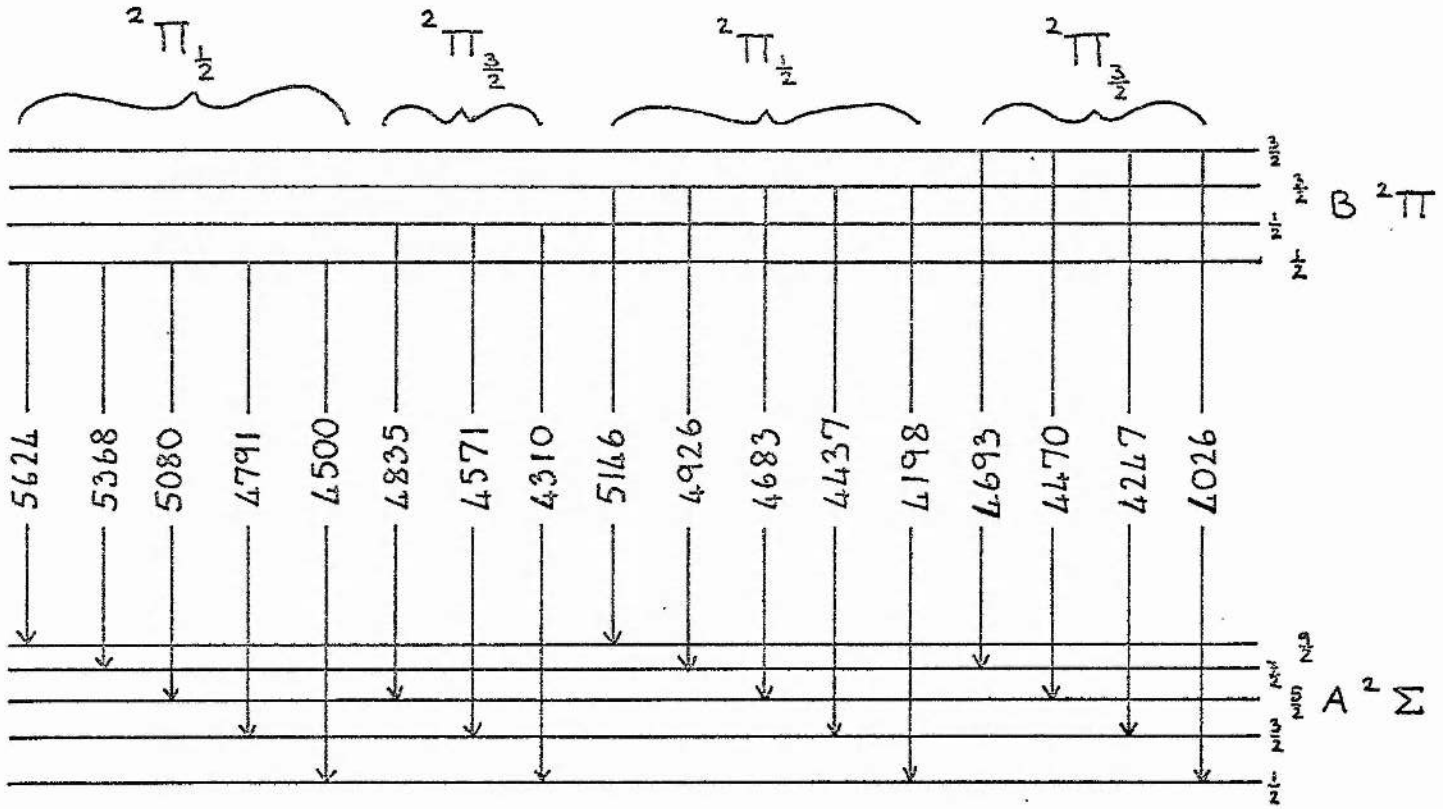

FIG 4.5(b) MOLECULAR BAND SYSTEM OF Cd H (BENDER, 1930).
TRANSITION WAVELENGTHS ARE IN ANGSTROMS.

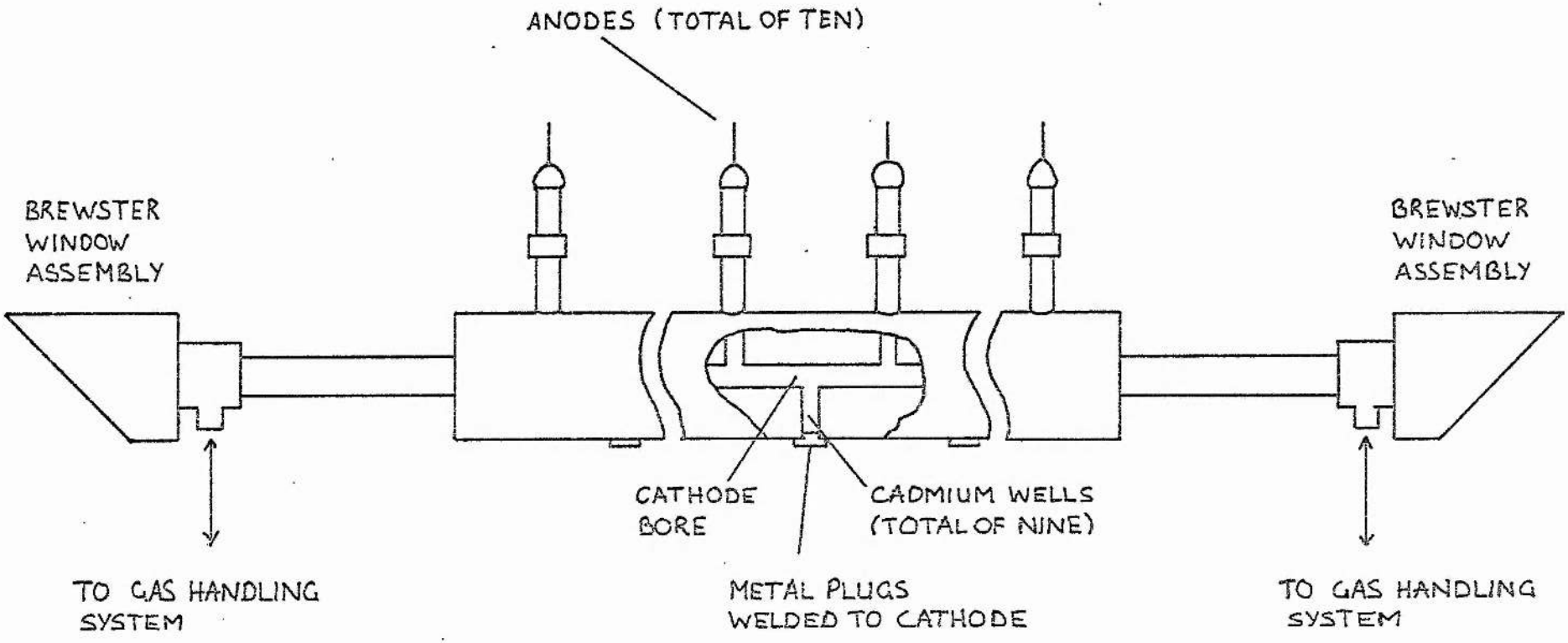

FIG 4.6 OVERALL LAYOUT OF TUBE No. 6.

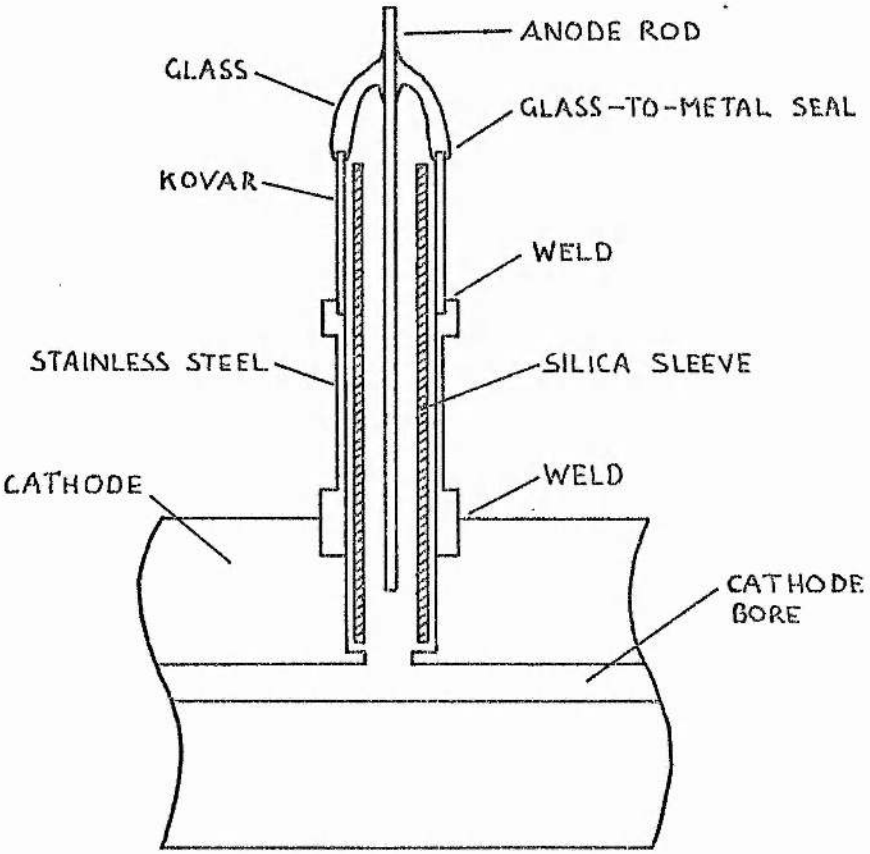

FIG 4.7 ANODE ASSEMBLY FOR TUBE No. 16.

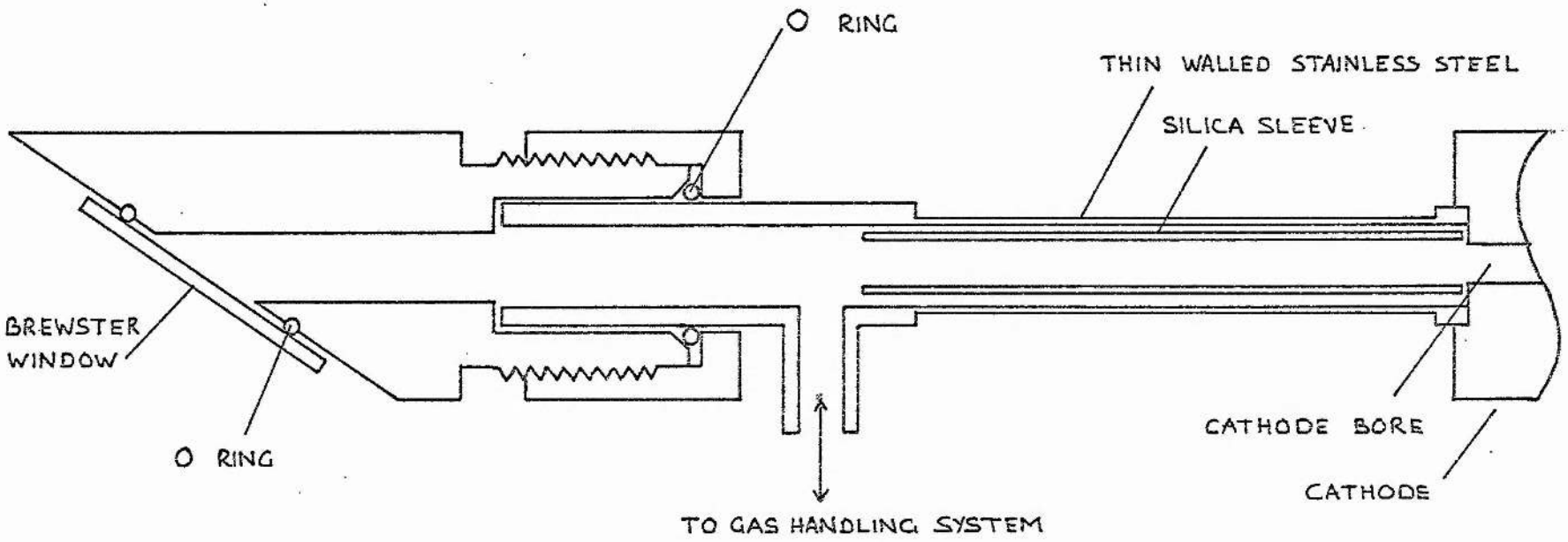

FIG 4.8 BREWSTER WINDOW ASSEMBLY FOR TUBE No. 6

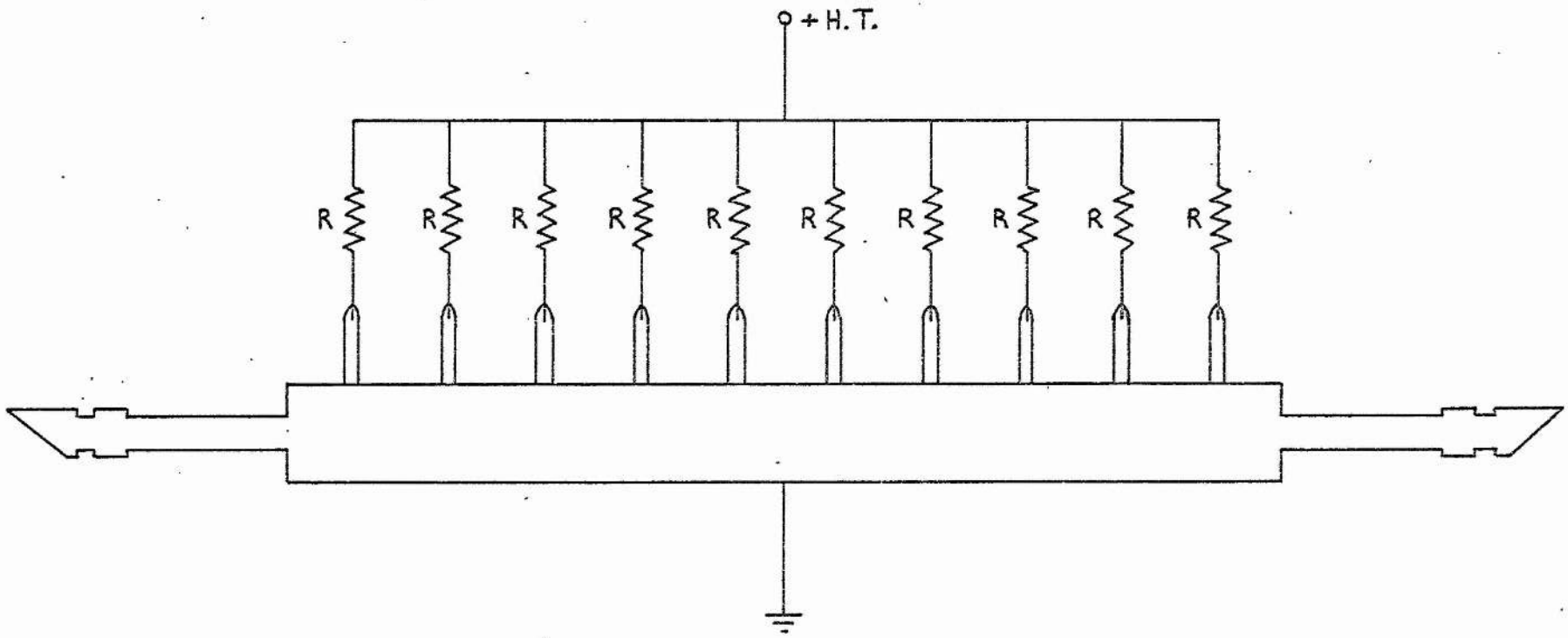

FIG 4.9 SCHEMATIC OF LASER CIRCUIT FOR TUBE No. 6 WHERE $R = 6\ k\Omega$.

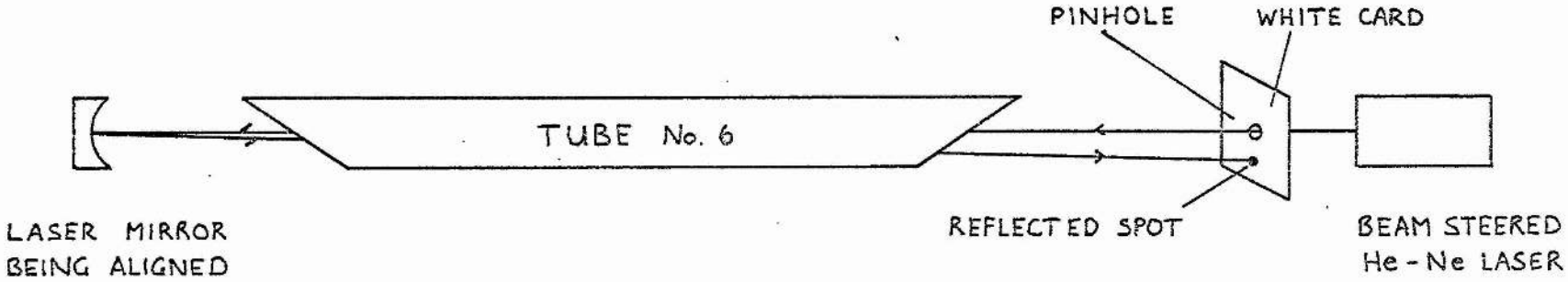

FIG 4.10 SCHEMATIC OF ALIGNMENT PROCEDURE FOR LASER MIRRORS. REFLECTED SPOT OBSERVED TO VARY IN INTENSITY WHILE DISCHARGE RUNNING IN TUBE No. 6.

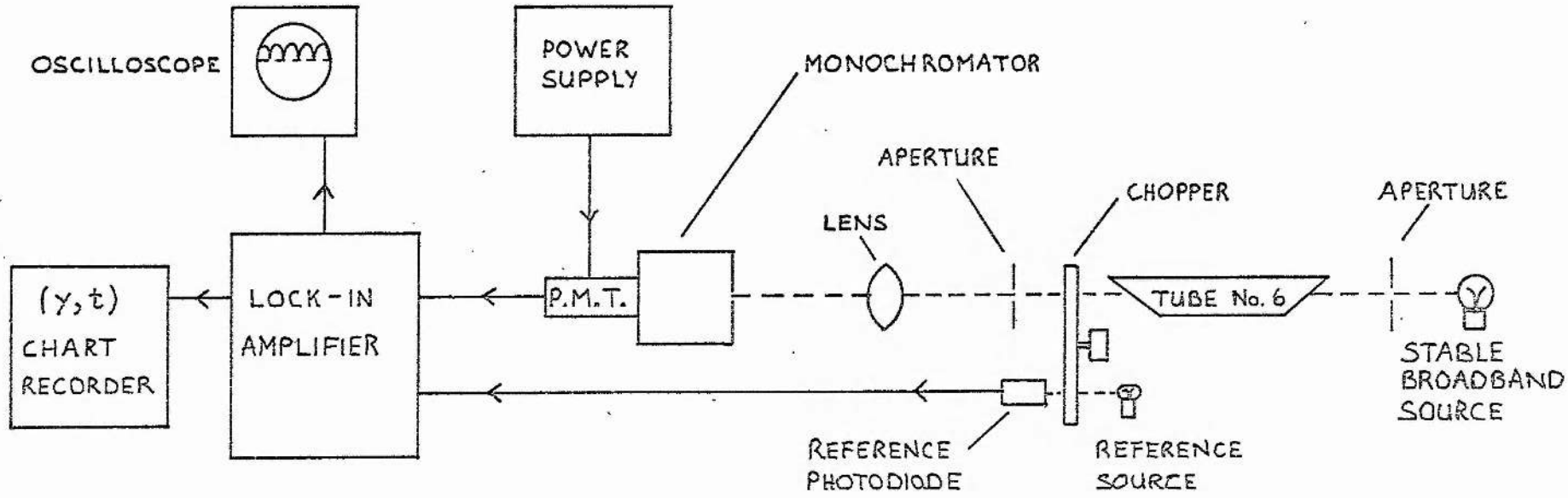

FIG 4.11 SCHEMATIC OF OPTICAL SYSTEM FOR ABSORPTION MEASUREMENTS FROM TUBE No. 6.

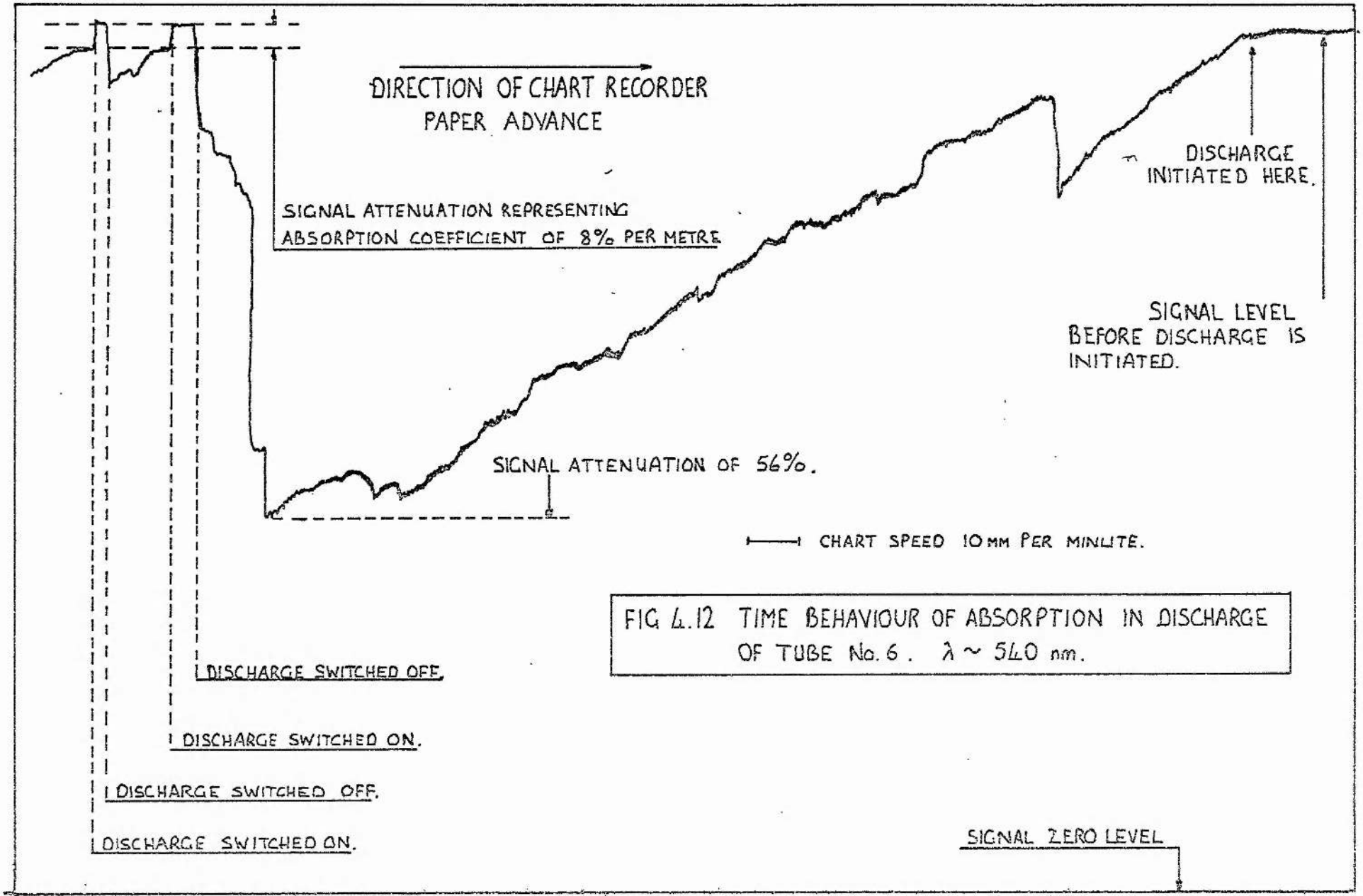

FIG 4.12 TIME BEHAVIOUR OF ABSORPTION IN DISCHARGE OF TUBE No. 6. $\lambda \sim 540$ nm.

CHAPTER FOUR BIBLIOGRAPHY.

BENDER, P.

Phys. Rev.,36,1535-1542,1930.

BROWN, S.C.

"Basic Data of Plasma Physics", Wiley (New York), Chapman and Hall (London),1961.

CSILLAG, L., HAN, C.Z., JANOSSY, M. and ROZSA, K.

Opt. Commun.,21,39-41,1977.

GRACE, J.R. and MCINTOSH, A.I.

J. Phys. D : Appl. Phys.,12,2043-2051,1979.

KOHL, W.H.

"Handbook of Materials and Techniques for Vacuum Devices", Reinhold (New York), 1967.

LIPSON, H.C. and MITCHELL, A.C.G.

Phys. Rev.,48,625-630,1935.

MIZERACZYK, J. and MEIGER, M.

XVI International Conference on Phenomena in Ionised Gases,210-211, Dusseldorf, West Germany, 1980.

PEARCE, R.W.B. and GAYDON, A.G.

"The Identification of Molecular Spectra",

Chapman and Hall (London), 1950.

SAWYER, R.

"Experimental Spectroscopy", Dover (New York), 1963.

TURNER-SMITH, A.R., GREEN, J.M. and WEBB, C.E.

J. Phys. B : Atom. Molec. Phys., 6, 114-130, 1973.

CHAPTER FIVE

THE DESIGN OF BROAD BAND OPTICS USING FLOW-GRAPH TECHNIQUES.

5.1 Introduction: Colourimetry and the He-Cd Hollow Cathode Laser.

Helium-cadmium lasers can oscillate on five transitions in the visible region of the spectrum, at 441.6 nm, 533.7 and 537.8 nm, and 635.5 and 636.0 nm. Under conditions of simultaneous oscillation, the laser output can appear white, and by changing the the relative proportions of each of the three colours, a wide variety of different colours may be obtained. To help quantify the suitability of the He-Cd system as a candidate for white light and coloured light production, it is necessary to discuss briefly the fundamentals of colourimetry. Colour measurement is based on the human visual system, and involves the comparison of two colours. In Young's experiment on colour mixing, red and green beams are superimposed on a screen and compared with a yellow beam (fig 5.1(a)). By adjusting the relative intensities of the red and green beams, a good match with the yellow can be obtained. This introduces the notion of colour "equations". The

colour equation for fig 5.1(a) is

$$R(R) + G(G) \equiv Y(Y). \qquad (i)$$

This means that R amount of colour (R) superimposed with G amount of colour (G), gives the same visual effect as Y amount of colour (Y). An important law of colourimetry states that any colour (C) can be matched by a suitable combination of three "independent" spectral colours, (X),(Y) and (Z). Thus, we have

$$C(C) \equiv X(X) + Y(Y) + Z(Z), \qquad (ii)$$

provided that X and/or Y and/or Z may be negative. If X is negative, this means that $X(X)$ superimposed on the desired colour $C(C)$ will give the same effect as $Y(Y)$ superimposed on $Z(Z)$. If the three colours (X),(Y) and (Z) are red, green and blue, then more colours can be matched by these than by any other combination. For example, W amount of white (W) may be produced by combining R amount of red (R), G amount of green (G) and B amount of blue (B), as follows

$$W(W) \equiv R(R) + G(G) + B(B). \qquad (iii)$$

The relative proportions in terms of lumens are

$$230(W) = 62(R) + 162(G) + 6(B). \qquad (iv)$$

The units of (R),(G) and (B) may be defined such that equal

amounts of the reference (primary) colours $(\mathcal{R})$, $(\mathcal{G})$ and $(\mathcal{B})$ produce white light. In terms of white (W) and colour (C), we may now write

$$3(W) \equiv 1(\mathcal{R}) + 1(\mathcal{G}) + 1(\mathcal{B}), \qquad (v)$$

and

$$C(C) = \mathcal{R}(\mathcal{R}) + \mathcal{G}(\mathcal{G}) + \mathcal{B}(\mathcal{B}), \qquad (vi)$$

where $\mathcal{R}$, $\mathcal{G}$ and $\mathcal{B}$ are called tristimulus values. Because of the choice of units in eq (v) above, we may write

$$C = \mathcal{R} + \mathcal{G} + \mathcal{B} \quad . \qquad (vii)$$

Equation (vi) may be written

$$(C) = \frac{\mathcal{R}}{C}(\mathcal{R}) + \frac{\mathcal{B}}{C}(\mathcal{B}) + \frac{\mathcal{G}}{C}(\mathcal{G})$$

$$= r(\mathcal{R}) + b(\mathcal{B}) + g(\mathcal{G}), \qquad (viii)$$

where we have made the substitutions

$$r = \frac{\mathcal{R}}{\mathcal{R}+\mathcal{G}+\mathcal{B}}, \quad g = \frac{\mathcal{G}}{\mathcal{R}+\mathcal{G}+\mathcal{B}}, \quad b = \frac{\mathcal{B}}{\mathcal{R}+\mathcal{G}+\mathcal{B}} \quad . \qquad (ix)$$

The coefficients r, g and b are called chromaticity co-ordinates, and since we now have

$$r + g + b = 1, \qquad (x)$$

it can be seen that only two chromaticity co-ordinates are required

to completely specify a colour. Colours are represented graphically, in terms of their chromaticity co-ordinates, on the chromaticity diagram of the International Commission of Illumination (CIE), (see fig 5.1(b)). The area enclosed by the solid line in fig 5.1(b) represents the locus of all possible colours. Also shown on the diagram are the He-Cd visible laser transition wavelengths. The area bounded by the dashed lines, which join the He-Cd laser wavelength points, encloses all the hues which may be reproduced on a He-Cd three colour laser system (likewise for any other three wavelengths). Note that since the sides of the locus of all possible hues are convex, no combination of three colours can produce all possible hues, without resorting to negative coefficients.

A three-colour He-Cd laser system would be capable of producing most of the hues on the chromaticity diagram, and thus much of the research involving He-Cd lasers has been devoted to the development of a sealed-off device with long life and stable three colour oscillation characteristics. An important component part of such a device is the three colour optical cavity consisting of a broadband "total" reflector and output coupler. An output coupler with reflectivity characteristics which were optimised for each of the three colours would be particularly useful. Difficulty has been experienced in the past by other workers in fulfilling this requirement (eg, Wang, 1980).

In this chapter, the novel application of a flow-graph method to the analysis of optical boundaries is developed, and the results obtained are verified by comparison with more conventional techniques such as ray summation and matrix

methods. The multilayer designs of a broadband total reflector and output couplers based on the flow graph model are then presented.

5.2 Introduction to the Flow Graph Model.

(Source: Adam, 1969)

In analysing general transmission and reflection problems, it is often useful to represent a given network as a "black-box", or as a collection of black boxes, each of which has a linear reflection coefficient on the signal. Using this representation, the contents of the box are unimportant, and only the effect the box has on an applied signal need be considered. Thus, a simple two port network may be represented as a black box (fig 5.2(a)). This simple representation may be transformed to a flow graph representation by noting that if a signal is applied to the input port, then it may be partly transmitted and partly reflected. The same applies to the output port. The flow graph representation is shown in fig 5.2(b), where there are two "nodes" for each port, one for the incident signal and the other for the reflected signal for that port. The incident nodes are termed the "a" nodes and the reflected nodes are termed the "b" nodes. The corresponding incident and reflected signal amplitudes are denoted by a_1 and b_1 respectively. In fig 5.2(b), where the incident signal enters the device at node a_1, the fraction k_{11} is returned along the k_{11} path and leaves the network via b_1. The remainder of the signal continues along the k_{21} path to the

b_2 node.

If another network having reflections associated with its input is connected to the output port of fig 5.2(b), then part of the signal leaving the b_2 node will be returned, due to these reflections, via the a_2 node. Part of this return signal may then be reflected back out of the network via the k_{22} path and b_2 node, and part may be transmitted along the k_{12} path to the b_1 node. Continuity at the nodes gives the following equations,

$$b_2 = a_2 k_{22} + a_1 k_{21} , \qquad (5.1)$$

$$b_1 = a_1 k_{11} + a_2 k_{12} . \qquad (5.2)$$

From equations like (5.1) and (5.2), a system of simultaneous equations describing the signal-flow in a network can be derived and solved.

5.3 Reflectivity of a Simple Glass Plate.

The reflectivity of a simple glass plate, with parallel plane surfaces, is derived by using the flow graph model to develop a system of simultaneous equations. The reflectivity is also calculated using a ray-summation technique and the result of this method is compared to that obtained using flow graphs.

5.3.1 Flow Graph Method.

In using flow graphs to analyse a simple glass plate, each optical boundary is represented by a two port network, as outlined above. Each port is assigned two nodes, one for the incident optical wave and the other for the reflected optical wave. The flow graph for a glass plate with plane parallel surfaces is illustrated in fig 5.3. The optical thickness of the glass is represented by the factor $e^{i\phi}$ where ϕ is given by,

$$\phi = \frac{2\pi}{\lambda} n_g t_g \quad , \qquad (5.3)$$

where λ is the wavelength of the incident light, n_g is the refractive index of the glass, and t_g the thickness of the glass plate. Thus the interconnecting pathways between each optical boundary of the two port network take the value $e^{i\phi}$.
The remaining pathways are represented by "k" parameters which are simply the Fresnel coefficients for reflection. Thus using

$$n = \frac{n_g}{n_a} \quad , \quad n' = \frac{n_a}{n_g} \quad , \qquad (5.4)$$

where n_a is the refractive index of air, the pathway values are given by the following

$$k_{11} = \frac{1-n}{1+n} \quad ,$$

$$k_{12} = \frac{2}{1+n'} = 1 - k_{11} \quad ,$$

$$k_{21} = \frac{2}{1+n} = 1 + k_{11} \quad ,$$

$$k_{22} = \frac{1 - n'}{1 + n'} = - k_{11} \quad , \tag{5.5}$$

for normal incidence. Phase changes of 180 ^{o} incurred by reflection from a rare-to-dense boundary are thus accounted for by the sign which the Fresnel coefficients take in accordance with eqs(5.5).

Use of continuity equations similar to eqs (5.1) and (5.2) yields the following simultaneous equations

$$b_1 = a_1 k_{11} + a_2 k_{12} \quad , \tag{5.6}$$

$$b_2 = a_1 k_{21} + a_2 k_{22} \quad , \tag{5.7}$$

$$a_2 = B_1 e^{i\phi} \quad , \tag{5.8}$$

$$B_1 = k_{22} A_1 \quad , \tag{5.9}$$

$$A_1 = b_2 e^{i\phi} \quad , \tag{5.10}$$

from which an expression for the complex ratio of reflected to incident amplitudes $\frac{b_1}{a_1}$ is obtained. Using eqs (5.8), (5.9) and (5.10) yields

$$a_2 = B_1 e^{i\phi} = k_{22} A_1 e^{i\phi} = k_{22} b_1 e^{2i\phi} \tag{5.11}$$

and thus, we have

$$b_2 = \frac{a_2}{k_{22} e^{2i\phi}} \tag{5.12}$$

Using eq (5.12) to eliminate b_2 from eq (5.7) yields

$$a_2 = \frac{k_{21}\, k_{22}\, a_1\, e^{2i\phi}}{1 - k_{22}^{\,2}\, e^{2i\phi}} \quad , \qquad (5.13)$$

which, when substituted in eq (5.6), yields an expression for the complex ratio of reflected to incident amplitudes,

$$\frac{b_1}{a_1} = k_{11} + \frac{k_{12}\, k_{21}\, k_{22}\, e^{2i\phi}}{1 - k_{22}^{\,2}\, e^{2i\phi}} \qquad (5.14)$$

Finally, using the relationship in eq (5.5) between the Fresnel coefficients for normal incidence, and defining $\Theta = 2\phi$, eq (5.14) simplifies to yield

$$\frac{b_1}{a_1} = \frac{k_{11}(1 - e^{i\Theta})}{1 - k_{11}^{\,2}\, e^{i\Theta}} \qquad (5.15)$$

The reflectivity is then defined as

$$R = \left| \frac{b_1}{a_1} \right|^2 \qquad (5.16)$$

which, together with eq (5.15), yields

$$R = \frac{2k_{11}^{\,2}\,(1 - \cos\Theta)}{1 - 2k_{11}^{\,2}\cos\Theta + k_{11}^{\,4}} \qquad (5.17)$$

The intervening algebraic steps, between eqs (5.15) and (5.17) are given in Appendix Four.

5.3.2 Ray Summation Method.

The validity of eq (5.12) may be verified using a more conventional ray summation technique. Figure 5.4 illustrates the multiple reflections resulting from a wave normally incident on a glass plate, where the diagram has been drawn for clarity such that the rays do not appear superimposed. The Fresnel coefficients k are the same as defined in eq (5.5) as is the phase angle ϕ.

The total amplitude of the reflected wave, with $\Theta = 2\phi$, is given by

$$\tau_t = k_{11} + k_{12} k_{21} k_{22} e^{i\Theta} + k_{12} k_{21} k_{22}^{3} e^{2i\Theta} + \cdots \quad (5.18)$$

Using eqs(5.5), this becomes

$$\tau_t = k_{11} - (1-k_{11}^{2})(k_{11} e^{i\Theta} + k_{11}^{3} e^{2i\Theta} + \cdots) \quad (5.19)$$

Summation of this geometrical progression yields

$$\tau_t = \frac{k_{11} - k_{11} e^{i\Theta}}{1 - k_{11}^{2} e^{i\Theta}} \quad (5.20)$$

which is identical to eq (5.15), and thus the reflectivity is given by

$$R = \frac{2k_{11}^{2}(1-\cos\Theta)}{1 - 2k_{11}^{2}\cos\Theta + k_{11}^{4}} \quad (5.21)$$

which is the same as eq (5.17).

5.4 Topographical Resolution of Flow Graphs.

Equation (5.15) above, for the complex ratio of reflected to incident amplitudes, was derived by solving a system of simultaneous equations. This was readily achieved because the number of equations was small. However, for cases where there are a large number of optical boundaries, the number of equations to be handled becomes large. Fortunately, this number can be reduced by applying a topographical method to the flow graph representation. The approach uses only four basic rules which are stated and proved below, and which enable a solution to be obtained without solving the relevant simultaneous equations.

RULE 1: Node Elimination.

Two branches, or pathways, whose common node has only one incoming and one outgoing branch, or pathway, (branches in series) may be combined to form a single branch whose coefficient is the product of the coefficients of the original branches. Thus the common node is eliminated, as illustrated in fig 5.5. The proof arises from the equations

$$E_3 = k_B E_2 , \quad E_2 = k_A E_1 \tag{5.22}$$

and, thus, by substitution,

$$E_3 = k_A k_B E_1 \tag{5.23}$$

RULE 2. Branch Elimination.

Two branches pointing from a common node (branches in parallel) may be combined into a single branch whose coefficient is the sum of the coefficients of the original branches (fig 5.6). The proof is obvious from the equation

$$E_2 = k_A E_1 + k_B E_1 = (k_A + k_B) E_1 \qquad (5.24)$$

RULE 3. Feedback Loop Elimination.

When a node possesses a self-loop (a branch which begins and ends at that node) of coefficient k_A, the self loop may be eliminated by dividing the coefficient of every other branch entering that node by the factor $(1 - k_A)$. To prove this, from fig 5.7, the following equation may be written

$$E_2 = k_A E_1 + k_B E_2 \qquad (5.25)$$

From this, we get

$$E_2 = \frac{k_A}{1 - k_B} E_1 \qquad (5.26)$$

RULE 4. Node Duplication.

A node may be duplicated (ie. split into two nodes that may be subsequently treated as two separate nodes) as long as the resulting flow graph contains, once and only once, each combination of input and output branches (excepting a branch which forms a self loop) connecting the original node. Any self loop attached to the original node must also be attached to each of the nodes resulting from duplication. From the flow graph on the LHS of fig 5.7, the following equations may be written

$$E_4 = k_C E_3 \quad ,$$

$$E_3 = k_A E_1 + k_B E_2 \quad ,$$

$$\Rightarrow \quad E_4 = k_C (k_A E_1 + k_B E_2) \quad ; \qquad (5.27)$$

and from the flow graph on the RHS of fig 5.7 where node E_3 is duplicated, we may write

$$E_3'' = k_A E_1 \quad , \quad E_3' = k_B E_2 \quad ,$$

$$E_4 = k_C E_3'' + k_C E_3' \quad ,$$

$$E_4 = k_C k_A E_1 + k_C k_B E_2 \quad . \qquad (5.28)$$

A topographical derivation of the expressions for the complex ratio of reflected to incident amplitudes for a simple glass plate is given in fig 5.9, steps (a)-(j). The expression obtained in fig 5.9(j) is algebraically identical to that obtained

by solving simultaneous equations based on eqs (5.1) and (5.2). Note that the topographical solution in fig 5.9(j) also yields an expression for the complex ratio of transmitted to incident amplitudes. As a check on the self-consistency of the flow-graph method, as applied to optical boundaries, it is shown in Appendix Five that R + T = 1.

5.5 Reflectivity of a Simple Thin Film Combination.

The reflectivity of a simple 3-layer structure on a substrate is now derived using the flow graph method, and the results, in the form of a reflectivity against λ graph, are compared with those obtained using the conventional characteristic-matrix approach.

5.5.1 Flow Graph Method.

The structure and corresponding flow graph of the 3-layer mirror are illustrated in figs 5.10 and 5.11 respectively. Figure 5.10 also gives the values of refractive index used in the calculations. Each layer has an optical thickness of $\lambda_o/4$, where λ_o = 500 nm. Reflections from the back surface of the substrate are neglected.

Resolving the flow graph of fig 5.11 topographically

and using the relations between the Fresnel coefficients for normal incidence yields the following simplified expressions

$$C_0 = r_s \,, \tag{5.29}$$

$$C_1 = \frac{-k_{11} + C_0 e^{i\theta}}{1 - k_{11} C_0 e^{i\theta}} \,, \tag{5.30}$$

$$C_2 = \frac{k_{11} + C_1 e^{i\theta}}{1 + k_{11} C_1 e^{i\theta}} \tag{5.31}$$

$$C_3 = \frac{r_a + C_2 e^{i\theta}}{1 + r_a C_2 e^{i\theta}} \tag{5.32}$$

where, we have

$$\theta = \frac{\pi \lambda_0}{\lambda} \,, \quad r_0 = -\left(\frac{n_s - n_H}{n_s + n_H}\right) \,,$$
$$k_{11} = -\left(\frac{n_L - n_H}{n_L + n_H}\right) \,, \quad r_a = -\left(\frac{n_H - n_a}{n_H + n_a}\right) \tag{5.33}$$

Thus, C_3 represents the complex ratio of reflected to incident amplitudes for the 3-layer structure. The reflectivity, $R = |C_3|^2$, is shown as a function of λ in fig 5.12 The calculations of reflectivities were computed using the St. Andrews University Digital VAX/VMS computer.

5.5.2 Characteristic Matrix Approach.

In the conventional matrix approach to thin film analysis, the k^{th} layer in the stack has a characteristic matrix given by

$$M_k = \begin{bmatrix} \cos\theta_k & i\, n_k \sin\theta_k \\ -i\, n_k \sin\theta_k & \cos\theta_k \end{bmatrix}, \qquad (5.34)$$

where n_k is the refractive index of the k^{th} layer, $i = \sqrt{-1}$, and θ_k is given by

$$\theta_k = \frac{\pi \lambda_0}{2 \lambda}, \qquad (5.35)$$

for layers with an optical thickness of $\lambda_0/4$.

The principles underlying the matrix representation are considered in many text books on light (Born and Wolfe, 1965; Maitland and Dunn, 1968; Fowles, 1975) and will not be discussed here. The characteristic matrix for the whole stack is then given by

$$M_c = M_1 * M_2 * M_3, \qquad (5.36)$$

where $*$ denotes matrix multiplication. The transmitted flux is then given by

$$T = 1 - R = \frac{4}{2 + \frac{n_0}{n_s} C_{11}^2 + \frac{n_s}{n_0} C_{22}^2 + \frac{1}{n_0 n_s} C_{21}^2 + n_0 n_s C_{12}^2} \qquad (5.37)$$

where, we have

$$M_c = \begin{bmatrix} C_{11} & i C_{12} \\ i C_{21} & C_{22} \end{bmatrix} \tag{5.38}$$

Thus the characteristic matrix for the 3-layer stack illustrated in fig 5.10 is

$$M_c = \begin{bmatrix} A & i \frac{B}{n_H} \\ i n_H B & A \end{bmatrix} \begin{bmatrix} C & i \frac{D}{n_L} \\ i n_L D & C \end{bmatrix} \begin{bmatrix} A & i \frac{B}{n_H} \\ i n_H B & A \end{bmatrix} \tag{5.39}$$

where A , B , C and D are related by

$$A = C = \cos \frac{\pi \lambda_o}{2 \lambda} \quad , \quad B = D = \sin \frac{\pi \lambda_o}{2 \lambda} \tag{5.40}$$

Carrying out the multiplication in eq (5.39) yields

$$\begin{aligned} C_{11} &= A - AB \left(1 + \frac{n_L}{n_H} + \frac{n_H}{n_L} \right) = C_{22} \, , \\ C_{21} &= AB \left(\frac{1}{n_L} + \frac{2}{n_H} \right) - B \frac{n_L}{n_H} \, , \\ C_{12} &= AB \left(n_H + 2 n_L \right) - B \frac{n_L}{n_H} \, . \end{aligned} \tag{5.41}$$

From eqs (5.41) and (5.37), the reflectivity R may be calculated. The results obtained using the matrix approach are identical with those obtained using the topographically resolved flow graph for this simple 3-layer structure.

5.6 Reflectivity of Multilayer Mirrors.

The flow graph calculations undertaken so far have been for relatively simple problems where the number of optical boundaries has been small. However, for high reflectivity laser mirrors over an extended spectral region, the number of optical boundaries required to give the desired results is larger. In the next section, for example, it is found that broad band laser mirrors for He-Cd hollow cathode lasers require upwards of 20 layers. The flow graphs for such mirrors are cumbersome and their step-by-step resolution is tedious. It may be noted, however, from the previous examples using flow graphs, that the topographical method yields characteristic flow graph parameters of the form

$$C_m = \frac{k_m + C_{m-1} e^{i\theta_m}}{1 + k_m C_{m-1} e^{i\theta_m}} \qquad (5.42)$$

for the m^{th} optical interface, numbered from the substrate where $m = 0$ to the last layer, where m is the number of layers. In this case, the relevant Fresnel coefficient is given by

$$k_m = -\left(\frac{n_m - n_{m+1}}{n_m + n_{m+1}}\right) \qquad (5.43)$$

and the phase term is is given by

$$\theta_m = \frac{4\pi}{\lambda} t_m \qquad (5.44)$$

where t_m is the optical thickness of the m^{th} layer. The characteristic flow graph parameter for the m^{th} layer is

C_m. The refractive indices of the m^{th} and $(m+1)^{th}$ layers are n_m and n_{m+1}, respectively. Complicated layer structures having many optical boundaries may thus be resolved using eq (5.42) without having to write down and resolve the flow graph for the particular case.

5.7 Broad Band Mirrors For He-Cd Lasers.

The designs presented below, for a broad band total reflector and two output couplers, are based upon the superposition of three multilayer dielectric stacks. Each stack consists of a different number of $\lambda_o/4$ layers, where the three values of λ_o correspond approximately to the three primary colours of He-Cd. For convenience, the design method we shall use is based on a "trial and error" method of calculation. This arises because, although the reflectivity of a given layer structure may be readily calculated, the inverse process is not easily performed. In other words, it is very difficult to calculate the layer structure required if the desired reflectivity characteristics are given as initial data. The problem is further complicated since under certain conditions two quarter wave stacks at λ_{o1} and λ_{o2} may give rise to deep interference minima in the reflectivity characteristics, depending on the values of λ_{o1} and λ_{o2} chosen. It is therefore essential, in practice, to develop a method of calculation, using eq (5.42), in which the given layer structure may be altered readily and results quickly reviewed.

This was achieved using the local Digital VAX/VMS computer. Based on quarter wavelength stacks where $n_H = 2.3$, $n_L = 1.38$, $n(\text{substrate}) = 1.5$ and $n(\text{air}) = 1.0$, subroutines were written for each kind of boundary that may arise in the final layer structure. The calculation thus consists of a series of calls to the various subroutines. The labelling of each subroutine was chosen to enable the composition of the layer structure to be easily reviewed and altered. The different types of optical boundary which may arise, together with the relevant subroutine names describing each boundary, are as shown in Table 5.1. It can be seen that this method of programming, together with the chosen nomenclature, enables layer structures to be easily altered and results to be quickly reviewed. A sample programme is given in Appendix Six.

The layer structures derived for a broad band total reflector and two different output couplers are shown in figs 5.13, 5.14(a), and 5.14(b). White light laser optics for He-Cd lasers require upwards of 20 layers, where the refractive indices are $n_L = 1.38$ (MgF_2) and $n_H = 2.3$ (ZnS).

5.8 Concluding Remarks

The flow graph technique, which is well established in the field of microwave network analysis (Adam, 1969), has been successfully applied to the analysis of optical interfaces in general, and to thin film laser optics in particular. Based on the equations which arise from the flow graph technique, designs of

broad band optics for He-Cd white light lasers have been presented.

The flow graph model can be modified to account for absorption in optical materials by using the complex form for the refractive index

$$n_c = n(\text{real}) + i\, n(\text{imaginery}) \qquad (5.45)$$

which gives rise to a negative exponential terms in the phase term.

The flow graph model may also be extended for arbitrary angles of incidence by using the general Fresnel coefficients for reflection and transmission instead of the simplified normal incidence coefficients used above.

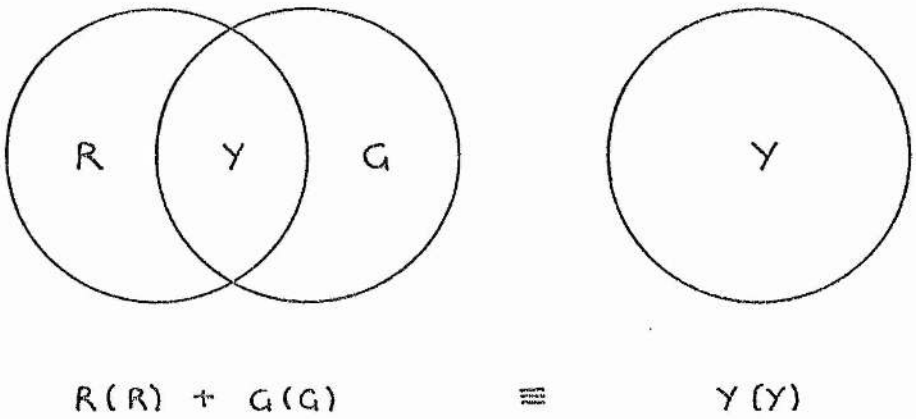

FIG 5.1 (a) COLOURED SPOTLIGHT COMPARISON EXPERIMENT AND EQUIVALENT "COLOUR EQUATION".

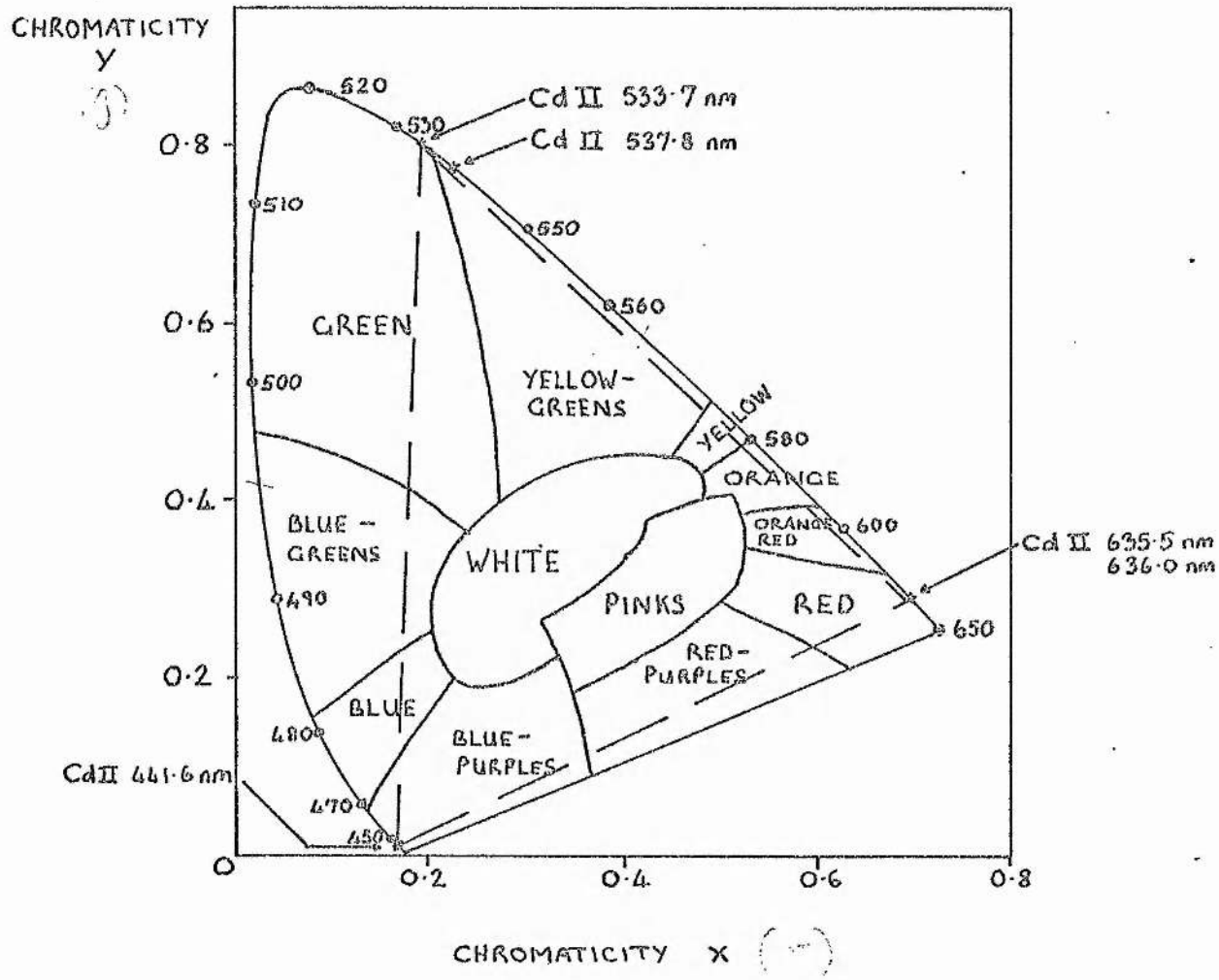

FIG 5.1 (b) CIE CHROMATICITY DIAGRAM SHOWING HUES REPRODUCIBLE ON He – Cd BASED LASER SYSTEM.

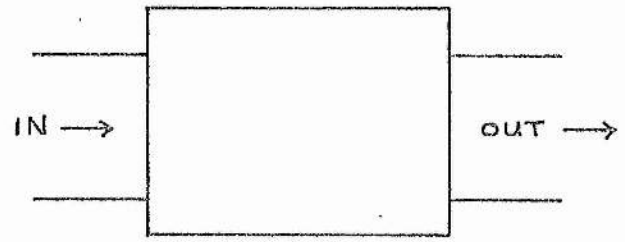

FIG 5.2(a) BLACK BOX REPRESENTATION OF TWO PORT NETWORK

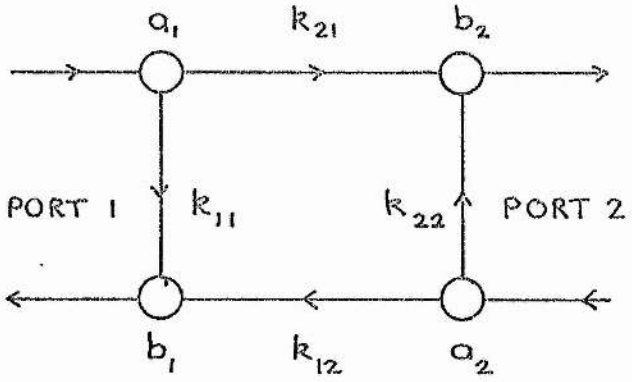

FIG 5.2 (b) FLOW GRAPH REPRESENTATION OF TWO PORT NETWORK

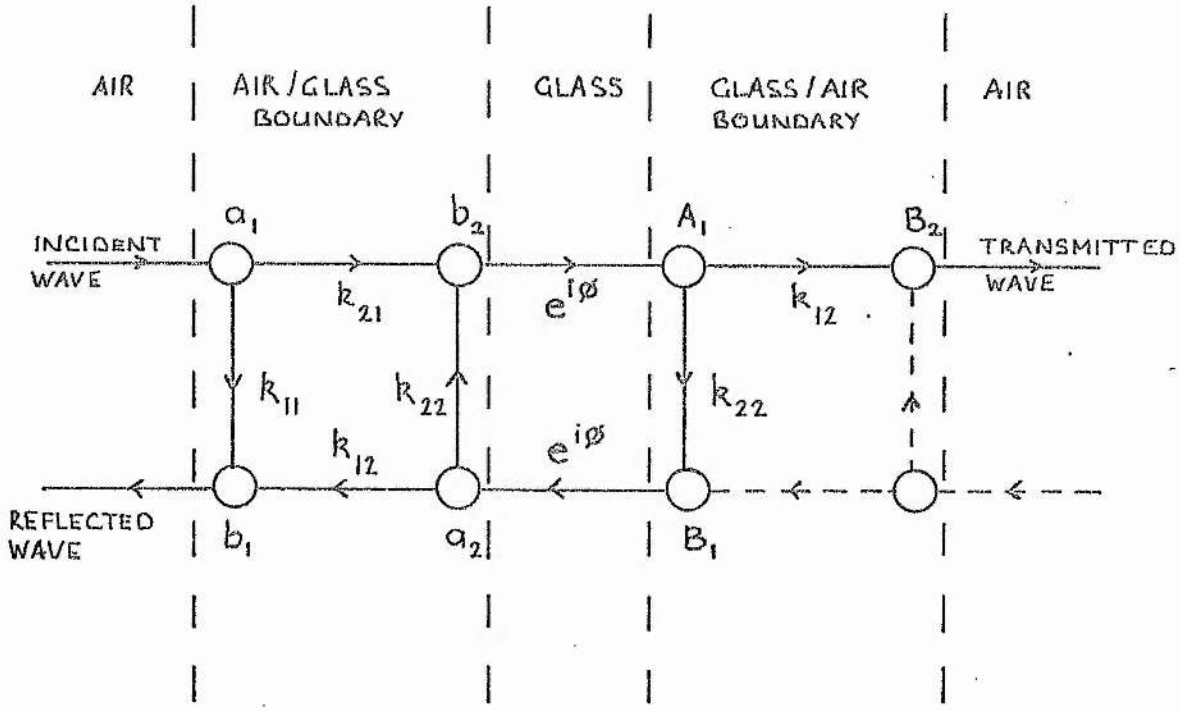

FIG 5.3 FLOW GRAPH FOR GLASS PLATE.

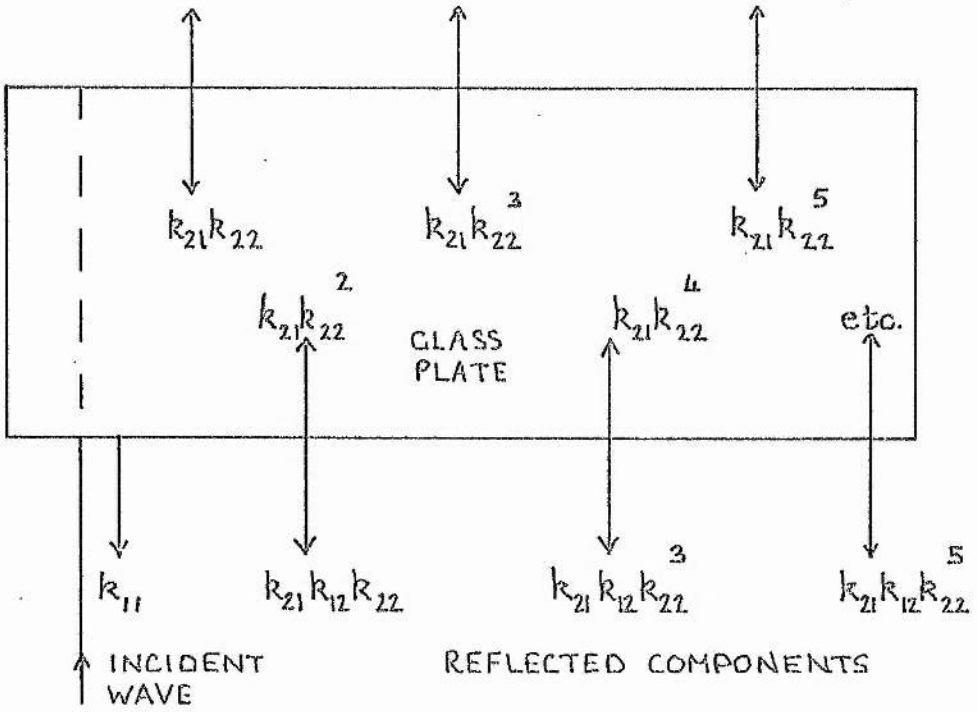

FIG 5.4 MULTIPLY REFLECTED RAYS WITHIN A GLASS PLATE. PHASE TERMS NOT DRAWN.

FIG 5.5 NODE ELIMINATION.

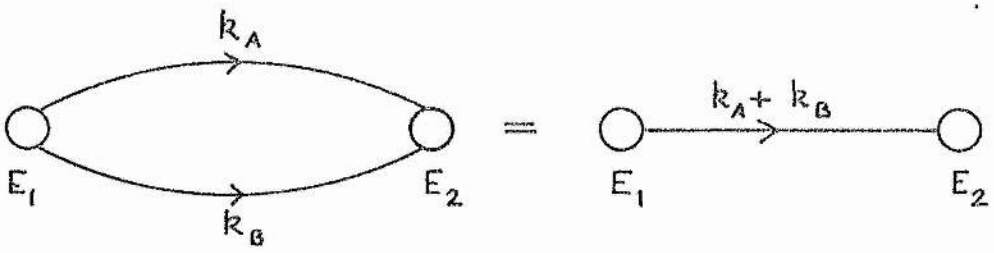

FIG 5.6 BRANCH ELIMINATION.

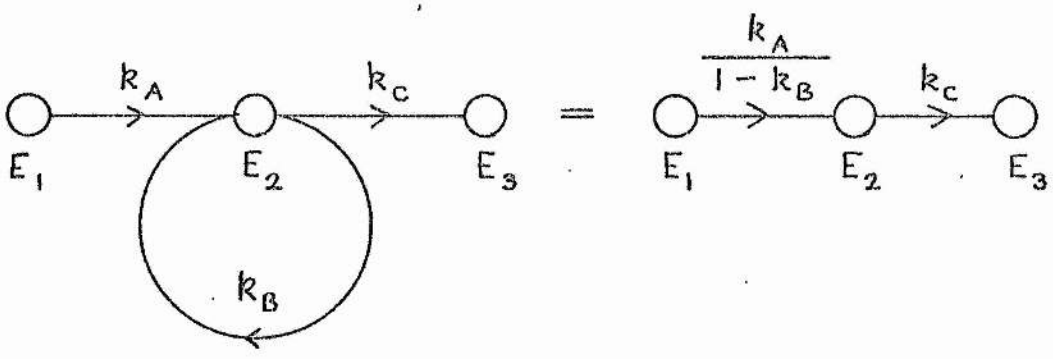

FIG 5.7 FEEDBACK LOOP ELIMINATION.

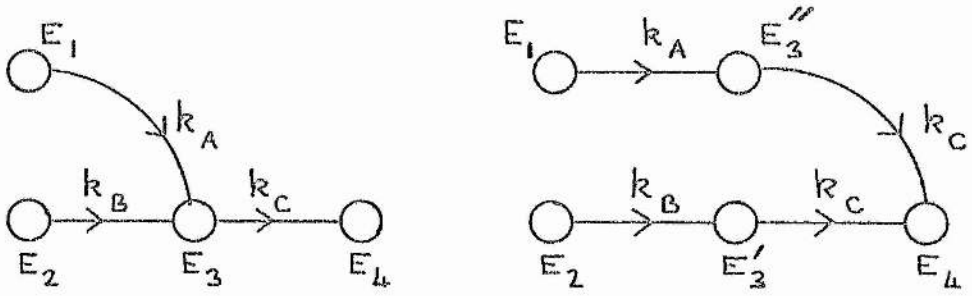

FIG 5.8 NODE DUPLICATION.

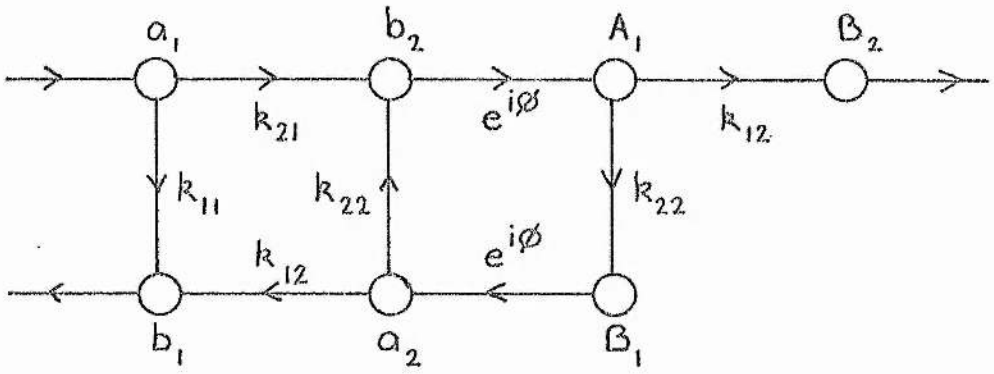

FIG 5.9(a) FLOW GRAPH FOR GLASS PLATE.

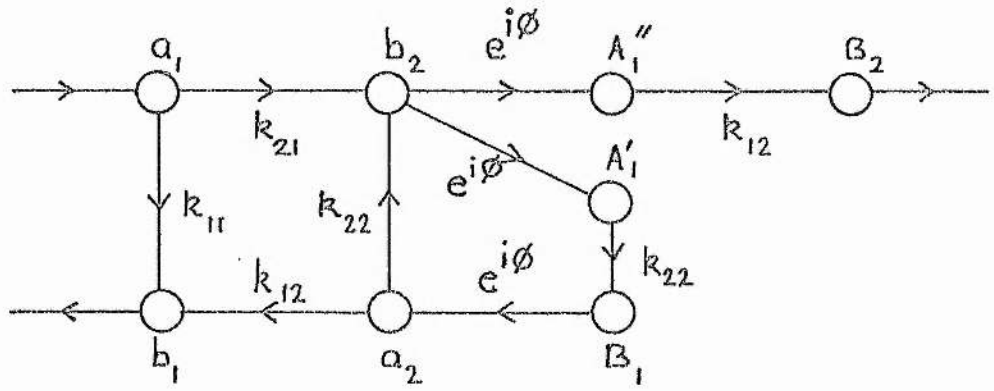

FIG 5.9 (b) DUPLICATION OF NODE A_1.

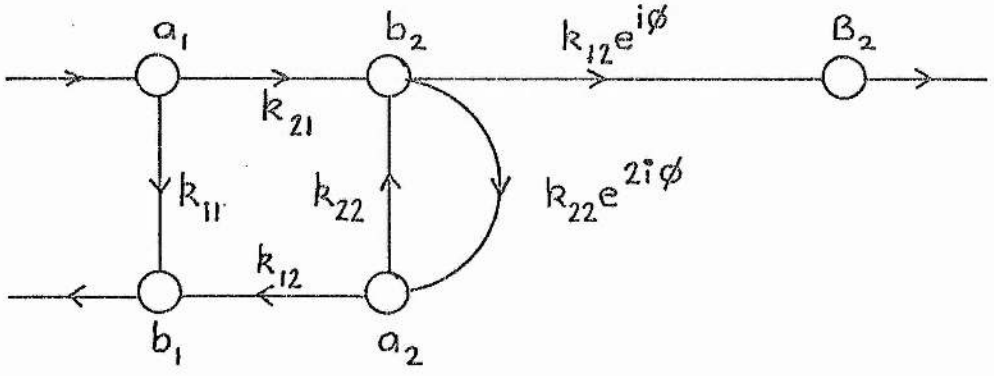

FIG 5.9 (c) ELIMINATION OF NODES A_1', A_1'', B_1.

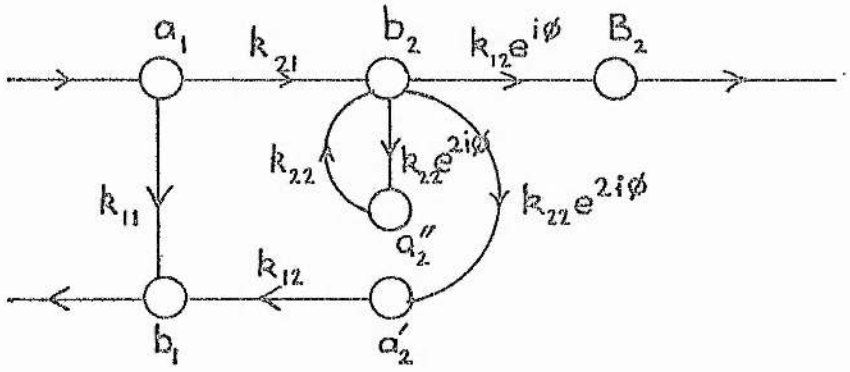

FIG 5.9 (d) DUPLICATION OF NODE a_2 FORMING FEEDBACK LOOP.

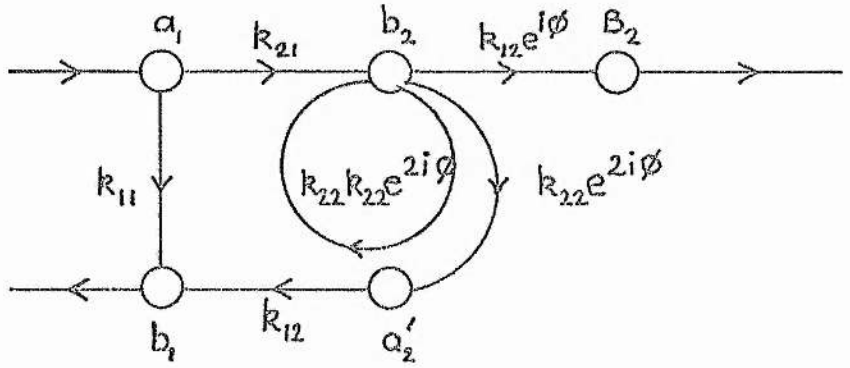

FIG 5.9 (e) ELIMINATION OF NODE a_2''.

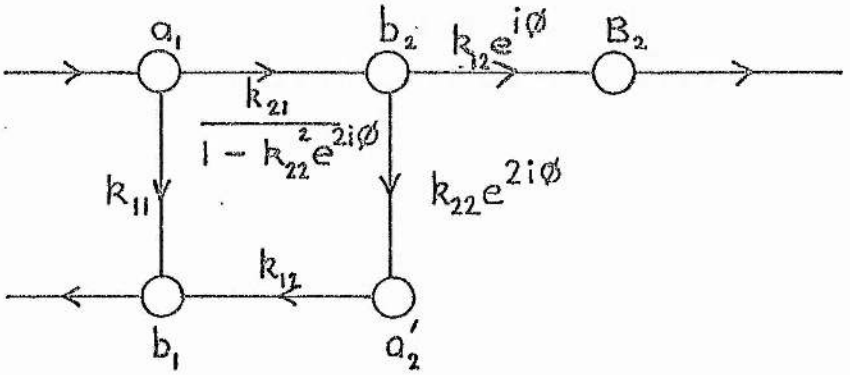

FIG 5.9 (f) ELIMINATION OF FEEDBACK LOOP.

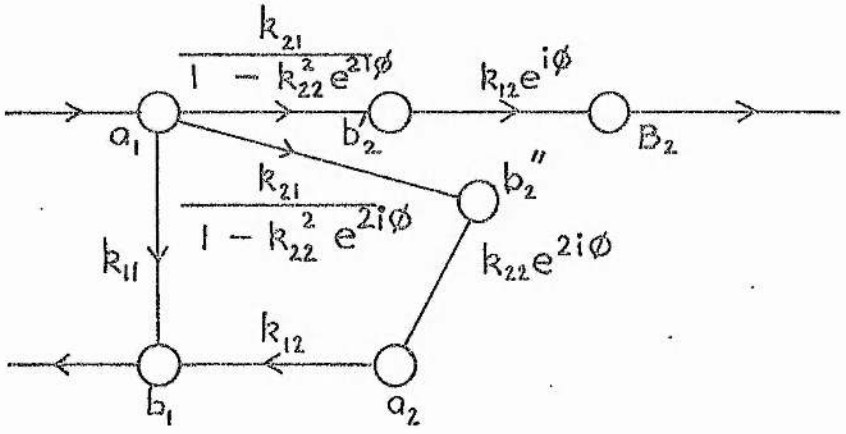

FIG 5.9 (g) DUPLICATION OF NODE b_2.

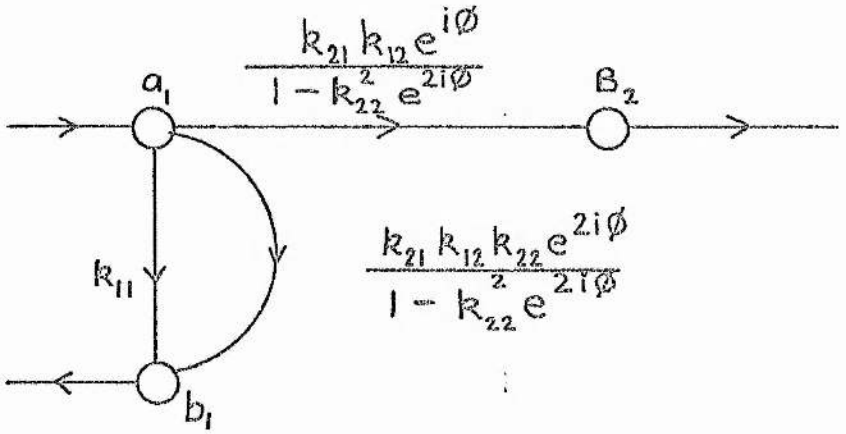

FIG 5.9 (h) ELIMINATION OF NODES b_2', b_2'', a_2.

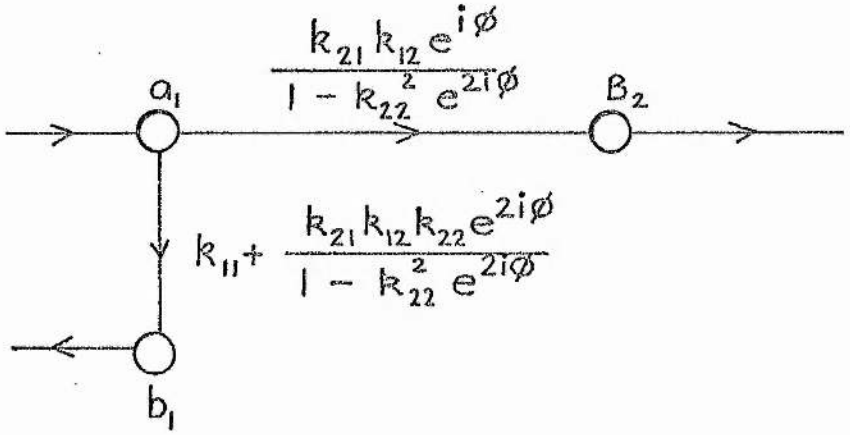

FIG 5.9 (j) BRANCH ELIMINATION.

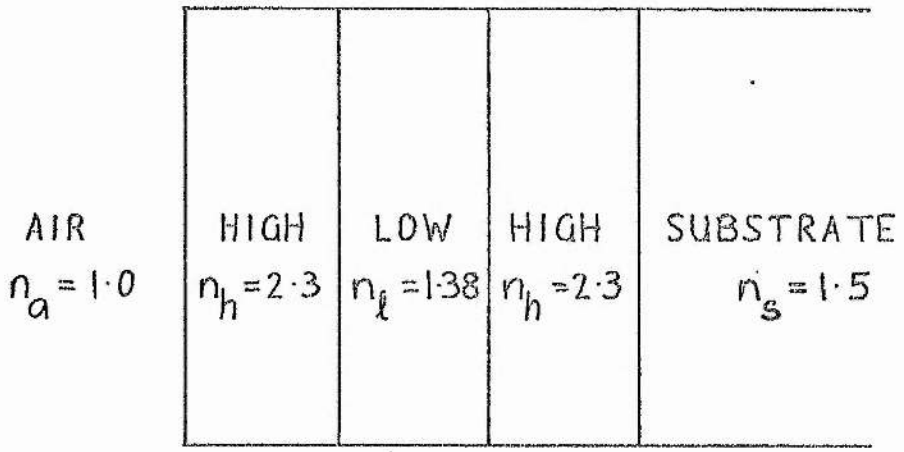

FIG 5.10 THREE LAYER MIRROR STRUCTURE.

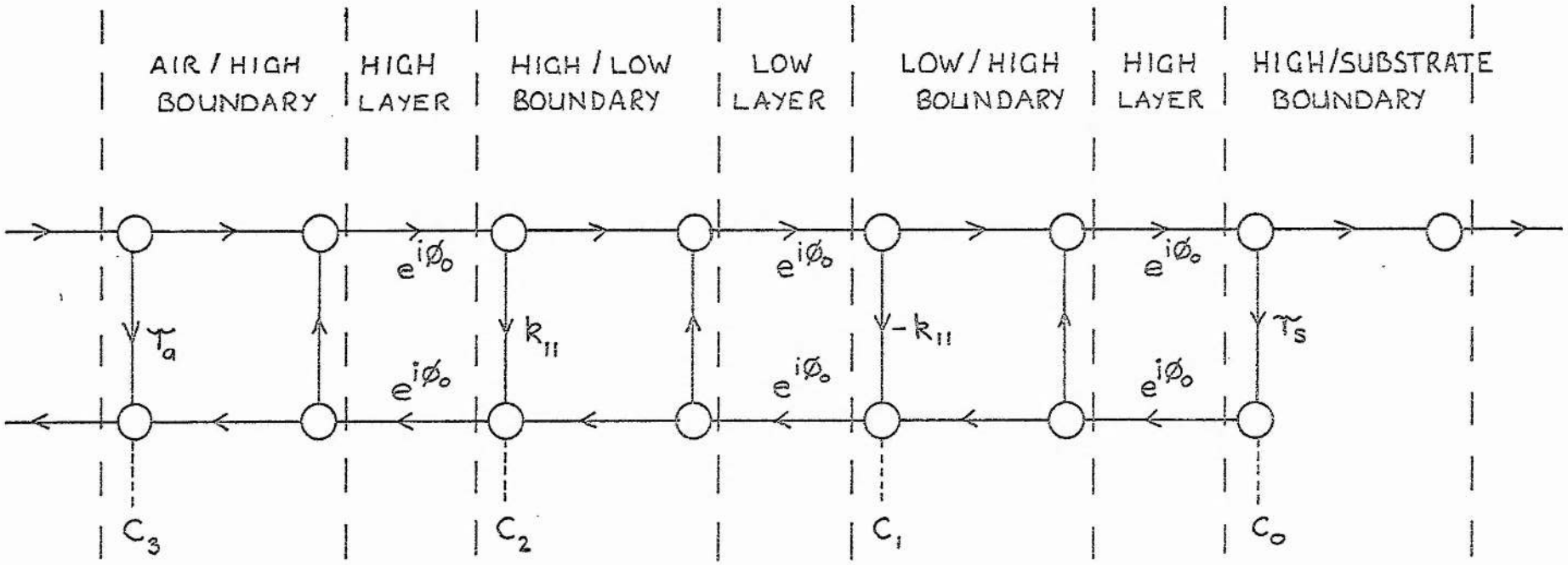

FIG 5.11 FLOW GRAPH FOR THREE LAYER STRUCTURE.

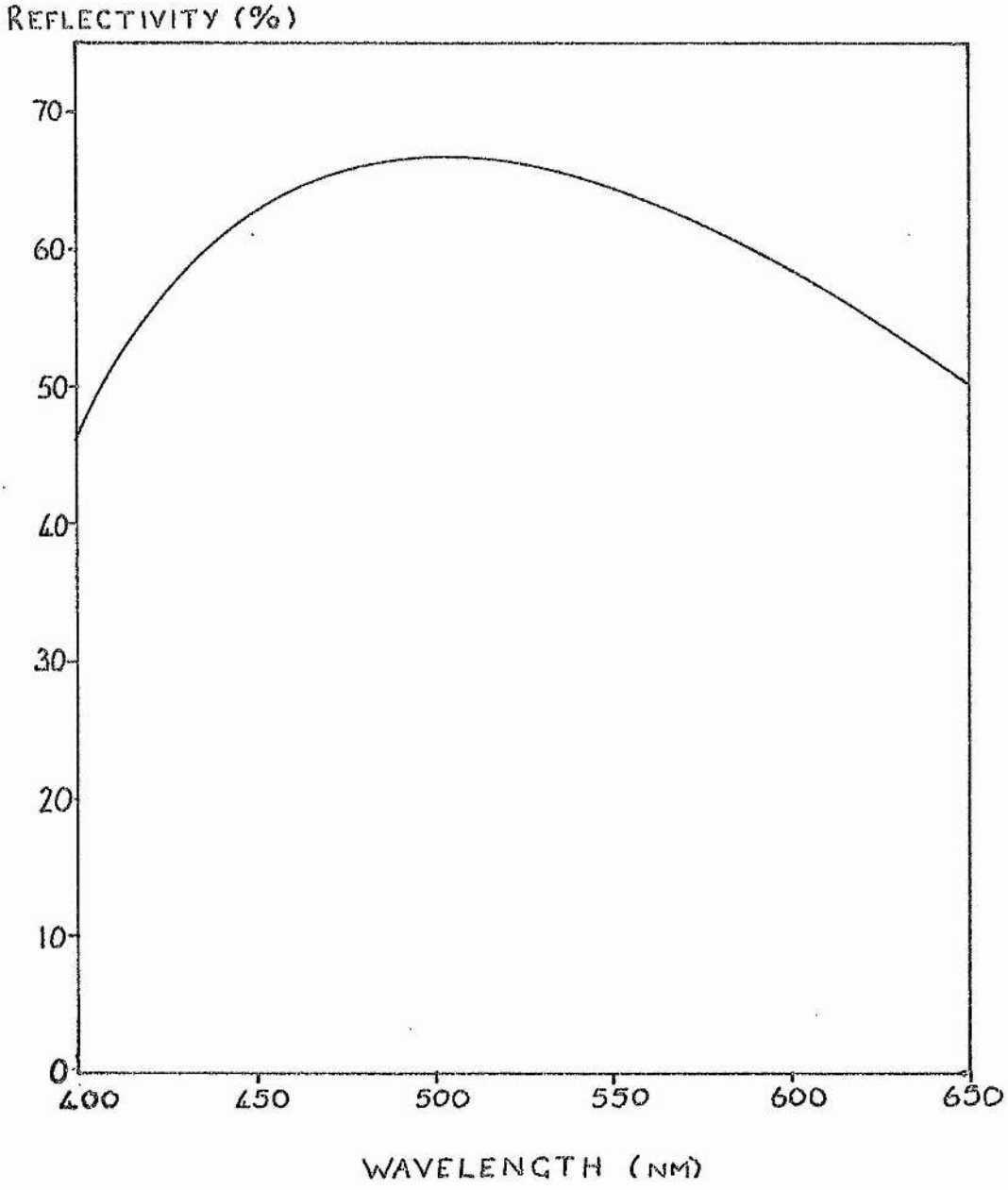

FIG. 5.12 REFLECTIVITY CHARACTERISTICS FOR 3-LAYER STRUCTURE.

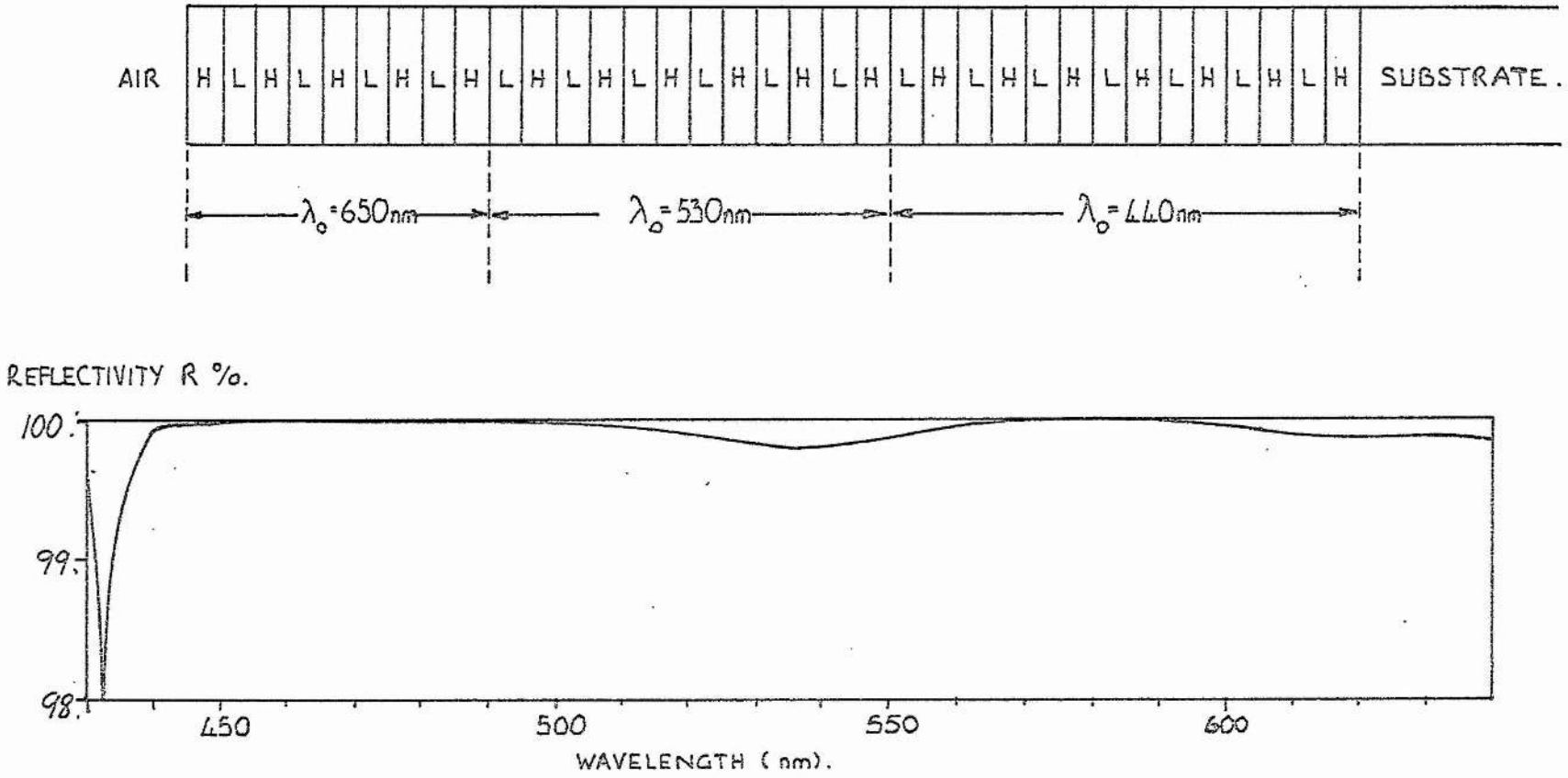
AIR
H L H L H L

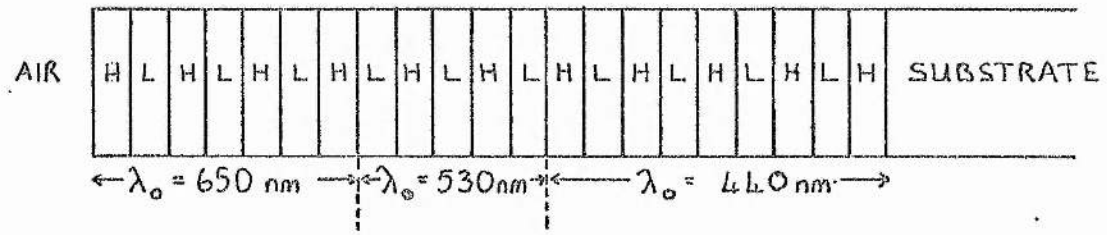

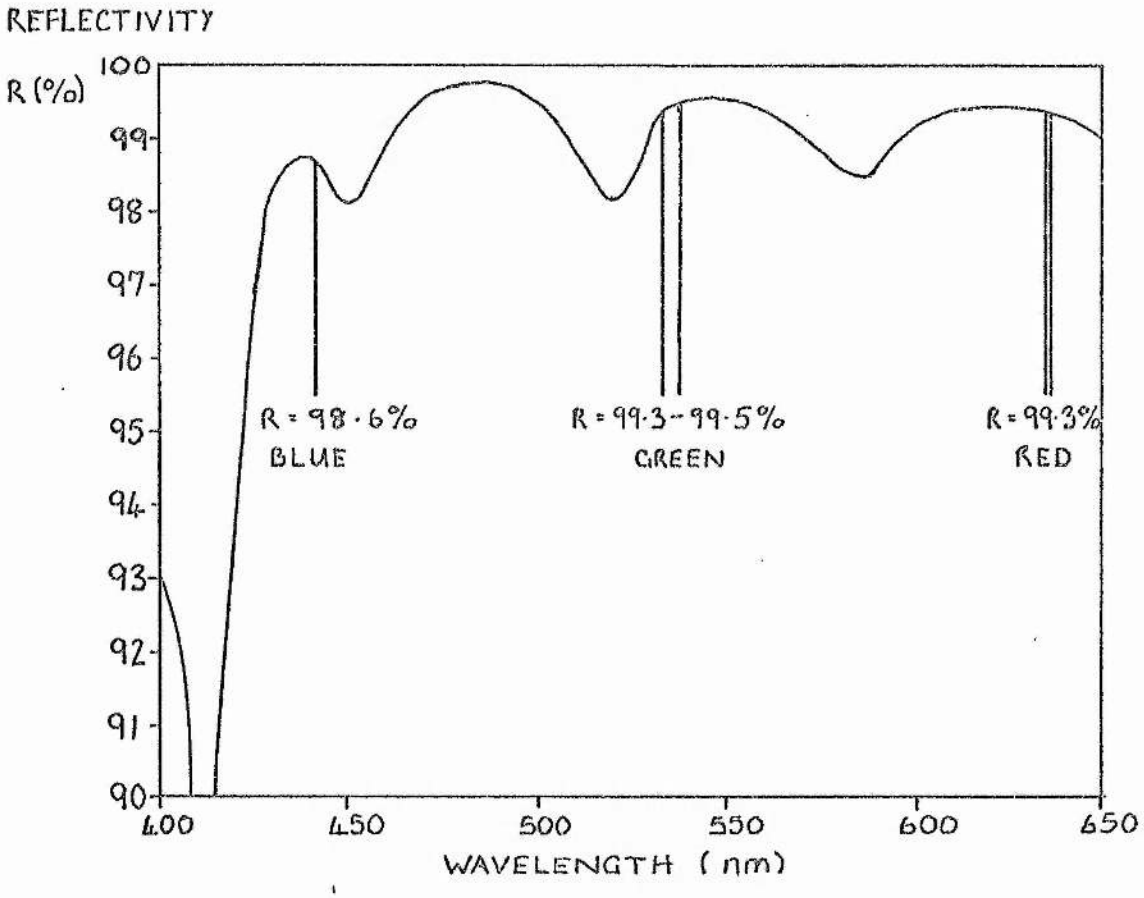

FIG 5.14(a) MULTI-LAYER COMPOSITION AND REFLECTIVITY CHARACTERISTICS FOR He-Cd OUTPUT COUPLER.

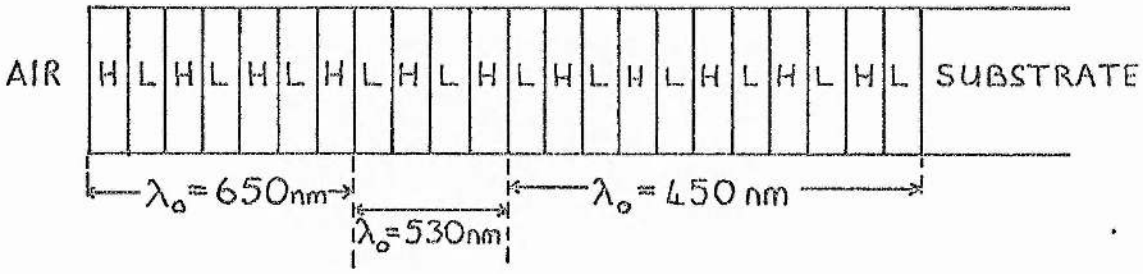

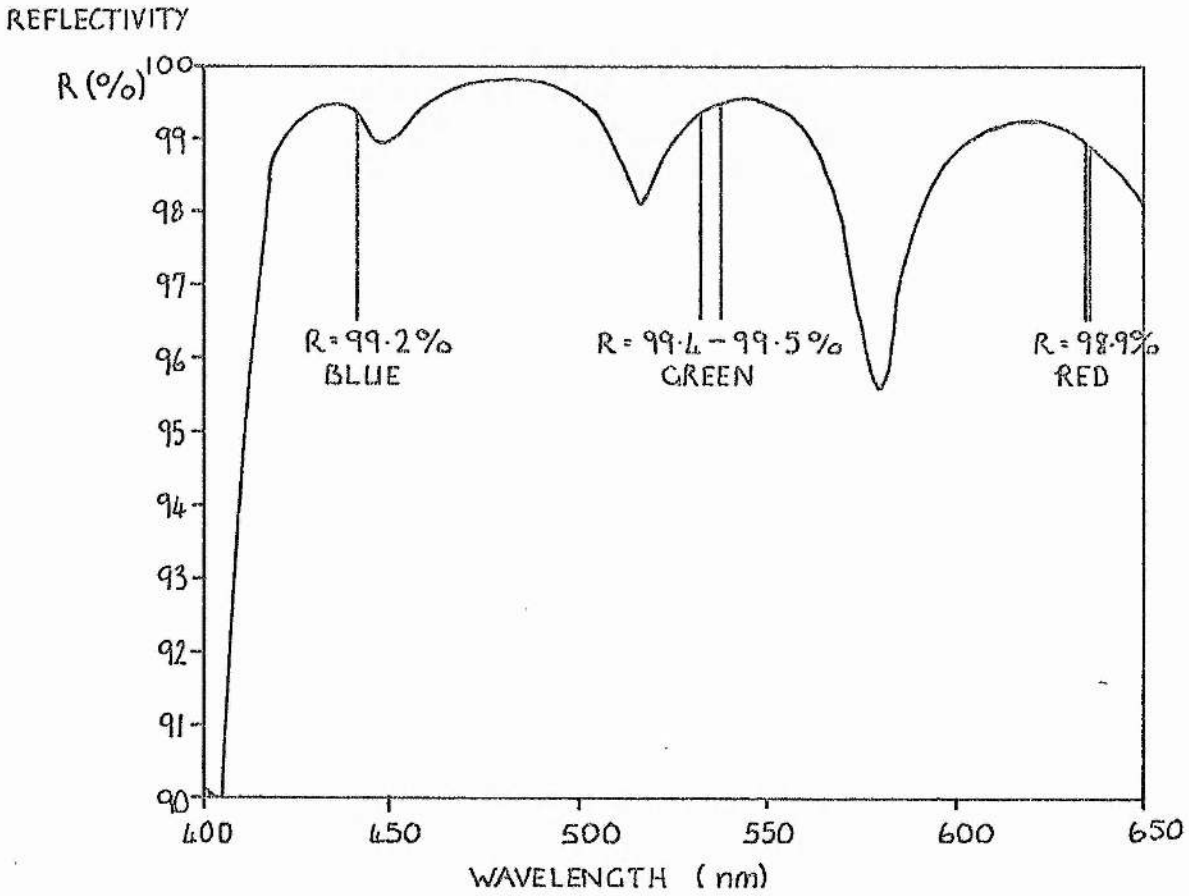

FIG 5.14 (b) MULTI-LAYER COMPOSITION AND REFLECTIVITY CHARACTERISTICS FOR He-Cd OUTPUT COUPLER.

OPTICAL BOUNDARY ENCOUNTERED BY INCIDENT RADIATION	SUBROUTINE NAME
FROM AIR TO LAYER OF HIGH REFRACTIVE INDEX.	AH
FROM AIR TO LAYER OF LOW REFRACTIVE INDEX.	AL
FROM LAYER OF LOW REFRACTIVE INDEX TO LAYER OF HIGH REFRACTIVE INDEX.	LH
FROM LAYER OF HIGH REFRACTIVE INDEX TO LAYER OF LOW REFRACTIVE INDEX.	HL
FROM LAYER OF HIGH REFRACTIVE INDEX TO SUBSTRATE.	HS
FROM LAYER OF LOW REFRACTIVE INDEX TO SUBSTRATE.	LS

TABLE 5.1 OPTICAL BOUNDARIES AND SUBROUTINE NAMES FOR COMPUTER DESIGN OF LASER MIRRORS.

CHAPTER FIVE BIBLIOGRAPHY.

ADAM, S.F.

"Microwave Theory and Applications", Prentice-Hall,1970.

BORN, M. and WOLF, E.

"Principles of Optics", Pergamon (London),1959.

FOWLES, G.R.

"Introduction to Modern Optics", New York,1975.

HAITLAND, A. and DUNN, M.H.

"Laser Physics", Van Nostrand (London and Amsterdam),1969.

WANG, S.C.

Proceedings of the Society of Photo-Optical Instrumentation Engineers,232,42-46,1980, (International Optical Computing Conference, 1980).

APPENDIX ONE

Electronic Temperature Controller

The "electronic thermostat" used for controlling the temperature of cadmium sources and/or cathodes in tubes Nos. 4, 5 and 6, is based on a zero-voltage switch integrated circuit (IC), available from RS Components Ltd., (stock number 305-000). The circuit is illustrated in fig A1.1, where the temperature sensing element is a thermistor, which was mounted in close thermal contact with the heater element. The heater element consists of a length of 34 swg eureka wire, which was covered with high temperature electrically insulating sleeving. The length of the wire depended on the particular application for which the heater was intended, as did several of the component values used in the circuit of fig A1.1. For small heating requirements, (eg, the oven appendage of tube No.4), 50 cm of wire was adequate. For larger heating requirements, (eg, the cathode of tube No.6), up to 500 cm were required. The circuit components and parameters which required alteration for these different applications were the supply voltage V, the load resistance R_l (eureka wire), the series resistance R_s, and the fuse in series with the load. The circuit in fig A1.1 maintains a chosen temperature in the range 250 - 350 ^{o}C, to within $\pm$ 2 ^{o}C.

The circuit operates as follows. The voltage on

pin 2 of the IC is determined by the values of R_V and R_T (senseing thermistor), as illustrated in fig A1.2. The IC compares the voltage on pin 2 with an internally generated ramp voltage, which appears on pin 1 of the IC. When pin 2 is at a lower voltage than the bottom of the ramp, the heater is on, and when pin 2 is at a higher voltage than the top of the ramp, the heater is switched off (see fig A1.3). Voltages on pin 2 lying between the bottom and the top of the ramp produce sufficient bursts of power to the load to make up for thermal losses. The heater is thus continuously turned on and then off again, at the same frequency as the ramp voltage (typically 1 Hz), resulting in maintainence of a stable temperature at the chosen value. A further advantage of this device is that the load is turned on at a zero-voltage point (see fig A1.3), which minimises electromagnetic interference. Further information on the zero-voltage IC is contained in RS data sheet No. 2129.

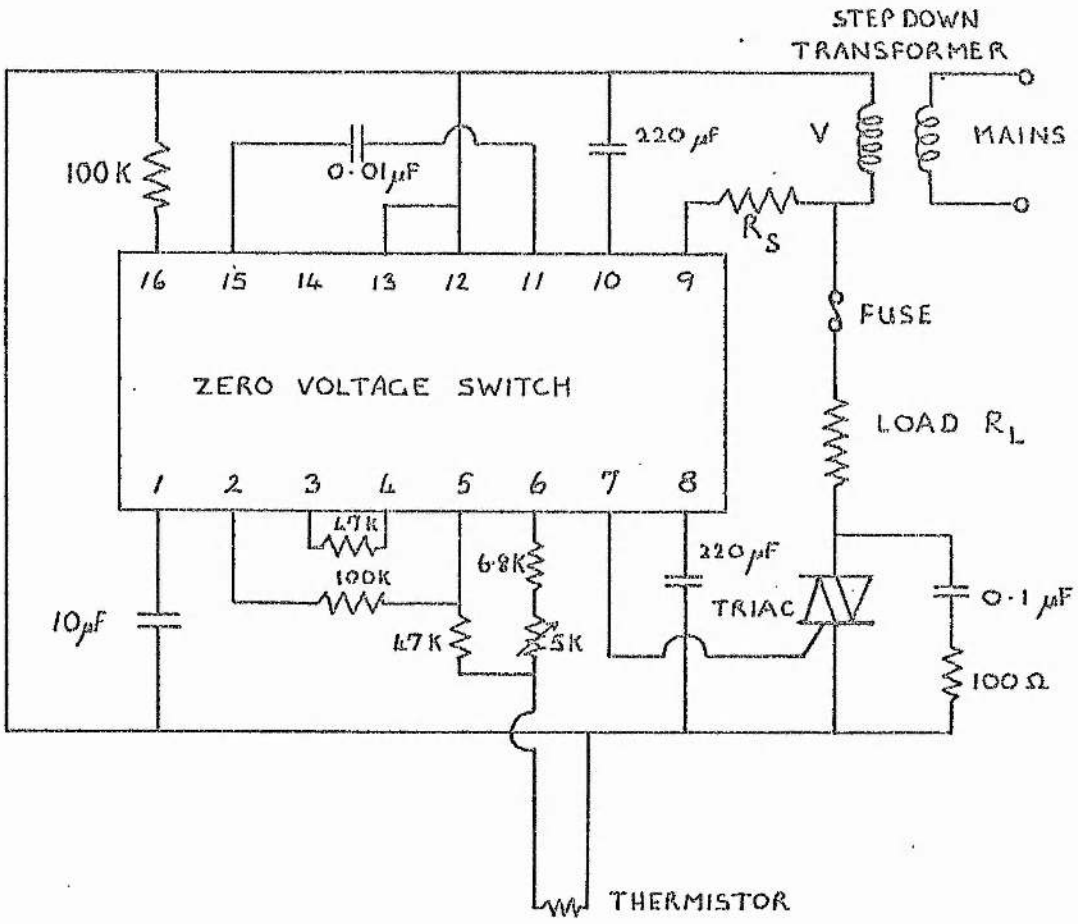

FIG AI.1 CIRCUIT DIAGRAM FOR TEMPERATURE CONTROLLER.

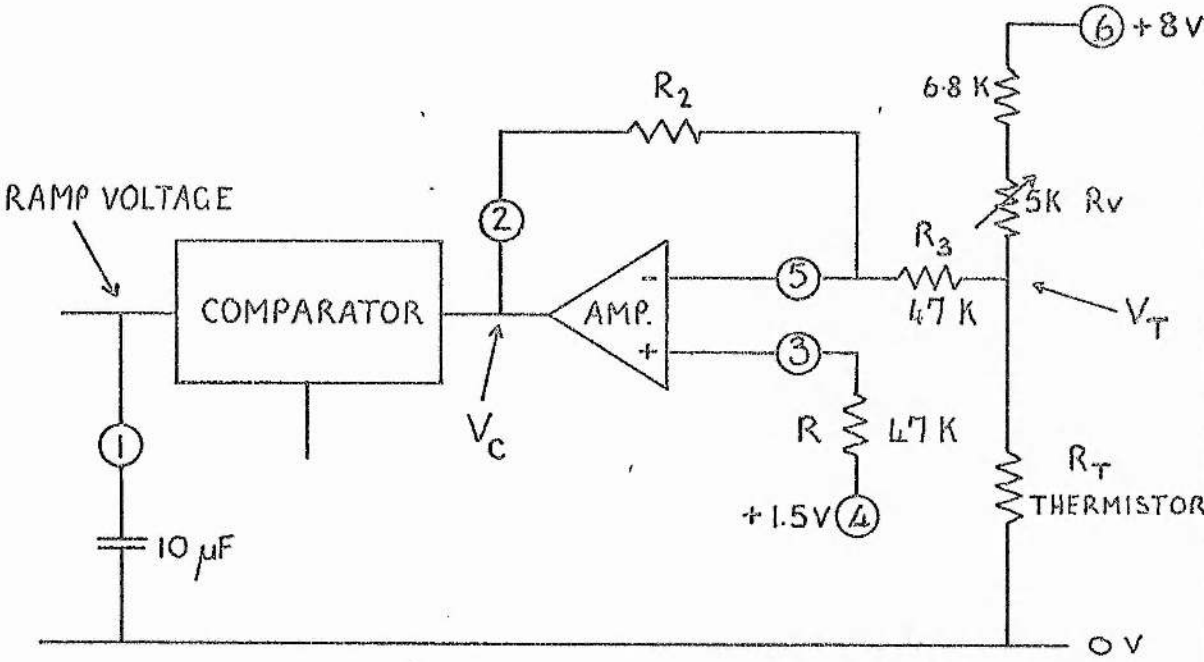

$$V = \frac{R_2}{R_3}(1{\cdot}5 - V_T) \text{ VOLTS}$$

FIG A1.2 TEMPERATURE SENSING CIRCUITRY.

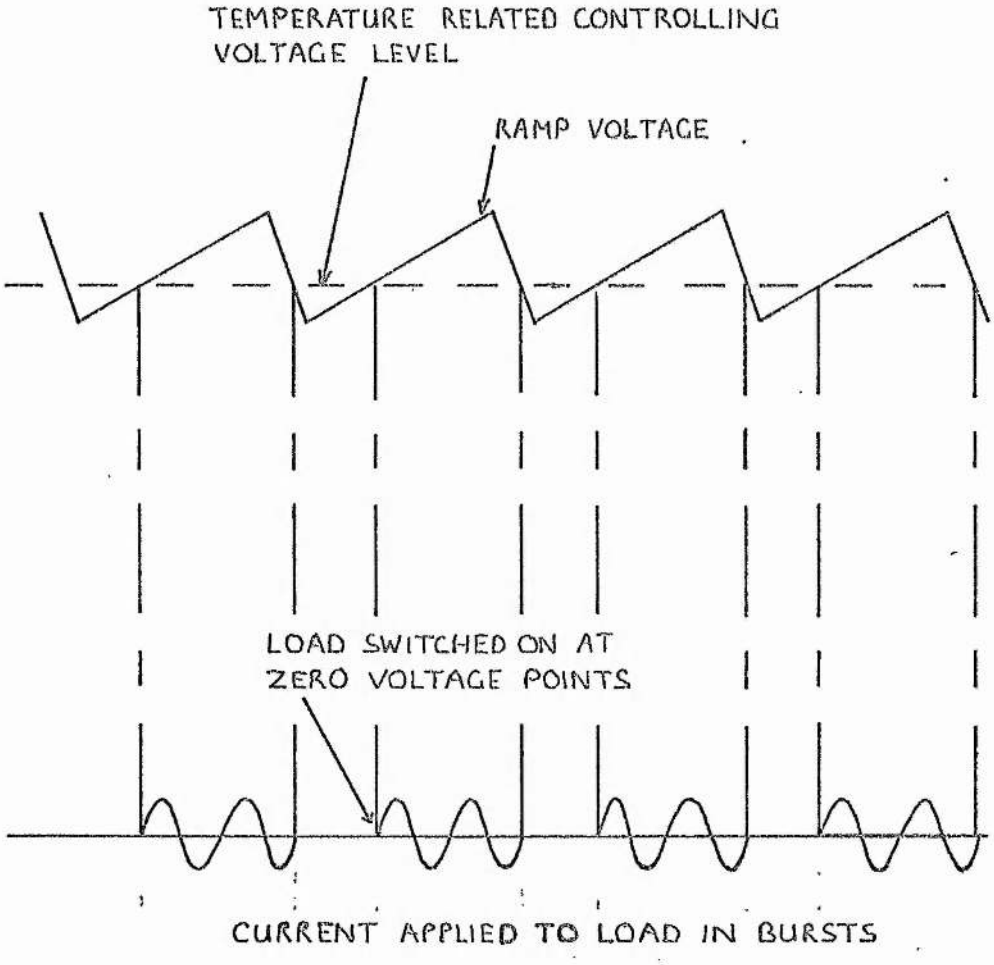

FIG A1.3 PRINCIPLE OF OPERATION OF TEMPERATURE CONTROLLER.

APPENDIX TWO

In Chapter Three, eq (3.15) describes the temperature distribution in a cylindrical conductor as follows,

$$\frac{dt}{dx} = -\sqrt{\left[\left(\frac{dt}{dx}\right)^2_{X=0} + \frac{2a}{5}\left(t^5 - t_H^5 - 5t_o^4 (t - t_H) \right) + \frac{8b}{9}\left((t - t_o)^{9/4} - (t_H - t_o)^{9/4} \right) \right]} \qquad (A2.1)$$

where all of the parameters are as defined in Chapter Three. An expression for $\left(\frac{dt}{dx}\right)_{X=0}$ was obtained as follows,

$$\left(\frac{dt}{dx}\right)_{X=0} = -\sqrt{\left[\frac{2a}{5}\left(t_H^5 - t_c^5 - 5t_o^4 (t_H - t_c) \right) + \frac{8b}{9}\left((t_H - t_o)^{9/4} - (t_c - t_o)^{9/4} \right) \right]} \qquad (A2.2)$$

by assuming that $\left(\frac{dt}{dx}\right)_{x=L} = 0$. If we assume that $\left(\frac{dt}{dx}\right)_{X=L}$ is not equal to zero, then an involved calculation, outlined below, can be undertaken which leads to a value for $\left(\frac{dt}{dx}\right)_{X=0}$ that is numerically the same as that obtained by using eq (A2.2) above.

Equation (3.16) in Chapter Three is the starting point of the calculation,

$$\int_{\left(\frac{dt}{dx}\right)_{x=0}}^{\left(\frac{dt}{dx}\right)_{x=L}} p\, dp = \int_{t_H}^{t_c} a(t^4 - t_o^4) + b(t - t_o)^{5/4}\, dt \qquad (A2.3)$$

Integration of eq (A2.3) yields

$$\left(\frac{dt}{dx}\right)^2_{x=L} - \left(\frac{dt}{dx}\right)^2_{x=0} = S_1 \qquad (A2.4)$$

where we have

$$S_1 = 2\int_{t_H}^{t_c} a(t^4 - t_o^4) + b(t - t_o)^{5/4}\, dt \qquad (A2.5)$$

Equation (A2.4) yields an expression for $\left(\frac{dt}{dx}\right)_{x=0}$ in terms of $\left(\frac{dt}{dx}\right)_{x=L}$, which we have assumed is not equal to zero. We thus seek a second expression involving both $\left(\frac{dt}{dx}\right)_{x=0}$ and $\left(\frac{dt}{dx}\right)_{x=L}$, so that we may eliminate $\left(\frac{dt}{dx}\right)_{x=L}$. To achieve this, we require the differential equation, eq (3.10) in Chapter Three,

$$\frac{d^2t}{dx^2} = a(t^4 - t_o^4) + b(t - t_o)^{5/4} \qquad (A2.6)$$

Integration of eq (A2.6) yields

$$\left(\frac{dt}{dx}\right)_{x=L} - \left(\frac{dt}{dx}\right)_{x=0} = \int_0^L a(t^4 - t_o^4) + b(t - t_o)^{5/4}\, dx \qquad (A2.7)$$

Equation (A2.7) may be rewritten, using $dx = (\frac{dx}{dt})\,dt$, as follows,

$$\left(\frac{dt}{dx}\right)_{x=L} - \left(\frac{dt}{dx}\right)_{x=0} = \int_{t_H}^{t_c} a(t^4 - t_o^4)\frac{dx}{dt}\,dt + \int_{t_H}^{t_c} b(t - t_o)^{5/4}\frac{dx}{dt}\,dt \qquad (A2.8)$$

$$= \quad I_1 \quad + \quad I_2 \qquad (A2.9)$$

We now evaluate I_1 and I_2 separately.

We have

$$I_1 = \int_{t_H}^{t_c} a(t^4 - t^4)\frac{dx}{dt}\,dt$$

$$= \frac{a}{5}(t^5 - 5t^4 t)\frac{dx}{dt}\Bigg|_{t_H}^{t_c} - \int_{t_H}^{t_c}\frac{a}{5}(t^5 - 5t^4 t)\frac{d^2x}{dt^2}\,dt \qquad (A2.10)$$

The second term in eq (A2.10) involves $\frac{d^2x}{dt^2} = 1 \Big/ \frac{d^2t}{dx^2}$ for which we can substitute using eq (A2.6).

This yields

$$I_1 = \frac{a}{5}(t_c^5 - 5t_o^4 t_c)\left(\frac{dx}{dt}\right)_{x=L} - \frac{a}{5}(t_H^5 - 5t_o^4 t_H)\left(\frac{dx}{dt}\right)_{x=0}$$

$$- \int_{t_H}^{t_c} \frac{a}{5}\,\frac{t^5 - 5t_o^4 t\;\;dt}{a(t^4 - t_o^4) + b(t - t_o)^{5/4}} \qquad (A2.11)$$

Writing the following,

$$c = \frac{a}{5}(t_c^5 - 5t_o^4 t_c) \quad ,$$

$$d = \frac{a}{5}(t_H^5 - 5t_o^4 t_H) \quad ,$$

$$S_2 = \int_{t_H}^{t_c} \frac{a(t^5 - 5t_o^4 t)dt}{5a(t^4 - t_o^4) + 5b(t - t_o)^{5/4}} \quad , \tag{A2.12}$$

we can express I_1 as follows

$$I_1 = c\left(\frac{dx}{dt}\right)_{X=L} - d\left(\frac{dx}{dt}\right)_{X=0} - S_2 \quad . \tag{A2.13}$$

Turning to I_2 in eq (A2.9), we may write

$$I_2 = \int_{t_H}^{t_c} (t - t_o)^{9/4} \left(\frac{dx}{dt}\right) dt$$

$$= \frac{4b}{9}(t - t_o)^{9/4} \left(\frac{dx}{dt}\right)\Bigg|_{t_H}^{t_c} - \int_{t_H}^{t_c} \frac{4b}{9}(t - t_o)^{9/4} \frac{d^2x}{dt^2} dt \tag{A2.14}$$

The second term in eq (A2.14) contains $\frac{d^2x}{dt^2}$, for which we again substitute, using eq (A2.6), to obtain

$$I_2 = \frac{4b}{q}(t_c - t_o)^{9/4}\left(\frac{dx}{dt}\right)_{x=l} - \frac{4b}{q}(t_H - t_o)^{9/4}\left(\frac{dx}{dt}\right)_{x=0} - \int_{t_H}^{t_c} \frac{4b(t-t)^{9/4}\,dt}{9a(t^4 - t_o^4) + 9b(t-t_o)^{5/4}} \quad . \tag{A2.15}$$

Writing the following,

$$e = \frac{4b}{q}(t_c - t_o)^{9/4} ,$$

$$f = \frac{4b}{q}(t_H - t_o)^{9/4} ,$$

$$S_3 = \int_{t_H}^{t_c} \frac{4b(t-t_o)^{9/4}\,dt}{9a(t^4 - t_o^4) + 9b(t-t_o)^{5/4}} , \tag{A2.16}$$

we can express I_2 as follows

$$I_2 = e\left(\frac{dx}{dt}\right)_{x=l} - f\left(\frac{dx}{dt}\right)_{x=0} . \tag{A2.17}$$

Combinination of eqs (A2.9), (A2.13) and (A2.17) yields an equation involving both $\left(\frac{dt}{dx}\right)_{x=l}$ and $\left(\frac{dt}{dx}\right)_{x=0}$, as follows,

$$\left(\frac{dt}{dx}\right)_{x=L} - \left(\frac{dt}{dx}\right)_{x=0} = (c+e)\left(\frac{dx}{dt}\right)_{x=L} - (d+f)\left(\frac{dx}{dt}\right)_{x=0} - (S_2 + S_3) \qquad \text{(A2.18)}$$

Equations (A2.4) and (A2.18) are two equations in two unknowns. We write the following to allow easier algebraic manipulation of the equations,

$$x = \left(\frac{dt}{dx}\right)_{x=0},$$

$$y = \left(\frac{dt}{dx}\right)_{x=L},$$

$$p = (c+e),$$

$$q = (d+f),$$

$$r = (S_2 + S_3). \qquad \text{(A2.19)}$$

Equations (A2.4) and (A2.18) may thus be rewritten as follows

$$y^2 - x^2 = S_1, \qquad \text{(A2.20)}$$

$$y - x = \frac{p}{y} - \frac{q}{x} - r. \qquad \text{(A2.21)}$$

We now eliminate y from eqs (A2.20) and (A2.21) to obtain an expression for X (= $\left(\frac{dt}{dx}\right)_{x=0}$). Re-arranging eq (A2.21) yields

$$\frac{1}{X}(x^2 - rx - q) = \frac{1}{y}(y^2 - p) \qquad \text{(A2.22)}$$

Squaring eq (A2.22), and combining with eq (A2.20) to eliminate y (= $\left(\frac{dt}{dx}\right)_{x=l}$) yields the following

$$(x^2 - rx - q)^2 (S + x^2) - x^2 (x^2 + S - p)^2 = 0 \qquad \text{(A2.23)}$$

which reduces to a fifth power polynomial in X with coefficients as follows

$$\begin{aligned}(-2r)\, x^5 &+ (2p + r^2 - S_1 - 2q)\, x^4 \\ &+ (2rq - 2rS_1)\, x^3 \\ &+ (r^2 S_1 - 2qS_1 + q^2 + 2pS_1 - S_1^2 p^2)\, x^2 \\ &+ (2raS_1)\, x \\ &+ q^2 S_1 = 0 \end{aligned} \qquad \text{(A2.24)}$$

A numerical solution to eq (A2.24) was sought using the NAG library of subroutines available on the the St. Andrews University Digital

VAX/VMS computer. There are five possible values of $(\frac{dt}{dx})_{x=0}$, but only one root has physical significance. The other roots have either non-zero imaginery parts and/or positive real parts. The numerical solution which this calculation yields is the same as that obtained using eq (3.16) in Chapter Three, where implicit assumption is that $(\frac{dt}{dx})_{x=L}$ is identically zero. This assumption is thus justified.

APPENDIX THREE

Sample Computer Program for Thermal Analysis

The thermal analysis presented in Chapter Three involved the numerical solution of a differential equation. This was achieved using the NAG library subroutines available on the St. Andrews University Digital VAX/VMS computer. A sample program, written in Fortran, is shown below (thin-walled approximation). There are calls to two NAG library subroutines; these are labelled D01AHF and D02EBF. Wherever possible, variable names have been chosen so that they coincide as closely as possible with the parameters used in Chapter Three. For example, the variables representing t_c and t_o are called "tc" and "t0" in the program below. In other cases, "common sense" names such as "sigma" and "pi", which represent Stefan's constant and π respectively, have been chosen. Explanatory statements are included in the program, which give a brief account of the main constituent parts.

```
C   THIS IS THE MAIN PART OF THE PROGRAM, FROM
C   WHICH CALLS TO THE SUBROUTINES MAXLEN,
C   SOLVE, HEATLOSS AND OUTPUT ARE MADE.
C   THE PARAMETERS "a" AND "b", AND dtdx0
C   ARE ALSO CALCULATED.
  implicit real*8(a-h,o-z)
```

```
common t0,tc,th,em,k,sigma,r1,r2,wt,a,b,hl,
open(unit=65,name='gen.dat',type='old')
rewind 65
pi=3.1415927
t0=293.0
th=723.0
em=0.2
k=25.0
sigma=5.67d-8
r2=0.5*0.0254*0.5
wt=0.50d-3
tc=373.0
r1=r2-wt
a=em*sigma*2.0*r2/(k*(r2**2.0-r1**2.0))
b=1.32*((2.0*r2)**0.75)/(k*(r2**2.0-r1**2.0))
dtdx0=(8.0*b/9.0)*((tc-t0)**2.25-(th-t0)**2.25)
dtdx0=dtdx0+(2.0*a/5.0)*(tc**5.0-th**5.0-5.0*(tc-th)*t0**4.0)
dtdx0=-dsqrt(-dtdx0)
dtdx0=dtdx0-1.0d-2
call maxlen
call solve
call heatloss
call output
stop
end
C   THIS SUBROUTINE SOLVES THE DIFFERENTIAL EQUATION
C   USING THE NAG LIBRARY SUBROUTINE D02BDF, AND
C   THE TEMPERATURE DISTRIBUTION IS CALCULATED.
```

```
C    CALLS ARE MADE TO THE SUBROUTINES "OUT"
C    AND "FCN".
      subroutine solve
      implicit real*8(a-h,o-z)
      dimension w(1,7),y(1)
      integer ifail,ir,j,n
      common t0,tc,th,em,k,sigma,r1,r2,wt,a,b,hl,ans4,dtdx0,pi
     *  ans4,dtdx0,pi
      external fcn,out
      n=1
      ir=0
      tx0=th
      tx1=tc
      y(1)=0.0
      ifail=0
      tol=0.1d-10
      write(65,100)
100         format(/2x'Temperature Distribution For Segment:',/,
     *  9x'Distance',9x'Temp',/)
      call D02BBF(tx0,tx1,n,y,tol,ir,fcn,out,w,ifail)
      return
      end
      subroutine fcn(t,y,fi)
      dimension t,fi(1),y(1)
      common t0,tc,th,em,k,sigma,r1,r2,wt,a,b,hl,ans4,dtdx0,pi
      temp=(8.0*b/9.0)*((t-t0)**2.25-(th-t0)**2.25)+dtdx0**2.0
      temp=temp+(2.0*a/5.0)*(t**5.0-th**5.0-5.0*(t-th)*t0**4.0)
      fi(1)=1.0/(-dsqrt(temp))
```

```
      return
      end
      subroutine out(tx0,y)
      implicit real*8(a-h,o-z)
      dimension y(1)
      common t0,tc,th,cm,k,sigma,r1,r2,wt,a,b,hl,ans4,dtdx0,pi
      write(65,191)y(1),tx0
191         format(10x,f6.4,10x,f5.1)
      tx0=tx0-(th-tc)/10.0
      return
      end
C     THIS SUBROUTINE CALCULATES THE SLEEVE LENGTH
C     AND USES THE SUB-PROGRAM "FUN4".
      subroutine maxlen
      implicit real*8(a-h,o-z)
      common t0,tc,th,cm,k,sigma,r1,r2,wt,a,b,hl,ans4,dtdx0,pi
      integer npts4,nlimit4,ifail4
      double precision D01AHF
      external fun4
      ifail4=0
      nlimit4=0
      a4=th
      b4=tc
      epsr4=0.1d-4
      ans4=D01AHF(a4,b4,epsr4,npts4,relerr4,fun4,nlimit4,ifail4)
      return
      end
      double precision function fun4(t)
```

```
      implicit real*8(a-h,o-z)
      common t0,tc,th,em,k,sigma,r1,r2,wt,a,b,hl,ans4,dtdx0,pi
      temp=(8.0*b/9.0)*((t-t0)**2.25-(th-t0)**2.25)
      temp=temp+(2.0*a/5.0)*(t**5.0-th**5.0-5.0*(t-th)*t0**4.0)
      fun4=1.0/(-dsqrt(dtdx0**2.0+temp))
      return
      end
       C    THIS SUBROUTINE CALCULATES THE HEAT LOST
       C    BY THE SLEEVE.
      subroutine heatloss
      implicit real*8(a-h,o-z)
      common t0,tc,th,em,k,sigma,r1,r2,wt,a,b,hl,ans4,dtdx0,pi
      hl=-k*pi*(r2*r2-r1*r1)*(dtdx0)
      write(65,29)hl
   29 format(/1x'Anodic Heat Loss = ',d15.4,1x'Watts'/)
      return
      end
       C    THIS SUBROUTINE FORMATS THE OUTPUT DATA.
      subroutine output
      common t0,tc,th,em,k,sigma,r1,r2,wt,a,b,hl,ans4,dtdx0,pi
      write(65,99)t0,tc,th,r1,r2,wt,dtdx0,dtdx1,em
   99 format(//7x'Temperatures: T0 = ',f5.1,2x,'Tc = ',f5.1,2x
     *  ,'Th = ',
     *  f5.1,2x,//,
     *  2x'Radial Dimensions: Inner = ',f6.4,2x,'Outer = ',f6.4,
     *  2x'Wall Thick.= ',f7.5,//,
     *  1x'Temp. Gradients At  X=0: ',d10.3,/21x'X=L: ',d10.3,
     *  //,11x'Emissivity = ',f3.1)
```

```
return
end
```

APPENDIX FOUR

In Chapter Five, eq (5.15) was derived using flow graphs,

$$\tau = \frac{b_1}{a_1} = \frac{k_{11}(1 - e^{i\theta})}{1 - k_{11}^2 e^{i\theta}} \quad . \qquad (A4.1)$$

This expression gives the complex ratio of reflected to incident amplitudes when light is normally incident on a glass plate. Multiplying the numerator and the denominator of eq (A4.1) by the complex conjugate of the denominator to obtain real and imaginery parts yields

$$\tau = \frac{k_{11}(1 - e^{i\theta})(1 - k_{11}^2 e^{-i\theta})}{1 - 2k_{11}^2 \cos\theta + k_{11}^4} \qquad (A4.2)$$

$$= \frac{k_{11}[(1 + k_{11}^2)(1 - \cos\theta) + i \sin\theta (k_{11}^2 - 1)]}{1 - 2k_{11}^2 \cos\theta + k_{11}^4} \qquad (A4.3)$$

The reflectivity is then given by

$$R = \frac{k_{11}^2[(1 + k_{11}^2)^2(1 - \cos\theta)^2 + \sin^2\theta (k_{11}^2 - 1)^2]}{(1 - 2k_{11}^2 \cos\theta + k_{11}^4)^2}$$

$$= \frac{k_{11}^2[2 - 2\cos\theta + 2k_{11}^4(1 - \cos\theta) + 2k_{11}^2(1 - 2\cos\theta + \cos^2\theta - \sin^2\theta)]}{(1 - 2k_{11}^2 \cos\theta + k_{11}^4)^2}$$

$$= \frac{2k_{\parallel}^{2}[(1-\cos\theta) - 2k_{\parallel}^{2}\cos\theta(1-\cos\theta) + k_{\parallel}^{4}(1-\cos\theta)]}{(1 - 2k_{\parallel}^{2}\cos\theta + k_{\parallel}^{4})^{2}} .$$

This simplifies to give the following,

$$R = \frac{2k_{\parallel}^{2}(1-\cos\theta)}{1 - 2k_{\parallel}^{2}\cos\theta + k_{\parallel}^{4}} ,$$

which is the same as the eq (5.17) in Chapter Five.

APPENDIX FIVE

Self-Consistency of the Flow Graph Method

The expressions obtained by the topographical resolution of the flow graph for a glass plate are, from fig 5.9(j) in Chapter Five, as follows,

$$r = k_{11} + \frac{k_{12} k_{21} k_{22} e^{2i\phi}}{1 - k_{22}^2 e^{2i\phi}} \quad , \qquad \text{(A5.1)}$$

$$t = \frac{k_{21} k_{12} e^{i\phi}}{1 - k_{22}^2 e^{2i\phi}} \quad . \qquad \text{(A5.2)}$$

These equations represent the complex ratio of reflected to incident amplitudes (r), and the complex ratio of transmitted to incident amplitudes (t), respectively. Equations (A5.1) and (A5.2) may be simplified using the relations between the Fresnel coefficients (eq (5.5) in Chapter Five) as follows,

$$r = \frac{k_{11} - k_{11} e^{2i\phi}}{1 - k_{11}^2 e^{2i\phi}} \qquad \text{(A5.3)}$$

$$t = \frac{(1 - k_{11}^2) e^{i\phi}}{1 - k_{11}^2 e^{2i\phi}} \qquad \text{(A5.4)}$$

The reflection and transmission coefficients are then given by

$$R = |r|^2 \quad , \tag{A5.5}$$

$$T = |t|^2 \quad . \tag{A5.6}$$

Combining eqs (A5.3) and (A5.5) yields

$$R = \frac{2k_{\parallel}^2(1-\cos 2\phi)}{1-2k_{\parallel}^2\cos 2\phi + k_{\parallel}^4} \quad , \tag{A5.7}$$

as outlined in Appendix Four. Similarly, eqs (A5.4) and (A5.6) may be combined to give

$$T = \frac{1-2k_{\parallel}^2+k_{\parallel}^4}{1-2k_{\parallel}^2\cos 2\phi + k_{\parallel}^4} \quad . \tag{A5.8}$$

Adding eqs (A5.7) and (A5.8) together, we obtain

$$R + T = 1 \quad , \tag{A5.9}$$

which provides a self-consistency check for the application of flow graphs to optical boundaries.

APPENDIX SIX

Sample Program for Flow Graph Design of Broad Band Laser Optics

The sample program shown below calculates the reflectivity characteristics of a multi-layer dielectric laser mirror, designed for use as an output coupler for a He-Cd white light laser. The program is written such that the layer structure can be quickly reviewed and, if necessary, altered. This facilitates the design of multi-layer mirrors, where the design is based on a "trial and error" method.

The program consists of two large sub-programs and several smaller subroutines. The first sub-program calculates the reflectivity of the layer structure, in 1 nm steps, by making calls to the second sub-program, each time the wavelength "wv" is altered. The second sub-program contains information about the layer structure, and makes calls to the subroutines HL, LH, LS, HS, AH and/or AL in the order in which they have been written. There are three values of λ_o, called "wv0" in the second sub-program, which correspond approximately to the three primary colours. The program includes explanatory statements which give a brief outline of the constituent parts.

```
      C    THIS IS THE FIRST SUB-PROGRAM, WHICH
      C    CHANGES THE WAVELENGTH IN 1 nm STEPS
      C    AND CALCULATES THE REFLECTIVITY AT EACH
      C    WAVELENGTH BY MAKING CALLS TO THE SECOND
      C    SUB-PROGRAM. COMPLEX VARIABLES START
      C    THE LETTER "c".
      implicit complex*8(c)
      implicit real*4(a-b,d-h,o-z)
      common crkhs,crkls,crkhl,crklh,crkah,crkal,
     *  cd,Cls,Chs,Chl,Clh,Cal,Cah,cth0
      external fun
      dimension wave(301),ref(301)
      open(unit=50,name='flow1.dat',type='old')
      wv=375.0e-9
      do 10 i=1,301
      wave(i)=wv
      ref(i)=fun(wv)
      wv=wv+1.0e-9
   10 continue
      do 30 i=1,301
      write(50,20)wave(i),ref(i)
   20 format(1x,e12.3,f8.1)
   30 continue
      stop
      end
      C    THIS IS THE SECOND SUB-PROGRAM, WHICH CONTAINS
      C    THE LAYER STRUCTURE OF THE LASER MIRROR.
```

```
C    CALLS ARE MADE TO THE SUBROUTINES HL, LH,
C    AL, AH, HS AND/OR LS IN THE SAME ORDER AS
C    APPEAR BELOW. REFRACTIVE INDICES START
C    THE LETTERS "ri", AND FRESNEL COEFFICIENTS
C    WITH THE LETTERS "rk".
real function fun(wv)
implicit complex*8(c)
implicit real*4(a-b,d-h,o-z)
common crkhs,crkls,crkhl,crklh,crkah,crkal,
  *  cd,Cls,Chs,Chl,Clh,Cal,Cah,cth0
ris=1.5
ril=1.38
rih=2.3
ria=1.0
rkhs=-(ris-rih)/(ris+rih)
rkls=-(ris-ril)/(ris+ril)
rkhl=-(ril-rih)/(ril+rih)
rklh=-(rih-ril)/(rih+ril)
rkah=-(rih-ria)/(rih+ria)
rkal=-(ril-ria)/(ril+ria)
crkhs=cmplx(rkhs,0.0)
crkls=cmplx(rkls,0.0)
crkhl=cmplx(rkhl,0.0)
crklh=cmplx(rklh,0.0)
crkah=cmplx(rkah,0.0)
crkal=cmplx(rkal,0.0)
rpi=3.1415927
wv0=450.0e-9
```

```
th0=rpi*wv0/wv
cth0=cmplx(0.0,th0)
call LS
call HL
call LH
call HL
call LH
call HL
call LH
call HL
call LH
call HL
call LH
call HL
wv0=530.0e-9
th0=rpi*wv0/wv
cth0=cmplx(0.0,th0)
call LH
call HL
call LH
call HL
wv0=650.0e-9
th0=rpi*wv0/wv
cth0=cmplx(0.0,th0)
call LH
call HL
call LH
call HL
```

```
call LH
call HL
call AH
tempe=cabs(Cd)
fun=(tempe**2.0)*100.0
return
end
 C   THE REMAINDER OF THE PROGRAM CONSISTS OF
 C   SUBROUTINES, ONE FOR EACH OF THE OPTICAL
 C   BOUNDARIES WHICH MAY BE REQUIRED IN THE
 C   DESIGN OF THE LASER MIRROR. EACH SUBROUTINE
 C   THUS CONTAINS THE CHARACTERISTIC FLOW GRAPH
 C   PARAMETER FOR THE PATICULAR BOUNDARY WHICH
 C   IT DESCRIBES.
subroutine LS
implicit complex*8(c)
implicit real*4(a-b,d-h,o-z)
common crkhs,crkls,crkhl,crklh,crkah,crkal,
  *  cd,Cls,Chs,Chl,Clh,Cal,Cah,cth0
Cd=cmplx(0.0,0.0)
Cls=(ckrls+Cd*cexp(cth0))/(1.0+ckrls*Cd*cexp(cth0))
Cd=Cls
return
end
subroutine HS
implicit complex*8(c)
implicit real*4(a-b,d-h,o-z)
common crkhs,crkls,crkhl,crklh,crkah,crkal,
```

```
     *   cd,Cls,Chs,Chl,Clh,Cal,Cah,cth0
    Cd=cmplx(0.0,0.0)
    Chs=(crkhs*Cd**cexp(cth0))/(1.0+crkhs*Cd**cexp(cth0))
    Cd=Chs
    return
    end
    subroutine LH
    implicit complex*8(c)
    implicit real*4(a-b,d-h,o-z)
    common crkhs,crkls,crkhl,crklh,crkah,crkal,
     *   cd,Cls,Chs,Chl,Clh,Cal,Cah,cth0
    Clh=(crklh*Cd**cexp(cth0))/(1.0+crklh*Cd**cexp(cth0))
    Cd=Clh
    return
    end
    subroutine HL
    implicit complex*8(c)
    implicit real*4(a-b,d-h,o-z)
    common crkhs,crkls,crkhl,crklh,crkah,crkal,
     *   cd,Cls,Chs,Chl,Clh,Cal,Cah,cth0
    Chl=(crkhl*Cd**cexp(cth0))/(1.0+crkhl*Cd**cexp(cth0))
    Cd=Chl
    return
    end
    subroutine AH
    implicit complex*8(c)
    implicit real*4(a-b,d-h,o-z)
    common crkhs,crkls,crkhl,crklh,crkah,crkal,
```

```
     *   cd,Cls,Chs,Chl,Clh,Cal,Cah,eth0
    Cah=(erkah*Cd**cexp(eth0))/(1.0+erkah**Cd**cexp(eth0))
    Cd=Cah
    return
    end
    subroutine HH
    implicit complex*8(c)
    implicit real*4(a-b,d-h,o-z)
    common erkhs,erkls,erkhl,erklh,erkah,erkal,
     *   cd,Cls,Chs,Chl,Clh,Cal,Cah,eth0
    Chh=(0.0+Cd**cexp(eth0))
    Cd=Chh
    return
    end
    subroutine AL
    implicit complex*8(c)
    implicit real*4(a-b,d-h,o-z)
    common erkhs,erkls,erkhl,erklh,erkah,erkal,
     *   cd,Cls,Chs,Chl,Clh,Cal,Cah,eth0
    Cal=(erkal*Cd**cexp(eth0))/(1.0+erkal**Cd**cexp(eth0))
    Cd=Cal
    return
    end
```